The role of the bacterial cell surface and extracellular macromolecules in U(VI) biosorption and biomineralisation.

The University of Sheffield
Faculty of Social Science
Department of Geography

Joseph Hufton
May 2016

Supervisors: Dr. María Romero-González and Prof. John Harding

Submitted to The University of Sheffield in part-fulfilment of the requirements for the degree of Doctor of Philosophy.

Declaration

The work described herein was conducted at The University of Sheffield between September 2012 and May 2016 under the supervision of Dr. María Romero-González and Prof. John Harding. This thesis and the work described within it was completed solely by the author and has not been submitted in whole or part for any other degree at this or any other institution.

Joseph Hufton

May 2016

Acknowledgments

I would like to thank Dr. María Romero-González and Professor John Harding for their support and giving me the opportunity to undertake this research. I would like to thank, in particular, Dr. Emma Wharfe, Dr. Mathew Pringle, Dr. Gwen Chimonides, Dr. Harry Langford, Dr. Rachel Walton, Thomas Turton, Lygia Eleftheriou and Debbie Hill. When it was hard, their help and advice made it much easier and a thoroughly enjoyable environment to work in.

I would like to extend my thanks to Professor Mohamed Merroun for his invitation to conduct experimental work at the University of Granada. Professor Thomas Smith and Dr. Sarah Haywood-Small at Sheffield Hallam University require special thanks for letting me utilise their instrumentation. Their expertise has been influential in the development of my project. I want to acknowledge the EPSRC and Santander for funding this work.

Finally, I would especially like to thank my family (Michael and Andrea Hufton) and friends (Alex, Scott, Craig, to name a few) for their encouragement and support that has kept me sane throughout this process.

Summary

Uranium biosorption and biomineralisation are processes exhibited by bacteria that aren't fully understood at a mechanistic level, making it difficult to consider their use and application in remediation, extraction and reuse. The aim of this study was, therefore, to deconstruct the bacterial cell and characterise the specific roles of cell surface structures and extra polymeric substances, in order to elucidate their contribution to the biosorption and biomineralisation of uranium within live cells.

The complexation and precipitation of uranium with extracellular DNA (eDNA) was predominantly mediated by negatively charged phosphate moieties within eDNA. The reaction was dependent on pH, where the formation of a precipitate was reduced as the pH increased. Towards circumneutral pH, acid phosphatase liberated phosphate from eDNA that precipitated uranium as a phosphate-bearing mineral.

The biosorption of uranium with bacteria is governed by the interactions with functional groups at the cell surface. The cell wall isolates and lysed cells of *B. subtilis* 168 exhibited a greater uranium retention capacity in comparison to those from *P. putida* 33015, live cells and cell membrane isolates from both strains. Carboxyl groups and phosphate groups, from proteins and phosphorylated biopolymers, were responsible uranium biosorption with the cell surface structures.

The viability and metabolic activity of live cells of *P. putida* 33015 and *D. radiodurans* R1 in the presence of uranium was evaluated. An increase in uranium concentration was directly linked to cell toxicity in both strains. At low concentrations of U(VI) and circumneutral pH, viable cells likely sequestered uranium either through biosorption or through the precipitation of enzymatically generated uranium phosphate minerals that were tethered to the cell surface or within EPS as a tolerance mechanism to cope with uranium toxicity. At higher concentrations of uranium or at low pH where the bacterial growth wasn't favourable or there was cell death, biosorption to the bacterial biomass present likely occurred.

Publications and Presentations

PUBLICATIONS FROM THIS THESIS;

ROMERO-GONZALEZ, M., NWAOBI, B., HUFTON, J.M., GILMOR, D.J. 2016, *Ex-situ* bioremediation of U(VI) from contaminated mine water using *Acidithiobacillus ferrooxidans* strains. *Frontiers in Environmental Science*, 4(39)

HUFTON, J.M., HARDING, J.H., ROMERO-GONZALEZ, M. Submitted 2016, The role of extracellular DNA in uranium precipitation and biomineralisation. *Physical Chemistry Chemical Physics.*

HUFTON, J.M., HARDING, J.H., ROMERO-GONZALEZ, M. In preparation, Uranium biosorption with bacterial cell surface structures.

HUFTON, J.M., MERROUN, M.L., HAYWOOD-SMALL, S., HARDING, J.H., ROMERO-GONZALEZ, M. In preparation. Tolerance and toxicity mechanisms exhibited by bacteria to uranium.

POSTER PRESESENTATIONS AT CONFERENCES;

HUFTON, J.M., MERROUN, M.L., HARDING, J.H., ROMERO-GONZALEZ, M. Uranium biomineralisation from aqueous environments using bacteria and macromolecules of bacterial origin. *Biomineralisation Gordon Research conference (GRC)*, 2014, New London, New Hampshire, USA.

HUFTON, J.M., HARDING, J.H., ROMERO-GONZALEZ, M. The use of extracellular DNA in uranium biomineralisation, *Goldschmidt conference*, 2015, Prague, Czech Republic.

Abreviations

aPO_4	Abiotic orthophosphate
ATR	Attenuated Total Reflectance
CFU	Colony Forming Units
CTC	5-cyano-2,3-ditolyl tetrazolium chloride
DOE	Department of Energy
eDNA	Extracellular Deoxyribonucleic Acid
EDX	Energy-dispersive X-ray
ePO_4	Enzymatic orthophosphate
EPS	Extra Polymeric Substances
EXAFS	Extended X-Ray Absorption Fine Structure
FDA	Fluorescein Diacetate
FSC	Forward Scatter
FT-IR	Fourier Transform Infrared
FWHM	Full Width Half Maximum
HAADF-STEM	High-Angle Annular Dark Field-Scanning Transmission Electron Microscopy
ICDD	International Centre for Diffraction Data
ICP-AES	Inductively Coupled Plasma-Atomic Emission Spectroscopy
ICP-MS	Inductively Coupled Plasma-Mass Spectrometry
IR	Infrared
LPM	Low Phosphate Media
LPS	Lipopolysaccharide
MIC	Minimum Inhibitory Concentrations
MTC	Maximum Tolerated Concentration
OD	Optical Density
PI	Propidium Iodide
PZC	Point of Zero charge
SEM	Scanning Electron Microscopy
SSC	Side Scatter
TEM	Transmission Electron Microscopy
TRLFS	Time-Resolved Laser-Induced Fluorescence Spectroscopy
XANES	X-ray Absorption Near Edge Structure
XAS	X-ray Absorption Spectroscopy
XPS	X-ray Photoelectron Spectroscopy
XRD	X-ray Diffraction

Table of Contents

Chapter 1: Introduction.

1.1 Uranium in the environment

Uranium is a naturally occurring radioactive element found within the Earth's crust at a concentration of approximately 1.8 ppm, contributing towards low level background radiation (Lloyd and Renshaw, 2005, Appleton, 2007). Erosion and weathering cause uranium to be found in soils and groundwater. Within the environment, uranium naturally occurs as three isotopes; U^{234}, U^{235} and U^{238}. The latter two represent 0.72 % and 99.27 % of its abundance with half-lives of 7×10^8 and 4.4×10^9 years, respectively. The small percentage of U^{234} accounts for approximately half of its α-activity since it has a half-life of only 246,000 years (Gavrilescu et al., 2009).

An increase in uranium mining and milling for the nuclear fuel cycle and other industrial processes has resulted in elevated levels of uranium in the environment arising from releases during mining and from waste produced during enrichment and reprocessing (Lloyd and Renshaw, 2005). The large quantities of radioactive waste from the nuclear fuel fabrication process have been stored for decades. Leaching of these waste materials into nearby ground water and soil sediments, due to ineffective storage mechanisms, has resulted in uranium entering the food and water supply, ultimately becoming a hazard to human health. It has been reported that uranium concentrations exceeded the water drinking standard at 29 unregulated sources from abandoned mining areas within the territory of the Navajo nation which are used by up to 59,000 people (USA-EPA, 2014). Additionally, the concentration of uranium in ground water and supply wells in the Punjab (India) and California (USA) have been reported up to 200 ppb (Alrakabi et al., 2012, Belitz et al., 2015). Within the human body, uranium compounds can affect the renal system, resulting in kidney failure, amongst other toxic and carcinogenic effects (Choy et al., 2006, Gavrilescu et al., 2009). Therefore, the safe removal and detoxification of these contaminants is of great importance, with current bioremediation technologies showing promise.

Uranium can be found in soil and groundwater in various forms, such as complexes with various molecules, precipitates and reduced forms (Zhou and Gu, 2005). Within soils, the most common form of uranium is a soluble oxidised form such as uranyl carbonate (Roh et al., 2000). Factors affecting the mobility and solubility in soil include pH, temperature, water availability, redox and oxidation capabilities and microbial activity (Gavrilescu et al., 2009). Redox reactions are a main factor that affects the mobility of uranium within the environment. Uranium has five oxidation states; these are 0 (the

metal), +3, +4, +5 and +6. The +6 and +4 oxidation states are the most biologically important states and are involved in redox reactions that transform uranium within soil and ultimately regulate its mobility within the environment (Gavrilescu et al., 2009).

Uranium (VI) compounds are highly soluble in acidic conditions. The most common form is the toxic, highly mobile UO_2^{2+} cation in oxidising conditions. Hydroxyl complexes, such as $UO_2(OH)^+$, are found closer to neutral pH (Newsome et al., 2014, Markich, 2002). Within carbonate rich environments, UO_2^{2+} forms soluble complexes such as UO_2CO_3 at circumneutral pH and $UO_2(CO_3)_3^{4-}$ at more alkaline pH, affecting the degree of dissolution of uranium in contaminated soil and natural waters (Mason, 1997, Ikeda et al., 2007). Furthermore, UO_2^{2+} forms strong complexes with iron oxides, clay minerals and other organic materials within soils (Newsome et al., 2014) Additionally, it readily forms anionic complexes in solution with a strong binding affinity for phosphate ligands in comparison with other anions such as sulphate, chloride and fluoride (Dozol et al., 1993).

Uranium (IV) readily forms insoluble minerals such as uraninite (UO_2). This oxidation state of uranium is less toxic than U(VI) as it is far less soluble. The reduction of soluble U(VI) to insoluble U(IV) and its re-oxidation affects the mobility of the radioactive material within the environment. This reduction of uranium to a less toxic form forms the basis for many bioremediation practices (Gavrilescu et al., 2009). Uranium (III) is an unstable oxidation state in water as it easily removes hydrogen, oxidising to U(VI). Uranium (V) is also a highly unstable oxidation state, being readily oxidised to U(VI) or reduced to U(IV) (Gavrilescu et al., 2009).

Chemical and biological techniques have been applied to the remediation of uranium-contaminated soils in its ability to complex with organic substances and also its redox transformation capabilities are exploited. Chemical remediation technologies that are used to reduce radioactive waste include the degradation of the contaminant and redox reactions to affect the solubility of the contaminant (Zhou and Gu, 2005). These chemical techniques can increase the mobility of uranium within the environment, increasing its complexation capacity for subsequent concentration within biomass. This includes U(IV) leaching using sodium peroxide for subsequent concentration of U(VI) in bacterial biomass (Abd El-Sabour, 2007) and citric acid to promote uranium mobility for subsequent removal (Lenhart et al., 2000, Gavrilescu et al., 2009). Furthermore, utilising the uranium-carbonate speciation capabilities within solution, U(VI) can be leached from

solution by the addition of carbonate and bicarbonate ions to form soluble tricarbonate complexes, increasing its dissolution and recovery using ion exchange resin (Mason, 1997). U(VI) can also be extracted from phosphate bearing minerals since uranium has a preferential binding affinity for carbonate at higher pH (Buck et al., 1996). However, these techniques had low specificity for targeting metal remediation and are cost-ineffective. Another drawback is the difficulty of applying chemicals without generating large quantities of secondary hazardous waste materials (Francis et al., 1998).

Although there are plenty of additional chemical techniques available, biologically based remediation techniques (bioremediation) provide a cheap and efficient alternative that can utilise the enzymatic reductive power of bacteria to produce U(IV) minerals and their biosorbent and enzymatic precipitation capabilities to sequester U(VI) phases (Merroun and Selenska-Pobell, 2008, Neu et al., 2010, Newsome et al., 2014, Choudhary and Sar, 2015).

The requirement of an anaerobic environment for sustained immobilisation of uranium in its reduced, +4, oxidation state is an important factor in harnessing microorganism's enzymatic reductive power. The enzymatic redox transformations of U(VI) and U(IV) have been studied comprehensively (Wall and Krumholz, 2006). The first mechanisms proposed by which U(VI) was reduced to U(IV) were investigated using the Fe(III) reducing bacteria *Geobacter metallireducens* (Lovley et al., 1991, Gorby and Lovley, 1992). This early work has formed the basis for many future studies that demonstrated the importance of *c*-type cytochrome proteins in the transfer of electrons between membranes of Gram-negative bacteria for U(VI) reduction. *D. vulgaris* (Lovley et al., 1993), *G. sulferreducens* (Lloyd et al., 2003, Orellana et al., 2013) and *Shewanella* species (Wall and Krumholz, 2006) have all shown this reduction ability. Uraninite (UO_2) has been characterised as a common product of this enzymatic reduction with precipitates located both at the cell surface and extracellular (Lovley and Phillips, 1992, Suzuki et al., 2002, Lee et al., 2010). Non-crystalline (monomeric) products of U(VI) reduction that incorporated inorganic ligands such as phosphate have been found such as ningyoite (Bernier-Latmani et al., 2010). This was formed following the reduction of the U(VI)-phosphate complex uramphite by *T. ferrireducens* (Khijniak et al., 2005). *In situ* U(VI) reduction had previously been demonstrated in a number of field studies with varying degrees of success. These sites included the former uranium ore reprocessing facility US

DOE rifle site in Colorado, the Oak Ridge waste disposal site in Tennessee and the fuel fabrication site at Hanford, Washington (Newsome et al., 2014).

The poor stability of these reduced products within aerobic environments resulted in the reoxidation of U(IV) minerals, suggesting that the development of bioremediation technologies that harness the enzymatic reductive power of bacteria is not feasible (Wall and Krumholz, 2006, Merroun and Selenska-Pobell, 2008). Reoxidation of U(IV) minerals has been observed in the presence of oxygen (Abdelouas et al., 1999, Duff et al., 1999), nitrates or nitrites (Finneran et al., 2002, Senko et al., 2002, Senko et al., 2005b), carbonates (Choudhary and Sar, 2015), Fe(III) hydroxides (Senko et al., 2005a, Nevin and Lovley, 2000), organic ligands (Luo and Gu, 2011, Singh et al., 2014) and microbial oxidation activity (Dispirito and Tuovinen, 1982, Newsome et al., 2015a). Due to this poor stability of UIV) minerals, the biosorbent and U(VI) precipitating capabilities of indigenous bacteria to sequester aqueous U(VI) from aerobic environments have been investigated. However, the processes involved are not yet fully understood.

1.2 Uranium bioremediation using bacterial biomass in aerobic environments

1.2.1 Biosorption and bioaccumulation

1.2.1.1 What is biosorption?

Biosorption is a metabolism-independent biological process by which metal species, compounds and particulate materials can be removed from solution through complexation with biomass (Gadd, 1993). The origin of this biomass can vary depending on the sorbate requiring removal from solution, the environmental origin of the reactant materials and the availability of functional groups within the sorbent material. Live and dead biomass and associated biomolecules can be used to remove metals from industrial processes from solution, reducing the level of contaminants within the environment that can be a hazard to human health (Wang and Chen, 2009, Dobson and Burgess, 2007). The generation and application of this biomass is relatively inexpensive compared to the chemical and physical removal technologies used, such as chemical complexation, solvent extraction and ion exchange resins (Volesky, 2001, Gavrilescu et al., 2009). Understanding the bacterial cell surface for the mechanistic processes involved in biosorption is therefore essential (Das, 2010).

Uranium-microbial biosorption interactions are unique for each bacterial species with specific parameters varying, such as solution pH, physiological cell state and the presence of certain polymers affecting the availability of uranium favourable functional groups (Merroun and Selenska-Pobell, 2008).

1.2.1.2 Bacterial cell surface characterisation

Bacterial biomass retains uranium from aqueous environments through electrostatic and chemical interactions at its surface, independent of metabolic activity. The complex surface structures of bacterial biomass provide a large number of binding sites for U(VI) species that vary with pH and ionic strength. The outermost region of the bacterial cell is its cell wall and associated biopolymers that are exposed to the external environment. These provide support, shape and protection from osmotic lysis and toxic materials. Therefore it is hypothesised that U(VI) species interact more favourably with functional groups within the cell wall structures. The availability of functional groups varies with bacterial strain, in particularly due to their cell wall architecture; whether it is of Gram-

positive or Gram-negative origin (Merroun and Selenska-Pobell, 2008, Wang and Chen, 2009).

The Gram-positive cell wall is made primarily of a carboxylic rich 25-80 nm thick peptidoglycan layer composed of alternating repeating subunits *N*-acetyl glucosamine (NAG) and *N*-acetylmuramic acid (NAM). The latter can interact with peptide chains of alternating D and L- amino acids through carboxyl groups while cross bridges can form between adjacent peptide chains. The presence of other proteins associated with cell walls contribute to the number of amino groups within the Gram-positive cell surface. The Gram-positive cell wall also contains large amounts of teichoic and lipoteichoic acids, the latter of which are covalently anchored to a plasma membrane lipid. Teichoic acids are polyphosphate polymers of modified ribotol or glycerol phosphate interconnected by negatively charged phosphate groups that covalently bind to the peptidoglycan through NAM. These extend the surface of the cell wall, exposing negatively charged phosphate and carboxyl groups from interconnected polymers and associated peptide protein chains. This aids in giving the bacterial surface an overall net negative charge, ideal for metal cation biosorption (Wang and Chen, 2009).

The cell wall structure of Gram-negative bacteria is more complex. The peptidoglycan layer is much smaller in size (approximately 2 to 7 nm thick with far fewer peptide cross bridges) and is covalently bound to a characteristic outer membrane that is composed of phospholipids, associated proteins and lipopolysaccharides (LPS). Additional transmembrane proteins, called porins, facilitate the movement of hydrophilic small molecules through the outer membrane. Several different porins exist either of specific or non-specific binding origin. The intermediate space between the outer and cell surface membrane is the periplasmic space and is filled with a gel-like matrix (periplasm) that contains various enzymes and proteins (Madigan, 2008).

LPS is a macromolecular complex consisting of 3 regions; lipid A, the core polysaccharide region and the repeating O-antigen. The lipid A is anchored into the outer membrane with the remaining subunits protruding from the Gram-negative cell wall into the external environment. Phosphorylated sugars within the core polysaccharide and carboxyl groups within the protruding regions contribute to the overall negative charge that has been demonstrated to interact with metal cations (Ferris and Beveridge, 1986, Langley and Beveridge, 1999, Barkleit et al., 2008, Barkleit et al., 2011).

The cell surface membranes surround the internal environment and control the transport of substances in and out of the cells. Microbial cell surface membranes are composed primarily of a phospholipid double layer with the hydrophobic lipid groups facing inwards and the hydrophilic phosphate groups exposed to the aqueous environment inside and outside the cell. Hydrophobic proteins transverse the fatty acid bilayer and incorporate into the membrane while hydrophilic proteins and metal cations could attach to the phosphate surface.

Many bacterial species can produce and secrete biomolecules, known as extra polymeric substances (EPS), into their external environment. Bacterial EPS was originally believed to be predominantly composed of polysaccharides and other carbohydrate related molecules. Recent characterisation of EPS from various bacteria suggests a far more complex array of various biomolecules, such as nucleic acids, proteins and peptides, lipid, glycolipids and lipopolysaccharides (Marvasi et al., 2010, Wingender et al., 1999). Although not essential for sustained bacterial growth and cell viability, the presence of EPS is important for cell survival within natural environments through the formation of microbial biofilms and their adhesion to surfaces (Tay et al., 2001, Sutherland, 2001, Comte et al., 2006, Knox et al., 2008, Beveridge, 1988).

The composition of EPS varies between bacterial species and not all bacteria produce EPS. For example, EPS extracted from *Acinetobacter* sp. 12S was very carbohydrate and sugar-acid rich, containing biomolecules such as pyruvic and uronic acids accounting for 548 mg g^{-1} of EPS (Pirog et al., 2004). *T. ferrooxidans* R1 had approximately a 50:50 total sugar : lipid content (Gehrke et al., 1998) while capsulated and free EPS extracted from *P. putida* contained far more proteins than carbohydrates (Kachlany et al., 2001). The composition and production of EPS can differ under different environmental conditions and stresses. It has been suggested that a lack of essential nutrients such as phosphate and an excess of carbon stimulated EPS synthesis (Gehrke et al., 1998). Furthermore, in the presence of heavy metals, elevated levels of protein, carbohydrates and extracellular DNA (eDNA) were produced (Priester et al., 2006).

Extracellular DNA is an important component in many bacterial biofilms in soil and water and can contributed numerous functional moieties essential for extracellular uranium biosorption. It can be used as a carbon, nitrogen and phosphorus nutrient source (Pinchuk et al., 2008) while the nucleotides can be reabsorbed by bacteria (Pietramellara et al., 2009). The main source of eDNA is likely to be the lysis of dead bacterial cells

(Nielsen et al., 2007, Levy-Booth et al., 2007). The lysis of dead cells is mediated by quorum-sensing dependent mechanisms such as acylated homoserine lactones (AHL) and *Pseudomonas* quinolone signals (PQS). The production of cell lysis factors such as prophages and phenazines induced cell lysis and subsequent eDNA release (Allesen-Holm et al., 2006, Das et al., 2013). Furthermore, the production of autolysins, such as proteases and other enzymes, promoted cell surface breakdown and eDNA release. *Deinococcus radiodurans* secrete damaged portions of genomic DNA into its EPS. These are then replaced by *de novo* synthesis (Battista, 1997). Other genera such as *Bacillus* and *Pseudomonas* released eDNA into their liquid media during bacterial growth (Matsui et al., 2003). This suggested that in certain species, such as *Pseudomonas putida* and *Bacillus cereus,* eDNA is up to 50 % more abundant than cellular DNA and is fundamental in biofilm formation (Vilain et al., 2009, Steinberger and Holden, 2005). Furthermore, the presence of eDNA may enhance the mechanical stability of the bacterial biofilm and promote bacterial adhesion to mineral surfaces. This will encourage subsequent biofilm formation through the acid-base attaction between electron accepting and donating moieties on surface substrate bacterial cells and eDNA binding with EPS biopolymers and metabolites (Das et al., 2011, Das et al., 2013). A schematic of the bacterial cell surface is shown in Figure 1.

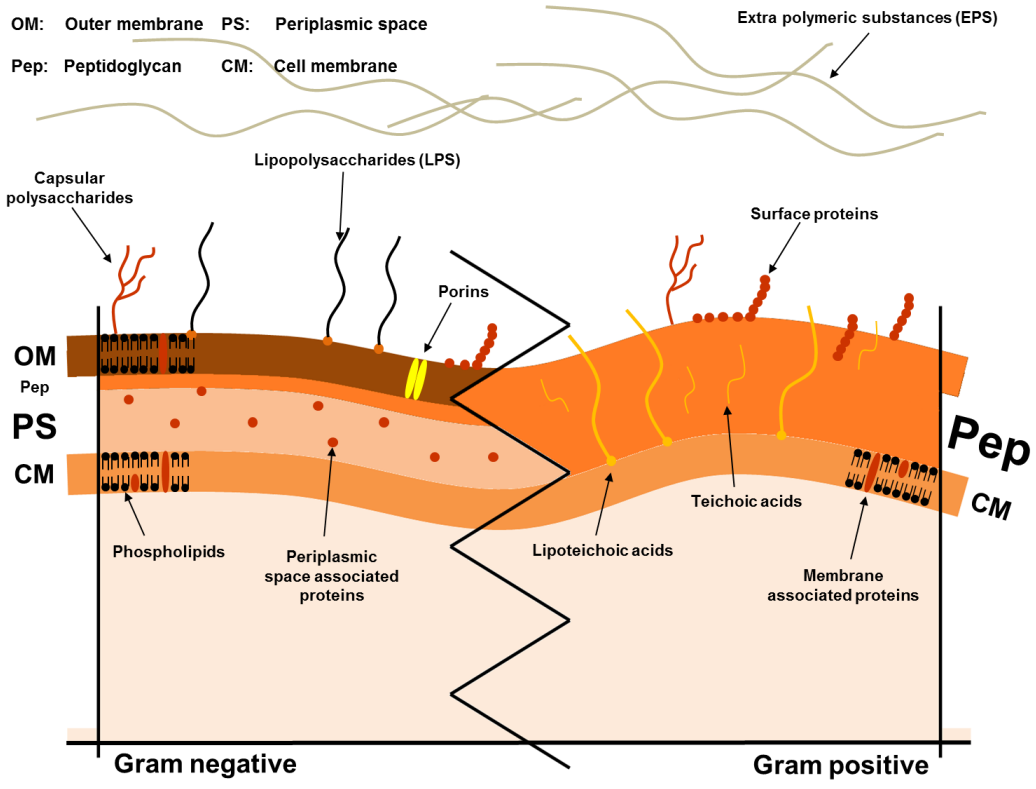

Figure 1. Cell surface composition of Gram-negative and Gram-positive bacteria.

1.2.1.2.1 Cell surface characterisation techniques

Experimental techniques can be used to characterise the bacterial cell surface and associated biopolymers. They help to determine the presence of functional groups, their protonation state, essential for characterising the processes involved in uranium biosorption

1.2.1.2.1.1 Fourier transform infrared (FT-IR) spectroscopy

FT-IR is a well established technique to identify the functional groups and chemical cell properties of bacterial biomass by analysing the positions and relative intensities of infrared adsorption bands. These adsorption bands correspond to biological functional groups within the bacterial biomass and their relative intensity gives the relative abundance of the biologically related molecules and their associated functional groups. Any changes in the cell structure due to interaction with other components in the environment will therefore be reflected in their infra-Red (IR) spectra. IR spectroscopy utilises IR radiation to interact with a sample whose functional groups absorb the radiation at certain wavelengths. Changes in the dipole moment of a bond is due to either bending, stretching and twisting vibrations of that bond. The frequency (wavenumber, cm^{-1}) of these vibrations in the mid-infrared region (4000-400 cm^{-1}) corresponds to specific bonds, with weaker bonds requiring less energy to vibrate, such as single bonds. Double bonds and bonds with lighter atoms (e.g. O-H) vibrate at a higher frequency. These frequencies can be used to characterise the functional groups associated with proteins, lipids, polysaccharides, polyphosphates in bacterial cells (Ojeda and Dittrich, 2012, Baker et al., 2014).

Typically, an IR spectrum is generated by measuring the intensity of the infrared radiation before and after it passes through the sample. The adsorption (A) at a given frequency can be calculated as below, Equation 1, where I_o is the initial beam intensity and I is the beam intensity following sample absorption.

$$A = -\log_{10}\frac{I}{I_O} \qquad \text{Equation 1.}$$

Infrared radiation is generated and directed towards the interferometer using a sequence of mirrors where the radiation is separated into two by a strategically placed beam splitter. The two beams are reflected off an immobile mirror at a known distance and transmitted through the beam splitter again to reflect with a mobile mirror at a measureable distance. The beams recombine and constructive interference is produced

from the reflected beam and destructive interference from the transmitted beam. The distance separating the mobile and immobile mirrors determines the level of interference. This process produces two beams, one of which is directed towards the sample and measured as an interferogram of the infrared radiation transmitted through the sample by a detector, with the other beam directed back to the power source. The rapid analysis of all frequencies within a given region is achieved by the converter that Fourier transforms the interferogram to produce a frequency spectrum, Figure 2.

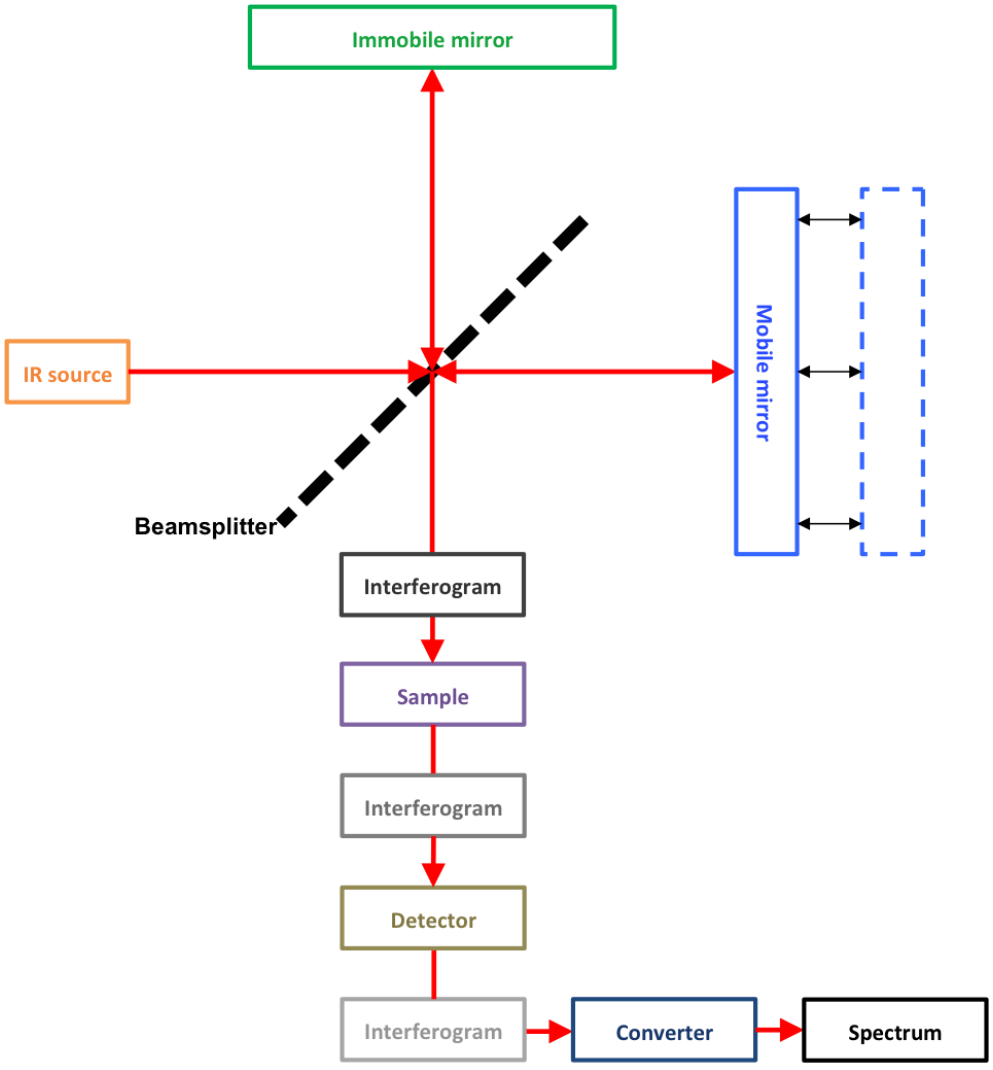

Figure 2. FT-IR schematic sketch including the interferometer.

When measuring the infrared spectrum of biological samples, hydration can be an issue because the infrared absorption of water (ν (O-H)) is very strong. This can result in large peaks that can conceal other biologically relevant functional groups in close proximity. To overcome this issue without sample dehydration, attenuated total reflectance (ATR) FT-IR can be used, rather than commonly used transmission techniques. An ATR

accessory contains a crystal with a high refractive index (such as germanium or diamond). When using an ATR accesary, the infrared beam is directed through the crystal and reflects from the internal surface to create an evanescent wave. This wave penetrates and is partially absorbed by the sample (that is in direct contact with the crystal) and the remaining reflected radiation is sent to the detector, Figure 3.

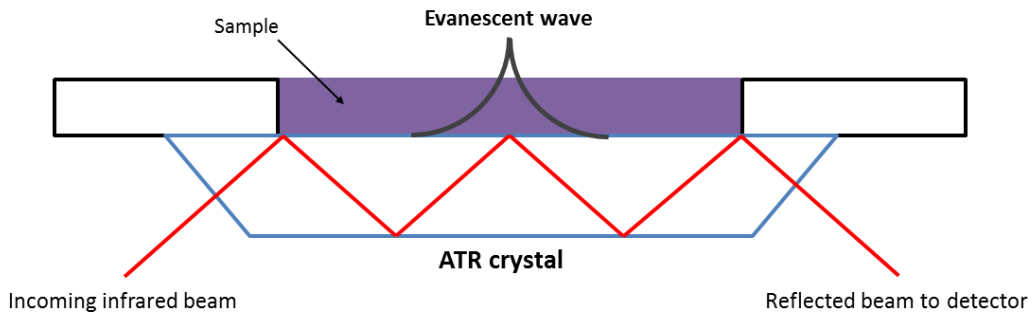

Figure 3. ATR schematic.

This non-destructive sample technique has been used to characterise the functional groups present within whole cells (Ojeda et al., 2009, Ojeda et al., 2008a, Parikh and Chorover, 2006), cell wall isolates and associated biomolecules (Jiang et al., 2004, Barkleit et al., 2011), cell surface membranes (Kamnev et al., 1999, Shakirova et al., 2013) and EPS (Ueshima et al., 2008, Omoike and Chorover, 2004, Bura et al., 1998, Eboigbodin and Biggs, 2008, Ha et al., 2010). Differences in the absorption bands present and their relative intensities correlate with the relative abundance of biomolecules present. This experimental technique has been used to investigate the interactions of uranium with bacterial biomass. The presence of a U-O ligand when uranium is present within a sample is confirmed by a characteristic vibrational peak at approximately 910-920 cm^{-1}. Shifts in adsorption band position and changes in absorption intensity of spectral bands within the biomass indicate uranium binding with these functional groups, as demonstrated by numerous studies (Kazy et al., 2009, Choudhary and Sar, 2011, Theodorakopoulos et al., 2015, Pan et al., 2015). ATR-FT-IR has been used to characterise cell components (Chapter 3) and investigate uranium interactions with bacterial biomass (Chapter 2 and Chapter 4) within this study.

1.2.1.2.1.2 Surface charge characterisation

The bacterial cell surface exhibits protonation and deprotonation of its functional groups as a function of pH, and therefore bacterial biomass demonstrates a pH-dependent charge, resulting in differences in uranium binding. The point of zero charge (pzc) of the

bacterial surface is used to determine the overall net surface-charge as a function of pH. Furthermore, potentiometric titrations can be used to quantify the protonation and deprotonation of functional groups within bacterial biomass as a function of pH (Claessens et al., 2006, Ojeda et al., 2008a). The resulting pK_a values obtained from the fitting of the titration data corresponded to functional groups within the surface of the bacterial biomass where the acid-base protonation-deprotonation behaviour occurs. Within bacterial biomass, pK_a values of approximately 3.5, 5.7 and 9.1 correspond to the protonation-depotonation behavior of carboxyl, phosphate and amine, and hydroxyl groups, respectively (Ojeda et al., 2008a, Merroun et al., 2011).

Potentiometric titrations have been used to establish the cell surface properties that could be involved in metal binding as a function of pH. The experimental technique has been used to characterise the functional groups within live and dead cells (Merroun et al., 2011, Fein et al., 2005, Ojeda et al., 2008a, Borrok and Fein, 2005, Claessens et al., 2006). As the uppermost layer of the bacterial cell surface is its cell wall, many studies interpret the results obtained from using whole bacteria as the functional groups characterised within the cell wall (Dittrich and Sibler, 2005, Fang et al., 2009, Mishra et al., 2010, Kenney and Fein, 2011a) and associated biomolecules such as LPS (Barkleit et al., 2008). Additionally, the presence of EPS and its contribution to the presence of functional groups has been examined using potentiometric titrations (Kenney and Fein, 2011b, Fang et al., 2010, Wei et al., 2011, Yue et al., 2015).

1.2.1.2.1.3 X-ray photoelectron spectroscopy (XPS)

XPS is an experimental technique that provides chemical analysis of surfaces. It has been applied to characterise the cell surfaces of microorganisms since the X-rays only penetrate the top 2 to 5 nm of the surface, ideal for characterising functional groups and abundances of biomolecules within the cell wall. XPS involves the ejection of photoelectrons from core levels of the atoms of a sample due to irradiation by an X-ray beam. The kinetic energy of these emitted photoelectrons is analysed and the corresponding binding energies of these electrons calculated. The inelastic scattering of electrons in the sample concerns only the top layer of the sample where the X-ray penetrates. The peaks of an XPS spectrum are characteristic of a binding energy of a core electron for a given chemical element in the sample, but its position is influenced by its precise chemical binding environment (Dufrene et al., 1997, van der Mei et al., 2000).

When the biomolecular composition of the bacterial cell surface is understood in relation to the relative abundance of bacterial biomolecules that make up the bacterial cell wall, the presence and relative concentration of bioavailable functional groups for each cell wall constituent can be identified. High-resolution scans of the C_{1s}, O_{1s}, N_{1s} and P_{2p} peaks and their subsequent binding energies can be used to determine the precise chemical binding environment of these elements and elucidate any specific functional groups present within the bacterial biomass surface, such as the carboxylate, amide and phosphate groups (Ojeda et al., 2008a).

The molecular composition of bacterial cell surfaces has been calculated by XPS in terms of three classes of carbon containing cell wall constituents; polysaccharides, peptides and hydrocarbon-containing compounds (i.e. lipids) (Rouxhet et al., 1994, Dufrene et al., 1997). Simplifications in the calculations resulted in a lack of distinction between cell wall constituent subclasses. For example, an exact quantification of phospholipids within the Gram-negative cell surface was impossible due to the presence of lipidic materials such as LPS. Furthermore, the leakage of intracellular components can interfere with the cell surface analysis quantification. Freeze drying methods have been used to overcome this issue.

A combination of these cell surface characterisation techniques to determine the presence of functional groups and abundance of biomolecules at the bacterial cell surface is important for understanding the mechanisms of the biosorption processes whereby bacterial biomass removes uranium from solution. Cell surface components were characterised using XPS in Chapter 3.

1.2.1.3 Uranium biosorption and bioaccumulation

Bacterial biosorption is a well-defined metabolism-independent process that removes aqueous U(VI) species from contaminated environments. Numerous bacteria from diverse origins have displayed various binding affinities for uranium. The process is affected by pH, ionic strength, sorbent and sorbate concentrations, cell physiological state and the presence of other soluble polymers within solution (Merroun and Selenska-Pobell, 2008).

The Gram-positive genus *Bacillus* (in particular *B. subtilis*) has been studied extensively for its ability to retain uranium from aqueous environments using biosorption, on the presumption that the biosorption process was dependent on the cell wall since that is

the outermost layer of the bacterial cell surface (Gorman-Lewis et al., 2005, Fowle et al., 2000, Panak et al., 2002, Kelly et al., 2002). It was suggested that, at very low pH, covalent bonding occurred between the uranium and the cell surface due to protonation of the functional groups (Gorman-Lewis et al., 2005). The point of zero charge of the *B. subtilis* surface was calculated at ~ pH 2.2 (Fein et al., 1997). As the pH increased, deprotonation of the functional groups occurred and electrostatic interactions became more favourable between the positively charged uranium species and the negatively charged surface. Complexation occurred with neutral phosphate and deprotonated carboxyl functional groups in the bacterial cell wall (Fowle et al., 2000). This was further supported by EXAFS (Extended X-Ray Absorption Fine Structure) studies investigating the uranium coordination environment within the bacterial cell surface at low pH, which suggested that phosphate and carboxyl groups were the preferential binders of uranium to the Gram-positive bacterial cell surface. There was little difference in uranium coordination between live and dead *Bacilli* (Kelly et al., 2002, Panak et al., 2002). However, it was suggested that dead biomass was a more suitable biosorbent material since the effects of metal toxicity are then irrelevant (Suzuki and Banfield, 1999). Additionally, at low pH, *Paenibacillus* sp. JG-TB8 accumulated uranium at its cell surface through organic phosphate groups (Reitz et al., 2014). The composition of the cell walls of Gram-positive bacteria suggests that these preferential surface functional groups originate from the peptidoglycan and proteins (carboxyl) and secondary teichoic and lipoteichoic acids (phosphate).

Structural differences in cell wall architecture between Gram-positive and Gram-negative bacteria suggested differences in uranium biosorption to the cell surface. The biosorption of uranium to Gram-negative bacteria has been demonstrated by a variety of strains (Haas et al., 2001, Haas and Northup, 2004, Luetke et al., 2012). *S. putrificiens* biosorbed uranium through forming surface complexes with carboxyl and protonated phosphate groups; the amount of biosorption was dependant on pH and ionic strength (Haas et al., 2001). This was further supported through the biosorption to cell components of *Idiomarina loihiensis* MAH1, demonstrated by TEM (Morcillo et al., 2014). *P. fluorescens*, isolated from a granitic rock aquifer, sequestered uranium at low pH via protonated phosphate and carboxyl groups on the cell surface. At neutral pH, uranium coordination was mediated by deprotonated phosphate groups (analysed via time-resolved laser-induced fluorescence spectroscopy (TRLFS) (Luetke et al., 2012)). This behaviour was similar to that of other Gram-negative isolates such *Cupriavidus*

metallidurans CH34 and *Rhodopseudomonas palustris* (Llorens et al., 2012). Alongside the phosphate groups within the outer membrane phospholipids, LPS could be involved in uranium binding at the Gram-negative cell surface (Ferris and Beveridge, 1986, Langley and Beveridge, 1999, Barkleit et al., 2008, Barkleit et al., 2011). Uranium coordination with purified LPS was revealed using a combination of potentiometric titrations, TRLFS, EXAFS and FT-IR spectroscopy. Results suggested that uranium coordinated predominantly with phosphate moieties. Fewer carboxyl interactions were formed and the concentration of LPS was the governing factor for uranium coordination, with pH influence only minor.

Other cellular structures can be involved in uranium biosorption, such as S-layer proteins and endospores. As the outermost layer of many microbial species, the S-layer is composed of protein and glycoproteins. The function of S-layers is relatively unknown; it was hypothesised that the S-layer may protect the microorganism from the external environment (Sleytr, 1997). Purified S-layer proteins contained carboxyl and phosphate groups in *B. sphaericus* species that were involved in the binding of uranium (as determined by EXAFS analysis (Merroun et al., 2005)). Gram-positive bacteria form spores as a survival mechanism when subject to harsh living conditions. Rich in peptidoglycan, the spores accumulated more uranium per gram of biomass than either live or dead cells (Panak et al., 2002).

Many metallic species such as iron and copper are accumulated into bacteria via energy-dependent transport mechanisms, as they are necessary for cell function. Uranium, on the other hand, has no known cellular function and its accumulation with intracellular components may be due to increased cell membrane permeability caused by uranium toxicity (Suzuki and Banfield, 1999). This uranium toxicity could result in partial cell lysis and breakages to the bacterial cell wall resulting in uranium biosorption and accumulation within other cell surface structures that are not in the uppermost layer. Therefore, in such structures (for example the cell surface membrane) the availability of functional groups within these structures would be more apparent. The binding to the cell surface membrane could therefore result in increased membrane permeability and further accumulation of uranium with intracellular components and lysed bacterial biomass (Panak et al., 2002).

The accumulation of uranium with polyphosphate bodies has been well documented for numerous strains of bacteria, in particular those of the *Pseudomonas* species.

Polyphosphate bodies are linear chains of inorganic phosphate residues with varying chain length (Vanveen et al., 1993) that may chelate metals as a tolerance mechanism (Keasling and Hupf, 1996). This mechanism has been observed in numerous bacteria, most particular those of Gram-negative origin. For example, *A. ferrooxidans* (Merroun et al., 2003b), *Sphingomonas* species S15-S1 (Merroun et al., 2006) and various *Pseudomonas* strains (Renninger et al., 2004, Kazy et al., 2009, Choudhary and Sar, 2011) showed rich intracellular uranium deposits while showing no signs of cell lysis. The accumulation of uranium ions into *Bacillus* species has been observed through the lysis of the cell wall and release of decomposition products (Panak et al., 2002). It was recently suggested that an amorphous uranium phase biosorbs onto the cell surface and is transformed into a crystalline uranium phase as it passed into the cell (Pan et al., 2015). A similar mechanism has been proposed for the Gram-positive *Microbacterium* sp. A9 from the Chernobyl exclusion zone. Theodorakopoulos et al., (2015) proposed that there was passive diffusion of U(VI) into the cytosolic region of the bacterium due to increased membrane permeability. High concentrations of uranium–inorganic phosphate complexes were formed which were excised from the cell. The release of inorganic phosphate from the cell prevented further U(VI) accumulation inside the cell.

Extracellular remediation of uranium through biosorption and bioaccumulation has been documented for certain strains of bacteria. EPS, obtained from bacteria isolated from both uranium contaminated and non-contaminated environments, has shown a high binding affinity for uranium and other heavy metals. For example, the EPS of *A. ferrooxidans* has been associated with the binding of uranium from aqueous environments, as confirmed by TEM-EDX and EXAFS. These showed dense accumulations external to the cell (Merroun et al., 2003b) even at very low pH. The complexes showed a similar structure to that of uranium-sugar phosphate coordination (Koban et al., 2004). Since other bacteria showed only sorption to the cell surface or intracellular accumulation at this pH, this suggests a pH-dependent process for uranium accumulation by the EPS of some strains of bacteria (Jroundi et al., 2007, Morcillo et al., 2014). Individual strains showed preferential binding of uranium to their EPS at different pH. Additionally, it was suggested that other microbial remediation processes may be involved in uranium retention by EPS of certain bacteria, such as precipitation (Merroun and Selenska-Pobell, 2008, Choudhary and Sar, 2015). A schematic of the biosorption and bioaccumulation processes involved within bacterial biomass is shown in Figure 4.

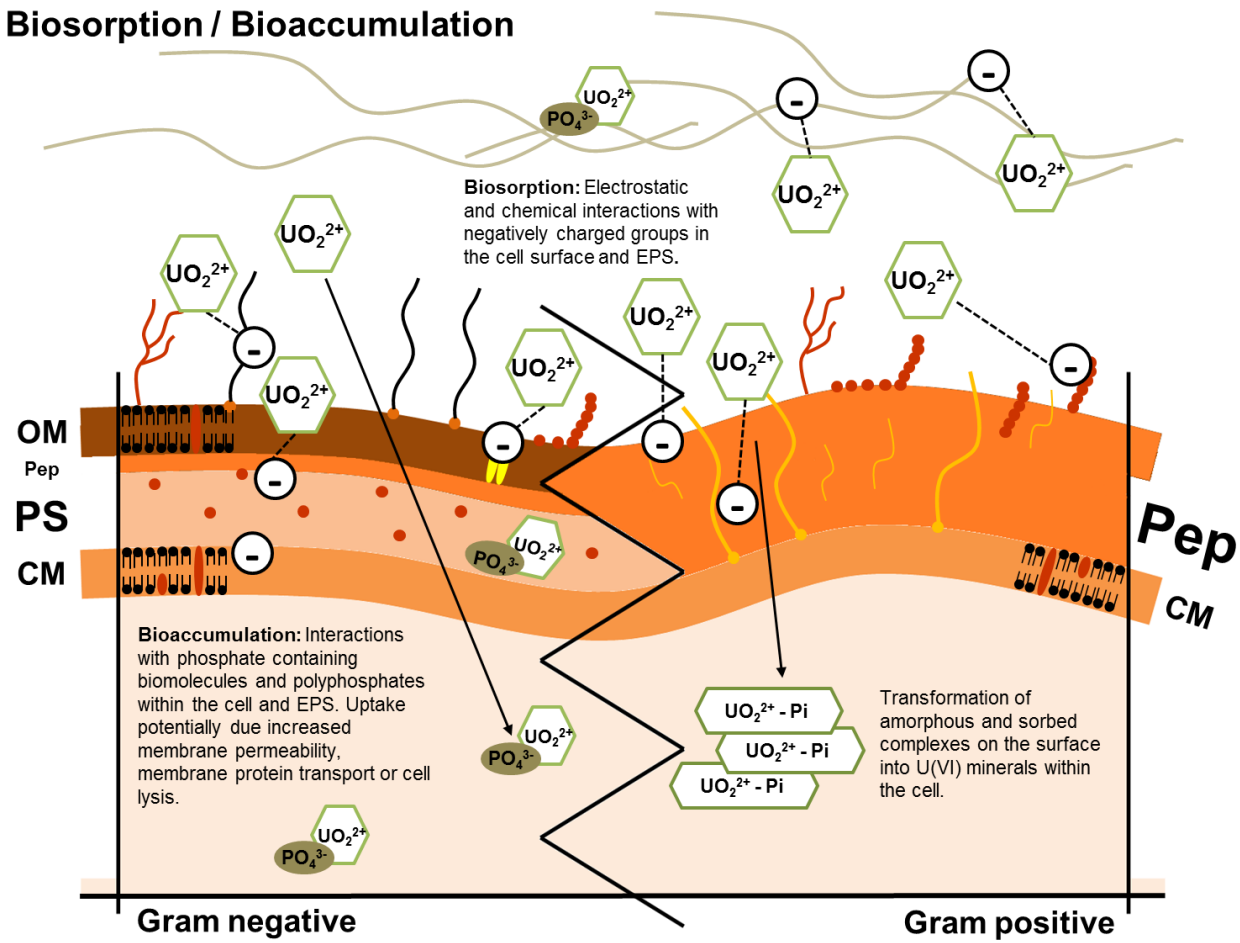

Figure 4. Uranium biosorption and bioaccumulation using bacterial biomass.

The extensive amount of published results point out the potential that bacterial biomass has to remove uranium from solution through biosorption and bioaccumulation. However, the processes at a mechanistic level and the contribution of cell surface structures and macromolecules to these processes are not fully understood due to the complexity of the bacterial cell surface. The numerous factors controlling the efficiency of this process need to be characterised, including the uranium species adsorbed and the biosorbent capacities of the chosen biomass.

The solution pH is potentially the most critical variable for optimal uranium removal due to uranium speciation with hydroxides and carbonates at neutral to alkaline pH values. Protonation of the bioavailable functional groups occurs at very low pH, leaving a small window for optimal uranium removal, where the uranium species is the highly mobile uranyl ion and the overall net charge of the bacterial cell surface is negative. This small window changes with bacterial species due to differences in the abundance of different functional groups, the presence of uranium-accumulating EPS and the bioaccumulating capabilities of individual bacteria. Additionally, the ionic strength of solutions influences the biosorption process. The extra cations in solution may compete with uranium in binding to the negatively charged sites in the bacterial surface. Also, anions in solutions (such as chloride) may bind metal species and so reduce biosorption. Some authors (Borrok and Fein, 2005, Das, 2010) have suggested that the effect of ionic strength on metal adsorption onto bacterial cell surfaces is small. Other variables to take into consideration are temperature and agitation rates. Many laboratory experiments are conducted at higher temperatures than those of environmental relevance (Choudhary and Sar, 2011, Kazy et al., 2009). However, it has been suggested that temperature changes between 20 °C and 35 °C do not significantly influence biosorption activity. Agitation rates used may also fail to reflect environmental conditions (Aksu et al., 1992).

1.2.2 Biomineralisation

1.2.2.1 What is biomineralisation?

Biomineralisation is the process by which organisms form minerals. Uranium biomineralisation is the process whereby uranium minerals are precipitated from solution by microbially generated ligands that act as a precursor for nucleation (Merroun and Selenska-Pobell, 2008, Newsome et al., 2014, Choudhary and Sar, 2015). These minerals are usually sulphides and phosphates at acidic to circumneutral pH and carbonates or hydroxides in alkaline conditions. These ligands are located closely to the cell surface confining the biomineralisation process to the cell surface and extracellular matrix (Macaskie et al., 2000).

It has been suggested that phosphate-generated ligands liberated from microbial phosphatase activity were responsible for uranium biomineralisation (Macaskie et al., 1992). It has been demonstrated that a membrane-bound phosphatase enzyme released inorganic phosphate from glycerol-2-phosphate that was used for the subsequent U(VI) mineralisation as extracellular hydrogen uranyl phosphates. Other research suggested that acid phosphatase was associated with the periplasmic space (Jeong et al., 1997). This pioneering work has formed the basis of further studies investigating the enzymatic phosphate precipitation process by various laboratory and indigenous strains, indicating that geographical location (i.e. where the microorganism was isolated) was not a factor in phosphatase activity.

1.2.2.2 Uranium biomineralisation by bacterial biomass

Biomineralisation mediated by acid phosphatase has been reported to occur at pH values ranging from 4.5 to 7, where the aqueous phosphate exists predominantly as $H_2PO_4^-$ and HPO_4^{2-} within this range. *Bacillus* and *Rahnella* strains were isolated from the DOE Oak Ridge Field Research Center (ORFRC). The species precipitated uranium via phosphatase activity using glycerol-3-phosphate (G-3-P) as an organic phosphate stimulant at an optimum pH of around 5.0-5.5. The precipitates were characterised by EXAFS as being of meta-autunite origin (Beazley et al., 2007, Martinez et al., 2007). Further studies from this site suggested that, in the presence of high calcium concentrations, other bacteria from this environment could hydrolyse inorganic phosphate from G-3-P. When coupled with nitrate reducing and aerobic conditions, the bacteria incorporated uranium into hydroxyapatite precipitates (Shelobolina et al., 2009).

An external organic phosphate source for phosphatase activity and U(VI) precipitation was mainly used in these studies. In further studies, in which no external phosphate source was added to the experiments, indigenous phosphatase activity was displayed by *B. sphaericus* JG-7B and *Sphingomonas* sp. S15-S1 in the presence of uranium at pH 4.5. The uranium was precipitated close to the cell surface as a meta-autunite mineral-like phase (Merroun et al., 2011). This organic phosphate source could arise from the lysis of dead cells or the presence of organic phosphate constituents within bacterial EPS.

At very low pH, diminished phosphatase activity resulted in adsorption of U(VI) onto the cell surface through phosphate functional groups. This supported the principle that acid phosphatase activity is pH specific, occurring towards circumneutral conditions, whereas adsorption could occur over a wider acidic pH range. This principle was apparent in previous studies investigating the uranium biomineralisation within bacteria such as *Microbacterium* (Nedelkova et al., 2007, Merroun et al., 2006). More recent studies using *Idiomarina loihiensis* MAH1 showed that precipitation only occurred under neutral conditions (Morcillo et al., 2014). Another limiting factor for uranium biomineralisation is the environmentally unfavourable anaerobic experimental conditions. A *Rahnella* strain was able to precipitate the U(VI)-bearing mineral chernikovite ($H_2(UO_2)_2(PO4)_2$) in high nitrate reducing conditions by respiring nitrate. However this process was very slow at releasing inorganic phosphate in comparison to aerobic conditions (Beazley et al., 2009). This was further investigated using the facultative anaerobe *Paenibacillus* sp. JG-TB8 that in anaerobic conditions exhibited no phosphatase activity. A substantial decrease in orthophosphate release was observed from cells at pH 4.5-6, in comparison to the precipitation of a meta-autunite mineral-like phase within aerobic conditions where there was a high enzymatic activity and a higher release of orthophosphate. Interestingly, at low pH where biomineralisation was unfavourable, there was no difference between the biosorption under different aeration conditions, further supporting the conclusion that the biomineralisation process depends on pH (Reitz et al., 2014). Utilising the power of acid phosphatase-mediated uranium biomineralisation, *D. radiodurans* has been genetically modified to harbour the non-specific acid phosphatase gene *phoN*, to precipitate uranium as uranyl hydrogen phosphate (HUO_2PO_4) from acidic to neutral pH waste (Appukuttan et al., 2006, Misra et al., 2012).

Uranium precipitates were predominantly deposited close to the cell surface where there was a greater availability of microbially generated ligands, either from

phosphatase activity or from those present within bacterial EPS (Macaskie et al., 2000). Numerous indigenous (Kumar et al., 2013) and laboratory strains (Chapter 5) precipitated U(VI)-phosphate bearing minerals close to the cell surface at mildly acidic to circumneutral conditions (Macaskie et al., 1992, Nedelkova et al., 2007, Merroun et al., 2011, Lopez-Fernandez et al., 2014, Morcillo et al., 2014, Reitz et al., 2014). Elemental maps displayed the accumulation of uranium and phosphorus within the precipitates formed using High-Angle Annular Dark Field-Scanning Transmission Electron Microscopy (HAADF-STEM) coupled with Energy Dispersive X-ray analysis (EDX). This demonstrated the ability of the yeast *Rhodotorula mucilaginosa* BII-R8 to precipitate U(VI) phosphate minerals (Lopez-Fernandez et al., 2014). It was suggested that cell surface architectures and microbially generated ligands in close proximity prevent over-accumulation of the uranium precipitates on the cell surface and maintain cell function. For example, the LPS of *Citrobacter* have been proposed as a preliminary nucleation site whereby phosphate groups and enzymatically liberated phosphate produce U(VI)-phosphate minerals tethered to the cell surface, without diminishing function and potentially increasing metal toxicity resistance (Macaskie et al., 2000).

Uranium biomineralisation occurred outside the cell using microbially generated ligands in conjunction with bacterial EPS (Suzuki and Banfield, 1999, Nedelkova et al., 2007, Jroundi et al., 2007, Merroun and Selenska-Pobell, 2008, Morcillo et al., 2014, Theodorakopoulos et al., 2015). *D. radiodurans* was able to precipitate chernikovite nanocrystals outside the cell in acidic conditions while the EPS of *M. xanthus*, *M. oxydans, P. stutzeri* DSMZ 5190 and *I. loihiensis* MAH1 precipitated uranium as a meta-autunite mineral-like phases from pH 4.5 to neutral conditions, as confirmed by TEM, XAS and EXAFS analysis (Jroundi et al., 2007, Nedelkova et al., 2007, Merroun and Selenska-Pobell, 2008, Morcillo et al., 2014). The power of alkaline phosphatases to precipitate U(VI)-phosphate-bearing minerals has also been investigated. *Caulobacter crescentus* and recombinant *Deinococcus radiodurans* precipitated U(VI) outside the cell from the secretion of phosphate using the power of the alkaline phosphatase gene *phoK* (Yung and Jiao, 2014, Kulkarni et al., 2013). The precipitation of uranium using microbially generated phosphate outside the cell suggested that phosphatase activity associated with the cell surface can liberate phosphate from live cells and secrete this anionic ligand outside the cell, or liberate this anion from phosphate-containing biopolymers within EPS. A similar mechanism was proposed for the interactions of uranium with *Microbacterium* sp. A9 by which intracellular polyphosphate granules were

hydrolysed through induced enzymatic activity, such as acid phosphatase and exopolyphosphatase (Kornberg et al., 1999). This activity released inorganic phosphate outside the cell for subsequent uranium precipitation and so prevented intracellular localisation of uranium and therefore reduced the potential toxic effects (Theodorakopoulos et al., 2015). A schematic for uranium biomineralisation with bacterial biomass is shown in Figure 5.

These mechanisms have been demonstrated in field studies at the DOE ORFRC. G-3-P was added to stimulate the power of indigenous bacteria to precipitate uranium through small flow-through columns aerobically in circumneutral pH conditions. Elevated levels of orthophosphate released in the columns to which G-3-P was added, coupled with XAS analysis indicated the precipitation of uranium phosphate minerals (Beazley et al., 2011). Similar studies using G-2-P enriched sediments and EXAFS analysis suggested a preferential precipitation of U(VI) phosphate-bearing minerals in anaerobic conditions close to neutral pH (Salome et al., 2013). Strains isolated from same field study displayed varying phosphatase capabilities. However, the exposure of certain strains to uranium significantly decreased their culturability, indicating the toxic effects of uranium on bacterial growth (Beazley et al., 2007, Martinez et al., 2007). Furthermore, the addition of organophosphate substrates to ORFRC at different pH suggested varying levels of microbial phosphate metabolism and an increase in abundance of these microorganism towards circumneutral pH (Martinez et al., 2014).

The accumulation of metal precipitates close to the cell surface could prevent many metabolic functions, resulting in increased cellular toxicity, (Lloyd and Macaskie, 2000, Newsome et al., 2014). However, the biomineralisation could also be a coping mechanism to reduce the toxic effects of increased concentration of uranium in solution (Benzerara et al., 2011). The effects of uranium toxicity and precipitate accumulation on the growth and subsequent microbial phosphatase activity have been studied using various strains isolated from contaminated environments. *Rhodanobacter* sp. A2-61 was able to grow in the presence of 500 μM uranium at pH 5 in low phosphate media (LPM) and accumulate 120 μM uranium from solution as a meta autunite mineral-like phase, as confirmed by XRD (Sousa et al., 2013). The minimum inhibitory concentrations (MIC) of natural isolates from Spanish clay deposits indicated a high tolerance to uranium of up to 8 mM (~pH 7). Colony counting and flow cytometry measurements suggested a decrease in the number of viable cells as the concentration of uranium increased in LPM

and when there was precipitation of uranium phosphate minerals on the cell surface (Lopez-Fernandez et al., 2014). The effect of pH was investigated using fluorescent microscopy with *Paenibacillus* sp. JG-TB8 cells in the presence of 500 µM uranium. The results suggested an increase in the number of viable cells as the pH increased to 6 where precipitation of uranium as a phosphate-bearing mineral on the cell surface occurs (Reitz et al., 2014). Furthermore, the influence of U(VI) on the metabolic activity of multispecies biofilms was investigated by fluorescent microscopy. This indicated that there was a higher respiratory activity of bacteria in the uppermost layers of biofilms that tolerated the toxic effects of aqueous uranium. This resulted in the precipitation of U(VI) minerals within bacterial EPS (Krawczyk-Baersch et al., 2008).

In the light of the above, utilising microbial phosphatase activity is a promising technique for producing stable uranium minerals in aerobic environments. However, there are limitations to utilising this mechanism. Many studies have utilised an external glycerol phosphate source for subsequent microbial phosphatase activity. Lloyd and Macaskie, (2000) suggested that the utilisation of this organic phosphate source may not be economic and sustainable due to poor commercial availability and high production costs. Other studies have investigated various phosphate sources for enzymatic activity with varying degrees of success. This was ascribed to by-products produced from enzymatic hydrolysis and different compositions depending on the origin of the source (Thomas and Macaskie, 1996, Paterson-Beedle et al., 2010). More recent studies have investigated the effect of not adding an organic phosphate source on microbial phosphatase activity. This suggested that bacteria can use organic phosphate sources within their EPS arising from the lysis of dead cells (Merroun et al., 2011). Therefore, the contribution of macromolecules at the cell surface and those associated with EPS need evaluating to understand their contribution to uranium biomineralisation at a mechanistic level, as previous studies have mainly focused upon a whole cell system.

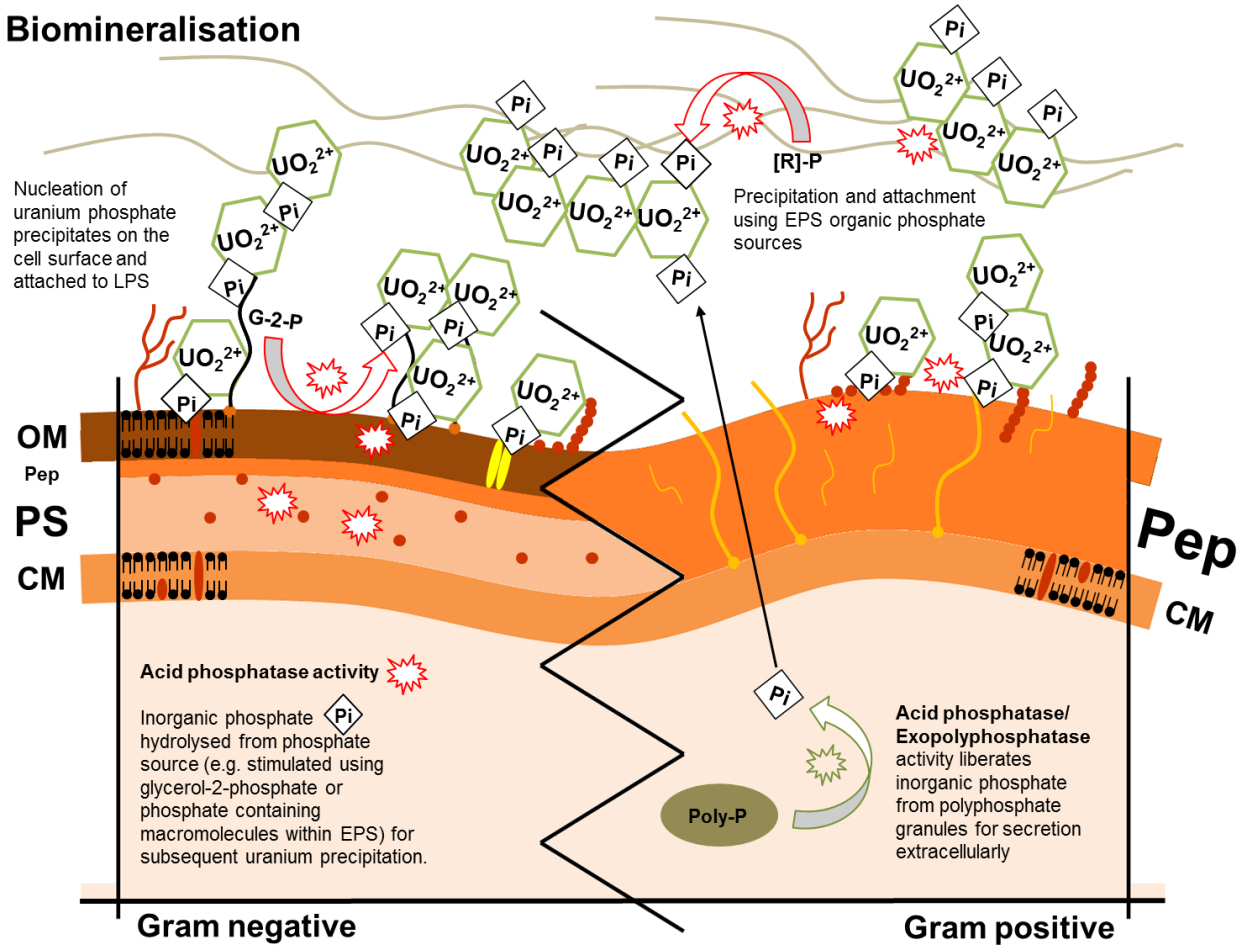

Figure 5. Uranium biomineralisation using microbial phosphatase activity.

1.2.2.3 Uranium biomineralisation characterisation

A combination of microscopic, analytical and spectroscopic techniques has been used to identify the localisation, elemental coordination environment and the mineral structure of the precipitates formed. Understanding the processes involved is important to further our understanding of uranium biomineralisation at a mechanistic level.

1.2.2.3.1 Scanning Electron (SEM) and Transmission Electron (TEM) Microscopies

SEM and TEM are useful techniques to identify the location and structural morphology of uranium precipitates associated with uranium biomineralisation. Unlike ordinary optical microscopes that use visible light to view samples, TEM uses a high-energy electron beam, fired through a thinly sliced specimen to produce a high-resolution image.

A high-energy electron beam is generated using high-voltage electricity supplied from a cathode. The beam passes through two electromagnetic coils that focus it onto the thinly sliced specimen that is sealed in a vacuum to ensure efficient electron transport within the chamber. When in contact with the specimen, the electron beam is deflected by elements (such as radionuclides and heavy metals) that are heavier than biologically relevant elements (such as carbon, nitrogen, oxygen and phosphorus). The image is formed when the electron beams hits the fluorescent screen at the base of the instrument. The deflection of electrons by uranium makes possible the visualisation of precipitates within bacterial biomass (Merroun, 2007).

Unlike TEM, where the electron beam penetrates thinly sliced specimens for visualisation, SEM uses a beam of electrons to scan over a specimen to produce a magnified image. As before, the electron beam is fired into the vacuum chamber where a positively charged electrode accelerates the beam through an electromagnetic coil to focus it. An additional coil allows movement of the electron beam to scan the surface of the sample. Scattered electrons are detected to produce an image of the sample. Schematics of TEM and SEM instrumentation are displayed in Figure 6.

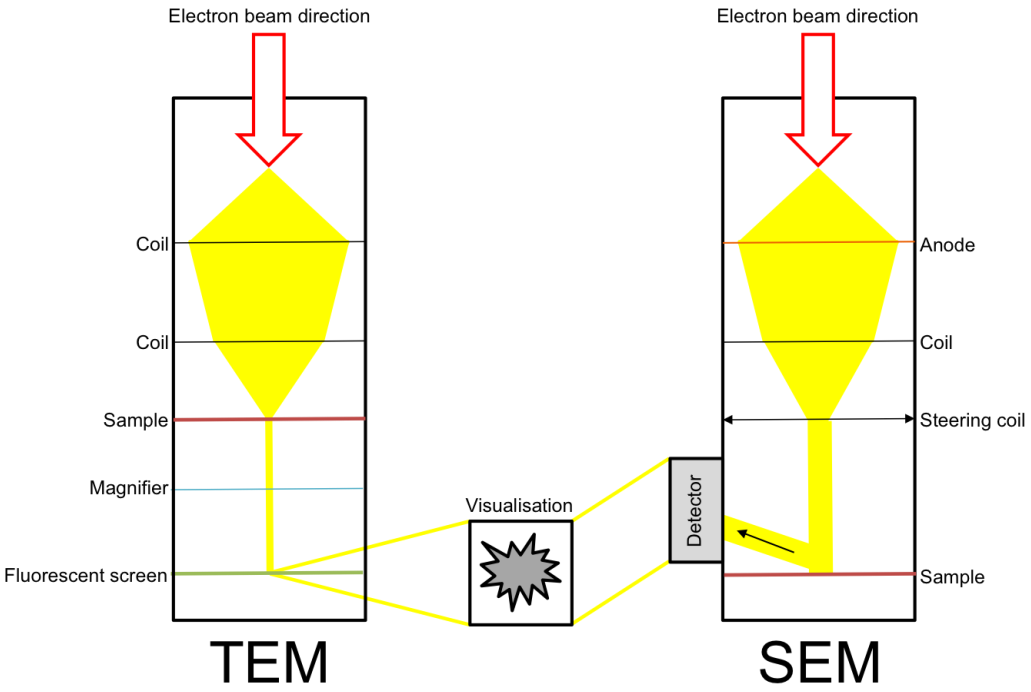

Figure 6. A schematic of the instrument running for TEM and SEM.

When these techniques are coupled with Energy-Dispersive X-ray (EDX) spectroscopy (in which the specific energy of X-rays that are emitted when an electron moves to a different electron shell is measured) the identification of elements can be achieved. High-Angle Annular Dark-Field-Scanning Transmission Electron Microscopy (HAADF-STEM) uses EDX to produce elemental maps to identify the distribution of elements within a sample. TEM-EDX has been used to investigate uranium accumulation within bacterial biomass. Numerous studies have investigated whether it is accumulated on the cell surface, inside the cell or in conjunction with bacterial EPS (Nedelkova et al., 2007, Jroundi et al., 2007, Merroun and Selenska-Pobell, 2008, Merroun et al., 2011, Morcillo et al., 2014, Reitz et al., 2014, Theodorakopoulos et al., 2015). Elemental mapping suggesting the formation of precipitates from uranium-phosphate origin (Lopez-Fernandez et al., 2014), as shown in this study, Chapter 5.

SEM has been used to identify both the structural morphology of bacteria (Nedelkova et al., 2007) and uranium precipitates, whether on the cell surface (Kazy et al., 2009, Sousa et al., 2013, Pan et al., 2015, Yang et al., 2015) or outside the cell (Handley-Sidhu et al., 2014), as shown in this study, Chapter 2.

1.2.2.3.2 Powder X-ray powder diffraction (XRD)

XRD is an analytical technique used to identify crystalline material phases of finely ground samples and determine the average composition of bulk samples. With this technique, X-rays are generated using an X-ray cathode tube that is heated to create electrons that are then accelerated by applying a voltage. These electrons bombard a target anode material and displace inner shell electrons that produce a characteristic X-ray spectrum, consisting of 2 main components, K_β and K_α, the latter of which is important for XRD. The X-rays are filtered using a monochromator, for example with copper (CuK_α= 1.5418 Å) - the most commonly used radiation source or molybdenum (MoK_α= 0.7093 Å). The latter was used in this study, Chapter 2 and Chapter 4. Graphite and silicon monochromators are employed to eliminate as much unwanted K_β radiation as possible. The filtered X-rays are directed towards the sample, that is rotated, and the reflected X-rays are recorded (as a count rate) as a function of 2θ. The distance between lattice planes in a crystal (*d*-spacing) can be used to characterise the minerals formed as the X-ray wavelength (λ) is known and the incident angle (θ) is measured as the X-ray beam hits the sample while the diffracted X-rays are collected at an angle of 2θ, Figure 7.

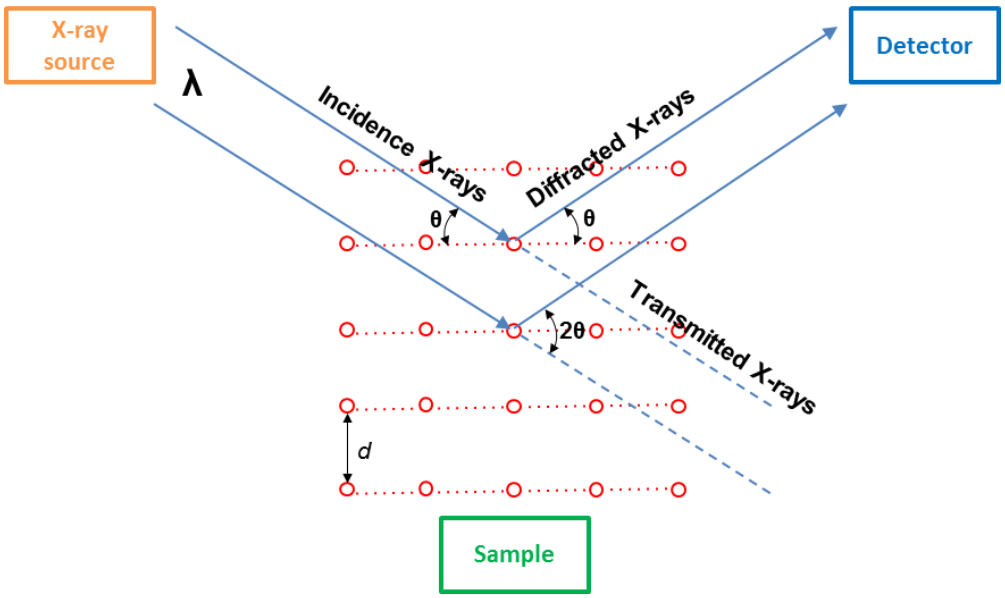

Figure 7. A schematic of XRD instrumentation and the generation of diffracted X-rays.

Using the collected 2θ values and the known X-ray wavelength, Bragg's equation (Equation 2) can be used to calculate *d*-spacing values for mineral characterisation. *n* is the integer and indicates which atomic layer diffraction has occurred, *λ* is the X-ray wavelength, *d* is the spacing between atomic lattices and θ (in radians) is the incident

angle measured. The equation can be rearranged to calculate *d*-spacing values of unknown samples (Equation 3) that can then be used to identify the mineral structure by comparison with PDF files from the International Centre for Diffraction Data (ICDD).

$$n\lambda = 2d\ sin\theta \qquad \text{Equation 2}$$

$$d = \frac{n\lambda\ \div sin\theta}{2} \qquad \text{Equation 3}$$

XRD has been applied to analyse the mineral structure of uranium precipitates either those synthesised chemically or through microbiological processes. Chemically synthesised uranium precipitates to immobilise aqueous waste through the incorporation of other elements (Wellman et al., 2005, Yagoubi et al., 2013) have been confirmed by XRD. The precipitation of uranium phosphate minerals such as meta-autunite and nano-uramphite has been characterised in microbiological systems (Choudhary and Sar, 2011, Sousa et al., 2013, Handley-Sidhu et al., 2014, Pan et al., 2015). Uranium precipitates following microbial phosphatase activity were characterised using biomolecules found within EPS, Chapter 2.

1.2.2.3.3 Other spectroscopies used in previous studies

Other spectroscopic techniques (not used in this study) have demonstrated the ability of bacterial biomass to biosorb and biomineralise uranium. These include X-ray Absorption Spectroscopy (XAS) and Time Resolved Induced Laser Fluorescence Spectroscopy (TRLFS). XAS is a non-destructive technique that can utilise synchrotron radiation to investigate the coordination environment of chemical elements within bulk material, of either amorphous or crystalline origin, at relatively low concentrations where other diffraction techniques (i.e. XRD) were not sensitive to the material being investigated.

With XAS, synchrotron-generated X-rays are used to excite electrons within the electronic shells of elements present. The incoming electromagnetic radiation will be either absorbed by the electrons (to excite them) or scattered. The absorption increases dramatically at certain wavelengths (absorption edge) followed by the X-ray absorption near edge structure (XANES) where the photon energy equals that of the ionisation energy to excite and emit core electrons. This is unique for each element and can be used to determine the oxidation state of elements within a sample, ideal for concluding whether uranium precipitates analysed are formed by either enzymatic reduction or biosorption/biomineralisation. The extended X-ray absorption fine structure (EXAFS) is a

result of the single scattering of high-energy ejected electrons with neighbouring atoms. With this information, the structural environment of uranium can be determined following interactions with biomass (Merroun, 2007).

The enzymatic reduction of uranium using bacteria in anaerobic conditions has been characterised using XANES and EXAFS. The precipitates were characterised as microbially reduced uraninite (Suzuki et al., 2002). Recent data suggests that the mechanism involves phosphate mediated U(IV) reduction with the precipitation of U(IV)-phosphate minerals such as ningyoite (Khijniak et al., 2005, Fletcher et al., 2010, Bernier-Latmani et al., 2010, Dalla Vecchia et al., 2010, Boyanov et al., 2011, Ray et al., 2011, Rui et al., 2013, Alessi et al., 2014, Newsome et al., 2015b). EXAFS has been used to determine the uranium coordination environment in sorbed uranium phases and U(VI) mineral precipitates by bacterial biomass such as meta-autunite (Kelly et al., 2002, Merroun et al., 2003b, Merroun et al., 2005, Nedelkova et al., 2007, Beazley et al., 2007, Merroun et al., 2011, Salome et al., 2013, Beazley et al., 2011, Llorens et al., 2012, Morcillo et al., 2014, Reitz et al., 2014, Krawczyk-Barsch et al., 2015).

TRLFS is an extremely sensitive spectroscopic technique that can be used to investigate the coordination environment of metal ions following complexation with charged surfaces such as bacterial biomass. This enables different uranium species to be identified. The measured fluorescence lifetime and intensity of excited metal ions can be used to define their coordination environment. This technique can distinguish between the processes of biosorption and biomineralisation since sorbed uranium phases and precipitated species display characteristic peaks and different wavelengths. This technique has been used to investigate the formation of U(VI)-sugar complexes (Koban et al., 2004), uranium species biosorbed onto live bacteria, precipitated U(VI) minerals (Renninger et al., 2004, Luetke et al., 2012, Morcillo et al., 2014, Reitz et al., 2014, Theodorakopoulos et al., 2015), interactions with cell surface components (Barkleit et al., 2008) and biofilms (Krawczyk-Barsch et al., 2015). A combination of the techniques described is necessary to fully characterise the bioremediation of uranium within aerobic environments, whether it be a process of biosorption or biomineralisation.

1.2.2.4 Cell toxicity characterisation

Within a live cell system, the cell toxicity to uranium must be characterised in order to achieve optimum bacterial growth and subsequent uranium biomineralisation. This has been investigated with numerous bacteria isolated from contaminated environments.

The minimum inhibitory concentrations (MIC) for bacterial growth and subsequent cell viability and cellular activity have been investigated as a function of initial uranium concentration in growth media (Martinez et al., 2007, Nedelkova et al., 2007, Choudhary and Sar, 2011, Llorens et al., 2012, Sousa et al., 2013, Reitz et al., 2014, Lopez-Fernandez et al., 2014, Theodorakopoulos et al., 2015).

1.2.2.4.1 MIC determination

The minimum inhibitory concentration (MIC) is a measure of the uranium concentration at which there is complete inhibition of bacterial growth (Rossbach et al., 2000). Understanding the MIC of bacteria within experimental and *in-situ* scenarios is fundamental for understanding the processes involved in uranium biomineralisation. This has been achieved by thoroughly investigating colony formation on low phosphate media (LPM) agar to determine uranium tolerance as a function of concentration (Nedelkova et al., 2007, Lopez-Fernandez et al., 2014). Similarly, colony forming units (CFU) were used to determine the cell viability following exposure of live cultures to uranium, in which viable cells regrow in the presence of fresh media and the corresponding CFU are counted (Martinez et al., 2007, Choudhary and Sar, 2011, Theodorakopoulos et al., 2015).

Optical density measurements in aqueous media at a wavelength of 600 nm (characteristic of most bacteria) are used to determine the growth of microbial populations. They have also been used to investigate the growth of bacteria as a function of uranium concentration within solution and pH over a period of time. Phosphate concentrations in solution were kept to a minimum to avoid uranium precipitation (Llorens et al., 2012, Sousa et al., 2013), as demonstrated in this study, Chapter 5.

1.2.2.4.2 Fluorescent staining

Staining of bacterial biomass with fluorescent compounds can be used to investigate various cell functions and hence the toxic effects of uranium on bacteria. Various fluorescent stains are used to target specific cellular components where specific cellular processes occur.

Fluorescently stained cells can be analysed quantitatively using flow cytometry as well as qualitatively by fluorescent microscopy. In the latter, fluorescence signals from the excitation of the fluorochrome are detected. Fluorescent microscopy requires stained cells to be transferred and fixed on a microscope slide. A filtered high intensity light

source excites the sample at a specific wavelength characteristic of the fluorescent labels tagged onto the sample. Electrons within the sample are excited to a higher energy level and emit a fluorescent signal as this energy level decays. This is filtered to become visible due to having a lower energy and longer wavelength than what is used for excitation.

Flow cytometry measures the characteristics of individual cells as they travel singly through a detector. Information such as cell size, shape, complexity and the fluorescent intensity of attached fluorescent compounds can be measured by flow cytometry. Single cells within the fluid stream are passed through a laser detector beam (at a specific wavelength) and scatter the laser light at its intercept. The scattered and emitted fluorescent light is diverted towards detectors through a combination of positioned lenses, beam splitters and filters. Forward scatter (FSC) determines cell size and side scatter (SSC) determines cell complexity. Fluorescent detectors and filters detect the emission of any fluorescent signals characteristic of cellular processes. Cellular information is represented as a scatter plot of individual cells or a histogram, following fluorescence-activated cell sorting (FACS).

To measure the number of viable bacteria within a sample following uranium exposure, a combination of fluorescent stains can be applied. For example fluorescein diacetate (FDA) and propidium iodide (PI), utilise the cellular enzyme activity and membrane integrity. The acetylated dye relinquishes the dye's fluorescent capabilities but promotes the ability to passively diffuse through the phospholipid bilayer of intact (viable) cell membranes. Within the cell cytoplasm, bacterial esterase activity promotes the cleavage of the acetyl groups from FDA, liberating the de-acetylated fluorescein while producing acetic acid and acetaldehyde. The negatively charged fluorescein is retained within live cells and fluoresces green under the correct excitation, indicating live cells (Boyd, 2008). Counter staining with nucleic acid stains that cannot pass through the impermeable cell surface indicates the number of dead cells. PI intercalates with the DNA of membrane-damaged or dead cells. In these cases the fluorescent stain can displace the FDA accumulated stain to distinguish between viable and non-viable cells (El Arbi et al., 2011, Taylor and Wang, 1989, Hammes et al., 2011). This assessment was based on the assumption that bacteria dead cells exhibit no esterase activity and live cells demonstrate a high esterase activity.

The metabolic activity of bacteria following uranium exposure can be investigated using a number of different fluorescent stains. 3,3'-dihexyloxacarbocyanine iodide ($DiOC_6$) is a lipophilic, green fluorescent dye that can permeate the cell surface and is used to determine the cell surface membrane potential. This fluorescent dye investigates the activity of proton pumps, electron transport systems and changes in electrochemical potential due to cellular respiration. The cell fluorescence intensity correlates with the magnitude of membrane potential (Rottenberg and Wu, 1998). Similarly, 5-cyano-2,3-ditolyl tetrazolium chloride (CTC), when counterstained with nucleic acid stains such as DAPI and SYBR green, can differentiate between respiring and non-respiring bacteria in solution. CTC is a colourless non-fluorescent dye under oxidising conditions and is reduced to a CTC-formazan red fluorescent stain by respiring bacteria and their electron transport systems (Rodriguez et al., 1992). The emission intensity corresponds to the concentration of reduced product. A schematic of the fluorescent stains used to investigate uranium toxicity is shown in Figure 8.

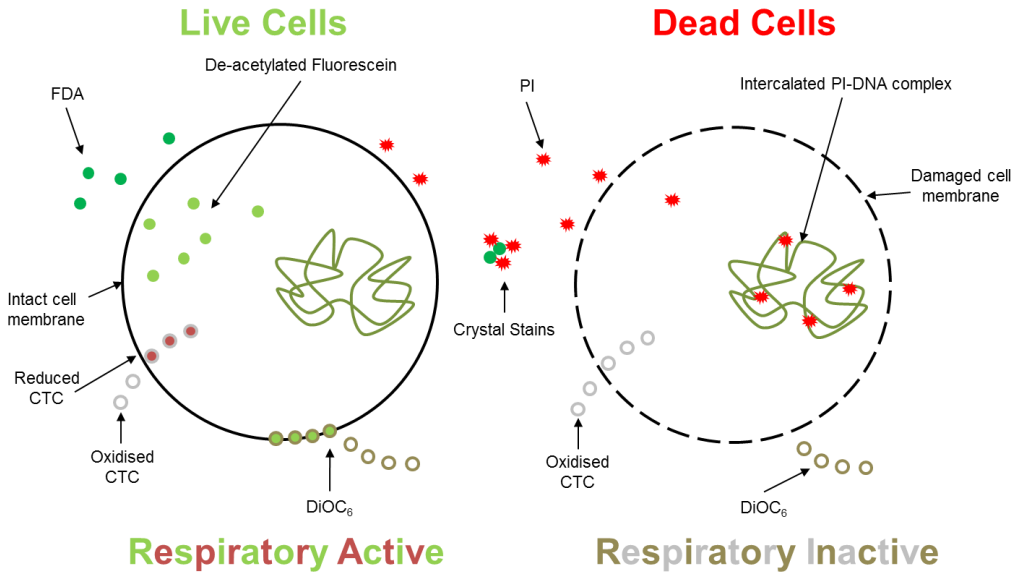

Figure 8. Fluorescent staining to measure uranium toxicity as a function of cell viability and respiratory activity.

Fluorescent microscopy has been used to visualise viable bacteria in numerous studies under stress conditions (Grootaert et al., 2011, El Arbi et al., 2011) including those investigating the toxic effects of uranium at different pH (Reitz et al., 2014) with the latter determining the percentage number of viable cells by cell counting. Propidium iodide can accumulate in all cells. However within healthy living cells, the PI should not accumulate and will be pumped out of the cell. This removal of PI can be ineffective due

to intercalation with cytoplasmic RNA and give false negatives using fluorescent microscopy, overestimating cell death (Rieger et al., 2010). To overcome this, flow cytometry can be used, as demonstrated previously, with results suggesting that the increase in uranium concentration coincided with a decrease in cell viability (Lopez-Fernandez et al., 2014). Furthermore, CTC staining has been used to investigate the respiratory activity and toxicity of uranium in multispecies biofilms with results suggesting an increased activity corresponding to the precipitation of U(VI) minerals (Krawczyk-Baersch et al., 2008). It is important to use a combination of fluorescent staining techniques, as described here, in order to understand the toxic effects of uranium on the growth and sustainability of bacterial cultures for uranium remediation purposes and how uranium biomineralisation and biosorption affects cell toxicity, as demonstrated in Chapter 5.

1.3 Aims and Objectives

Numerous studies have characterised the role of whole microbial cells in U(VI) biosorption and biomineralisation. These suggested that cell surface structures, such as the bacterial cell wall, and EPS were responsible for uranium retention within aerobic environments. Characterisation of these processes has mainly focused upon a whole cell system. With this characterisation, macromolecular structures not associated with U(VI) sequestration may interfere with and affect analysis. Therefore, the mechanistic processes involved are not fully understood, making it difficult to consider their use and application in remediation, extraction and reuse. Characterisation of individual cell surface components is required to provide a more detailed resolution and determine their specific role in the processes involved in uranium biosorption and biomineralisation.

The principal aim of this project was ***to determine the specific roles of microbial cell surface structures and EPS in U(VI) bioremediation from aerobic environments***. This aim was based upon a review of current literature, which resulted in the central research hypothesis:

'The binding and precipitation of soluble, positively charged uranium species to the bacterial cell surface is mediated by negatively charged functional groups of macromolecules present in cell surface structures or secreted extracellulary within EPS.'

The work presented in this study has been developed to investigate U(VI) biosorption and biomineralisation external to the cell and at the cell surface and hence to see whether these processes affect the growth of live microbial cells. To fulfil the aim and establish the research hypothesis, three main research objectives were constructed;

- Objective 1: *To investigate the role of macromolecules associated with EPS in U(VI) biomineralisation*. Extracellular DNA will be used as a representative biomolecule of bacterial EPS for U(VI) precipitation reactions and phosphatase activity. Characterisation of the precipitated U(VI)-eDNA complexes and enzymatic U(VI) minerals will be performed using a combination of spectroscopic and analytical techniques to determine the specific interactions involved with U(VI) retention. This study is shown in Chapter 2.

- Objective 2*: To characterise the bacterial cell surface structures and investigate their ability to retain uranium from aqueous environments*. To fully understand the

role of the outermost layers of the bacterial cell surface in U(VI) sequestration, the cell wall and membrane of a selection of bacterial species will be isolated and purified. A combination of spectroscopic techniques are to be used to understand the macromolecular composition of these isolates while batch U(VI) biosorption experiments will be conducted to understand the roles of each structure in U(VI) retention. Spectroscopic characterisation of cell surface structures is shown in Chapter 3 and their role in U(VI) biosorption is shown in Chapter 4.

- Objective 3: *To identify whether the biomineralisation and biosorption processes that occur with purified cell surface components are similar to those observed with live cells and therefore assess how these U(VI) interactions affect cell viability and activity*. The tolerance of bacterial species used within this study to U(VI) will be monitored during growth experiments by flow cytometry. In addition, U(VI) biomineralisation will be monitored by electron microscopy and phosphatase activity assays. The results from this study are shown in Chapter 5.

From the work described in this thesis, the main conclusions were as follows;

- The biosorption and biomineralisation with extracellular DNA were mediated by phosphate moieties within eDNA or those hydrolysed by acid phosphatase, to either produce a uranium-eDNA precipitate or uranium phosphate-bearing mineral.
- The purified Gram-positive cell wall of *B. subtilis* exhibited greater uranium retention capacity compared to the Gram-negative cell wall of *P. putida* and those of live cells and cell surface membranes. Phosphate and carboxyl groups, from phosphorylated biopolymers and proteins, were responsible for uranium biosorption at the cell surface.
- Gram-negative strains exhibited a higher tolerance to uranium than Gram-positive strains in this study. Live cells enzymatically precipitate uranium phosphate minerals tethered to the cell surface, or within EPS, as a tolerance mechanism to cope with uranium toxicity at low uranium concentration and towards circumneutral pH. At higher concentrations of uranium or at low pH, biosorption to the bacterial biomass present likely occurs, when bacterial growth was not favourable and cell death.

Chapter 2: The role of extracellular DNA in uranium precipitation and biomineralisation.

2.1 Abstract

Bacterial extra polymeric substances (EPS) have been associated with the extracellular retention of uranium. Here we report findings on the precipitation and biomineralisation of uranium, with extracellular DNA (eDNA) used as a model biomolecule representative of EPS. The precipitation was investigated as a function of pH, ionic strength and varying concentrations of reactants. The role of phosphate moieties in the biomineralisation mechanism was studied by enzymatically releasing phosphate (ePO_4) from eDNA compared to abiotic phosphate (aPO_4). The eDNA-uranium precipitates and uranium minerals formed were characterised by Attenuated Total Reflectance- Fourier Transform Infrared (ATR-FT-IR) Spectroscopy, Scanning Electron Microscopy- Energy Dispersive X-Ray Analysis (SEM-EDX), X-Ray Powder Diffraction (XRD) and X-Ray Photoelectron Spectroscopy (XPS).

ATR-FT-IR showed that at pH 5, the eDNA-uranium precipitation mechanism was predominantly mediated by interactions with phosphate moieties from eDNA. At pH 2, the uranium precipitation with eDNA occurred with phosphate and the nitrogenous bases. The reaction was dependent on pH, where the formation of a precipitate was reduced as the pH increases. XRD confirmed the formation of a uranium phosphate synthesised using ePO_4. XPS and SEM-EDX studies indicated the incorporation of contaminants such as carbon and nitrogen from the enzymatic orthophosphate hydrolysis. These results suggested that eDNA within EPS can precipitate uranium from solution as a uranium-eDNA complex or uranium phosphate mineral of the type $(UO_2HPO_4)\bullet xH_2O$. This demonstrated that eDNA from bacterial EPS is a key contributor to uranium biomineralisation.

2.2 Introduction

The biosorption of soluble uranium species, such as the highly mobile uranyl ion (UO_2^{2+}), has been associated with constituents of bacterial extra polymeric substances (EPS) at acidic pH (Krawczyk-Baersch et al., 2008, Finlay et al., 1999, Merroun et al., 2003b, Jroundi et al., 2007, Merroun and Selenska-Pobell, 2008). Bacterial EPS consists of large quantities of biopolymers, such as phosphorylated peptides, polysaccharides, lipids and nucleic acids, that have either been secreted by the bacteria or released into the surrounding environment from the lysis of dead bacteria (Barkleit et al., 2011). Due to the complexity of bacterial EPS, it is difficult to identify detailed mechanisms for extracellular uranium biomineralisation. Merroun et al. (2011) suggested that phosphate-containing and phosphorylated biopolymers were responsible for sequestering uranium through biosorption to negatively charged functional groups, or through acid phosphatase activity that liberates inorganic phosphate from biological molecules to mineralise uranium.

Extracellular DNA (eDNA) is a major constituent of EPS. Elevated levels of eDNA production have been reported following investigations of metal interactions with bacterial biofilms (Priester et al., 2006). eDNA can be incorporated into EPS through numerous mechanisms. The main source of eDNA is from the lysis of dead bacteria (Nielsen et al., 2007, Levy-Booth et al., 2007, Allesen-Holm et al., 2006, Das et al., 2013). Additional sources of eDNA originate from bacterial extrusion, used as a survival or nutrient enrichment mechanism (Battista, 1997, Matsui et al., 2003, Vilain et al., 2009, Steinberger and Holden, 2005). Purified DNA has been used for the removal of metal cations from solution (Duguid et al., 1995, Alex and Dupuis, 1989, Takahashi et al., 2014). It can be hypothesised that the biosorption of uranium with EPS is facilitated by eDNA within acidic conditions through phosphate interactions, due to the large amounts of phosphate within DNA in comparison to that found in sugars or lipids.

Acid phosphatase activity has been associated with the precipitation of uranium phosphate mineral-like phases (Macaskie et al., 2000, Merroun et al., 2011, Martinez et al., 2007, Sousa et al., 2013). It has been suggested that uranium biomineralisation from microbial acid phosphatase activity is neither dependant on microbial structure, be it of gram positive or gram-negative origin, but instead, depends on pH (Merroun and Selenska-Pobell, 2008). Enzymatic uranium precipitation occurs at mildly acidic to circumneutral conditions through the formation of uranium phosphate mineral-like

phases, such as meta-autunite, HUO_2PO_4 and $NaUO_2PO_4$, both inside and outside the cell. By contrast, the bioprecipitation with phosphate groups in biomolecules more commonly occurs under mild to acidic conditions (Merroun and Selenska-Pobell, 2008, Macaskie et al., 2000, Macaskie et al., 1992, Koban et al., 2004). This suggested that free phosphate of biogenic origin plays an important role in the mineralisation of uranium. Additionally, it has been demonstrated that DNA can be utilised as a sole source of phosphorus liberated through extracellular phosphatase activity for metal reduction (Pinchuk et al., 2008). Commercially available purified acid phosphatase has been used to hydrolyse organic phosphate from biological samples for total phosphate analysis (He and Honeycutt, 2005, Johnson and Hill, 2011).

Previous studies have described the use of indigenous and genetically modified bacteria in the biomineralisation of uranium through acid phosphatase activity (Macaskie et al., 2000, Merroun et al., 2011, Martinez et al., 2007, Sousa et al., 2013, Reitz et al., 2014). Other work has merely found a potential mechanism within a whole cell system. To date, no studies have used purified acid phosphatase to liberate inorganic phosphate from biological molecules found within EPS for subsequent uranium biomineralisation. Additionally, uranium biosorption to EPS has been studied only at the level of a complete process (Jroundi et al., 2007, Morcillo et al., 2014).

The aim of this work was to demonstrate the significance of two possible uranium sequestration mechanisms; the precipitation of uranium with eDNA and the biomineralisation of a uranium phosphate mineral phase utilising enzymatically liberated orthophosphate (ePO_4). It was hypothesised that enzymatically liberated phosphate would bind to the highly mobile U(VI) species in acidic conditions. FT-IR and XRD were used to determine the mechanisms involved in the interactions of eDNA and ePO_4 to uranium in acidic conditions. FT-IR was a suitable tool to identify the functional groups involved in binding since there are well-defined changes in peak position and intensity upon uranium binding to biomass. XRD was used to determine the mineral structures of uranium precipitates formed following accumulation (Choudhary and Sar, 2011, Lu et al., 2013, Merroun et al., 2003b, Sousa et al., 2013). eDNA was used as a model biomolecule to represent uranium biomineralisation within complex bacterial EPS for three reasons: i) it contains phosphate moieties bound to organic compounds, which allow us to quantify the efficiency of organic phosphate to precipitate uranium, ii) DNA-organic phosphate can be enzymatically released as phosphate (ePO_4) which could be

used to mineralise uranium, and iii) there is a large abundance of eDNA within the EPS of many bacteria

The novelty of this work consists in the fact that, whereas previous uranium biomineralisation experiments resorted to investigating whole bacteria and their corresponding EPS, this study aimed to quantify the process by using representative biomolecules (purified DNA and acid phosphatase) to investigate whether phosphate-containing biomolecules were responsible for the uranium biomineralisation within EPS. Understanding the mechanistic processes involved in uranium binding to eDNA and ePO_4 provides insight on how bacterial EPS interacts with uranium.

2.3 Experimental Procedures

2.3.1 Materials and stock solutions

The composition of eDNA from bacteria was comparable to the composition of DNA from other organisms (Pinchuk et al., 2008). In order to simplify the experiments, lyophilised DNA from salmon sperm was obtained from Sigma-Aldrich (D1626) since it is ready available. DNA stock solutions of 2 mg mL^{-1} (referred to from here on as eDNA) were prepared using DNase/RNase-free water. Purified acid phosphatase (6.3 units mg^{-1} solid) was obtained from Sigma-Aldrich (P1146) and solutions were prepared directly before use using DNase/RNase-free water. U(VI) solutions were prepared using 0.1 M uranyl nitrate hexahydrate ($UO_2(NO_3)_2 \bullet 6H_2O$) in 1 % HNO_3 (Fluka Analytical: 94270). The pH of solutions was altered by the addition of HCl or NaOH while the ionic strength was controlled by the addition of NaCl.

2.3.2 Uranium-eDNA precipitation

Uranium-eDNA precipitation experiments were designed to determine the amount of uranium removed from solution by a given quantity of extracellular DNA (eDNA). 1 mg mL^{-1} eDNA was incubated with 0.5 mM U(VI) in 0.1 M NaCl (pH 5). All experiments were carried out at room temperature for 1 hour. To investigate the effects of pH, ionic strength and reactant concentrations on the precipitation process, the pH range studied was 2 - 7. The ionic strength was systematically varied between 1000 to 1 mM NaCl, DNA concentrations ranged from 2.0 to 0.25 mg mL^{-1} and U(VI) concentrations ranged from 0.05 to 2 mM. A minimum of 6 replicates was performed for each investigation.

To quantify the free uranium remaining in solution, residual not precipitated from solution by uranium DNA was removed. The eDNA-uranium complexes and subsequent precipitates were removed from solution by centrifugation at 10,000 *g* for 10 minutes (4 °C), lyophilised and stored for spectral analysis. 50 µL 3 M sodium acetate buffer (pH 5.0) and 550 µL of 2-propanol were added sequentially to 500 µL of the supernatant. Samples were stored on ice for 15 minutes and centrifuged at 10,000 *g* for a further 15 minutes (4 °C). Supernatants were acidified using 1 % HNO_3 and uranium was quantified by Inductively Coupled Plasma-Mass Spectrometry (ICP-MS) (ELAN DRC II, Perkin Elmer).

The Quant-iTTM PicoGreen® dsDNA reagent kit from Life Technologies (P11496) was used to quantify unbound eDNA in solution following the removal of the DNA-uranium precipitate. Free DNA was diluted using 1 × TE buffer (10 mM Tris-HCl, 1 mM EDTA, pH

7.5) to below 100 µg/mL while the Quant-iTTM PicoGreen® dsDNA reagent (Component A) was diluted 50 fold using 1 × TE buffer for analysis. 10 µL of free DNA was added to 200 µL of reagent and analysed using the FLUOstar OPTIMA fluorescent microplate reader with samples excited at 485 nm and fluorescence emission intensity recorded at 545 nm. DNA was quantified by comparison to known standards and relative fluorescence units to obtain a linear calibration.

2.3.3 Enzymatic orthophosphate hydrolysis

Inorganic enzymatic orthophosphate (ePO_4) was quantified following eDNA interactions with acid phosphatase to determine the optimum phosphate release for subsequent uranium precipitation. Acid phosphatase was incubated with eDNA to investigate the effects of enzyme concentration, DNA concentration, pH, ionic strength, temperature and uranium concentration on phosphate liberation. Standard parameters were 2 units mL^{-1} acid phosphatase, 1 mg mL^{-1} DNA, 0.1 M NaCl at 37 °C (pH 5).

Subsamples were removed periodically and aseptically to precipitate out any remaining phosphate-containing DNA from solution. The supernatant was quantified for enzymatic inorganic orthophosphate (ePO_4) using a molybdenum blue based method (He and Honeycutt, 2005). To 80 µL of sample, 100 µL of 0.1 M ascorbic acid containing 0.5 M trichloroacetic acid (TCA), 50 µL 0.01 M ammonium molybdate and 50 µL 0.1 M sodium citrate containing 0.2 M sodium arsenite were added sequentially. Samples were incubated at room temperature for 30 minutes with gentle agitation and the absorbance of molybdenum blue was measured at 850 nm.

2.3.4 Uranium biomineralisation using enzymatically generated phosphate

Enzymatic phosphate from eDNA (ePO_4) was hydrolysed from 1 mg mL^{-1} DNA using 2 units mL^{-1} acid phosphatase in the presence of 0.1 M NaCl (pH 5) for 72 hours at 37 °C; solutions were centrifuged and membrane filtered (0.45 µm PES) to remove the acid phosphatase and any other particulates. ePO_4 was incubated with uranium at varying molar ratios (pH 5) for 24 hours at 37 °C. Precipitates were removed by centrifugation and stored for further analysis while the supernatant was aliquoted to determine remaining phosphate and acidified to quantify uranium removed from solution.

2.3.5 Fourier Transform Infra-Red Spectroscopy (FT-IR)

For spectroscopic analysis of uranium precipitates and minerals, samples were centrifuged at 10,000 *g* for 15 minutes (4 °C), supernatant removed and pellet lyophilised (Alpha 1-2 LD Plus freeze dryer). Measurements were performed using Attenuated Total Reflectance (ATR) – FT-IR. These were obtained using a Silver Gate Evolution ATR accessory, consisting of a germanium crystal, coupled to a Perkin Elmer Spectrum One FT-IR spectrometer. A total of 30 scans were performed on each sample within the scanning range of 2000-800 cm^{-1}. An average spectrum was obtained from three replicates, baseline corrected and normalised to 1.5 arbitrary units using the 1063 cm^{-1} peak from the control eDNA spectra, corresponding to the vibrational stretching of phosphate groups. All data acquisition and processing was performed using PerkinElmer Spectrum version 3.3.

2.3.6 Scanning Electron Microscopy (SEM)

Scanning Electron Microscopy (SEM) with Energy Dispersive X-ray (EDX) analysis was carried out using an FEI Quanta 650 Environmental Scanning Electron Microscope (ESEM) with a tungsten thermionic emission gun equipped with an Oxford Instrument's Aztec EDX system. Lyophilised uranium minerals powders were immobilised on PELCO^{TM} carbon conductive tabs (12 mm) and samples were carbon coated to a 10 nm approximate thickness using a Quorum Industries K150 carbon coating unit before analysis.

2.3.7 X-ray powder diffraction (XRD) analysis

XRD patterns of lyophilised eDNA-uranium precipitates and uranium minerals were recorded using a STOE STADI P diffractometer with a molybdenum radiation source (λ (α) = 0.71 Å) over the range of 3°-40° (2θ) with a step length of 0.01°. Before data acquisition, samples were flattened between 2 acetate sheets using a hydraulic press (SPECAC) and placed in the sample holder. The molecular structures of the eDNA-uranium precipitates and uranium minerals were identified through comparison with standard powder diffraction files (PDF-4+ International Centre for Diffraction Data's (ICDD) database).

2.3.8 X-ray photoelectron spectroscopy (XPS)

For XPS analysis, uranium minerals formed from the reaction of ePO4 with uranium were immobilised on double-sided carbon adhesive tape and mounted onto sample studs. XPS analysis was conducted using a KRATOS AXIS 165 Ultra Photoelectron spectrometer using an Al Kα X-ray source (1486.6 eV). Each sample was analysed by a wide survey scan (pass energy 160 eV, 1.0 eV step size) and a high resolution scan (pass energy 20 eV, 0.1 eV step size) for carbon, oxygen, phosphorus and uranium. Binding energies were determined using the CasaXPS software (Version 2.3.16). Binding energies were determined using the C_{1s} component set at 285.0 eV, attributed to carbon bound only to carbon and hydrogen. The full width half maximum was kept constant for subsequent peak calibration.

2.4 Results and Discussion

2.4.1 Uranium removal by eDNA

Uranium and eDNA precipitated from solution, following their interaction, were quantified by ICP-MS and PicoGreen fluorescence, respectively. The percentage removal (Equation 4) of reactants was calculated over a variety of pH values, ionic strength and varying concentrations of reactants in solution, where C_O is the initial reactant concentration and C_I is the reactant remaining in solution.

$$\% R = \frac{C_O - C_I}{C_O} \times 100 \qquad \text{Equation 4.}$$

Figure 9 shows the percentage of uranium and eDNA removed as a function of pH. Changes in pH affected the adsorption of uranium to eDNA from aqueous solution, with an increase in the removal of both reactants as the pH decreased to as low as pH 2. Within a low pH environment, almost all the eDNA (1 mg mL^{-1}) was removed from solution by 0.5 mM uranium, in the presence of 0.1 M NaCl. 99.9 ± 0.2% of eDNA and 95.3 ± 0.4 % of uranium was removed at pH 2, decreasing to 92.3 ± 2.6 % eDNA removed and 88.2 ± 0.7 % U removed at pH 4. As the pH increased to 5, the amount of uranium precipitation with eDNA decreased substantially and 31.7 ± 13.9 % of eDNA and 42.6 ± 3.3 % of uranium were removed from solution.

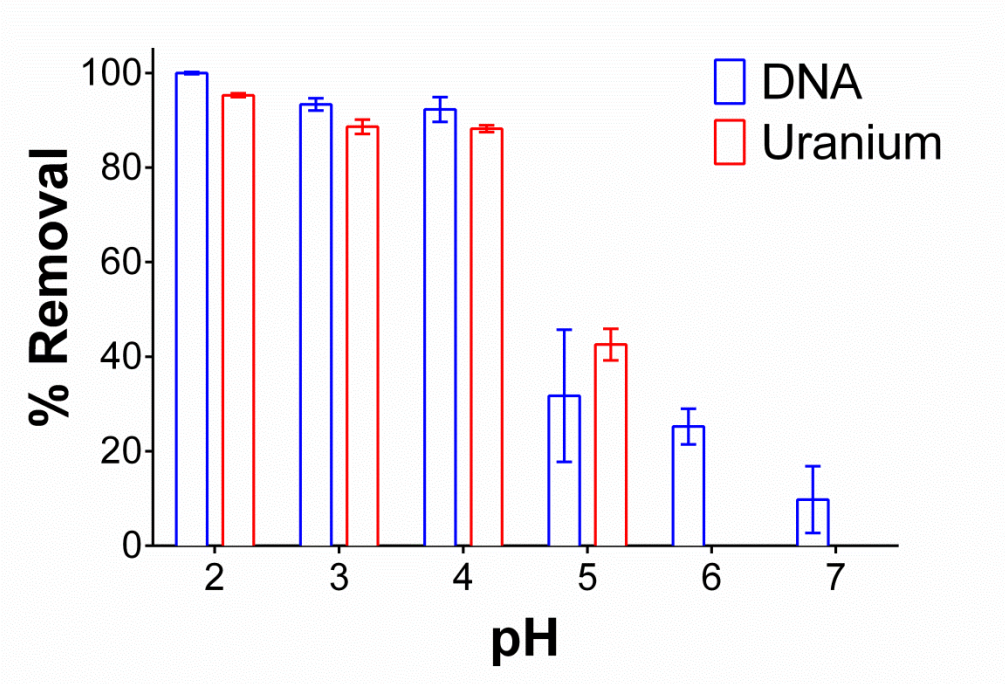

Figure 9. Uranium binding to eDNA as a function of pH and % removal of both reactants

DNA has an overall net negative charge in acidic solutions, due to its negatively charged deoxyribose phosphate backbone (Takahashi et al., 2014, Alex and Dupuis, 1989). The highly mobile positively charged U(VI) ion, UO_2^{2+} is the dominant uranium (VI) species at low pH (Appendix Table 1). UO_2^{2+} interacted favourably with eDNA at low pH, as results indicated almost complete removal of both reactants between pH 2 and pH 4. At pH 5 to 7, the uranium was in the form of larger U(VI) species such as $(UO_2)_3(OH)_5^+$ and $(UO_2)_4(OH)_7^+$. The difference in size and net charge of these U(VI) species, in comparison to UO_2^{2+}, may have hindered interactions with functional groups within the eDNA structure. At circumneutral pH, the uranium reached its solubility equilibrium and was not present in solution. However, between 10 – 20% of DNA was removed, possibly as a concomitant to the insoluble U(VI) species.

The precipitation of eDNA with U(VI) species decreased as the solution pH increased. However, uranium biosorption with EPS occurred over a wide range of pH (Jroundi et al., 2007, Morcillo et al., 2014). EPS is composed of various biomolecules, including polysaccharides, nucleic acids, peptides and lipids (Marvasi et al., 2010, Wingender et al., 1999). Polysaccharides have previously shown preferential binding to uranium closer to neutral pH than other biomass present within bacterial EPS (Kazy et al., 2008). At low pH, uranium would interact more favourably with components such as eDNA that have an overall net negative charge at low pH. As the pH increases, the net positive charge of eDNA increases; hence uranium binding preferences change to other biopolymers. The carboxyl groups of polysaccharides are deprotonated at pH higher than 5 and therefore, are more favourable to binding positively charged U(VI) species from solution at higher pH. These results indicated that there is preferential binding to different biomass present within EPS as a function of pH.

Changes in ionic strength, simulated by varying concentrations of sodium chloride with 0.5 mM U(VI) (pH 5), affected the precipitation of eDNA-uranium complexes from solution, Figure 10. As the concentration of sodium chloride decreased in solution, there was a reduction in the formation of eDNA-uranium precipitates. At 1 M sodium chloride (pH 5), the amount of 1 mg mL^{-1} eDNA and 0.5 mM uranium precipitated from solution were 36.8 % ± 6.9 % and 56.3 ± 2.2 %, respectively. This precipitation decreased to 13.7 ± 4.1 % eDNA and 10.6 ± 7.6 % uranium when no sodium chloride was present in the solution.

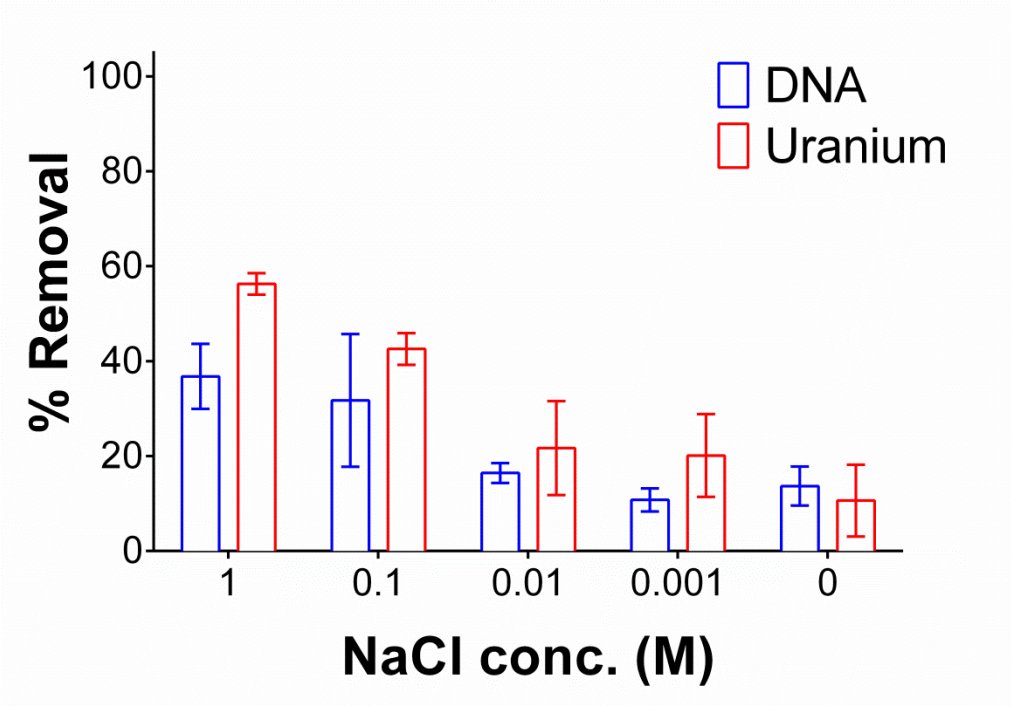

Figure 10. Uranium binding to eDNA as a function of NaCl concentration in solution and % removal of both reactants

The increase in uranium precipitating with eDNA was due to the increased ionic strength. As the ionic strength increased there was an overall increase in the negative net charge of the eDNA structure, facilitating the interaction. This finding agrees with other studies that have investigated the effect of ionic strength on the adsorption of protons to biomass of bacterial origin (Plette et al., 1995, Burnett et al., 2006). The uranium speciation also changed as a function of NaCl concentration (Visual MINTEQ- Appendix Table 2). In the presence of 1000 mM NaCl (at pH 5), the U(VI) species abundance was 16.3 % UO_2^{2+} and 40.9 % $(UO_2)_3(OH)_5^+$. As the NaCl concentration decreased to zero, the relative abundance of the former decreased to approximately 7.3 % and 62.1 %, respectively, making $(UO_2)_3(OH)_5^+$ the dominant species. The speciation of uranium hence controlled the reactivity of uranium with eDNA.

Changes in the initial concentration of reactants to determine the maximum binding of uranium to eDNA suggested that uranium binding to eDNA at pH 5 was poor at precipitating both reactants, Figure 11. With an initial concentration of 0.5 mM uranium and 2 mg mL^{-1} eDNA in solution, a maximum of 64.5 ± 6.9 % of uranium is removed by 16.0 ± 15.3 % of the eDNA. As this initial eDNA concentration decreased, the amount of uranium removed from solution decreased to 37.2 ± 4.3 % by 68.0 ± 7.2 % of 0.25 mg mL^{-1} eDNA, Figure 11A. The changes in the initial ratio of concentrations of both

reactants changed the efficiency of removal by changing the number of available reaction sites.

The increase of uranium concentration in solution resulted in a higher percentage removal of 1 mg mL^{-1} eDNA at pH 5, Figure 11B. In the presence of an initial concentration of 0.25 mM uranium, 40.0 ± 6.0 % was removed from solution by 16.3 ± 3.4 % of eDNA in solution. This removal of both reactants increased as 75.0 ± 4.2 % of uranium was removed by 96.2 ± 1.8 % of eDNA at an initial concentration of 2 mM. Up to an initial concentration of 1 mM uranium in solution, the removal of 1 mg mL^{-1} of eDNA was higher than that percentage of uranium removed from solution. At 2 mM uranium there was a higher percentage of DNA removed than uranium. This could be due to changes in the structural conformation of eDNA. Increasing concentrations of uranium and the size of U(VI) species could lead to the deformation of any secondary structures and breaking of the double helix. This change in structure could then lead to an increase in the availability of functional groups (that were not located on the surface of the eDNA molecule in its original conformation) for uranium binding (Babkina and Ulakhovich, 2005). At low concentrations, the quantity of U(VI) species in solution would result in mostly electrostatic interactions at the surface of the eDNA molecule (Alex and Dupuis, 1989).

From the quantification data of uranium-eDNA interactions, it was suggested that at low pH, where the overall net charge of eDNA is negative, there was a higher percentage removal of both reactants from solution due to the interactions between the positively charged U(VI) species and negatively charged biomolecule. This removal increased by increasing the ionic strength, where ions in solution may change the accessibility of certain functional groups, potentially due to conformational changes of the eDNA structure, leading to higher uranium binding and removal from solution.

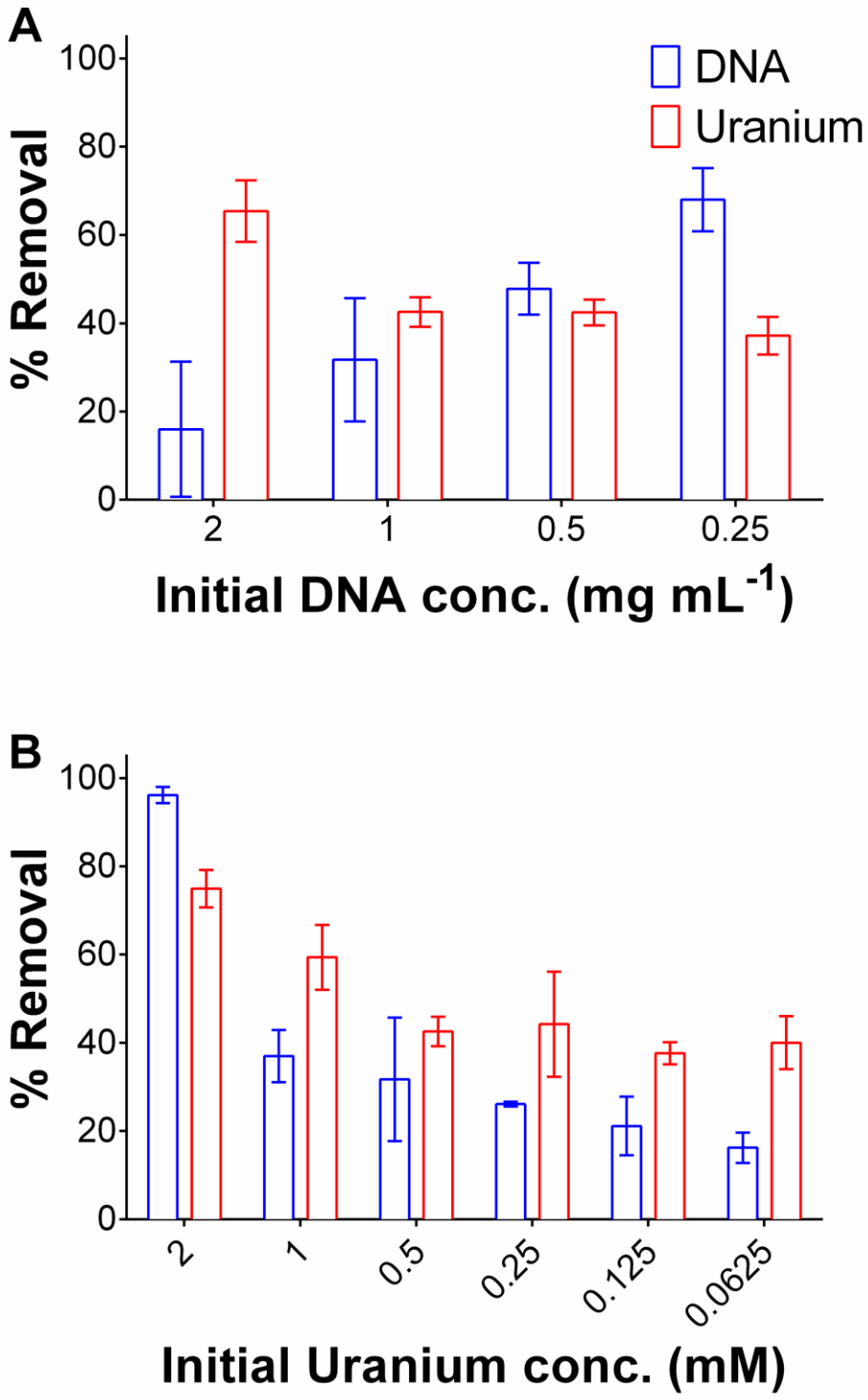

Figure 11. Uranium binding to eDNA as a function of initial DNA concentration [A] and initial uranium concentration [B] and % removal of both reactants at pH 5.

2.4.2 Characterisation of eDNA-uranium interactions using ATR-FT-IR

ATR-FT-IR spectra were collected in triplicate between 2000 and 800 cm^{-1} to identify the functional groups in eDNA involved in precipitating uranium from solution. The shifts, changes in shape and intensity of peaks can be attributed to a number of different functional groups in eDNA binding to uranium.

2.4.2.1 pH effect on uranium binding to eDNA

eDNA-uranium precipitates were formed by interacting 1 mg mL^{-1} eDNA with 0.5 mM uranium solution at pH values 2 - 5. Adsorption band assignments within the 2000 - 800 cm^{-1} region are displayed in Table 1 and spectra displayed in Figure 12.

Table 1. Band allocation for the FT-IR spectra of 0.5 mM uranium binding to 1 mg mL^{-1} eDNA at different pH

Control	pH 2	pH 3	pH 4	pH 5	Allocation*
1700 $_{sh}$	1689 $_{s}$	1700 $_{sh}$	1700 $_{sh}$	1700 $_{sh}$	ν (C-NH_2) bases; Guanine/ Adenine
1649 $_{m}$	1632 $_{sh}$	1646 $_{w}$	1647 $_{w}$	1649 $_{m}$	ν (C=O) nitrogenous bases
1606 $_{w}$	1599 $_{sh}$	1600 $_{w}$	1602 $_{w}$	1606 $_{w}$	-
1579 $_{vw}$				1579 $_{vw}$	Adenine/Cytosine
1529 $_{w}$	1534 $_{vw}$	1531 $_{vw}$	1529 $_{vw}$	1529 $_{w}$	δ (NH)/ ν (C=O), Cytosine/Guanine
1486 $_{m}$	1478 $_{w}$	1482 $_{w}$	1483 $_{w}$	1490 $_{m}$	C-NH_2 scissoring
1419 $_{w}$	1419 $_{vw}$	1419 $_{vw}$		1419 $_{w}$	-
1369 $_{w}$	1366 $_{vw}$	1365 $_{vw}$	1365 $_{vw}$	1367 $_{vw}$	ν (C=NH) nitrogenous bases
1230 $_{s}$	1209 $_{s}$	1212 $_{s}$	1214 $_{s}$	1218 $_{s}$	ν_{as} (PO_2)
1063 $_{vs}$	1059 $_{vs}$	1061 $_{vs}$	1064 $_{vs}$	1060 $_{vs}$	ν_{s} (PO_2), ν (C-OH, C-0-C, C-C)
965 $_{s}$	970 $_{m}$	970 $_{m}$	970 $_{m}$	970 $_{m}$	ν (P-O)
	928 $_{s}$	927 $_{s}$	930 $_{s}$	918 $_{s}$	ν (U–O_{ligand})

sh= shoulder vw= very weak w= weak m= medium s= strong vs= very strong

* Functional group assignment is based on (Cecal et al., 2012), (Alex and Dupuis, 1989), (Parikh and Chorover, 2006), (Kamnev et al., 1999), (Lumetta et al., 1999) and (Kazy et al., 2009)

An increase in shape and a shift in adsorption band position, corresponding to changes in vibrational stretching of the C-NH_2 band of nitrogenous bases (Cecal et al., 2012, Alex and Dupuis, 1989) were observed for the eDNA-uranium precipitates at pH 2. The shift from 1700 cm^{-1} to 1689 cm^{-1} suggested binding to nitrogenous bases at very acidic pH.

Shifts in the adsorption band position corresponding to the vibrational stretching of the C=O bond were observed as the pH increases from 2 to 5. At pH 2, the stretching was observed at 1632 cm^{-1}. As the pH increases to 3, 4 and 5, the adsorption band position shifted to 1646, 1647 and 1649 cm^{-1}, respectively. The vibrational stretching of C=O within the eDNA control spectra was observed at 1649 cm^{-1}; therefore it was suggested that the binding of uranium to carbonyl groups in nitrogenous bases was pH-dependent and bind at lower pH (Parikh and Chorover, 2006).

As the pH increased from 2 to 5, the shifts and intensity changes of adsorption bands within the region of 1550 and 1350 cm^{-1} corresponded to the binding of U(VI) species to the nitrogenous bases of eDNA. A shift in adsorption band position, corresponding to the changes in the vibrational scissoring mode of C-NH_2 groups following uranium interactions with eDNA at pH 2. This adsorption band shifted from 1486 cm^{-1} in the eDNA control spectra to 1478 cm^{-1}. This change in adsorption band position from the eDNA control spectra decreased as the pH increases, indicating a higher binding affinity to the bases at low pH. This was further supported by changes in adsorption band position at 1529 cm^{-1} (shifting to 1534 cm^{-1} as the pH decreases) and at 1369 cm^{-1} (shifting to 1366 cm^{-1}), corresponding to δ NH, ν C=O and ν C=NH, respectively, following uranium binding with eDNA at pH 5 (Parikh and Chorover, 2006, Alex and Dupuis, 1989, Cecal et al., 2012).

The adsorption band that corresponded to the vibrational asymmetric stretching of PO_2 groups was observed within the eDNA control spectra at 1230 cm^{-1}. A strong shift in adsorption band position was observed following the interactions with uranium at pH 2 - 5. At pH 5 the adsorption band was observed at 1218 cm^{-1}. As the pH decreased, there was a greater shift in position. At pH 2, the adsorption band position shifted further to 1209 cm^{-1}. This change in adsorption band position was attributed to the weakening of the P-O bond due to uranium binding (Kamnev et al., 1999, Choudhary and Sar, 2011). A shift in the 1063 cm^{-1} adsorption band of the eDNA control spectra, corresponding to vibrational symmetric stretching of PO_2 and the vibrations of C-OH, C-0-C, C-C was observed following uranium interactions with eDNA. This adsorption band position shifts to 1060 cm^{-1} when the solution pH of the experiment increased to 5 (Alex and Dupuis, 1989). This smaller shift in adsorption band position was most likely due to the lack of uranium interactions with C-OH, C-O-C and C-C from deoxyribose sugars (Parikh and Chorover, 2006).

Changes in adsorption band position within the eDNA control spectra were observed at 965 cm^{-1} following uranium interactions with eDNA at pH 2 - 5. In the presence of uranium, the adsorption bands shifted to 970 cm^{-1}, for all pH investigated (Alex and Dupuis, 1989, Kamnev et al., 1999). This change in adsorption band position was explained as U(VI) species binding to phosphate through the changes in vibrational frequency of the P-O single bond. A shift in adsorption band position of this functional group suggested preferential binding to phosphate groups over a wide range of acidic

pH. As the pH decreased, the highly mobile UO_2^{2+} U(VI) species bound to other functional groups within the eDNA, such as those present within the nitrogenous bases, Figure 13A.

Following the interaction of eDNA with uranium between pH 2 – 5, the presence of an additional adsorption band was observed within the spectral region of 928-918 cm^{-1}. This band corresponded to the vibrations of the U-O ligand (Lumetta et al., 1999, Kazy et al., 2008, Choudhary and Sar, 2011, Barkleit et al., 2011, Lu et al., 2013, Pan et al., 2015, Theodorakopoulos et al., 2015).

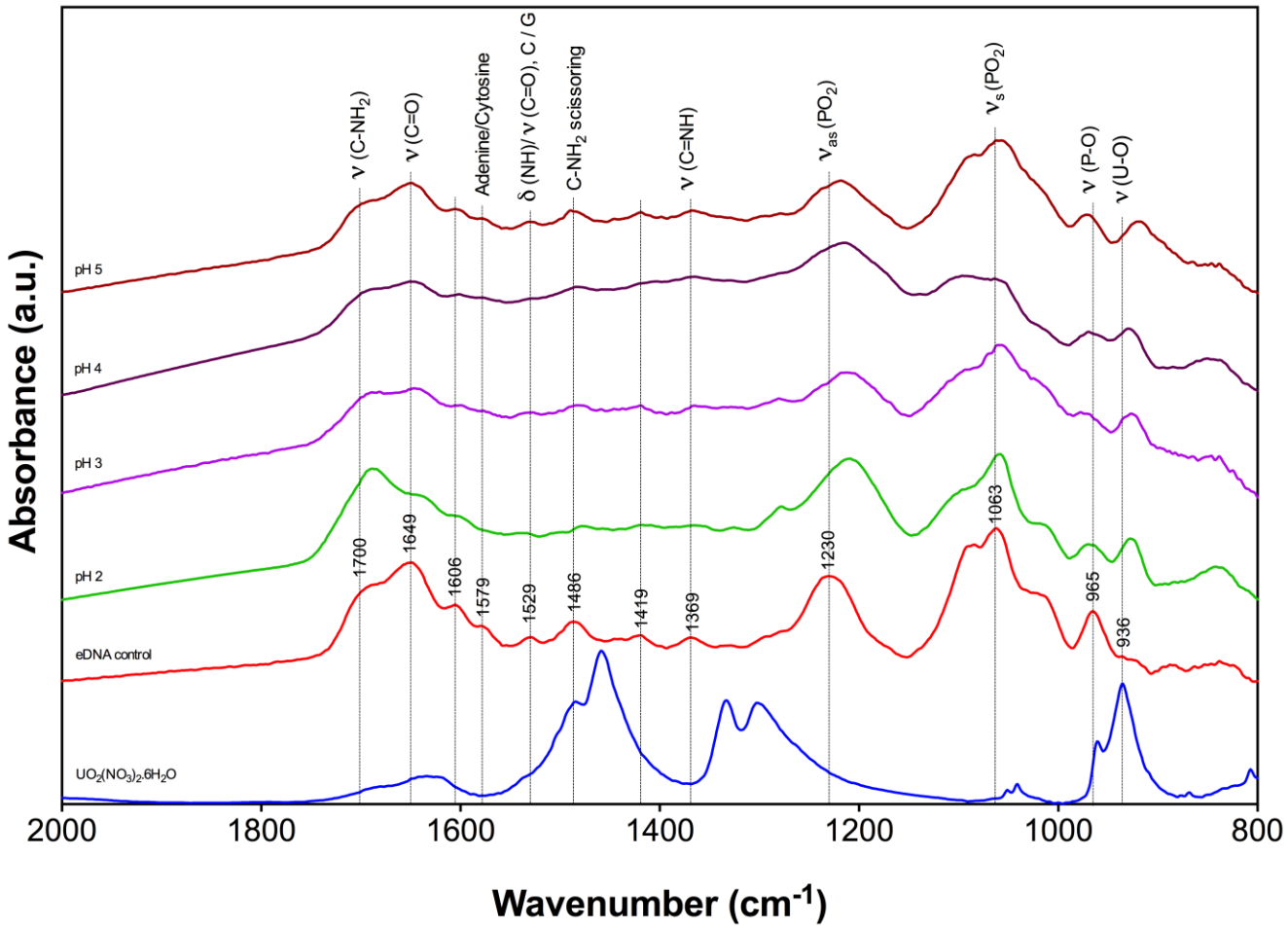

Figure 12. FT-IR spectra of 0.5 mM uranium binding to 1 mg mL^{-1} eDNA at increasing pH within the region 2000 – 800 cm^{-1}.

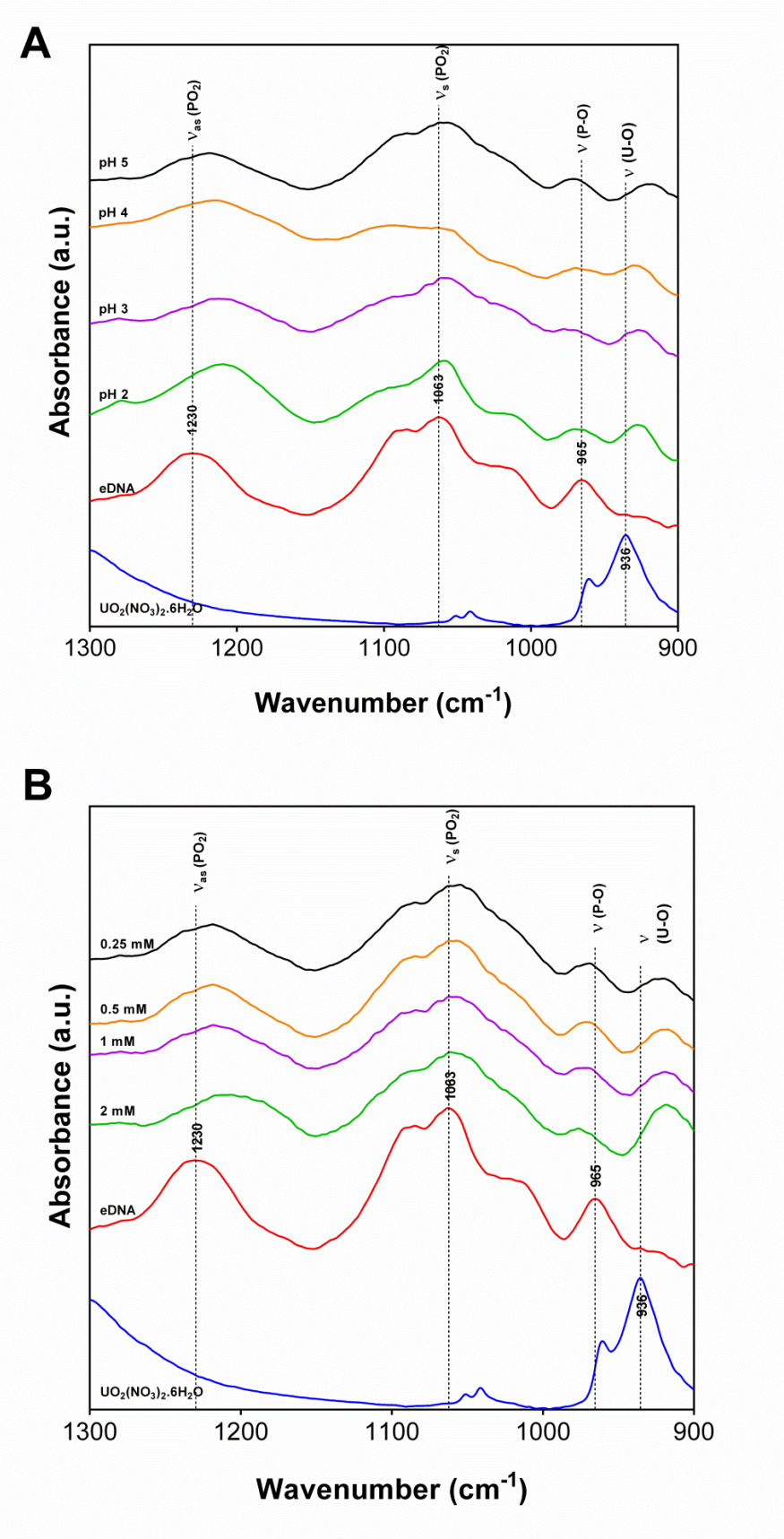

Figure 13. Phosphate and Uranium FT-IR region of uranium binding to eDNA [A] at increasing pH and [B} at increasing uranium concentration [B]

2.4.2.2 Reactant concentration effect on uranium binding to eDNA

To investigate the effect of varying initial reactant concentrations on uranium binding to eDNA, 1 mg mL^{-1} eDNA was mixed with uranium (pH 5) between 2 and 0.25 mM. Peak assignments within the 2000-800 cm^{-1} region are displayed in Table 2 and spectra displayed in Figure 14.

Table 2. Band allocation for the FT-IR spectra of 1 mg mL^{-1} eDNA binding to uranium (pH 5) at increasing concentrations.

Control	2 mM	1 mM	0.5 mM	0.25 mM	Allocation*
1700 $_{sh}$	1700 $_{sh}$	1700 $_{sh}$	1700 $_{sh}$	1700 $_{sh}$	ν (C-NH_2) bases; Guanine/ Adenine
1649 $_{m}$	1647 $_{m}$	1647 $_{m}$	1649 $_{m}$	1649 $_{m}$	ν (C=O)
1606 $_{w}$	1605 $_{w}$	1605 $_{w}$	1606 $_{w}$	1606 $_{w}$	-
1579 $_{vw}$	1578 $_{vw}$	1578 $_{vw}$	1579 $_{vw}$	1579 $_{vw}$	Adenine/Cytosine
1529 $_{w}$	1525 $_{w}$	1529 $_{w}$	1529 $_{w}$	1529 $_{w}$	δ (NH)/ ν (C=O), Cytosine/Guanine
1486 $_{m}$	1490 $_{m}$	1490 $_{m}$	1490 $_{m}$	1490 $_{m}$	C-NH_2 scissoring
1419 $_{w}$	1419 $_{w}$	1419 $_{w}$	1419 $_{w}$	1419 $_{w}$	-
1369 $_{m}$	1365 $_{m}$	1367 $_{m}$	1367 $_{m}$	1367 $_{m}$	ν (C=NH) nitrogenous bases
1230 $_{s}$	1206 $_{s}$	1218 $_{s}$	1218 $_{s}$	1218 $_{s}$	ν_{as} (PO_2)
1063 $_{vs}$	1061 $_{vs}$	1062/1057 $_{vs}$	1062/1057 $_{vs}$	1062/1055	ν_{s} (PO_2), ν (C-OH, C-0-C, C-C)
965 $_{s}$	976 $_{s}$	973 $_{s}$	970 $_{s}$	969 $_{s}$	ν (P-O)
	918 $_{s}$	919 $_{s}$	918 $_{s}$	920 $_{s}$	ν (U–O_{ligand})

sh= shoulder vw= very weak w= weak m= medium s= strong vs= very strong

* Functional group assignment is based on (Cecal et al., 2012), (Alex and Dupuis, 1989), (Parikh and Chorover, 2006), (Kamnev et al., 1999), (Lumetta et al., 1999) and (Kazy et al., 2009)

There was a small change in the adsorption band position that corresponded to changes in the ν (C=O) band at 1649 cm^{-1} in the eDNA control spectra, shifting to 1647 cm^{-1} as the uranium concentration increased to 2 mM in solution. Similarly, the adsorption band at 1529 cm^{-1} shifted to 1525 cm^{-1} as the uranium concentration increased. Since this band is assigned to the vibrations of C=O and N-H bending, it was suggested that, as the uranium concentration increased in solution at pH 5, the U(VI) species in solution bound to the nitrogenous bases of the eDNA. This was further confirmed by changes in position and slight broadening of the adsorption band at 1063 cm^{-1}, assigned to the vibrational stretching of C-OH, C-O-C and C-C as well as the vibrational symmetric stretching of phosphate groups.

The binding of uranium to the nitrogenous bases at higher initial uranium concentrations was further indicated by the shifts in adsorption band position assigned to C-NH_2 scissoring at 1486 cm^{-1}. In the presence of uranium this adsorption band shifts to 1490 cm^{-1}. Similarly, the ν (C=NH) adsorption band shifted from 1369 to 1365 cm^{-1} when eDNA interacted with 2 mM uranium solutions.

The most significant difference in adsorption band position as the initial uranium concentration in solution increased was associated with bands assigned to vibrational stretching of phosphate groups, Figure 13B. The adsorption band at 1230 cm^{-1} in the eDNA control spectra corresponded to the vibrational asymmetric stretching of phosphate groups within the deoxyribose phosphate backbone. In the presence of 0.25 mM uranium, this adsorption band shifted to 1218 cm^{-1}, indicating uranium binding to phosphate groups at relatively low concentrations of uranium. This was due to the electrostatic interactions between positively charged uranyl ions and negatively charged phosphate groups located on the surface of the eDNA (Alex and Dupuis, 1989). Up to 1 mM uranium, this adsorption band didn't change in position at 1218 cm^{-1} until in the presence of 2 mM uranium where it shifted further to 1206 cm^{-1}.

Similarly, following the interactions of eDNA with 0.25 mM uranium, the adsorption band at 965 cm^{-1} corresponding to the vibrational stretching of P-O bonds shifted to 969 cm^{-1}. This adsorption band shifted to 970, 973 and 976 cm^{-1} as the initial uranium concentration in solution increased to 0.5, 1 and 2 mM, respectively. There was a smaller shift in the 1063 cm^{-1} band attributed to both the ν_s (PO_2) and ν (C-OH, C-0-C, C-C) due to the carbon-related functional groups strongly adsorbed at this wavelength and their lack of strong interaction with uranium. The additional adsorption bands between 918 and 920 cm^{-1} were assigned to vibrational stretching of U-O ligand and indicated uranium binding, with an increase in adsorption intensity observed as the initial uranium concentration increases in solution (Lumetta et al., 1999, Kazy et al., 2008, Choudhary and Sar, 2011, Barkleit et al., 2011, Lu et al., 2013, Pan et al., 2015, Theodorakopoulos et al., 2015).

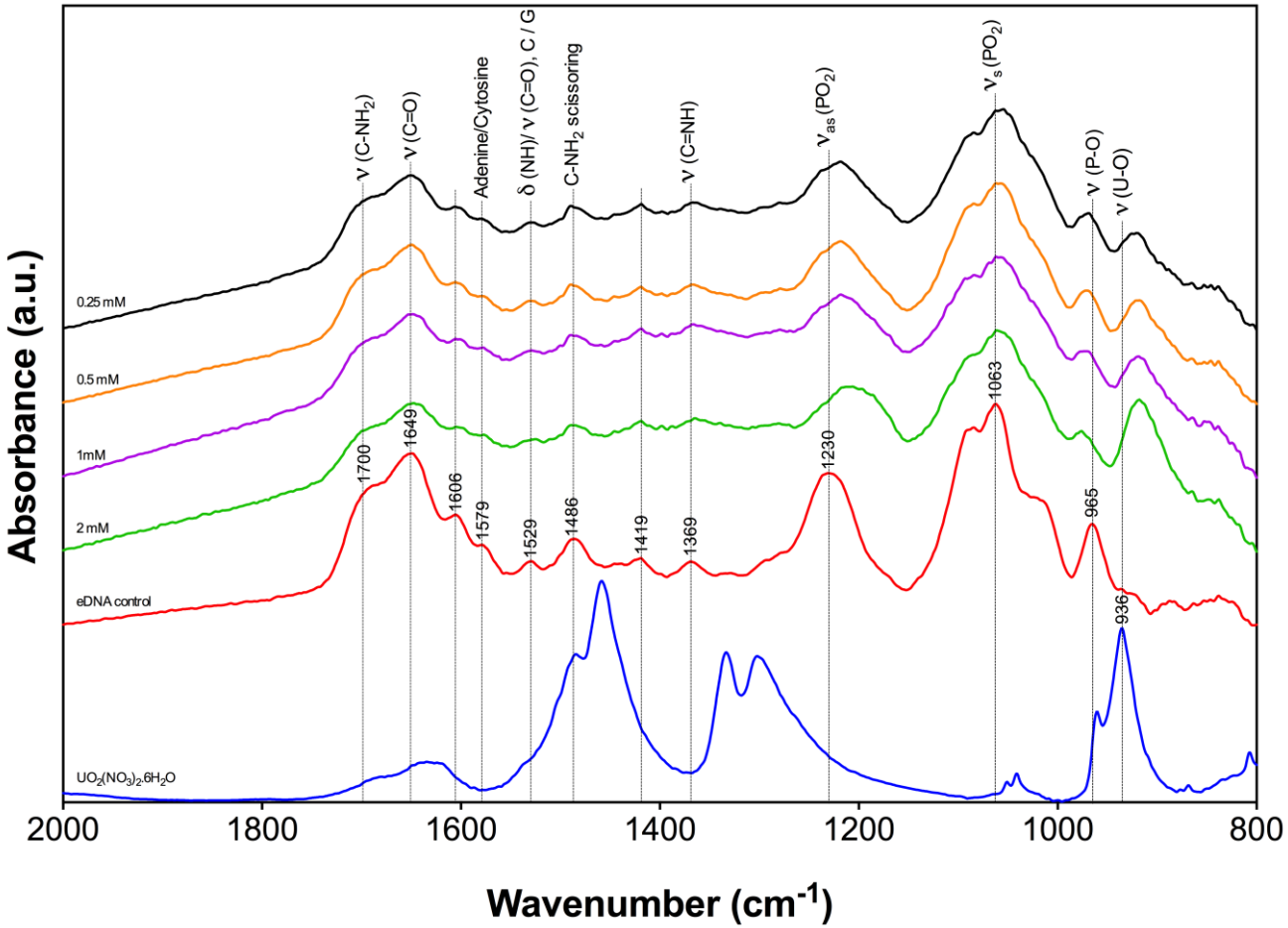

Figure 14. FT-IR spectra of 1 mg mL^{-1} eDNA binding to increasing concentrations of uranium (pH 5) within the region 2000 – 800 cm^{-1}.

2.4.3 The proposed binding of uranium to eDNA

Overall, FT-IR was found to be a suitable technique to investigate the interactions between eDNA and uranium as a function of pH and initial uranium concentration. Results suggested that, at very low pH, coordination of the U(VI) species with eDNA occurred predominantly through interactions with phosphate groups and the nitrogenous bases. As the pH increased to 5, phosphate groups alone mediate U(VI) coordination at a starting concentration of 0.5 mM uranium. At low U(VI) concentration, i.e. 0.25 mM, coordination with eDNA occurred through the negatively charged groups of the deoxyribose-phosphate backbone. Rare earth metal recovery using salmon milt DNA indicated adsorption of dysprosium and lutetium through phosphate groups, as determined using EXAFS (Takahashi et al., 2014).

Coordination with other functional groups such as the N-H, C=O and C-N of nitrogenous bases occurred more frequently as the uranium concentration increases, suggesting a preferential binding to phosphate groups until the availability of these groups decreases due to uranium saturation. Thereafter, uranium accumulation would occur through less preferential functional groups. This has been demonstrated when investigating the binding of cadmium to DNA to elucidate the toxic effects of the metallic species. At low concentrations Cd^{2+} primarily interacted with phosphate groups, with further coordination with guanine and adenine as the Cd^{2+} concentration increases (Alex and Dupuis, 1989). Similar interactions were observed following single and double stranded DNA interactions with transition metal species. Transition metal species, including Mn^{2+} and Co^{2+}, readily interacted with the N7 atom of guanine in dsDNA and phosphate groups, N1 and N7 atoms of purines and N3 atoms of pyrimidines of ssDNA, as well as other metal specific interactive sites (Duguid et al., 1995). Furthermore, chelation of heavy metal species between phosphate groups and N7 atoms of purines has been proposed in the application of the DNA-Based Biosensor for the determination of heavy metal species (Babkina and Ulakhovich, 2005).

The predominant interaction of U(VI) species with eDNA phosphate groups would depend on the net charge of the U(VI) species (Appendix Table 1-Appendix Table 3). The proposed U(VI) interactions with eDNA phosphate groups as a function of U(VI) species is shown in Equation 5.

$$x(eDNA\text{-}PO_4^-) + (UO_2)_y(L_z)^{x+} \rightleftharpoons x(eDNA\text{-}PO_4)(UO_2)_y(L_z)$$

Equation 5. The theoretical interaction between eDNA and U(VI) species within acidic conditions, in which x is the overall net charge of the U(VI) species, y is the number of uranyl ions in the U(VI) molecule and L_z is the number of additional ligands, i.e. OH groups.

U(VI) species with an overall net charge of +1 interact with one phosphate group in the eDNA structure (Figure 15A). U(VI) species with an overall net charge of +2 can interact with eDNA phosphate groups in more than one way; binding with two phosphate groups of multiple eDNA molecules (Figure 15B) or with two phosphate groups of one eDNA molecule (Figure 15C).

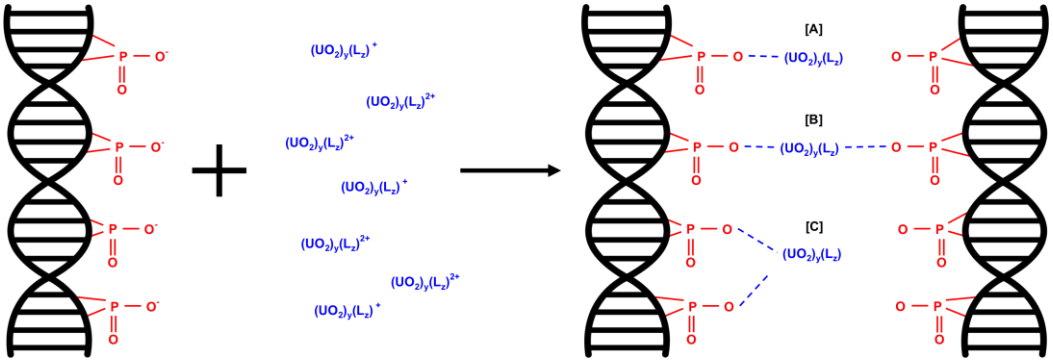

Figure 15. U(VI) interactions with eDNA phosphate groups within acidic conditions.

2.4.4 Extracellular acid phosphatase activity with eDNA

Acid phosphatase was incubated with eDNA under different conditions to determine the optimal condition for orthophosphate hydrolysis. Various experimental parameters were tested such as reactant concentrations, pH, ionic strength and temperature, all of which would affect the optimum enzyme activity. Standard values used in each experiment were 2 units mL^{-1} acid phosphatase, 1 mg mL^{-1} DNA, 0.1 M NaCl at 37 °C (pH 5). Orthophosphate release from eDNA following acid phosphatase activity under varying experimental conditions, as a function of time, are shown in Figure 16.

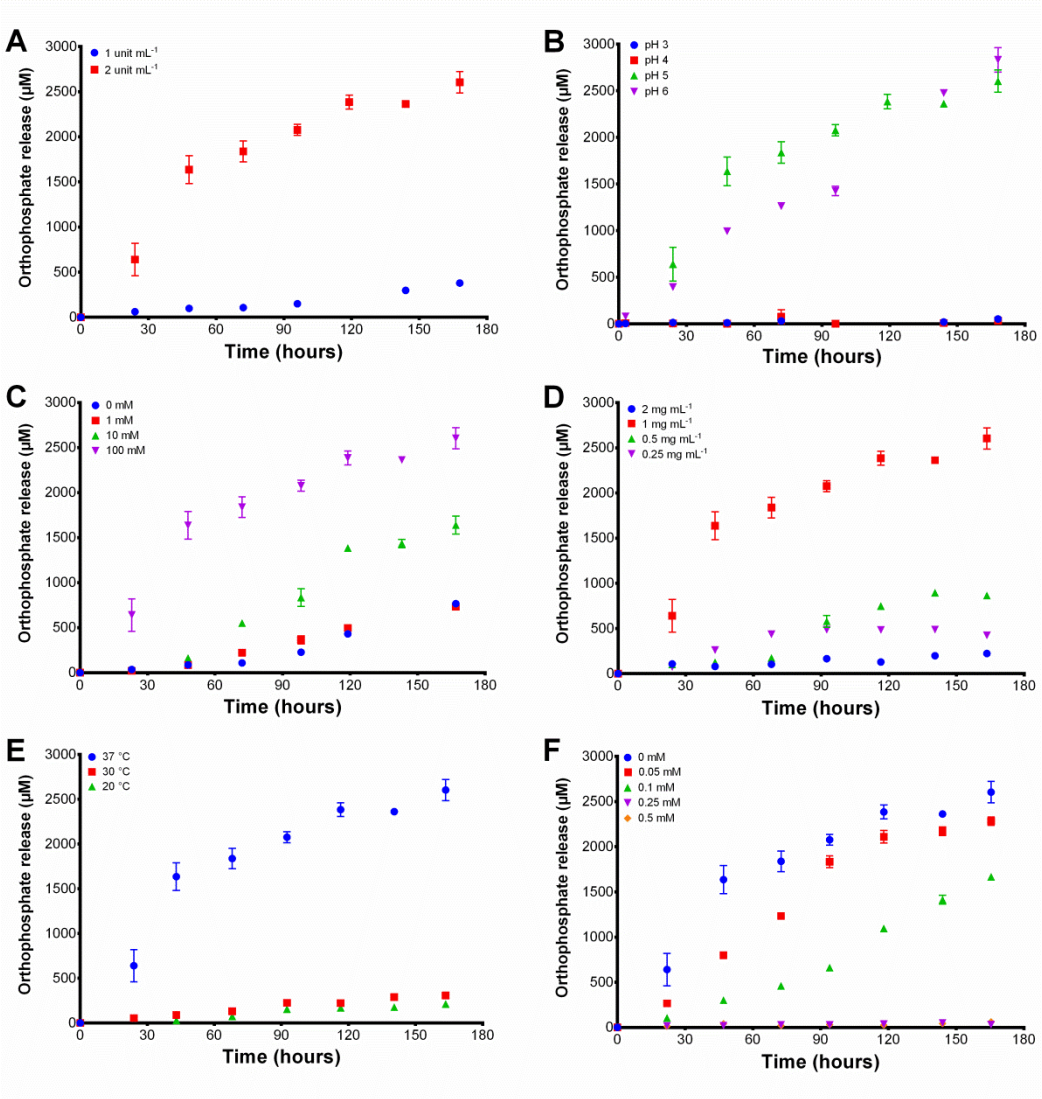

Figure 16. Orthophosphate release from eDNA as a function of [A] varying acid phosphatase concentrations, [B] varying pH, [C] varying ionic strength, [D] varying DNA concentration, [E] varying temperature and [F] varying uranium concentration.

A maximum of 2 units mL^{-1} acid phosphatase was used in this study (Figure 16A), consistent with enzyme activity concentrations previously demonstrated by certain

strains of bacteria, such as *B. sphaericus* JG-7B, isolated from uranium-contaminated environments (Merroun et al., 2011). As the enzyme concentration increased in solution, there was a greater release of orthophosphate over the time period investigated. At an enzyme concentration of 2 units mL^{-1}, after 168 hours, the orthophosphate release was around six times higher than for 1 unit mL^{-1}. At the higher concentration of enzyme, enzyme-substrate complexes formed more quickly, hydrolysing eDNA and releasing orthophosphate far faster.

The pH of the experimental environment plays an important role in acid phosphatase activity, phosphodiester bond cleavage and subsequent orthophosphate release. As shown in Figure 16B, no orthophosphate was found over the experimental time period for reactions at pH 3 and 4. As the pH increased to more neutral conditions, there was approximately 2500 µM orthophosphate released at both pH 5 and 6, but this release was quicker at pH 5. At low pH, the acid phosphatase enzyme becomes denatured and would not hydrolyse orthophosphate from eDNA. Similarly, microbial acid phosphatase activity associated with uranium biomineralisation through the formation of uranium phosphate minerals (such as meta-autunite and uramphite) was enhanced at pH close to 7 (Pan et al., 2015, Beazley et al., 2011, Sousa et al., 2013, Choudhary and Sar, 2011). However, biosorption to organophosphate functional groups occurred at pH values as low as 2 to 3 due to diminished acid phosphatase activity (Merroun et al., 2011, Reitz et al., 2014).

The ionic strength of the solution had a noticeable effect on the orthophosphate release over the experimental time period. There was a higher rate of orthophosphate release as a function of time as the NaCl concentration in solution increased up to 100 mM (Figure 16C). The presence of monovalent co-ions within the solution was an important parameter affecting enzyme activity. This could have been due to the additional co-ions within the solution acting as co-factors, causing movement of charged groups from amino acids within the acid phosphatase's catalytic site, for enzyme binding to the eDNA for subsequent phosphodiester bond hydrolysis. The effect of $CaCl_2$ concentration on enzyme activity was investigated but no orthophosphate was released over the time period investigated.

As the initial DNA concentration in solution increased to 1 mg mL^{-1} (Figure 16D), the overall orthophosphate release increased over the time period investigated due to the increased amount of substrate available for enzyme-mediated hydrolysis. Interestingly,

at a concentration of 2 mg mL^{-1} eDNA, there was diminished enzyme activity with approximately 200 µM orthophosphate released after 168 hours. An increase in viscosity of the solution caused by the higher concentration of eDNA decreased the mobility of the enzyme in solution and hence reduce the rate of phosphodiester bond hydrolysis and orthophosphate release. The optimum temperature for enzyme activity was determined to be 37 °C (Figure 16E) and the enzyme displayed diminished activity as the temperature decreased. Less than 500 µM orthophosphate was released over the time period investigated at temperatures below 30 °C. As the temperature was increased to 50 °C there was no acid phosphatase activity but complete DNA hydrolysis was observed due to a high orthophosphate release, as determined by a control reaction containing no acid phosphatase at 50 °C. This was due to denaturation of the acid phosphatase and DNA hydrolysis at high temperatures. Therefore the results were not presented in the figure.

Following the addition of uranium (pH 5) to the reaction solution at increasing concentration (Figure 16F), there was a decrease in quantifiable orthophosphate in the solution up to a concentration of 0.25 mM uranium, where there was no quantifiable orthophosphate after 168 hours. This decrease could be due to one or more of the following reasons: the released orthophosphate was removed from solution by the formation of a uranium phosphate mineral; diminished enzyme activity caused by the toxic properties of uranium; biosorption of uranium to eDNA which prevented enzyme activity. XRD patterns of the precipitates from this reaction, when compared to a DNA-uranium precipitated complex (Section 2.4.6.3, Appendix Figure 3), suggested that the decrease was due to uranium toxicity and uranium biosorption. This toxicity could be due to a lack of confinement for the enzyme. For certain strains of bacteria, the acid phosphatase enzyme is located within the cell membrane and periplasmic space (Macaskie et al., 1992, Choudhary and Sar, 2015, Yung and Jiao, 2014) whereas in this study the enzyme was in aqueous solution. The confinement of acid phosphatase to the cell membrane and periplasmic space in whole cells could prevent toxic interactions of the uranium with the acid phosphatase that can diminish its function. The boundary of the outer membrane would act as a biosorbent for the aqueous uranium. Also, since the acid phosphatase enzyme within this study was isolated from potato, it may be unlikely that it this particular enzyme is adapted to tolerate heavy metal and uranium interactions.

2.4.5 Uranium biomineralisation using enzymatically generated phosphate

The formation of uranium phosphate minerals was identified as the primary mechanism for the removal of uranium from solution, due to the low solubility of uranium phosphate complexes. Following the investigation of extracellular phosphatase activity on eDNA (Figure 16), the experimental parameters were optimised for maximum orthophosphate release for subsequent interactions with uranium. Enzymatic phosphate (ePO_4) was hydrolysed from 1 mg mL^{-1} eDNA using 2 units mL^{-1} acid phosphatase (0.1 M NaCl, pH 5) for 72 hours and interacted with uranium (pH 5) at various molar ratios. After 72 hours ~2000 µM of ePO_4 was released from eDNA. The stoichiometry of the biomineralisation reaction using ePO_4 and uranium was studied using varying molar ratios of both reactants. ePO_4 and uranium were quantified to determine the amount remaining in solution and by mass balance, the amount accumulated in the minerals formed. These findings were compared with the formation of an abiotic mineral (aPO_4) in which the phosphate in solution originated from 2000 µM sodium phosphate (NaH_2PO_4). At pH 5, the dominant U(VI) species present within solution was $(UO_2)_3(OH)_5^+$ (Appendix Table 3) at concentrations higher than 0.25 mM U(VI). The dominant phosphate species at pH 5 was determined to be $H_2PO_4^-$ at approximately 86 %, according to Visual MINTEQ calculations. The molar ratios of reactants were calculated accordingly using these dominant species, Figure 17.

Except at a molar ratio of 1.8 : 1 $H_2PO_4^-$: $(UO_2)_3(OH)_5^+$, uranium was the limiting reactant, and hence it was completely removed from solution and converted into a mineral using both ePO_4 and aPO_4. At this molar ratio, 72 % of the uranium was removed from solution using ePO_4 and approximately 28 % of unreacted uranium remained in solution, Figure 17A. At a molar ratio of 3.8 : 1 $H_2PO_4^-$: $(UO_2)_3(OH)_5^+$, almost all of both reactants were completely removed from solution, with approximately 6.5 % of $H_2PO_4^-$ remaining in solution. This suggested that a molar ratio of approximately 3.5 : 1 $H_2PO_4^-$: $(UO_2)_3(OH)_5^+$ was capable of removing all reactants from solution.

There were noticeable differences in $H_2PO_4^-$ removal depending on the molar ratio and $H_2PO_4^-$ source, Figure 17B. At a molar ratio of 1.8 : 1 $H_2PO_4^-$: $(UO_2)_3(OH)_5^+$, there was no ePO_4 and aPO_4 remaining in solution. In the presence of an excess of $H_2PO_4^-$ in solution, for example at a molar ratio of 37.6 : 1 $H_2PO_4^-$: $(UO_2)_3(OH)_5^+$, only 45 % of ePO_4 was removed from solution. No differences in orthophosphate remaining in solution were

observed when the concentration of uranium decreased in the starting solution. On the other hand, there was a relative decrease in aPO_4 removal up to a molar ratio of 150.4 : 1 $H_2PO_4^-$: $(UO_2)_3(OH)_5^+$ where 96 % aPO_4 remained in solution following the biomineralisation of uranium. The results suggested that all the uranium was incorporated into the minerals formed, with an excess of orthophosphate liberated from eDNA for uranium biomineralisation and subsequent remediation, thus suggesting that uranium was the limiting factor in this reaction. Differences in phosphate removal between ePO_4 and aPO_4 suggested the presence of other particulates from the enzymatic hydrolysis of eDNA may interact with reactants removing excess quantifiable phosphate.

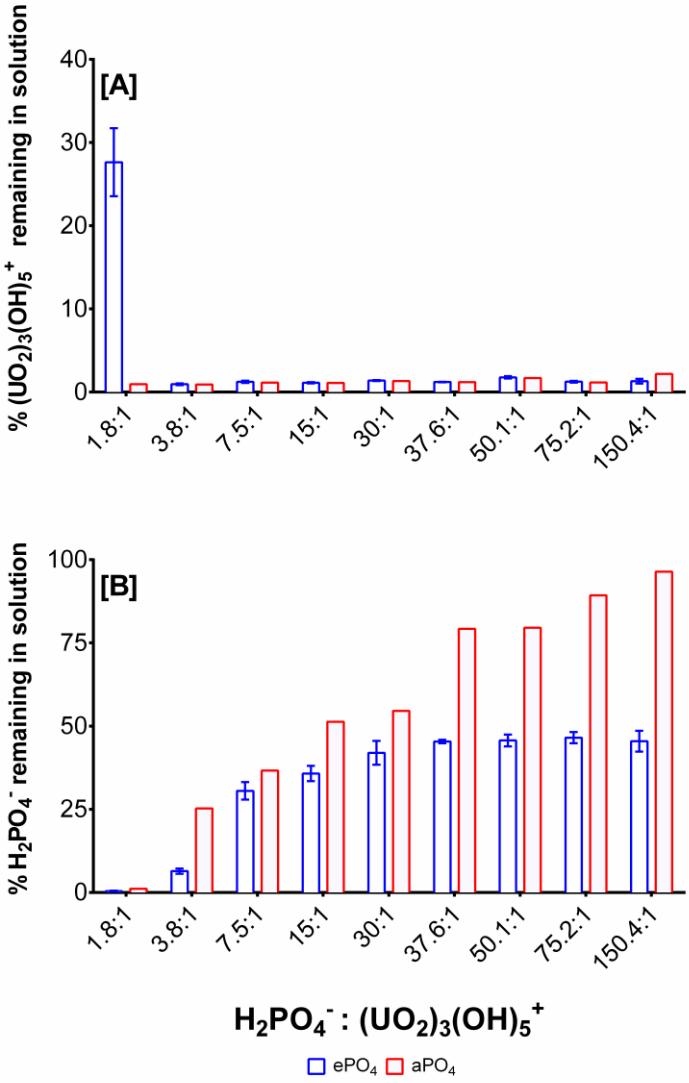

Figure 17. Uranium and phosphate removal as a function of phosphate to uranium molar ratio and phosphate origin.

2.4.6 Uranium ePO_4 mineral characterisation

2.4.6.1 Scanning Electron Microscopy (SEM)

SEM coupled with EDX was used to identify differences in structural morphology between the uranium minerals formed using enzymatic (ePO_4) or abiotic (aPO_4) phosphate at a molar ratio of 1.8 : 1 $H_2PO_4^-$: $(UO_2)_3(OH)_5^+$. The SEM micrographs showed that the particles produced by ePO_4 (Figure 18) appeared to be of varying shapes and sizes (but under 20 µm in diameter) with irregular surfaces and large amounts of aggregation. Particles produced using abiotic phosphate (Figure 19) were much smaller and of irregular shape with fewer areas of aggregation in the sample windows examined. The aggregates appeared to be made of particles less than 5 µm in diameter.

EDX analysis of particles and aggregates of both samples indicates similar chemical composition of the minerals formed but with one noticeable difference, the presence of nitrogen within the minerals formed with ePO_4 (Figure 18E). This peak was absent in the EDX spectrum of the aPO_4 precipitate (Figure 19E). The presence of nitrogen in the ePO_4 mineral was due to impurities in the enzymatic phosphate following enzymatic hydrolysis of the eDNA in which residual soluble components of the eDNA remain in solution. This could explain the differences in particle size, shape and aggregation between the two minerals. Other impurities could include carbon from the enzymatic phosphate hydrolysis of eDNA. However, it was impossible to distinguish this impurity incorporation due to the adherence of the samples to carbon tape and subsequent carbon coating.

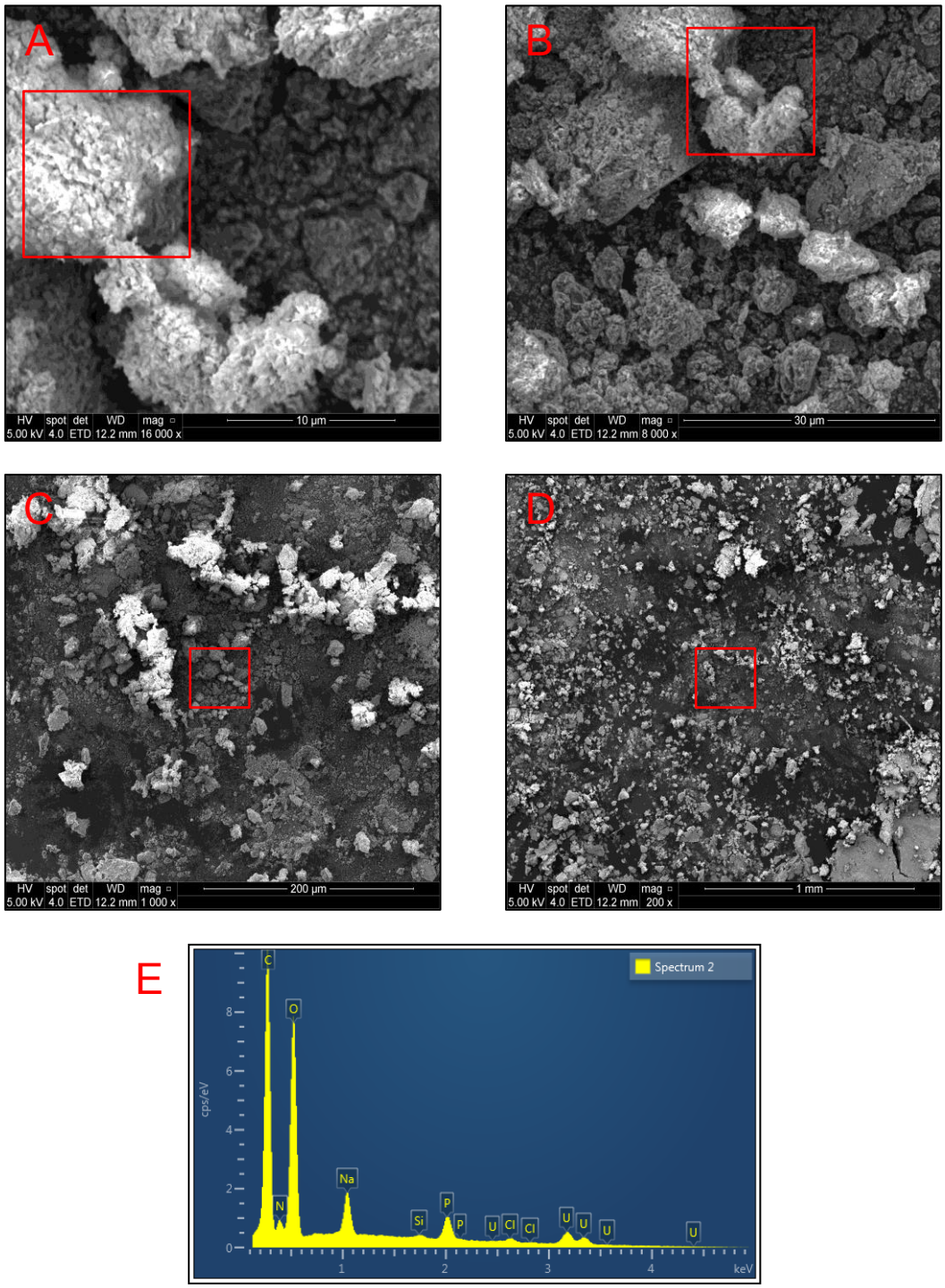

Figure 18. Scanning electron micrographs of carbon coated uranium minerals using ePO_4 at a molar ratio of 1.8 : 1 $H_2PO_4^-$: $(UO_2)_3(OH)_5^+$.

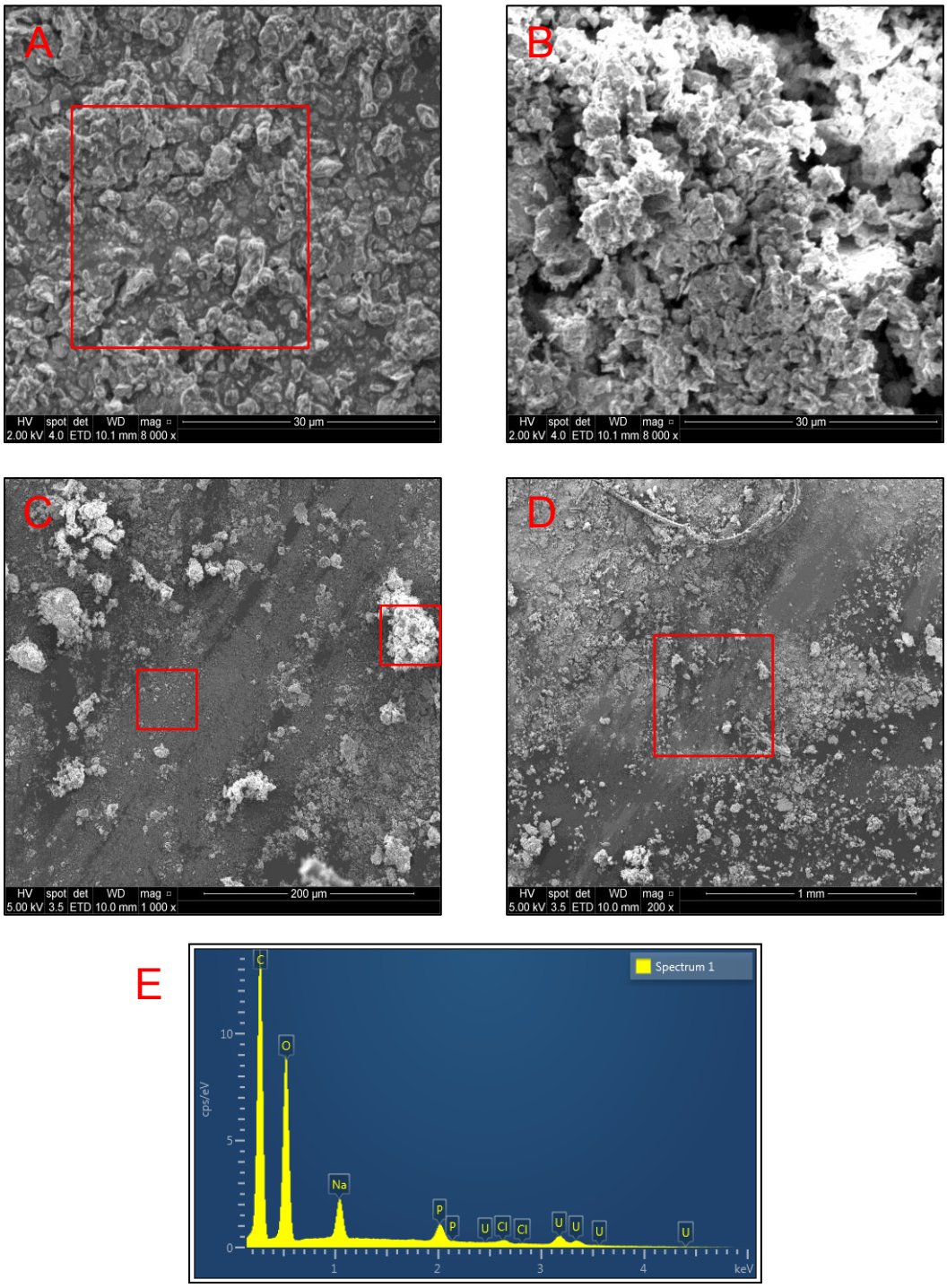

Figure 19. Scanning electron micrographs of carbon coated uranium minerals using aPO_4 at a molar ratio of 1.8 : 1 $H_2PO_4^-$: $(UO_2)_3(OH)_5^+$.

2.4.6.2 ATR-FT-IR characterization of enzymatic uranium minerals

ATR-FT-IR spectra of the uranium minerals were collected (as described in section 2.3.5) to identify any differences in the chemical composition between using ePO_4 and aPO_4 at an increasing molar ratio of $H_2PO_4^-$: $(UO_2)_3(OH)_5^+$. The changes and additions of adsorption bands were used to identify the presence of different functional groups between samples. Detailed functional group assignments for each uranium minerals are shown in Table 3. Comparison spectra of using ePO_4 and aPO_4 at a 1.8 : 1 ($H_2PO_4^-$: $(UO_2)_3(OH)_5^+$) molar ratio are presented in Figure 20, while comparison spectra of varying $H_2PO_4^-$: $(UO_2)_3(OH)_5^+$ molar ratios using ePO_4 are presented in Figure 21.

Table 3. Infrared adsorption bands of uranium minerals synthesised using ePO_4 and aPO_4 at varying molar ratios.

Allocation*			ν (C=O)	δ (N-H)	ν (PO_2)/ ν_{as} (P-O)	ν_s (P-O)	ν (U–O_{ligand})	
1.8:1	ePO_4	σ (cm^{-1})	**1641**	**1528**	**1123**	**993**	**914**	**-**
		I (a.u.)	0.153	0.113	0.248	1.5	0.453	-
	aPO_4	σ (cm^{-1})	**1641**	**-**	**1113**	**991**	**911**	**813**
		I (a.u.)	0.108	-	0.216	1.5	0.58	0.063
3.8:1	ePO_4	σ (cm^{-1})	**1641**	**1530**	**1118**	**990**	**904**	**-**
		I (a.u.)	0.185	0.12	0.3	1.5	0.578	-
	aPO_4	σ (cm^{-1})	**1640**	**-**	**1113**	**991**	**910**	**810**
		I (a.u.)	0.128	-	0.238	1.5	0.58	0.048
7.5:1	ePO_4	σ (cm^{-1})	**1641**	**1529**	**1119**	**991**	**907**	**-**
		I (a.u.)	0.362	0.259	0.478	1.5	0.644	-
	aPO_4	σ (cm^{-1})	**1639**	**-**	**1105**	**988**	**905**	**810**
		I (a.u.)	0.235	-	0.405	1.5	0.651	0.076
15:1	ePO_4	σ (cm^{-1})	**1641**	**1529**	**1122**	**992**	**912**	**-**
		I (a.u.)	0.441	0.348	0.56	1.5	0.691	-
	aPO_4	σ (cm^{-1})	**1639**	**-**	**1105**	**988**	**905**	**810**
		I (a.u.)	0.235	-	0.405	1.5	0.651	0.076

* Functional group assignment has been identified and based on (Baker et al., 2014), (Akyuz et al., 2008), (Garidel et al., 2000) and (Kazy et al., 2009).

FT-IR spectra of the uranium minerals formed using ePO_4 and aPO_4 at a 1.8 : 1 ($H_2PO_4^-$: $(UO_2)_3(OH)_5^+$) molar ratio exhibited almost identical adsorption band wavenumber assignments with slight differences in adsorption intensity (Figure 20D and E). These spectra were noticeably different from those of eDNA (Figure 20B), uranium precipitated eDNA (Figure 20C) and the $UO_2(NO_3)_2 \bullet 6H_2O$ salt source used within this experimental study (Figure 20A). Spectra were normalised to the most intense adsorption band in the sample, at approximately 990 cm^{-1}. This band corresponded to the P-O symmetric stretching vibrations (Akyuz et al., 2008). There was an increase in the adsorption intensity of the ν (U–O_{ligand}) in the minerals formed using aPO_4 rather than ePO_4 at a molar ratio of 1.8 : 1 ($H_2PO_4^-$: $(UO_2)_3(OH)_5^+$). This difference in uranium band intensity correlated with reactant quantification data (Figure 17A) that suggested a

decrease in uranium removal using ePO_4 at a molar ratio of 1.8 : 1 ($H_2PO_4^-$: $(UO_2)_3(OH)_5^+$). As the molar ratio of phosphate to uranium increased from 1.8 : 1 to 15 : 1 ($H_2PO_4^-$: $(UO_2)_3(OH)_5^+$), there was little difference in adsorption intensity between using ePO_4 and aPO_4 (Table 3), yet again correlating with the reactant removal data (Figure 17A) in which there was almost 100 % uranium removal at the stated molar ratios.

Differences in phosphate accumulation following quantification of reactant removal (Figure 17B) were also observed in FT-IR spectra, specifically in the adsorption band between 1123-1105 cm^{-1}, assigned to the ν (PO_2). There was an increase in adsorption intensity as the concentration of phosphate in the starting solution increased and a greater amount of phosphate in the uranium mineral formed. There was an increase in adsorption intensity in all samples at the molar ratios measured using ePO_4 rather than aPO_4. This difference in intensity correlated with the differences in orthophosphate removal at the changing molar ratios between the two different orthophosphate sources (Figure 17B).

Spectra of minerals formed using ePO_4 displayed more adsorption bands than those formed using aPO_4. These adsorption bands increased in intensity as the molar ratio of $H_2PO_4^-$: $(UO_2)_3(OH)_5^+$ increased from 1.8 : 1 to 15 : 1 and there was a greater amount of phosphate in the starting solution (Figure 21). At ~1529 cm^{-1}, there was an additional adsorption in all ePO_4 minerals corresponding to the δ (N-H) bands. This adsorption band was lacking in minerals formed using aPO_4 (Appendix Figure 1). This additional peak could be a consequence of impurities from ePO_4 solution (such as nitrogen arising from the enzymatic hydrolysis of eDNA), which became incorporated into the mineral. This was further confirmed by the EDX obtained from SEM analysis (Figure 18E). As the molar ratio of $H_2PO_4^-$: $(UO_2)_3(OH)_5^+$ increased to 15 : 1, the higher proportion of the impure ePO_4 resulted in the incorporation of other impurities from the enzymatic phosphate solution giving further additional adsorption bands in the FT-IR spectra.

Overall, the ATR-FT-IR analysis confirmed the incorporation of both uranium and phosphate within the minerals formed at varied molar ratios, where the adsorption intensity reflected the amount of each reactant accumulated. Additional adsorption bands in the spectra of minerals synthesised using ePO_4 arose from impurities from the enzymatic hydrolysis of eDNA and subsequent incorporation of impurities, such as nitrogen, into the minerals formed.

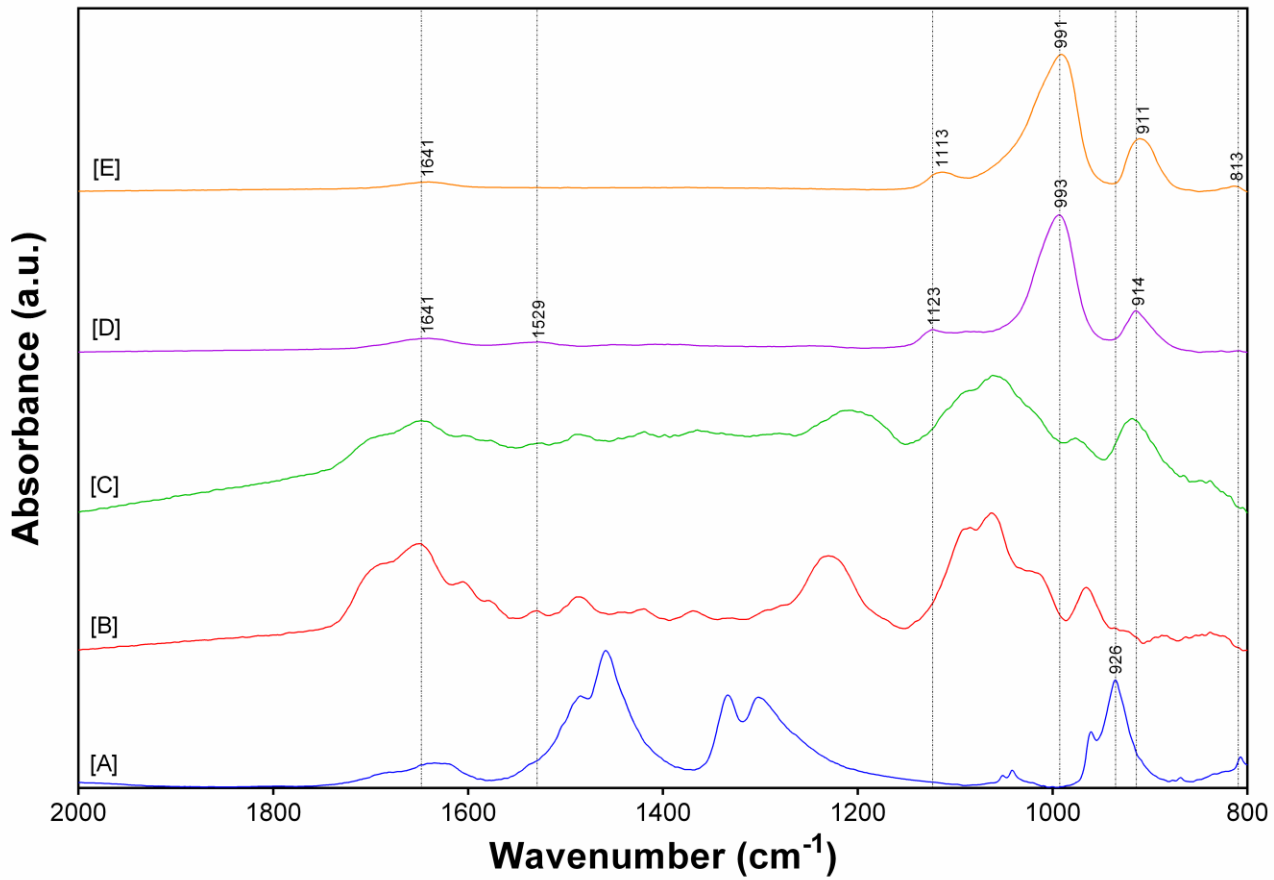

Figure 20. FT-IR spectra of minerals formed from the interaction of ePO_4 with uranium at a molar ratio of 1.8 : 1 $H_2PO_4^-$: $(UO_2)_3(OH)_5^+$ [D] in comparison with the same reaction using aPO_4 [E] within the region 2000 – 800 cm^{-1}. Reference spectra of uranyl nitrate hexahydrate [A], lyophilised DNA [B] and eDNA-U precipitate formed at a similar molar ratio of phosphate to uranium [C].

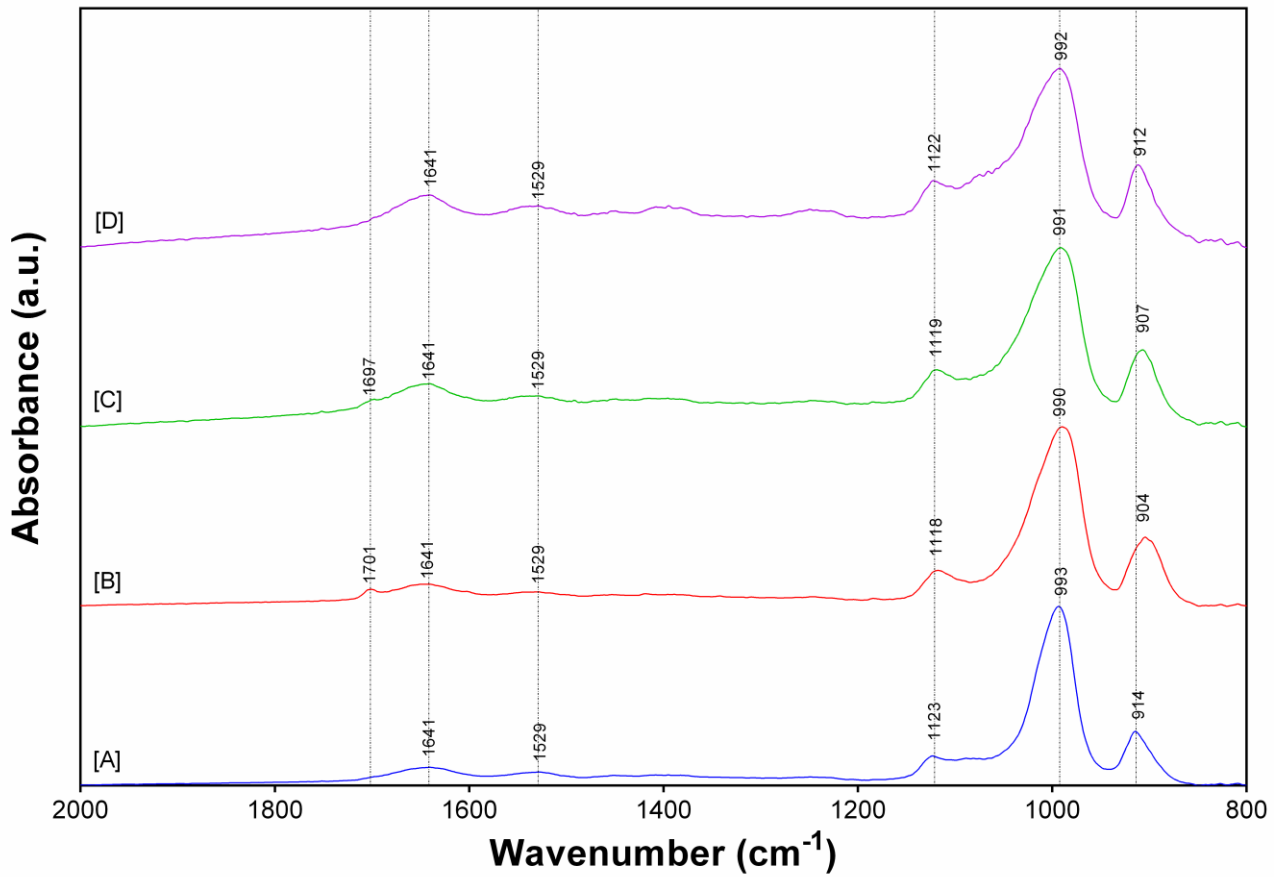

Figure 21. FT-IR spectra of minerals formed from the interaction of ePO_4 with uranium at increasing molar ratios; 1.8 : 1 [A], 3.8 : 1 [B], 7.5 : 1 [C] and 15 : 1 [D] $H_2PO_4^-$: $(UO_2)_3(OH)_5^+$ within the region 2000 – 800 cm^{-1}.

2.4.6.3 X-ray powder diffraction (XRD) analysis

The uranium minerals, formed using ePO_4 and aPO_4, were analysed by XRD to determine their chemical and structural nature at various molar ratios of $H_2PO_4^-$: $(UO_2)_3(OH)_5^+$), Figure 22. The XRD patterns of all samples showed the same peaks when overlaying the patterns. This result revealed they were the same uranium mineral phase at varying levels of crystallinity. At a molar ratio of 7.5 : 1, ePO_4 : uranium, (Figure 22A), the diffraction pattern showed poorly defined and broad peaks, suggesting an amorphous phase or poorly crystalline material. As the concentration of uranium increased within solution, together with its subsequent level of incorporation into the minerals formed (Figure 22B and C), the diffraction peaks were better defined with a greater intensity. This suggested an increased structural ordering and therefore a more crystalline material (Handley-Sidhu et al., 2014).

Similarly, the diffraction patterns obtained from the synthesis of the uranium mineral phase using aPO_4 rather than ePO_4, at the same molar ratio showed an increase in intensity and more clearly defined peaks in the XRD pattern, Figure 23. This suggested that the same mineral phase formed, but with a higher degree of crystallinity when aPO_4 was used. As with minerals formed using ePO_4, when the molar ratio of $H_2PO_4^-$ to $(UO_2)_3(OH)_5^+$ changed from 1.8 : 1 to 7.5 : 1 using aPO_4, there was a decrease in crystallinity, as shown by poorly defined diffraction peaks, Appendix Figure 2. The differences in degree of crystallinity between the uranium minerals could've been due to the incorporation of impurities from the ePO_4 synthesis, such as nitrogen- and carbon-containing compounds arising from the enzymatic hydrolysis of eDNA.

The corresponding *d*-spacing values for the XRD patterns obtained in this study were comparable to those from minerals such as meta-autunite ($Ca(UO_2)_2(PO_4)_2$, ICDD PDF 00-039-1351 and 04-012-5106) and other uranium phosphate hydrated minerals (ICDD PDF 00-037-0373 and 00-064-0815), Appendix Table 5. Interestingly, the *d*-spacing values obtained from this study do not closely match those of sodium-bearing but rather calcium-bearing meta-autunite, even though no calcium was present within the reaction. However, the calculated *d*-spacing values of 8.45, 4.91, 3.47 and 2.20 Å are characteristic of meta-autunite. It has been demonstrated using numerous strains of bacteria that meta-autunite minerals can be formed by indigenous acid phosphatase activity with formation observed at the cell surface (Merroun et al., 2011) or within

bacterial EPS, such as that of *Pseudomonas stutzeri* (Merroun and Selenska-Pobell, 2008).

XRD diffraction patterns (Appendix Figure 3) were obtained for lyophilised eDNA. eDNA was precipitated using 4mM U(VI) at pH 5 and the solid material obtained from the reaction of DNA with acid phosphatase in the presence of 0.5 mM uranium (pH 5), as shown in Figure 16F. XRD diffraction peaks obtained from the uranium precipitated with eDNA and the acid phosphatase eDNA hydrolysis reaction in the presence of uranium ions are the same. However, these peaks corresponded to the mineral structure of sodium chloride (ICDD PDF 00-005-0628, 04-002-1178) and were most likely due to accumulation of the salt in the DNA precipitate rather than residual left over following washing as the DNA control did not show any diffraction peaks. This suggested that the precipitation of uranium with eDNA gave no uranium mineral phase and was similar to that of a biosorption process. It was described as a surface complexation, similar to that of previous studies (Handley-Sidhu et al., 2014) and the product of the acid phosphatase DNA hydrolysis reaction while in the presence of uranium was not a mineral formed from the hydrolysis of enzymatic phosphate but rather a complexation of eDNA, uranium and acid phosphatase. Ultimately, this suggested that the differences in orthophosphate release from eDNA, in the presence of increasing uranium concentrations, was not due to accumulation of released orthophosphate but due to diminished phosphatase activity. Acid phosphatase was denatured due to the toxic properties of the uranium as its concentration increased in solution.

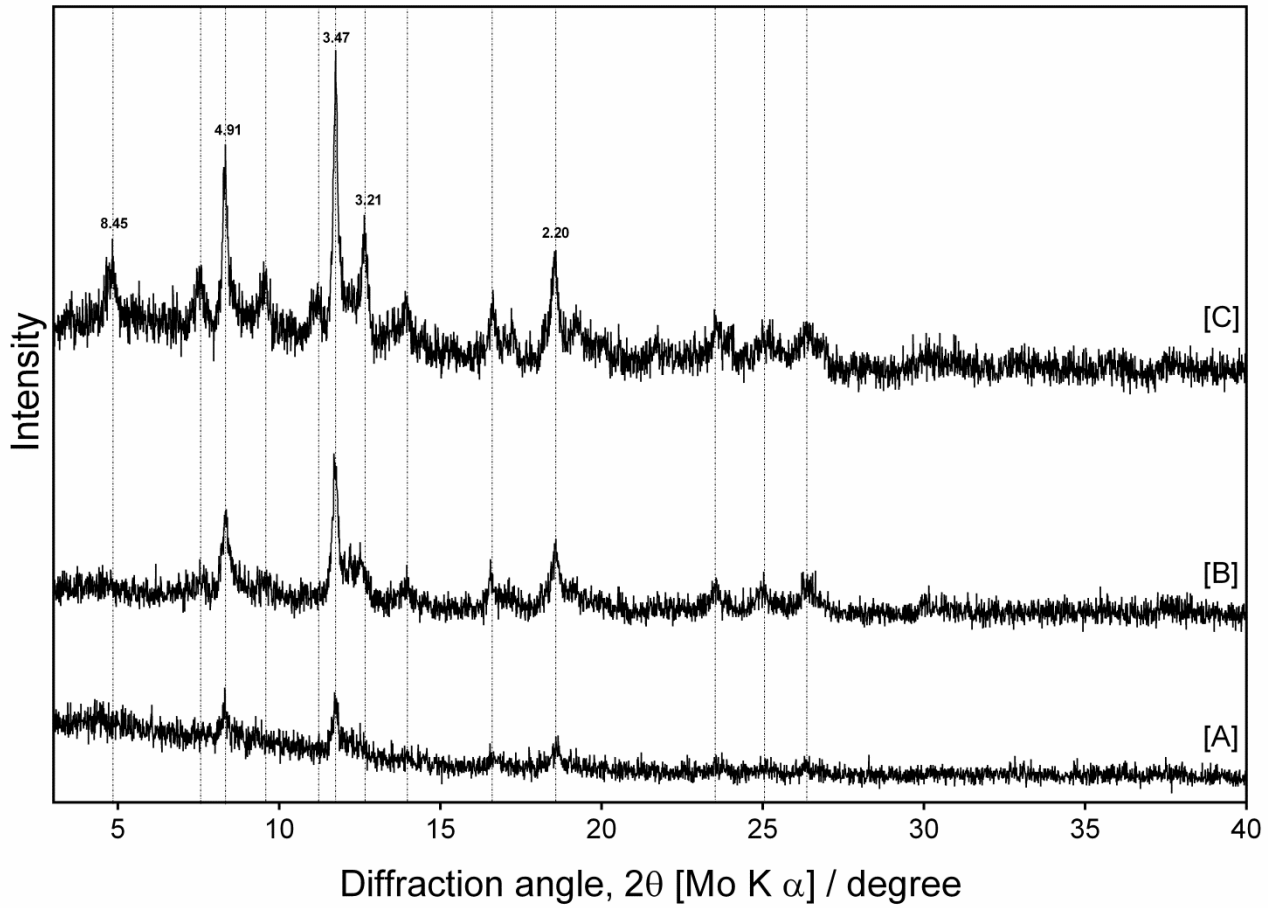

Figure 22. XRD patterns of the minerals formed at molar ratios of [A] 7.5 : 1, [B] 3.8 : 1 and [C] 1.8 : 1 ePO_4 : uranium (pH 5).

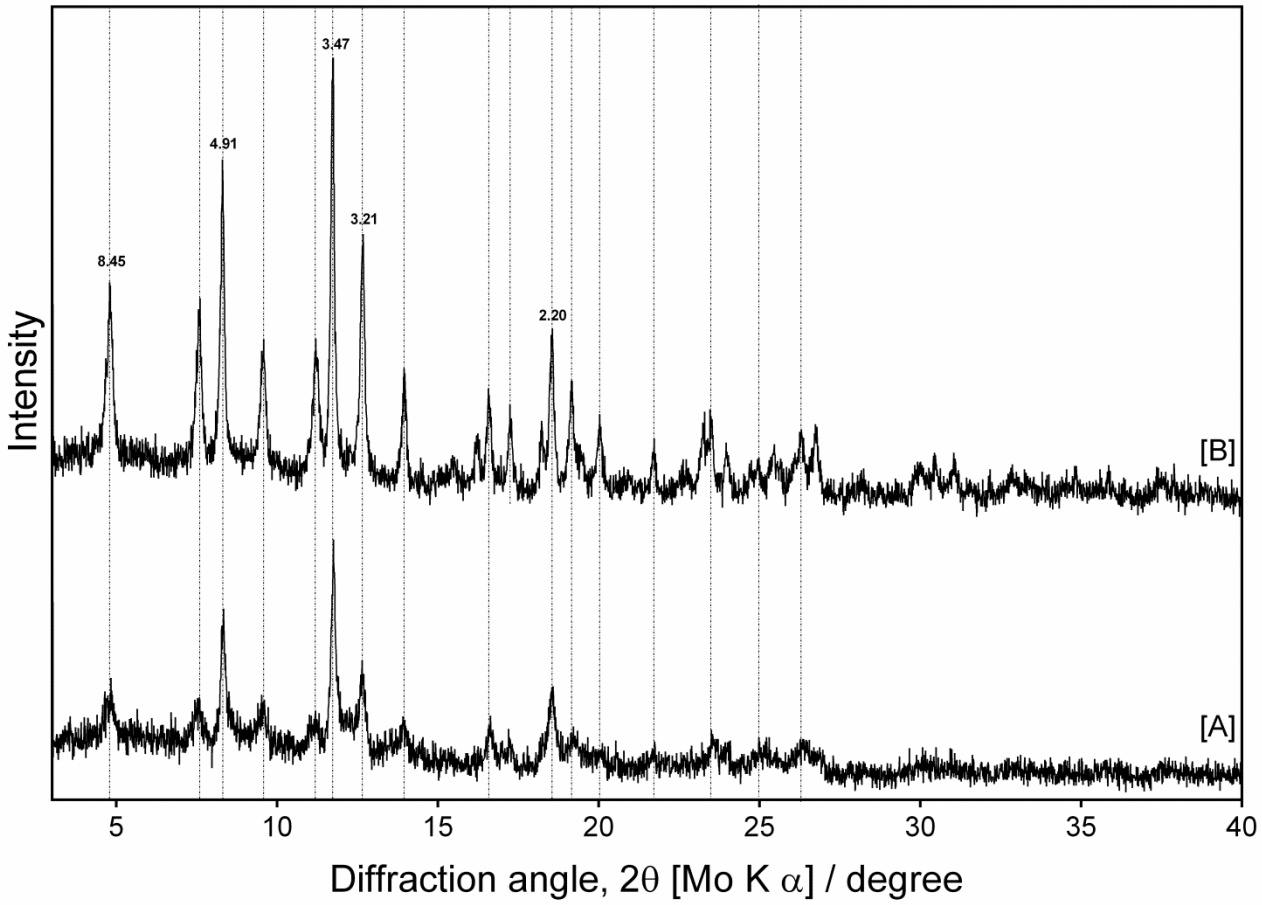

Figure 23. XRD patterns of the minerals formed at a molar ratio of 1.8 : 1 $H_2PO_4^-$: $(UO_2)_3(OH)_5^+$ using [A] ePO_4 and [B] aPO_4.

2.4.6.4 X-ray photoelectron spectroscopy (XPS)

A XPS wide-scan spectrum of the uranium minerals was gathered to determine the presence of any other elements within the sample, while a high-resolution scan of the C1s, O1s, P2p and U4f regions was used to determine any specific elemental interactions. Additional peaks in the wide-scan and high-resolution spectrum of uranium minerals synthesised using ePO_4 indicated the incorporation of impurities from the ePO_4 solution (Figure 24, Table 4).

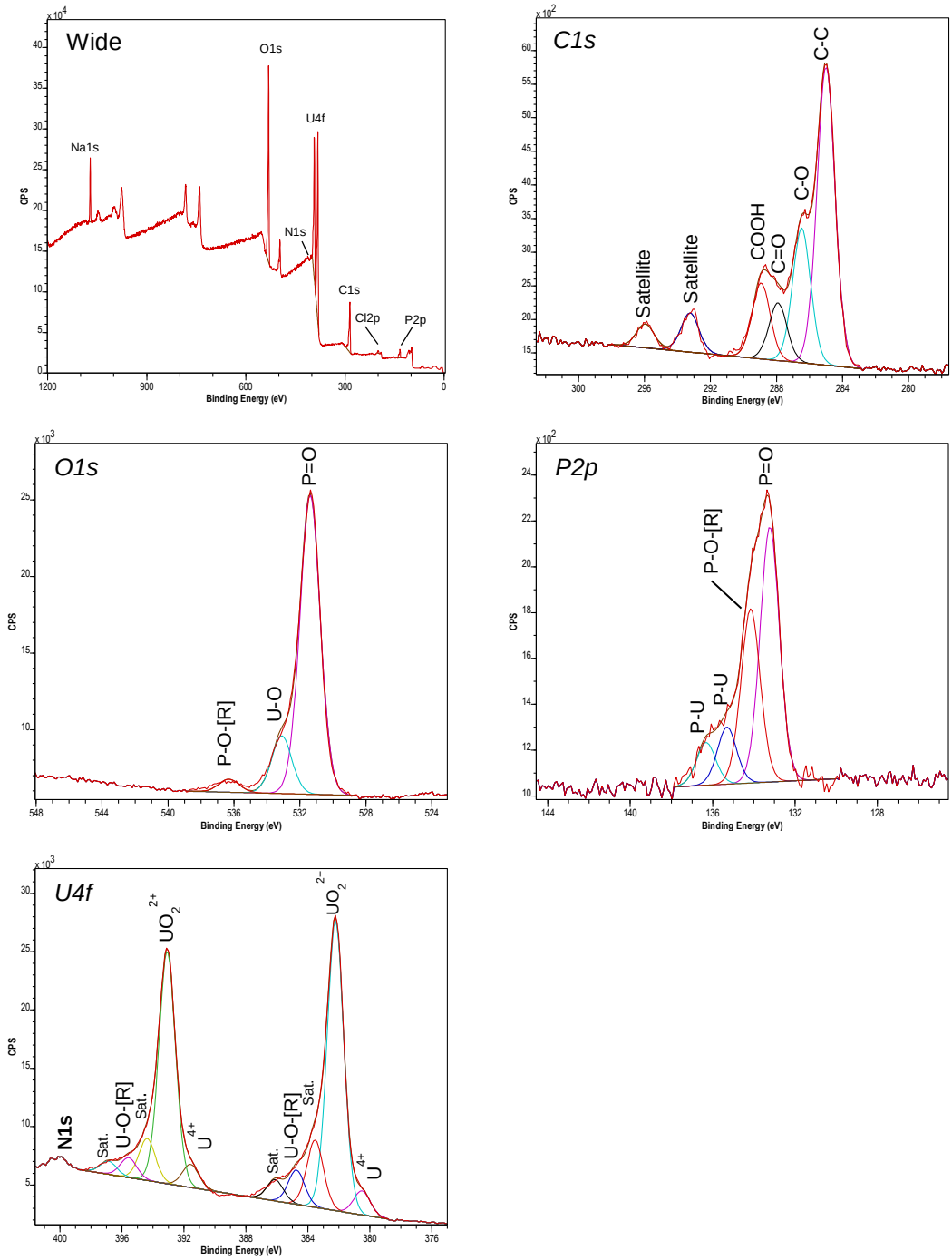

Figure 24. XPS spectrum of uranium minerals synthesised using ePO_4 at a molar ratio of 1.8 : 1 $H_2PO_4^-$: $(UO_2)_3(OH)_5^+$

Table 4. Binding energies (eV), FWHM, % area and assignment of XPS spectral bands of uranium minerals synthesised using ePO_4 at a molar ratio of 1.8 : 1 $H_2PO_4^-$: $(UO_2)_3(OH)_5^+$

Position (eV)	FWHM	% Area	Assignment
		C 1s	
285	1.282	52.67	C-C, H*
286.48	1.282	23.78	C-O* C-N
287.91	1.282	10.26	C=O, O-C-O, COOR
288.93	1.282	13.28	COOH*, O-C=O
293.24	1.282	N/A	Satellite
295.95	1.282	N/A	Satellite
		O 1s	
531.38	1.432	80.86	P=O, C=O
533.1	1.432	15.59	U-O, P/C-OH
536.29	1.432	3.56	P-O-[R], U-[R]
		P 2p	
133.23	1.092	48.26	P=O, P-OH
134.16	1.092	32.86	P-O-[R]
135.31	1.092	10.8	[R]-P-O-[R]
136.32	1.092	8.08	[R]-P-O-[R]
		U 4f	
380.5	1.25	3.16	U^{4+}
382.21	1.25	37.86	UO_2^{2+}, U-O
383.53	1.25	8.8	U-O-[R], Satellite
384.73	1.25	4.49	U-O-[R], Satellite
386.1	1.25	2.79	Satellite
391.56	1.25	3.01	U^{4+}
393.08	1.25	30.16	UO_2^{2+}, U-O
394.37	1.25	5.47	U-O-[R], Satellite
395.58	1.25	2.57	U-O-[R], Satellite
396.87	1.25	1.7	Satellite

* Carbon tape associated peaks

A wide scan spectrum of both minerals indicated the presence of uranium, oxygen, phosphorus, sodium and chlorine in both minerals and the addition of nitrogen formed using ePO_4, similar to the results obtained using SEM-EDX. Due to the adhesion of uranium minerals to carbon tape for both XPS and SEM analysis (Section 2.4.6.1), it was difficult to distinguish the incorporation of carbon into the ePO_4-synthesised mineral using a wide-scan spectrum and the SEM-EDX spectrum, Figure 18E. For the same reason, it was impossible to get an accurate percentage quantification of all elements in the samples. A high-resolution scan of the C1s region showed additional carbon-related peaks in the ePO_4 minerals (Figure 24 C1s) that were absent in minerals synthesised using aPO_4, Figure 25 C1s. A lack of carbon-containing compounds suggested that the carbon XPS peaks at 285, 286.49 and 288.88 eV (Table 5) were from the carbon tape rather than from any functional groups within the minerals formed. This was confirmed by the near identical spectral bands and similar percentage areas observed in carbon

tape alone, Appendix Figure 5. The additional C1s XPS peak at 287.91 eV of the minerals formed using ePO_4 corresponded to the carbon oxygen double bond. This additional peak, absent in minerals synthesised using aPO_4, suggested that uranium was mineralised with carbon present from the hydrolysis of enzymatic orthophosphate from eDNA. Additional carbon satellite peaks were present at 293.24 and 295.95 eV.

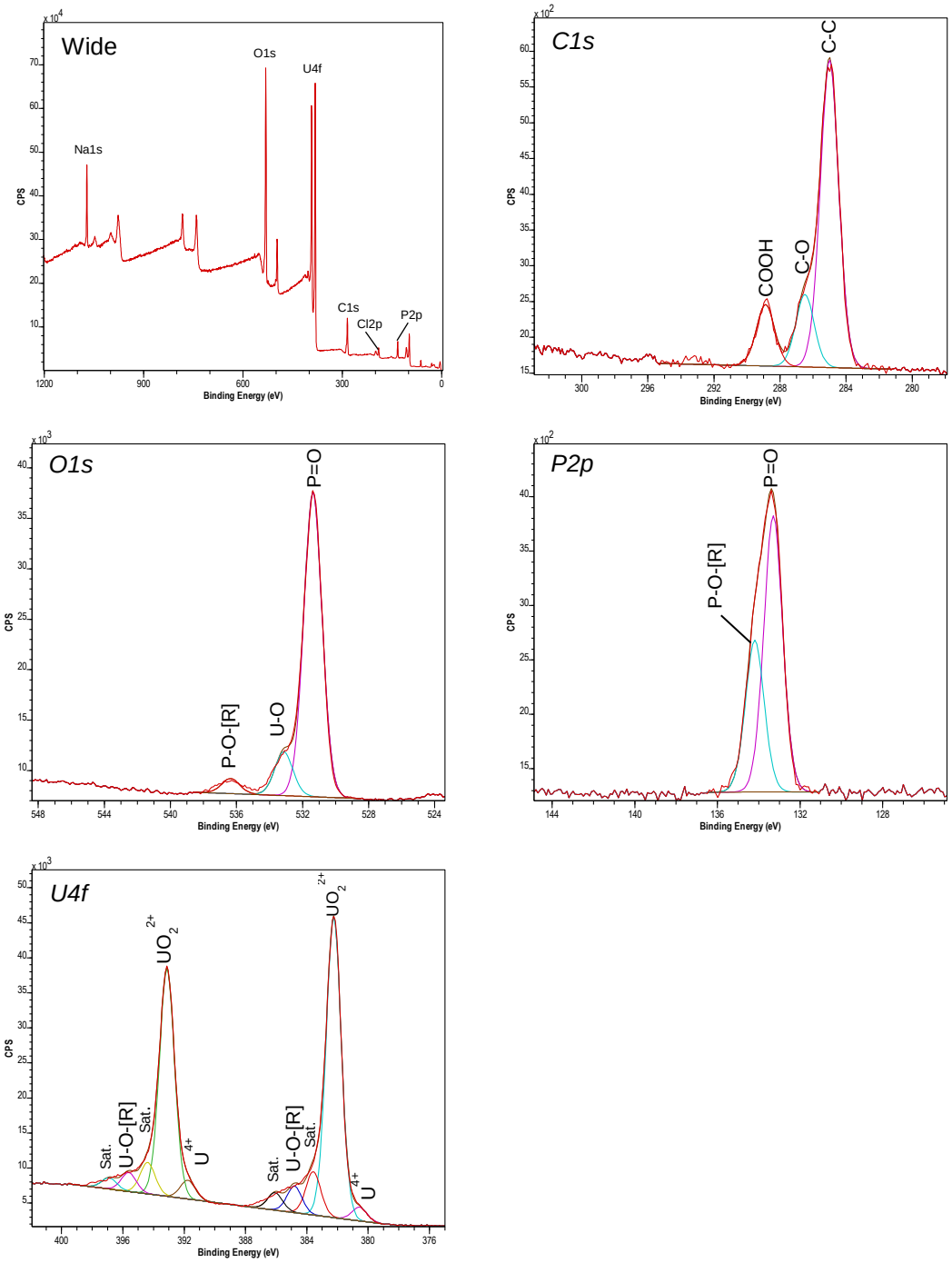

Figure 25. XPS spectrum of uranium minerals synthesised using aPO_4 at a molar ratio of 1.8 : 1 $H_2PO_4^-$: $(UO_2)_3(OH)_5^+$

Table 5. Binding energies (eV), FWHM, % area and assignment of XPS spectral bands of uranium minerals synthesised using aPO_4 at a molar ratio of 1.8 : 1 $H_2PO_4^-$: $(UO_2)_3(OH)_5^+$

Position (eV)	FWHM	% Area	Assignment
		C 1s	
285	1.295	69.66	C-C*
286.49	1.295	16.44	C-O-C*
288.88	1.295	13.9	COOH*
		O 1s	
531.37	1.285	83.78	P=O, C=O
533.13	1.285	12.07	U-O, P/C-OH
536.35	1.285	4.15	P-O-[R], P-[R]
		P 2p	
133.3	1.056	64.55	P=O, P-OH
134.19	1.056	35.45	P-O-[R]
		U 4f	
380.56	1.141	1.93	U^{4+}
382.25	1.141	42.47	UO_2^{2+}, U-O
383.58	1.141	6.14	U-O-[R], Satellite
384.81	1.141	3.73	U-O-[R], Satellite
386.07	1.141	2.46	Satellite
391.77	1.141	2.66	U^{4+}
393.12	1.141	31.95	UO_2^{2+}, U-O
394.38	1.141	4.43	U-O-[R], Satellite
395.62	1.141	2.65	U-O-[R], Satellite
396.89	1.141	1.57	Satellite

* Carbon tape associated peaks

The U4f XPS spectra of uranium minerals formed using both ePO_4 and aPO_4 showed a peak separation of 10.87 eV between $4f_{7/2}$ and $4f_{5/2}$. This peak separation was in agreement with that of $UO_2(NO_3)_2$•$6H_2O$ (Appendix Figure 4 U4f) and that reported in previous literature (Asuvathrarnan et al., 2015, Liu et al., 2009).

Aside from the main XPS peaks, there were additional peaks 1.35-1.71 eV lower than and up to 3.89 eV higher than the main uranium $4f_{7/2}$ and $4f_{5/2}$ peaks. The additional peaks at higher energy were satellite peaks and arose from the interactions of photoelectrons with valence electrons during the photo-excitation process. The satellite binding energy is much more sensitive to the oxidation state of the uranium than that of the main U4f peaks and (Asuvathrarnan et al., 2015, Kushwaha et al., 2012).

The U4f XPS region of $UO_2(NO_3)_2$•$6H_2O$ (with an oxidation state of +6) showed two additional peaks for both $4f_{7/2}$ and $4f_{5/2}$ peaks, Appendix Figure 4. Within both uranium minerals there are three additional peaks at higher energy for both $4f_{7/2}$ and $4f_{5/2}$ peaks. The highest additional peak (~3.7 eV) was also a satellite peak indicating that the majority of the uranium incorporated into the mineral is in oxidation state VI (Benard et

al., 1994). The other two higher energy peaks (at approximately +1.3 and +2.5 eV higher than the binding energies of the two most intense peaks) could be either satellite peaks or due to the interaction of uranium with the phosphate within the minerals formed. The latter can be further justified by the additional XPS peaks within the P2p region spectrum of both minerals formed, with the presence of further peaks in the minerals formed using ePO_4 indicating phosphate interactions with other impurities of the enzymatic phosphate solution.

Interestingly, there was evidence that not all the uranium in the uranium minerals formed using ePO_4 and aPO_4 was in the +6 oxidation state. The peaks at approximately 380.56 and 391.6 eV corresponded to uranium in the +4 oxidation state (Benard et al., 1994, Allen et al., 1982). Using the $U4f_{7/2}$ peak, the percentage of U as U(VI) (UO_2^{2+}) was 92.3% (leaving 7.7% as U(IV) (U^{4+})) for minerals formed using ePO_4. These percentages changed to 95.7 % and 4.3 % for aPO_4 minerals. The lack of this peak within $UO_2(NO_3)_2 \bullet 6H_2O$ supported the presence of multivalent uranium in the precipitate formed. This change could be attributed to the presence of impurities within ePO_4 sequestering uranium in the +4 oxidation state.

Overall, the XPS data of uranium minerals formed at a molar ratio of 1.8 : 1 $H_2PO_4^-$: $(UO_2)_3(OH)_5^+$ formed using ePO_4 and aPO_4 suggested slight differences in their chemical nature. The additional peaks associated with carbon and nitrogen within the ePO_4 minerals indicate that impurities were incorporated into the mineral structure, unlike the case when aPO_4 was used. Furthermore, the high-resolution scan of the U4f region indicated that most of the uranium incorporated into the minerals was in the +6 oxidation state, with a slight increase in the concentration of uranium in the +4 state when using ePO_4 to sequester uranium. The incorporation of other compounds in mineral structures has been demonstrated by various strains of bacteria that mineralise uranium using phosphate from acid phosphatase activity, most likely due to the high abundance of phosphate containing compounds external to and on the surface of bacteria. Calcium - and sodium - bearing autunite minerals are formed by certain strains of bacteria (Jroundi et al., 2007, Macaskie et al., 2000, Martinez et al., 2007, Merroun et al., 2011). Meta-autunite is mineralised by the marine bacterium *Idiomarina loihiensis* MAH1 (Morcillo et al., 2014). Furthermore, the incorporation of nitrogen compounds into the uranium minerals formed was demonstrated by the formation of nano-uramphite ($(NH_4)(UO_2)PO_4$) by *Bacillus thuringiensis* (Pan et al., 2015).

2.4.7 The proposed interaction of ePO_4 with U(VI)

Acid phosphatase (*APase*) hydrolyses phosphate esters from biological molecules (Vincent et al., 1992). Between pH 5 and 7, approximately 2 mM ePO_4 was hydrolysed from 1 mg mL^{-1} eDNA using 2 units mL^{-1} acid phosphatase. No ePO_4 was released from eDNA at pH 4 and below due to depletion in acid phosphatase activity. This is similar to that of microbial acid phosphatase activity in which uranium biomineralisation does not occur at pH as low as 2 to 3 (Merroun et al., 2011, Reitz et al., 2014). The proposed hydrolysis of ePO_4 (predominantly in the form of $H_2PO_4^-$ at pH 5) from eDNA using acid phosphatase is shown in Equation 6.

$$(APase) + eDNA{-}PO_4^- + H_2O \rightleftharpoons (APase)\text{-}eDNA{-}PO_4^- + H_2O$$

$$(APase)\text{-}eDNA{-}PO_4^- + H_2O \rightleftharpoons (APase){-}PO_3^- + eDNA\text{-}O + H_2O$$

$$(APase){-}PO_3^- + eDNA\text{-}O + H_2O \rightleftharpoons (APase) + eDNA\text{-}O + H_2PO_4^{-(*)}$$

Equation 6. The hydrolysis of ePO_4 (*) from eDNA using acid phosphatase at pH 5.

The stoichiometric data obtained from the biomineralisation of reacting ePO_4 with uranium at varying molar ratios indicated that approximately a 3.5 : 1 $H_2PO_4^-$: $(UO_2)_3(OH)_5^+$ molar ratio was responsible for the removal of reactants from solution. All of the uranium (in the form of $(UO_2)_3(OH)_5^+$) was formed using approximately 94 % of ePO_4 at an initial molar ratio of 3.8 : 1 in the starting solution, Figure 17. XRD analysis of the uranium minerals formed indicated that they were of uranium phosphate origin, Appendix Table 5. The uranium phosphate hydrated mineral $(UO_2HPO_4)\bullet\ xH_2O$ (ICDD PDF# 00-037-0373) displayed similar diffraction patterns to both ePO_4 and aPO_4 minerals. Therefore, it was proposed the biomineralisation uranium with ePO_4 occurred as described in Equation 7. This was based on a molar ratio of 3 : 1 $H_2PO_4^-$: $(UO_2)_3(OH)_5^+$. The difference in the proposed molar ratio and the recorded molar ratio (3.5 : 1) was probably due to the overestimation of uranium removed by ePO_4 from solution. A clear identification of these minerals was not possible due to the presence of impurities; however, the mineral formed can be identified as a simple uranium phosphate mineral such as UO_2HPO_4. These impurities were from organic material and nitrogen containing compounds from the enzymatic hydrolysis of eDNA complexing and removing additional phosphate from solution.

$$3H_2PO_4^- + (UO_2)_3(OH)_5^+ + 2H^+ \rightleftharpoons 3UO_2HPO_4\bullet 1.67H_2O$$

Equation 7. The proposed biomineralisation of uranium phosphate from enzymatic phosphate hydrolysis of eDNA.

Enzymatic phosphate released by microbial acid phosphatase has been associated with uranium biomineralisation through the formation of uranium phosphate-bearing minerals (Martinez et al., 2007). These include the formation of simple crystalline uranium phosphate compounds such as $(UO_2)_3(PO_4)_2 \bullet H_2O$ (Choudhary and Sar, 2011), chernikovite ($H_2(UO_2)_2(PO_4)_2$) (Beazley et al., 2009) and $HUO_2PO_4 \bullet 4H_2O$ (Macaskie et al., 2000). The incorporation of other elements into uranium phosphate minerals has been documented by numerous strains such as those that formed meta-autunite ($(Ca(UO_2)_2(PO_4)_2$) (Macaskie et al., 2000, Merroun et al., 2011) and nano-uramphite ($(NH_4)(UO_2)PO_4$) (Pan et al., 2015).

2.5 Conclusions

The present work revealed the mechanism whereby extracellular DNA precipitates uranium from solution. The binding and precipitation of uranium by eDNA was mainly mediated by negatively charged phosphate groups within the eDNA structure, with a higher percentage of precipitates formed at very low pH. This was due to an increased availability of phosphate and nitrogenous groups on the eDNA and the speciation of uranium in solution. Therefore the reaction was dependant on pH and uranium concentration. The minerals formed during this study all contained phosphates. At circumneutral pH, the enzymatic release of phosphate from acid phosphatase activity resulted in the formation of uranium phosphate-like mineral phases in which the uranium oxidation state was mainly VI. The structure of the mineral obtained showed a similar crystal structure to that of uranium phosphate-bearing minerals such as $(UO_2HPO_4) \bullet xH_2O$. The stoichiometry of the reaction was 3:1 $H_2PO_4^-$: $(UO_2)_3(OH)_5^+$ and the reaction occurred under mild acidic conditions (pH 5). The results demonstrated that DNA is a major contributor of the biomineralisation of uranium within bacterial EPS.

Chapter 3: Isolation and spectroscopic characterisation of bacterial cell surface structures.

3.1 Abstract

The cell surface architecture of bacteria governs their interactions with surfaces. Here we report the spectroscopic characterisation of whole *P. putida* 33015 and *B. subtilis* 168 cells and their isolated cell surface structures, alongside whole *D. radiodurans* R1 cells. Cell wall and membrane structures from *P. putida* and *B. subtilis* were isolated through disruption using a French pressure cell and differential based centrifugation. *D. radiodurans* could not be broken up to isolate cell surface structures. Characterisation of these isolates using XPS and ATR-FT-IR confirmed a proteinaceous and lipidic rich cell wall from *P. putida* and a polysaccharide and protein rich *B. subtilis* cell wall. Both strains have a similar macromolecular composition associated with their cell surface membranes.

The differences in macromolecular composition and functional group abundance associated between the isolated cell walls and whole cells of both *P. putida* and *B. subtilis* suggest interference with intracellular components with spectroscopic analysis. Therefore, to fully understand the structure of cell surface components, such as the cell wall, isolation from whole cells is required.

3.2 Introduction

The physiochemical interactions of bacteria with surfaces are governed by intermolecular forces between functional groups associated with the cell exterior and those of the interacting surface. This phenomenon is fundamental for bacterial growth on solid surfaces, biofilm formation and the biosorption of heavy metals or other particulates from solution (Ojeda et al., 2008a, Ojeda et al., 2008b, Ojeda et al., 2009). The availability of functional groups varies with bacterial strain, in particular whether their cell wall architecture is of Gram-positive or Gram-negative origin (Merroun and Selenska-Pobell, 2008, Wang and Chen, 2009). Understanding the macromolecular composition of the outermost cell regions, including the cell wall and cell surface membrane, therefore, is fundamental to determine the functional groups associated with the interactions of bacteria and surfaces.

X-ray photoelectron spectroscopy (XPS) is an experimental technique that provides elemental and functional group analysis of surfaces. This technique has previously been applied to the characterisation of the microbial cell surface due to the probing X-rays only penetrating the top 2 to 5 nm outermost layer of whole cells. It has been suggested that this technique is ideal for the characterisation of functional groups and the quantification of biomolecules within the cell wall, such as peptides, polysaccharides and lipidic like material (Rouxhet et al., 1994, Dufrene and Rouxhet, 1996, Dufrene et al., 1997, van der Mei et al., 2000, Ojeda et al., 2008a). Additionally, Fourier Transform-Infrared (FT-IR) spectroscopy has been used to identify the relative abundance of biological molecules and their associated functional groups in bacteria (Ojeda and Dittrich, 2012, Baker et al., 2014).

Most studies to date have investigated the bacterial cell surface using whole cells (Rouxhet et al., 1994, Dufrene and Rouxhet, 1996, Dufrene et al., 1997, van der Mei et al., 2000, Ojeda et al., 2008a, Ojeda and Dittrich, 2012, Baker et al., 2014). This can be problematic, in particular when using FT-IR, due to possible confusions in the interpretation of the FT-IR spectra that could arise from IR radiation interacting with functional groups associated with intracellular components. Studies have therefore isolated cell wall extracts from bacteria to minimise this interference when analysed by XPS (Dufrene et al., 1997) and FT-IR (Jiang et al., 2004). Cell membrane isolates have been investigated spectroscopically by FT-IR (Kamnev et al., 1999, Shakirova et al.,

2013). To date few studies have compared the macromolecular components of the cell surface structures by spectroscopic means from the same microorganism.

This work aimed to characterise the surface of *P. putida* 33015, *B. subtilis* 168 and *D. radiodurans* R1 using XPS and FT-IR. The spectroscopic characterisation of cell wall and membrane isolates from *P. putida* and *B. subtilis* was performed to compare the differences in macromolecular composition of cell surface structures. In doing this, the accuracy of using whole cells to characterise the composition of the cell surface using spectroscopic techniques was evaluated. Understanding the difference in macromolecular composition and functional groups between cell surface structures gives insight into the different mechanisms through which macromolecular components of the bacterial cell can interact with surfaces.

3.3 Experimental Procedures

3.3.1 Bacteria and growth conditions

Three bacteria were used in this study; *Pseudomonas putida* 33015 (ATCC 33015), *Deinococcus radiodurans* R1 (ATCC 13939) and *Bacillus subtilis* 168 (ATCC 23857) were obtained from LGC standards. *P. putida* 33015 was grown in sodium benzoate media (Appendix Table 14), *D. radiodurans* R1 in TYG media (Appendix Table 16) and *B. subtilis* 168 in nutrient broth in 1 L cultures until cells reached late exponential phase in their growth cycle, while shaking at 170 rpm (30 °C).

3.3.2 Cell fractionation

A cell fractionation method using a French pressure cell and ultracentrifuge was adapted and used (Smith and Foster, 1995) to isolate cell wall and membrane structures for spectroscopic characterisation and subsequent uranium biosorption experiments (Chapter 4). The cells from a 1 L culture of *P. putida* 33015 and *B. subtilis* 168 were harvested by centrifugation at 5,000 *g* (10 min), washed 3 times in 0.1 M NaCl and resuspended in 10 mL ice-cold double distilled H_2O. The concentrated cell suspension was passed through a French pressure cell (100 PSI, 4 °C) three times to break open the cells for cell wall and membrane isolation. The lysed cells were centrifuged (3,000 *g*, 4 °C, 2.5 min, twice) to remove any intact cells and any other debris from the cell disruption.

To isolate cell wall fragments, the cell lysate was centrifuged (27,000 *g*, 4 °C, 30 min) and the pellet stored at -20 °C. The remaining supernatant was subject to the same centrifugation parameters and pellets pooled to give cell wall fragments. To isolate cell membrane and associated proteins, the remaining supernatant was subject to ultracentrifugation (100,000 *g*, 4 °C, 60 min). The pellet was stored at -20 °C, remaining supernatant spun again and pellets pooled to give cell membrane fragments. The final supernatant was subsequently characterised as cell cytoplasm and associated proteins.

The isolated cell wall, membrane fragments and cytoplasm were lyophilized (Alpha 1-2 LD Plus freeze dryer) to determine dry weights. Because of this the cells were originally resuspended in double distilled H_2O rather than a buffered solution as previously prepared (Smith and Foster, 1995) to ensure the purity of the fragments for uranium biosorption experiments (Chapter 4).

No chemical or enzymatic lysis techniques were applied to break open the cells. This was to ensure that all the uranium was interacting with the biomass and not with any chemicals or enzymes from the fractionation process.

3.3.3 Molecular composition of cell surface structures as characterised using XPS

The percentage abundance of peptide, polysaccharide and hydrocarbon-like material (i.e. lipids) in the cell surface structures was characterised by XPS. The information given was used to determine the efficiency of the cell fractionation process and whether using whole cells to characterise the bacterial cell surface is an accurate approach. The XPS analysis was conducted using a KRATOS AXIS 165 Ultra Photoelectron spectrometer using an Al Kα X-ray source (1486.6 eV). Each sample was mounted on indium foil and analysed by a wide survey scan (pass energy 160 eV, 1.0 eV step size) and a high-resolution scan (pass energy 20 eV, 0.1 eV step size) for carbon, oxygen, nitrogen and phosphorus. Binding energies were determined using the C_{1s} component set at 285.0 eV, attributed to carbon bound only to carbon and hydrogen, using the CasaXPS software (Version 2.3.16). The full width half maximum was kept constant for subsequent peak calibration.

3.3.4 Cell surface functional groups assignment by FT-IR

Measurements were performed using Attenuated Total Reflectance (ATR) – FT-IR to identify the functional groups associated with each cell surface component. These were obtained using a Silver Gate Evolution ATR accessory, consisting of a germanium crystal, coupled to a Perkin Elmer Spectrum One FT-IR spectrometer. A total of 30 scans were performed on each sample within the scanning range of 4000-800 cm^{-1}. An average spectrum was obtained from 3 replicates, baseline corrected and normalised to 1.5 absorbance (arbitrary units) using the ~1650 cm^{-1} amide I peak within the control sample (containing no uranium). Data acquisition and processing were performed using PerkinElmer Spectrum version 3.3 to obtain peak positions and relative peak intensities.

3.4 Results and Discussion

3.4.1 Cell fractionation

Approximately 103 mg *P. putida* and 239 mg *B. subtilis* dry biomass was obtained from 1 L culture grown to the late exponential phase of their respective bacterial growth cycles. This biomass was processed using a French Pressure Cell to isolate the cell wall, membrane and cytoplasmic-associated components (termed fractions). The relative percentage abundance of the fractions from the dry biomass of 1 L of culture (six repeats) is presented in Figure 26.

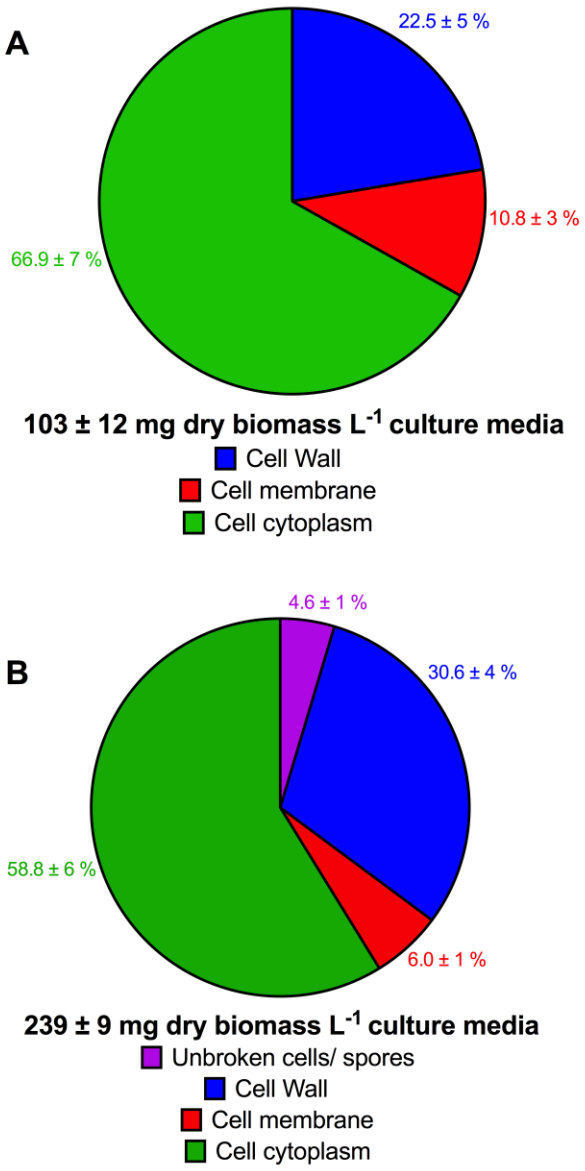

Figure 26. Percentage abundance of components isolated from the fractionation of [A] *P. putida* and [B] *B. subtilis.*

From the cell fractionation procedure, the majority of components in both bacteria was from the cell cytoplasm and associated biopolymers. *P. putida* was comprised of 25 % cell wall and 11 % cell membrane dry weight components (Figure 26A) while *B. subtilis* was comprised of 30.6 % cell wall and 6 % cell membrane dry weight components (Figure 26B). There were differences in composition of the cell wall and membrane between strains; *B. subtilis* had a greater percentage cell wall dry weight than *P. putida*. This difference could be attributed to *P. putida* having only small quantities of peptidoglycan with an outer membrane and a large periplasmic space containing the gel-like matrix periplasm whereas *B. subtilis* has a peptidoglycan-rich cell wall. Another explanation for this difference could be due to the bacterial cell morphology. Although both are classed as rod shaped bacteria, *B. subtilis* is spherical compared to *P. putida*, with the latter adopting the more classical long rod shape. There is therefore a greater surface area to volume ratio for *B. subtilis* in comparison to *P. putida*, suggesting a higher quantity of cell wall components per cell in comparison to intracellular components. On the other hand, the percentage dry weight composition of the cell membrane was higher in *P. putida* than *B. subtilis* and could be due to carry-over of the outer membrane between spins of *P. putida.* Its membrane fraction would then be a combination of the plasma surface membrane and small quantities of the outer membrane of the Gram-negative cell wall.

The small percentage of unbroken *B. subtilis* cells could be attributed to the formation of endospores. *B. subtilis* forms spores due to nutrient starvation as a survival mechanism (Smith and Foster, 1997). The culture production of *B. subtilis* for this experiment could have induced sporulation due to a lack of nutrients towards the end of the growth incubation. The endospores produced are much smaller in size and would pass through the French pressure cell without breakage. Other mechanical techniques are required to break them, such as bead-beating homogenisation (Smith and Foster, 1995, Smith and Foster, 1997).

It was not possible to isolate cell wall components from whole *D. radiodurans* cells. Numerous mechanical techniques were used to try to break open and harvest cell wall and membrane fractions. Techniques tried included the French pressure cell (Smith and Foster, 1995), bead-beating homogenisation (Smith and Foster, 1997) and freeze thawing using an 80/20 (v/v) methanol/water suspension (Winder et al., 2008) in order

to create ice crystals to break the cells for fraction harvest. Unfortunately, these were not a success and the cells of *D. radiodurans* could not be broken.

No chemical or enzymatic lysis techniques were applied and the fractions were resuspended in double distilled H_2O, rather than a buffered solution, for the differential based centrifugation, to ensure that the fractions were pure for their subsequent interactions with uranium. This was to ensure that all the uranium was interacting with the biomass and not with any chemicals or enzymes from the fractionation process.

3.4.2 XPS characterisation of cell surface structures

XPS was used to characterise the surface functional groups in the bacterial fractions and quantify the relative elemental abundance in the outermost layer of the sample analysed. The elemental composition calculated from the wide scan and the functional groups determined from the C1s, N1s, O1s and P2p high-resolution scans are displayed in Table 7- Table 9 for each fraction while representative spectra for each fraction type are shown in Figure 27 - Figure 33.

The high-resolution N1s spectra for all fractions and strains showed peaks at ~ 400.0 eV and protonated groups at ~ 401.7 eV, corresponding to non-protonated and protonated nitrogenous groups respectively, and were ascribed to amides and amines in proteins (Rouxhet et al., 1994, Dufrene et al., 1997, Ahimou et al., 2007, Ojeda et al., 2008a, Ramstedt et al., 2014). The high percentage of non-protonated nitrogenous groups contributed to the overall net-negative charge of the cell surface isolates. The high-resolution P2p spectra at ~ 133.7 eV corresponded to phosphate groups to the phosphodiester bonds in phospholipids and phosphorylated biomolecules (Dufrene et al., 1997, Ojeda et al., 2008a). Little to no phosphate was found in the outer most layer of *D. radiodurans* (Figure 30). A high-resolution scan of the C1s region showed 4 components; carbon-carbon and carbon-hydrogen interactions at 285 eV, carbon bound to oxygen or nitrogen at ~ 286.47 eV (most likely from amides in proteins), a carbon oxygen double bonded group corresponding to carbonyl, carboxylate or amide at 288.01 eV and carboxyl groups at 289 eV (Rouxhet et al., 1994, Dufrene et al., 1997, Ahimou et al., 2007, Ojeda et al., 2008a). An additional peak at approximately 293 eV in some samples corresponds to carbon satellite peaks and is not taken into consideration for analysis. These satellite peaks cannot be ascribed to carbon-associated functional groups since their appearance was due to strong electron shake up excitations of the final chemical state resulting in additional peaks several eV higher than the main C1s

peak at 285 eV (Jackson and Nuzzo, 1995). The high resolution scan O1s peak was fitted to 2 components at 531.4 eV corresponding to carbon - oxygen and phosphorus - oxygen double bonds from carboxyl, amides and phosphate groups while the peak at 532.8 eV corresponded to oxygen present within hydroxyl and phosphate groups.

The functional groups identified above confirm the presence of polysaccharide-like material, proteins and hydrocarbons in the outermost layer of each sample analysed. Changes in the percentage area of certain peaks were attributed to the relative abundance of the functional groups present within each fraction. For example, there was an increase in percentage area of the O1s peak at 531.4 eV with respect to the peak at 532.8 eV between the *P. putida* whole cells (39.6 %) and their cell wall (48.8 %) and membrane (59.5 %) isolates (Figure 27 – Figure 29). This suggested an increase in the number of carboxyl, phosphate groups and amides like those present within the phospholipid bilayer and proteins present within the cell wall and membrane of Gram-negative bacteria (Rouxhet et al., 1994, Dufrene et al., 1997, van der Mei et al., 2000, Ahimou et al., 2007, Ojeda et al., 2008a). This was also evident in changes of the relative percentage area of the O1s peaks of *B. subtilis* whole cells (40.3 %) and their cell wall and membrane isolates (Figure 31-Figure 33). There was an increase in the relative percentage area of the peak at 531.4 eV in membrane isolates (61.3 %) while there was a decrease in percentage area in cell wall isolates (30.6 %). This decrease was probably due to the increase in the number of carbonyl groups present within the carbohydrate rich cell wall region which contains a majority of peptidoglycan and teichoic acids, whereas within whole cells the penetration depth of the X-ray could take into account elements present within the cell membrane as well, for example if the whole cells were ruptured.

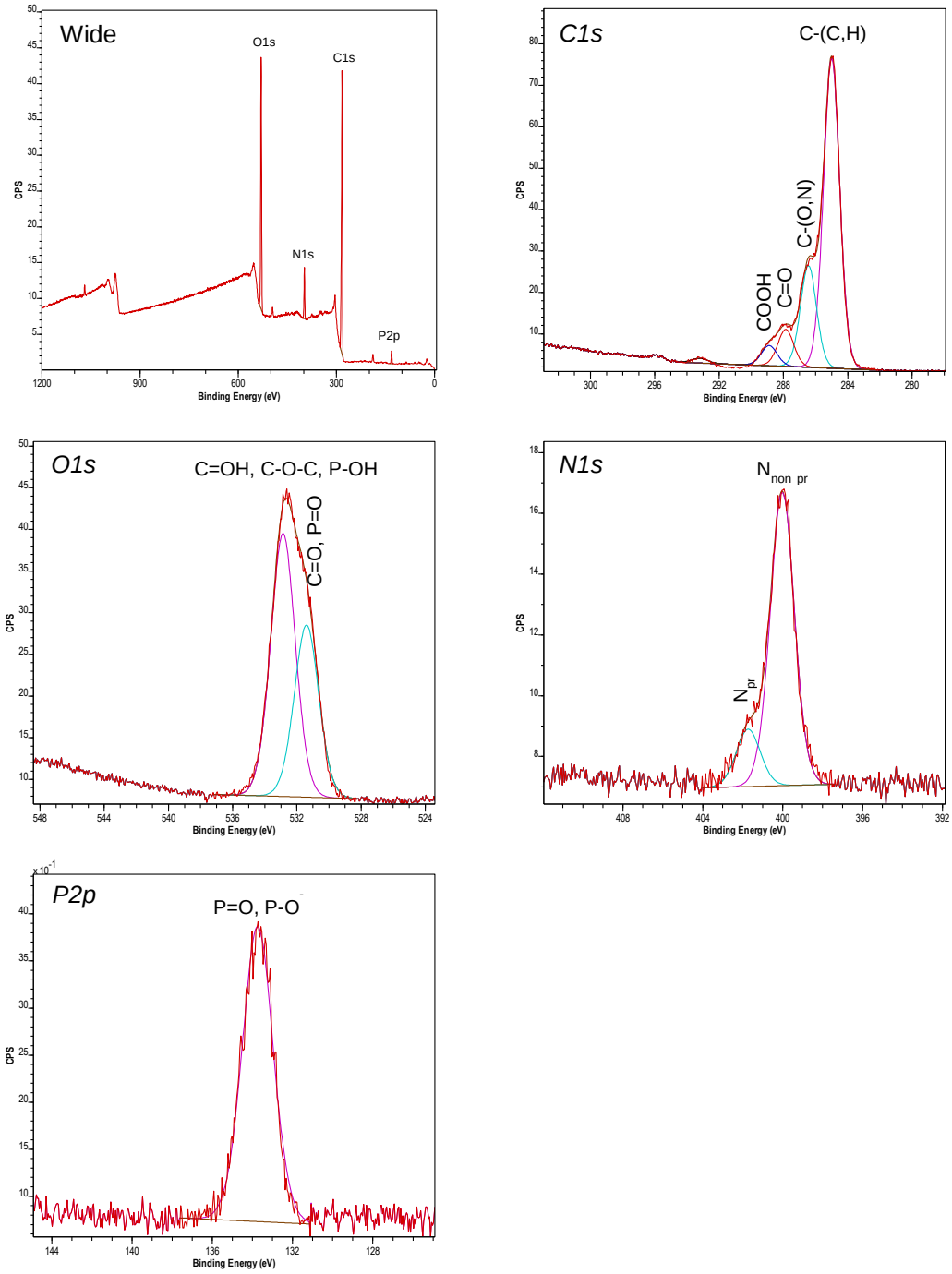

Figure 27. XPS wide and high resolution C1s, O1s, N1s and P2p scans of whole *P. putida* cells.

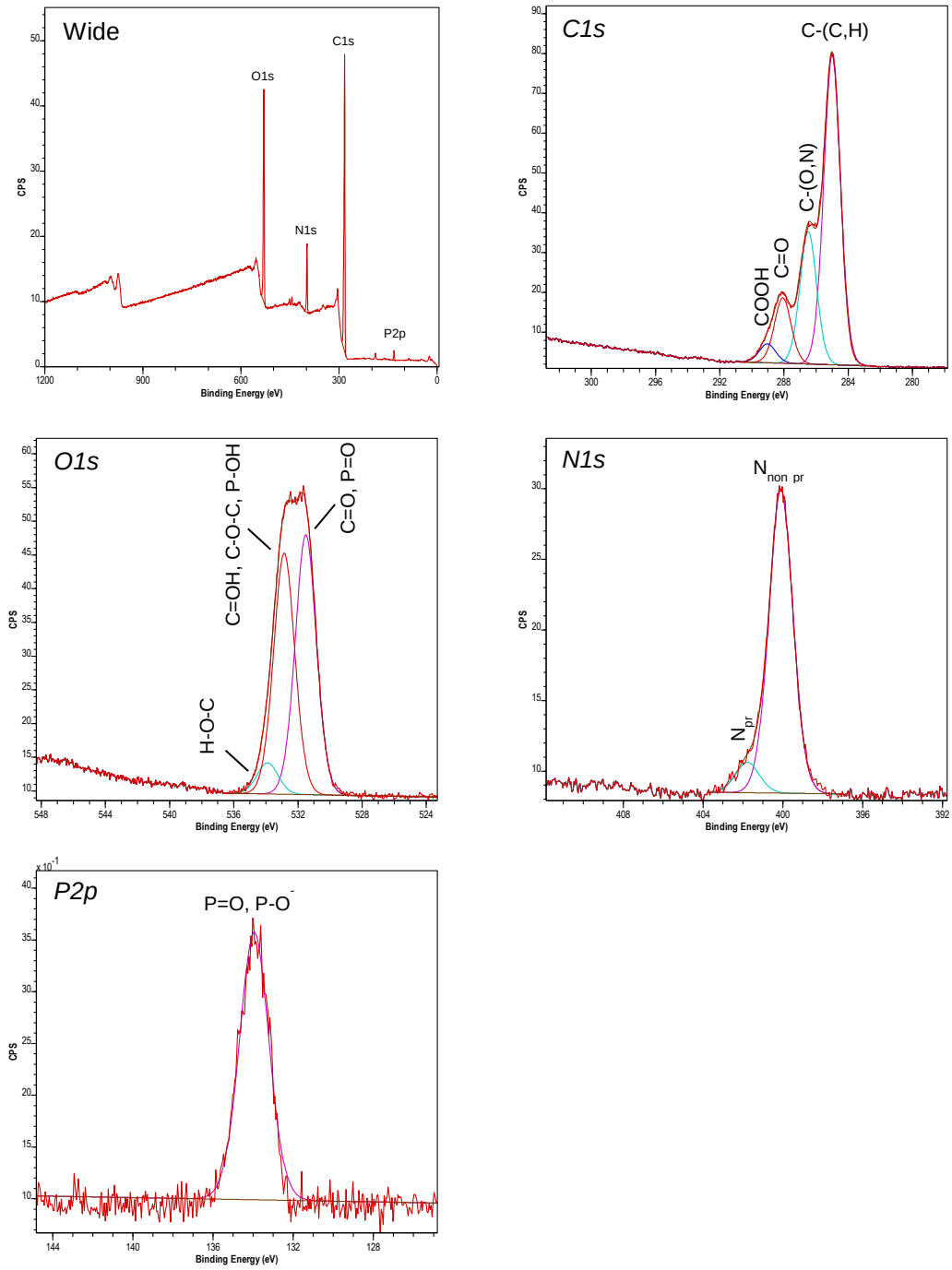

Figure 28. XPS wide and high resolution C1s, O1s, N1s and P2p scans of *P. putida* cell wall isolates.

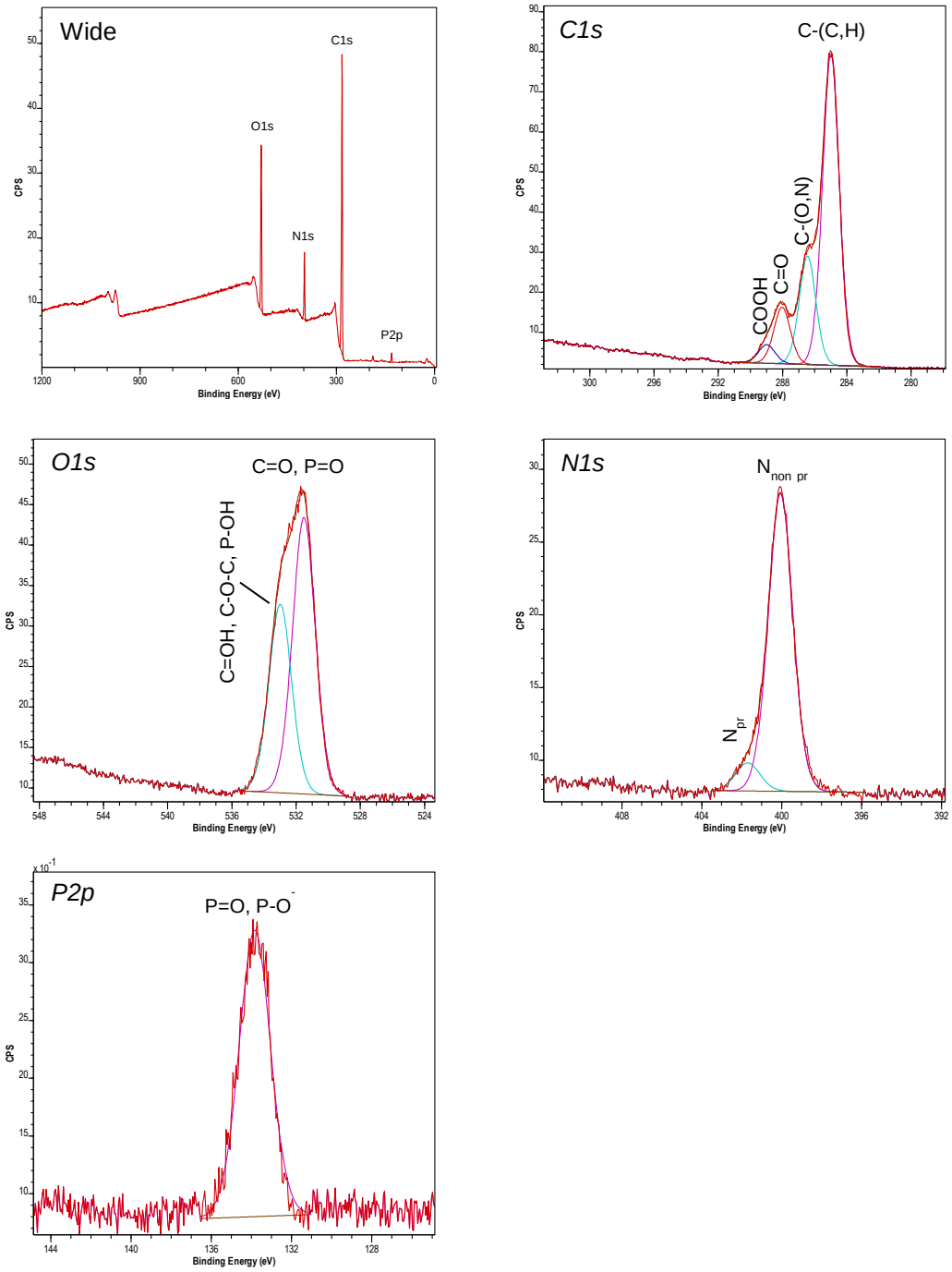

Figure 29. XPS wide and high resolution C1s, O1s, N1s and P2p scans of *P. putida* cell membrane isolates.

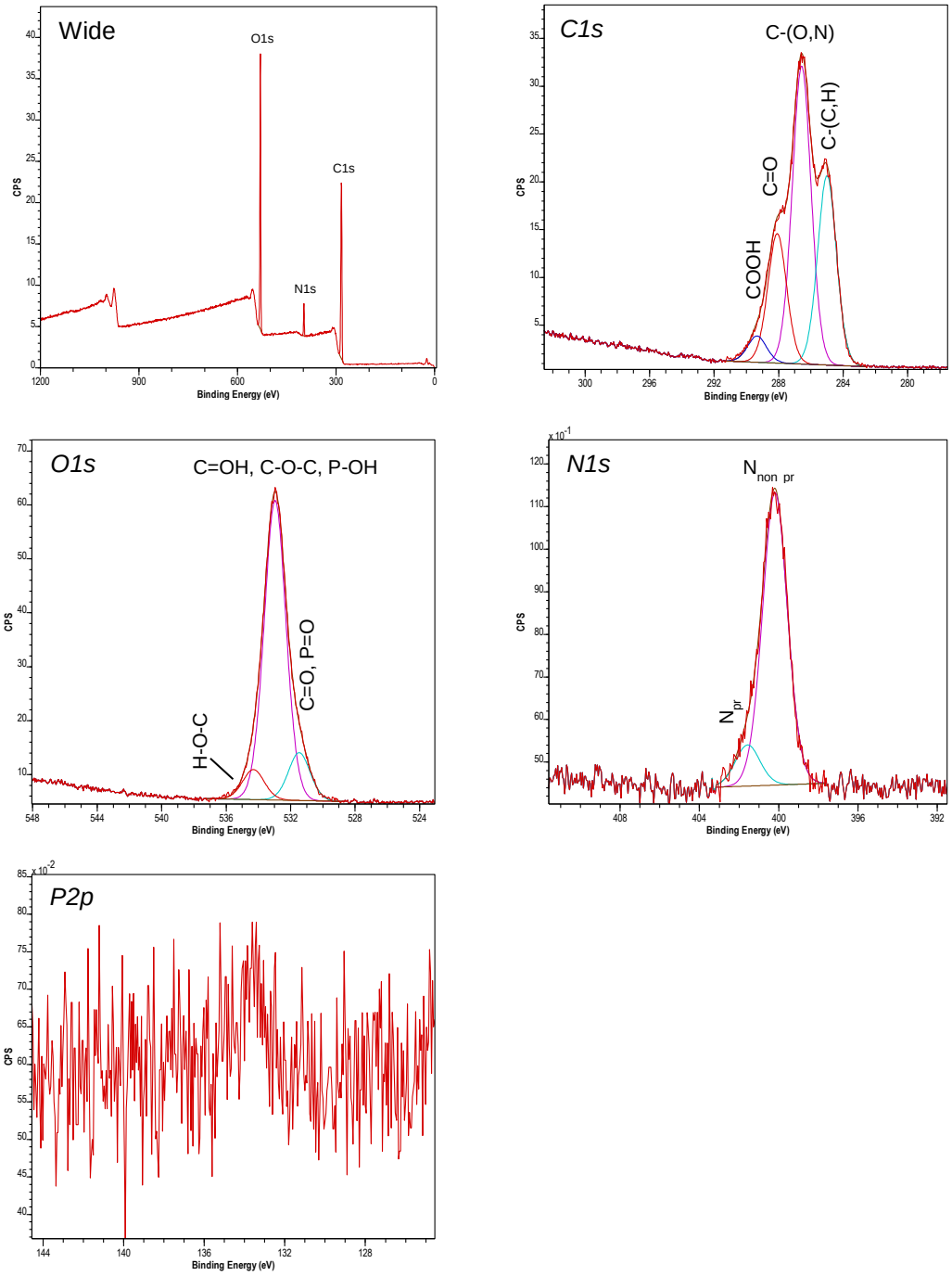

Figure 30. XPS wide and high resolution C1s, O1s, N1s and P2p scans of whole *D. radiodurans* cells.

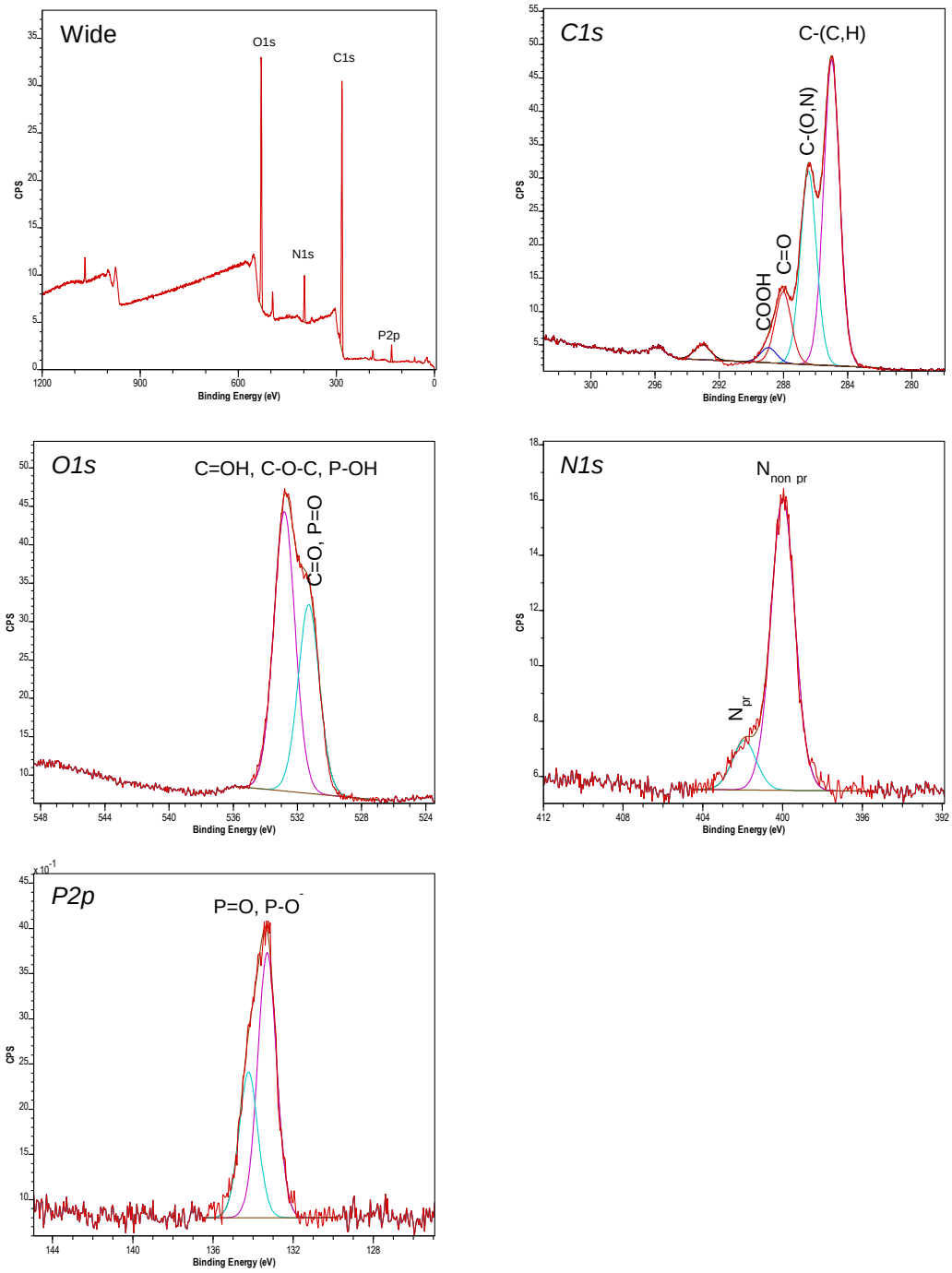

Figure 31. XPS wide and high resolution C1s, O1s, N1s and P2p scans of whole *B. subtilis* cells.

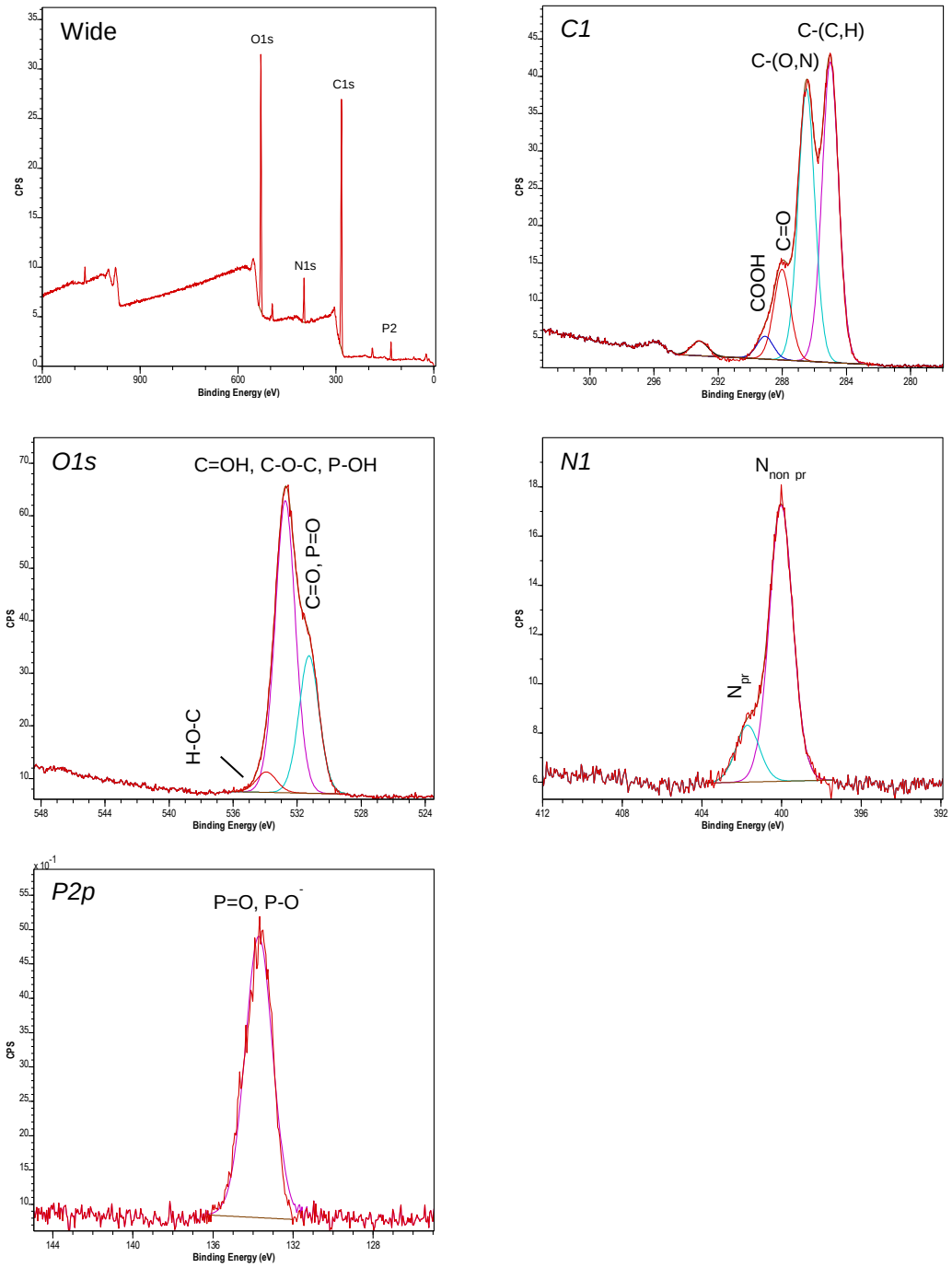

Figure 32. XPS wide and high resolution C1s, O1s, N1s and P2p scans of *B. subtilis* cell wall isolates.

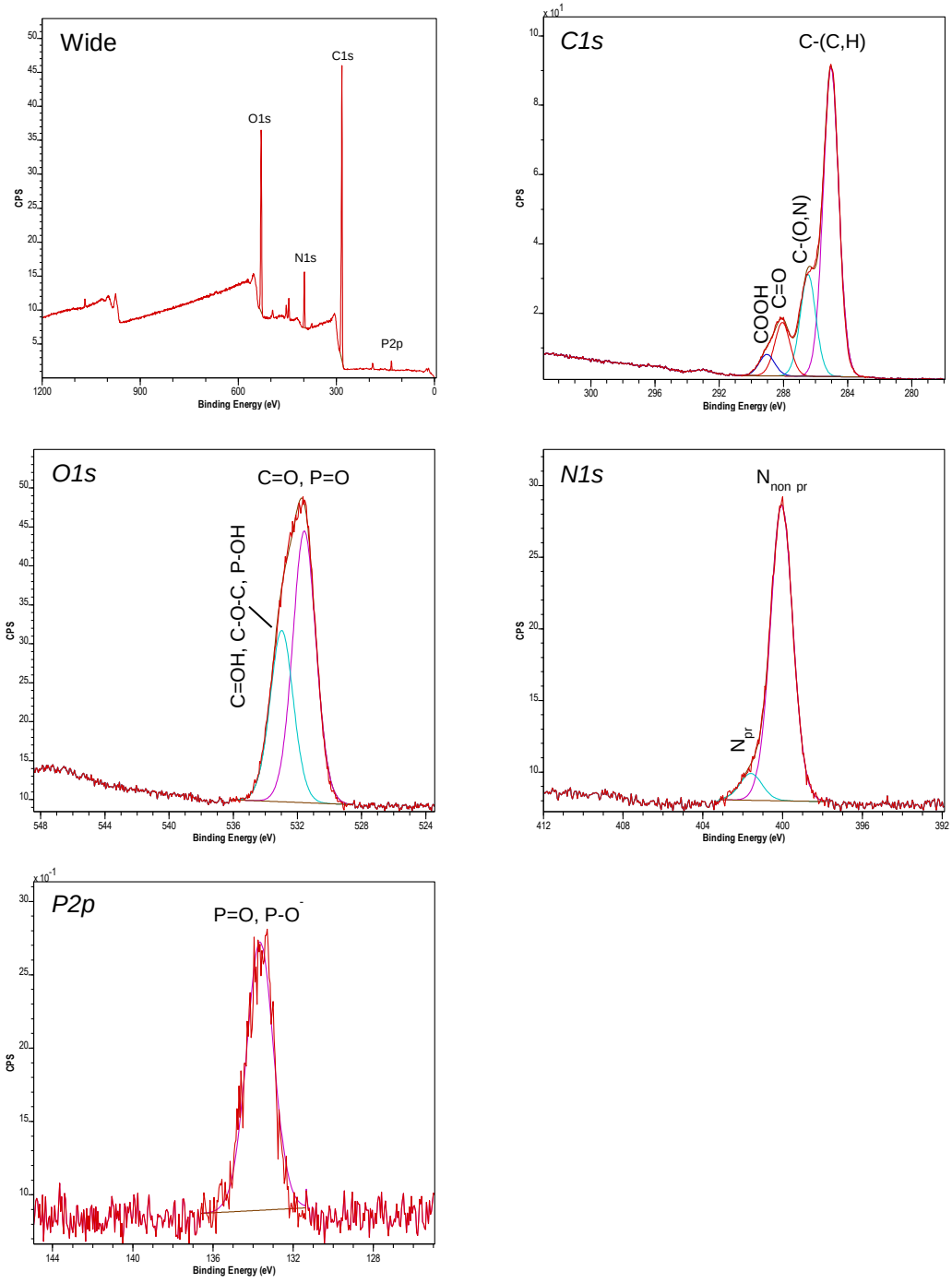

Figure 33. XPS wide and high resolution C1s, O1s, N1s and P2p scans of *B. subtilis* cell membrane isolates.

Using the percentage abundance of elements present within the surface of the sample, the abundance of polysaccharides, peptides and hydrocarbon-like compounds was determined (Rouxhet et al., 1994, Dufrene et al., 1997, Ojeda et al., 2008a). This approach compared the measured concentration ratios of O/C and N/C with the carbon concentration in the cell surface structures with respect to the atomic concentration ratios O/C and N/C for model compounds representative of the three classes of cell surface constituents, Table 6.

Table 6. The chemical composition of model compounds used for the calculation of cell surface constituent abundance.

Cell wall constituent	Model carbon compound	[Atomic] ratio (atom/atom)		[Carbon] (mmol g^{-1})
		O/C	N/C	
Polysaccharides	Glucan ($C_6H_{10}O_5$)	0.833	0.000	37.0
Peptides	*P. fluorescens* OE 28.3 OMP*	0.325	0.279	43.5
Lipid	Hydrocarbon $(CH_2)_n$	0.000	0.000	71.4

* Outer membrane protein (OMP) amino acid analysis for peptide atomic concentration ratios and relative protein abundance.

The following equations (Equation 8 - Equation 10) together with the carbon concentration of each model carbon compound (Table 6) were used to determine the percentage of polysaccharides, peptides and hydrocarbon-like compounds at the cell surface, where C_{PEP}, C_{PS}, and C_{LIP} are the atomic carbon concentrations of the peptides, polysaccharides and lipids within the bacterial surface biomass (Ojeda et al., 2008a).

$$O/C = 0.325\ (C_{PEP}/C) + 0.833\ (C_{PS}/C) \quad \text{Equation 8}$$

$$N/C = 0.279\ (C_{PEP}/C) \quad \text{Equation 9}$$

$$1 = (C_{PEP}/C) + (C_{PS}/C) + (C_{LIP}/C) \quad \text{Equation 10}$$

When whole cells were analysed by XPS, it has been previously assumed that only the outermost region (2-5 nm) was analysed since this distance is the maximum penetration of X-rays from the instrument (Rouxhet et al., 1994, Dufrene and Rouxhet, 1996, Dufrene et al., 1997, Ahimou et al., 2007, van der Mei et al., 2000). However, as the cell fractionation method used in this study is a well-defined method to isolate purified cell wall and membrane structures (Smith and Foster, 1995), it was expected that the abundance of biomolecules detected by XPS would be representative of the entire cell surface structure investigated. The calculated results indicated that there were

noticeable differences between the cell surface architecture of the three bacteria used within this study (Table 7- Table 9).

There appeared to be an almost equal abundance of peptide, polysaccharides and lipidic compounds near the surface of whole *P. putida* cells, as calculated from Equation 8 - Equation 10 (Table 7). This relative abundance changed between the *P. putida* cell wall and membrane isolates in which there was an increase in both peptides and hydrocarbon like compounds and a decrease in polysaccharides. A relative abundance of 34.3 ± 3.4 %, 21.1 ± 0.5 % and 14.7 ± 0.2 % polysaccharides was calculated for whole cells, cell wall and membrane isolates, respectively. This decrease in polysaccharides present between cell wall and membrane isolates was due to the fact that there are few if any polysaccharide-like compounds within the cell surface membranes while there are only small amounts, such as peptidoglycan, within Gram-negative cell walls. The higher relative concentration of polysaccharides within whole cells in comparison with cell wall isolates could be attributed to cell disruption and the migration of intracellular polysaccharides towards the cell surface where sample is analysed. The increase in relative abundance of peptides and hydrocarbons in isolates following cell fractionation was attributed to proteins and phospholipids present within the outer and cell surface membrane.

The surface of the whole *B. subtilis* cells is composed of almost equal amounts of peptides (38.0 ± 1.9 %) and polysaccharides (38.2 ± 1.0 %) while hydrocarbon-like compounds comprise 23.8 ± 2.0 %. It has been suggested that the hydrocarbon-like material found quantified in the surface of *B. subtilis* should probably be ascribed to lipoteichoic acids (Ramstedt et al., 2014) rather than ruptures of the cell wall and X-ray penetration of cell surface membrane phospholipids as it has been shown that freeze drying whole bacteria does not rupture the cell walls (Moriwaki et al., 2013). The relative abundance of peptides and polysaccharides increased to 42.1 ± 3.6 % and 41.7 ± 2.3 % respectively within cell wall isolates of *B. subtilis* following the fractionation of whole cells. Previous XPS analysis of whole *B. subtilis* cells characterised the cell surface to be rich in phosphate groups as well as protonated nitrogen, associated with pronated amino acids and alanine or (lipo) teichoic acids (Ahimou et al., 2007). A decrease in the relative abundance of lipids in the *B. subtilis* cell wall structure was likely ascribed to a decrease in lipoteichoic acid content due to it being covalently bound to the cell surface membrane. This was evident in both *B. subtilis* cells and cell wall isolates

(Figure 31 - Figure 32). The presence of high phosphate concentrations were likely attributed to phosphorylated proteins and polysaccharides within the Gram-positive cell wall was responsible for the surface negative charge at low pH in which a point of zero charge was previously calculated at pH 2.2 (Harden and Harris, 1953, Fein et al., 1997). Furthermore, the molecular composition of the *B. subtilis* cell wall changes as a function of pH and in the presence of adsorbed heavy metal species (Ramstedt et al., 2014). An increase in lipoteichoic acid content and a decrease in polysaccharide and peptide content was observed in the cell surface of whole *B. subtilis* cells as the pH of the solution the cell were suspended in increased.

Gram-negative strains contain a hydrocarbon-rich outer membrane in their cell wall structure. The relative abundance of hydrocarbon-like compounds was higher within cell membrane isolates (37.7 ± 2.6 %) while polysaccharide content was lower (20.5 ± 1.5 %) and the abundance of peptides was similar to whole cells (41.8 ± 3.6 %). The increase in hydrocarbon content was due to the presence of phospholipids and other lipidic material within the cell surface membrane. The relatively low abundance of polysaccharides could be attributed to cell membrane attached polysaccharides such as lipoteichoic acids (in Gram-positive strains) or contamination during the fractionation process in which cell wall or even cytoplasmic associated polysaccharides that were removed at 100,000 *g* (Rouxhet et al., 1994, Dufrene and Rouxhet, 1996, Dufrene et al., 1997, van der Mei et al., 2000, Ojeda et al., 2008a).

The differences in macromolecular composition, between the cell surface structures and whole cells suggests inaccuracies with the application of XPS to determine the macromolecular composition of the bacterial cell surface using whole cells that has been used extensively in previous studies (Rouxhet et al., 1994, Dufrene and Rouxhet, 1996, Dufrene et al., 1997, van der Mei et al., 2000, Ojeda et al., 2008a, Ojeda and Dittrich, 2012, Baker et al., 2014). Therefore, to accurately characterise the bacterial cell surface using spectroscopic techniques such as XPS, isolation and purification of cell surface structures from whole cells is required.

Table 7. Binding Energies (eV), assignments and quantification of XPS Spectral Bands of Freeze-Dried whole cell, cell wall and cell membrane isolates from *P. putida* 33015. Total carbon, nitrogen, oxygen and phosphorus to calculate the macromolecular composition were obtained from the low-resolution wide scan. Identification and quantification of the functional groups associated with each fraction were obtained from the C1s, N1s, O1s and P2p high-resolution spectra.

	Peak (eV ± SD)			Conc. (% ± SD)			[Atomic] ratio (± SD)		
Component	Whole cells	Cell wall	Cell membrane	Whole cells	Cell wall	Cell membrane	Whole cells	Cell wall	Cell membrane
Total C	285.0 ± 0.00	285.0 ± 0.00	285.0 ± 0.00	69.46 ± 1.84	71.37 ± 1.07	73.26 ± 0.68			
Total N	399.9 ± 0.25	400.0 ± 0.00	399.9 ± 0.25	5.44 ± 0.38	7.66 ± 0.52	8.27 ± 0.24			
Total O	532.1 ± 0.25	532.0 ± 0.00	531.8 ± 0.29	23.07 ± 1.67	19.49 ± 0.59	17.08 ± 0.34			
Total P	133.6 ± 0.25	133.9 ± 0.25	133.5 ± 0.00	2.02 ± 0.04	1.48 ± 0.14	1.37 ± 0.12			
O/C							0.332 ± 0.03	0.273 ± 0.01	0.233 ± 0.01
N/C							0.078 ± 0.01	0.107 ± 0.01	0.113 ± 0.00
P/C							0.029 ± 0.00	0.0214 ± 0.00	0.019 ± 0.00
Peptide				33.97 ± 2.35	46.58 ± 3.15	49.79 ± 1.50			
Polysaccharides				34.31 ± 3.39	21.11 ± 0.52	14.71 ± 0.24			
Hydrocarbons				31.72 ± 4.36	32.31 ± 3.01	35.5 ± 1.61			
Assignment	Position (eV)			FWHM			% Area		
				C1s					
C - (C,H)	285.00	285.00	285.00	1.163	1.208	1.202	65.46	58.78	62.93
C - (O,N)	286.45	286.49	286.45	1.163	1.208	1.202	21.69	25.20	21.91
C = O	287.88	288.08	288.03	1.163	1.208	1.202	8.32	12.43	11.41
COOH	288.96	289.03	288.98	1.163	1.208	1.202	4.52	3.59	3.75
				N1s					
$N_{non\ pr.}$	400.01	400.09	400.05	1.406	1.394	1.425	83.62	90.90	91.35
$N_{pr.}$	401.72	401.77	401.70	1.406	1.394	1.425	16.38	9.10	8.65
				O1s					
C = O, P = O	531.40	531.51	531.51	1.778	1.529	1.651	39.56	48.83	59.45
C = OH, C-O-C, P-OH	532.86	532.86	532.99	1.778	1.529	1.651	60.44	45.3	40.55
H-O-C		533.89			1.529			5.87	
				P2p					
P=O, P-O-	133.74	133.95	133.83	1.782	1.704	1.816	100	100	100

Table 8. Binding Energies (eV), assignments and quantification of XPS Spectral Bands of Freeze-Dried whole *D. radiodurans* R1 cells. Total carbon, nitrogen, oxygen and phosphorus to calculate the macromolecular composition were obtained from the low-resolution wide scan. Identification and quantification of the functional groups were obtained from the C1s, N1s, O1s and P2p high-resolution spectra.

Component	Peak (eV ± SD)	Conc. (% ± SD)	[Atomic] ratio (± SD)
Total C	285.0 ± 0.00	64.53 ± 1.10	
Total N	398.9 ± 0.25	4.79 ± 0.30	
Total O	531.4 ± 0.25	30.68 ± 0.82	
Total P	N/A	N/A	
O/C			0.475 ± 0.02
N/C			0.074 ± 0.01
P/C			N/A
Peptide		30.03 ± 1.89	
Polysaccharides		51.61 ± 1.15	
Hydrocarbons		18.36 ± 2.86	
Assignment	**Position (ev)**	**FWHM**	**% Area**
		C1s	
C - (C,H)	286.57	1.359	46.33
C - (O,N)	285.00	1.359	29.44
C = O	288.09	1.359	20.15
COOH	289.34	1.359	4.09
		N1s	
$N_{non\ pr.}$	400.19	1.467	87.97
$N_{pr.}$	401.57	1.467	12.33
		O1s	
C = O, P = O	532.96	1.572	79.37
C = OH, C-O-C, P-OH	531.46	1.572	12.68
H-O-C	534.3	1.572	7.95

Table 9. Binding Energies (eV), assignments and quantification of XPS Spectral Bands of Freeze-Dried whole cell, cell wall and cell membrane isolates from *B. subtilis* 168. Total carbon, nitrogen, oxygen and phosphorus to calculate the macromolecular composition were obtained from the low-resolution wide scan. Identification and quantification of the functional groups associated with each fraction were obtained from the C1s, N1s, O1s and P2p high-resolution spectra.

	Peak (eV ± SD)			Conc. (% ± SD)			[Atomic] ratio (± SD)		
Component	Whole cells	Cell wall	Cell membrane	Whole cells	Cell wall	Cell membrane	Whole cells	Cell wall	Cell membrane
Total C	285.00 ± 0.00	285.00 ± 0.00	285.00 ± 0.00	65.96 ± 0.74	62.87 ± 1.87	73.61 ± 0.95			
Total N	399.63 ± 0.25	399.38 ± 0.25	399.75 ± 0.29	6.03 ± 0.3	6.63 ± 0.56	6.89 ± 0.6			
Total O	532.00 ± 0.00	531.75 ± 0.29	531.75 ± 0.29	25.46 ± 0.54	27.77 ± 1.41	18.31 ± 0.48			
Total P	133.50 ± 0.00	133.13 ± 0.25	133.50 ± 0.00	2.56 ± 0.15	2.74 ± 0.11	1.19 ± 0.15			
O/C							0.386 ± 0.01	0.442 ± 0.04	0.249 ± 0.01
N/C							0.091 ± 0.01	0.105 ± 0.01	0.094 ± 0.01
P/C							0.039 ± 0.00	0.044 ± 0.00	0.016 ± 0.00
Peptide				38.02 ± 1.89	42.08 ± 3.59	41.80 ± 3.55			
Polysaccharides				38.15 ± 1.03	41.71 ± 2.25	20.48 ± 1.50			
Hydrocarbons				23.83 ± 1.97	16.21 ± 4.92	37.72 ± 2.64			
Assignment	Position (eV)			FWHM			% Area		
				C1s					
C - (C,H)	285.00	285.00	285.00	1.164	1.208	1.131	50.8	42.84	63.58
C - (O,N)	286.44	286.49	286.47	1.164	1.208	1.131	32.21	38.88	20.97
C = O	288.01	288.01	288.07	1.164	1.208	1.131	11.92	12.93	11.01
COOH	288.93	289.07	289.03	1.164	1.208	1.131	2.52	3.26	4.41
				N1s					
$N_{non\ pr.}$	399.99	400.03	400.05	1.399	1.376	1.305	85.47	82.94	91.66
$N_{pr.}$	401.92	401.7	401.6	1.399	1.376	1.305	14.53	17.06	8.34
				O1s					
C = O, P = O	531.29	531.26	531.57	1.548	1.469	1.684	40.31	30.56	61.32
C = OH, C-O-C, P-OH	532.81	532.74	532.95	1.548	1.469	1.684	59.69	64.91	38.68
H-O-C		533.92			1.469			4.53	
				P2p					
P=O, P-O-	133.3	133.71	133.65	1.094	1.609	1.572	64.54	100	100
P=O, P-O-	134.23			1.094			35.46		

3.4.3 ATR-FT-IR

ATR-FT-IR was used to identify the biological functional groups within each cell surface structure. 1 mg mL^{-1} of whole cells, cell wall and cell membrane isolates from *P. putida* and *B. subtilis* were resuspended in 0.1 M NaCl at pH 3, 4.25 and 5.5 for 48 hours and lyophilised prior to analysis to establish any differences in functional group behaviour as a function of pH. These reference spectra were used to compare with subsequent data from the uranium biosorption experiments, in which the species of uranium is expected to change as a function of the pH range investigated (Chapter 4). After sample preparation, the live cells were referred to as whole cells. The observed infrared bands and corresponding wavenumbers for the functional groups identified within the whole cells of *D. radiodurans*, *P. putida* and *B. subtilis* and the cell wall and cell membrane fractions of the latter two are summarised in Table 10. The FT-IR spectra of the whole cell, cell wall and cell surface membrane of *P. putida* and *B. subtilis* at the selected pH values are shown in Figure 34 and Figure 35, respectively.

Table 10.Infrared absorption bands and their corresponding function group assignments in live cells, cell wall and membrane fractions. ν denotes stretching vibrations, δ denotes bending vibrations. Subscript $_s$ labels symmetric stretching and subscript $_{as}$ labels asymmetric stretching.

Wavenumber (σ (cm^{-1}))	Functional group assignment*
~ 3300	ν (O-H) of hydroxyl groups, ν (N-H) of amino groups
~ 3000 - 2850	ν_{as} (CH_3), ν_{as} (CH_2) and ν_s (CH_2) from lipids
~ 1740 - 1720	ν_s (C=O) from esters in lipids, stretching of C=O from carboxylic acids
~ 1650	ν (C=O) from proteins (Amide I)
~ 1540	δ (N-H) from proteins (Amide II)
~ 1470 - 1450	δ_s (CH_2) from lipids and fatty acids
~ 1420 - 1380	ν_s (COO^-) from proteins
~ 1320	ν (C-N) from proteins
~ 1240 - 1220	ν_{as} (PO_2) from DNA, phospholipids and phosphorylated biopolymers
~ 1175	ν_s (PO_2) from DNA, phospholipids and phosphorylated biopolymers
~ 1080 - 1040	ν_s (PO_2, PO_3^{2-}) from DNA, phospholipids and phosphorylated biopolymers; ν (C-OH, C-0-C, C-C) from polysaccharides
~ 976	ν_s (PO_2) from DNA, phospholipids and phosphorylated biopolymers
~ 915 - 925	ν (U-O_{ligand}) from uranium following biomass accumulation.

* Functional group assignment is based on (Ojeda et al., 2009), (Baker et al., 2014), (Parikh and Chorover, 2006), (Alessi et al., 2014), (Ojeda et al., 2008a), (Jiang et al., 2004), (Kamnev et al., 1999), (Shakirova et al., 2013), (Lumetta et al., 1999), (Kazy et al., 2009) and (Yagoubi et al., 2013).

In comparison to whole *P. putida* cells (Figure 34), the cell wall isolates exhibited differences in adsorption bands that were attributed to the components of a Gram-negative cell wall. Increases in the intensity of adsorption bands between 3000 – 2800 cm^{-1} were observed, corresponding to the vibrational stretching of CH_3 and CH_2 from fatty acids and lipids, characteristic of those present within the outer membrane of the gram-negative cell wall (Ojeda et al., 2009, Baker et al., 2014). The additional shoulder observed at 1723 - 1734 cm^{-1}, that was not present in whole cell spectra, was due to the vibrational symmetric stretching of the carbon oxygen (C=O) bond from the increased relative abundance of lipids (Ojeda et al., 2009). Changes in adsorption band position, shape and increases in intensity of the bands corresponding to phosphate and C-OH, C-O-C, C-C groups associated with polysaccharides suggested an increase in the concentration of the functional groups within the cell wall biomass compared to whole cells. These changes could have been due to the presence of increased concentrations of polysaccharides and phosphate groups from the concentrating of the thin peptidoglycan layer, lipopolysaccharides (LPS) and the outer membrane phospholipids during the cell fractionation process (Parikh and Chorover, 2006, Baker et al., 2014).

The increase in absorption intensity between 3000 - 2800 cm^{-1} (attributed to CH_3 and CH_2 vibrational stretching) indicated the presence of a lipid-rich isolate attributed to the phospholipids within the cell membrane (Baker et al., 2014, Kamnev et al., 1999, Shakirova et al., 2013). Furthermore, additional adsorption band at 1724 - 1740 cm^{-1} (pH 3 – pH 5.5) was attributed the vibrational stretching of the C=O lipid bond that was not present in whole cells (Ojeda et al., 2009). This additional peak had a greater intensity than the peak observed for the *P. putida* cell wall isolates since the membrane fraction contained a greater relative abundance of lipids than that of the Gram-negative cell wall. The presence of a phospholipid-rich isolate was further characterised by an increase in the intensity of absorption bands at ~ 1232 cm^{-1} from the phosphate asymmetric stretching compared to whole cells (Shakirova et al., 2013, Baker et al., 2014). For whole cells, the adsorption band intensity $\nu_{as}(PO_2)$ increased as the pH increased from 3 to 5.5, respectively. In the cell membrane isolates, the absorption band intensity was greater between pH 3 – 5.5. This increase in absorbance was due to a higher concentration of phospholipids in cell membrane isolates in comparison to whole cells.

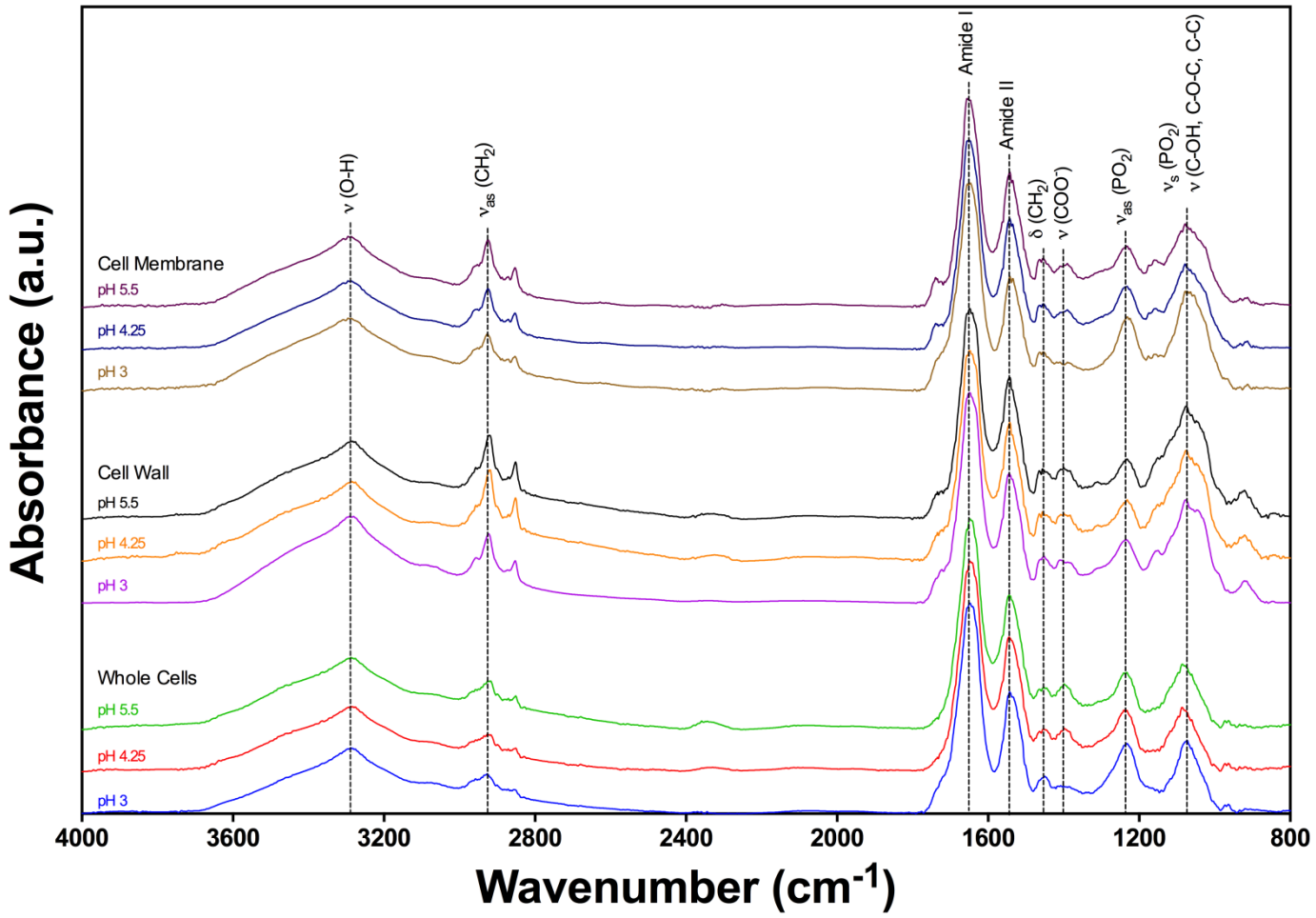

Figure 34. FTIR comparison spectra of the whole cells, cell wall and cell membrane isolates of *P. putida* as a function of pH.

There were differences between the spectra of the whole cells of *B. subtilis* and their cell wall isolates (Figure 35). The greatest difference was in the region of 1080 – 1040 cm^{-1}, corresponding to the absorption bands associated with the vibrational stretching of C-OH, C-O and C-C of carbohydrates. The functional group absorption band associated with carbohydrates within whole *B. subtilis* cells varied in position between 1060 – 1063 cm^{-1} and decreased in adsorption intensity as the pH increased from 3 to 5.5. This absorption band was between 1051 – 1052 cm^{-1} within the cell wall isolates and was noticeably greater in intensity between pH 3 and 5.5. This increase in intensity was due to an increased concentration of carbohydrates (i.e. peptidoglycan) within the cell wall isolates in respect to concentration of proteins in comparison to the concentrations found in whole cells, following normalisation of all spectra with the Amide I absorption band, the adsorption band characteristic of functional groups associated with bacterial proteins (Jiang et al., 2004). Additionally, a shoulder at 1724 – 1740 cm^{-1} in cell wall isolates was attributed to the vibrational stretching of C=O groups in lipoteichoic acids following fractionation (Jiang et al., 2004).

As with *P. putida*, the *B. subtilis* cell membrane isolates were characterised by an increase in intensity of the adsorption bands within the lipid-rich 3000 – 2800 cm^{-1} region. This indicated a greater relative abundance of phospholipid-rich biological molecules, compared to whole cells. The additional peak at 1739 cm^{-1} attributed to the ν_s (C=O) of lipids further supported this (Baker et al., 2014, Kamnev et al., 1999, Shakirova et al., 2013). Small changes in the adsorption band position and intensity within the 1470 – 1350 cm^{-1} region suggested changes in protein and lipid content, from the presence of a greater abundance of membrane-associated proteins such as porins (Wang and Chen, 2009). There was a decrease in absorption intensity of the carbohydrate associated functional group absorption band at ~1065 cm^{-1} in the cell membrane isolates compared to whole *B. subtilis* cells. The majority of carbohydrate like compounds was within the rich peptidoglycan cell wall of *B. subtilis* cells and not in cell membrane fractions. Therefore, we see a decrease in the functional groups associated with ν (C-OH, C-0-C, C-C) from carbohydrates (Baker et al., 2014, Ojeda et al., 2009, Shakirova et al., 2013). Unsurprisingly, there was a decrease in intensity of the absorption band associated with phosphate vibrational asymmetric stretching (~ 1220 – 1230 cm^{-1}). This difference in intensity was due to a larger quantity of phosphate functional groups within whole cells (i.e. cell wall and intracellular components) than just from phospholipids from the *B. subtilis* cell surface membrane.

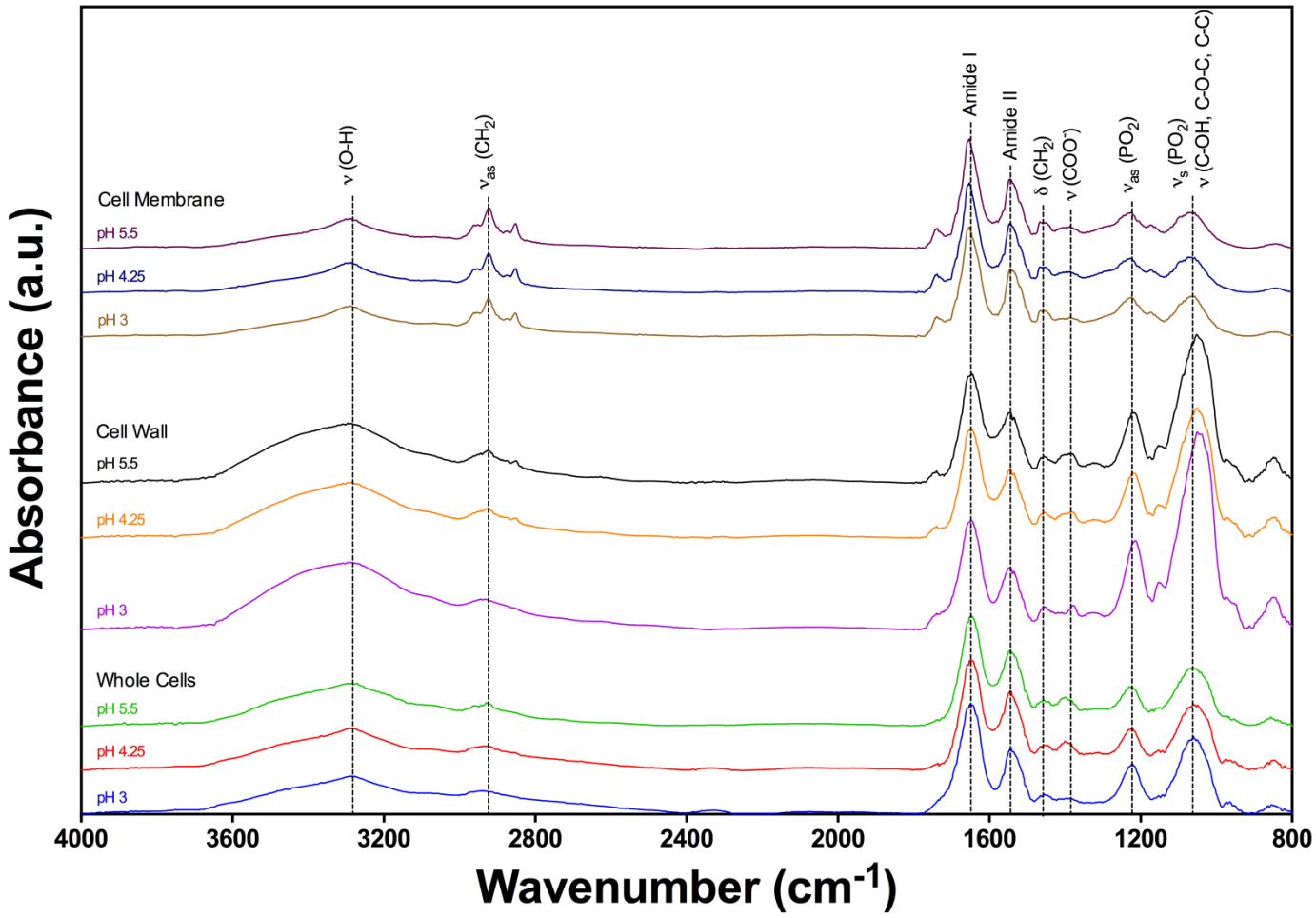

Figure 35. FTIR comparison spectra of the whole cells, cell wall and cell membrane isolates of *B. subtilis* as a function of pH.

3.5 Conclusions

The current work described the spectroscopic characterisation of cell surface architecture using XPS and ATR-FT-IR. The fractionation of cells from the bacteria studied was achieved using a French pressure cell was capable of breaking up 100 % of *P. putida* 33015 and 95 % of *B. subtilis* 168 cells. *D. radiodurans* R1 could not be fractionated despite the numerous cell disruption techniques explored, and therefore, only whole cells were characterised.

XPS analysis and subsequent calculations (Equation 8 - Equation 10) indicated a high proportion of peptide and hydrocarbon-like material within the Gram-negative cell wall of *P. putida* (Table 7) compared to the high proportion of polysaccharide-like material isolated from the cell walls of the Gram-positive *B. subtilis* (Table 9) following cell fractionation. A similar macromolecular composition was apparent for cell surface membrane isolates from both bacteria. These isolates were composed predominantly of peptide and hydrocarbon-like material. ATR-FT-IR analysis complemented the XPS data obtained and confirmed the differences in macromolecular composition of fractions due to changes in adsorption band shape, height and position which were attributed to the functional groups associated with specific biomolecules (Figure 34 - Figure 35).

The difference in macromolecular composition of purified cell wall and membrane structures from both strains suggested that the application of whole cells for the spectroscopic characterisation of the bacterial cell surface is an inaccurate approach due to interferences from intracellular components. Therefore, purification of cell surface structures is required to obtain a more reliable result. The difference in molecular composition of whole cell, cell wall and membrane isolates has implications for their use in uranium biosorption studies, in which the capacity for uranium retention using whole cells may be inappropriately determined due to a lack of interactions with intracellular components. Therefore, the utilisation of cell surface may be deemed more appropriate when determining mechanistic processes involved in uranium biosorption as it predominantly occurs at the cell surface.

Chapter 4: Understanding the role of cell surface structures in uranium biosorption.

4.1 Abstract

Living and dead bacterial biomass has uranium-sequestering capabilities either through the biosorption of aqueous uranium phases or through the precipitation of uranium minerals adhered to the cell surface. Due to the macromolecular complexity of the bacterial cell surface that varies between cell type, it is difficult to decide whether this process predominantly occurs at the outermost cell wall or can be associated with other cell surface structures such as the cell surface membrane. Here we report the findings of uranium interactions with the live cells of *D. radiodurans, P. putida, B. subtilis* and extracted cell surface structures of the latter two strains, through uranium biosorption experiments and Attenuated Total Reflectance- Fourier Transform Infrared (ATR-FT-IR) spectroscopy.

Cell wall isolates and lysed cells of both strains exhibited a higher uranium biosorption capacity than those of live cells and cell surface membrane isolates between pH 3 and 5.5, due to an increase concentration of uranium favourable functional groups. Deprotonation of functional groups raised the level of the uranium biosorption for all structures investigated as the pH increased. The cell walls of *P. putida* and *B. subtilis* retained 2.22 and 2.93 mol U(VI) kg^{-1} biomass from 4 mM uranium solution at pH 5.5. ATR-FT-IR indicated that phosphate and carboxyl groups associated with the macromolecular constituents (such as proteins and phosphorylated biopolymers) of each cell surface structure were responsible for uranium retention.

It can be concluded that uranium biosorption onto cell surface structures occurs predominantly at the bacterial cell wall, since they are the outermost layer of the cell surface. The bacterial cell surface and associated structures have a greater uranium biosorption capacity as the pH increases, due to deprotonation of interactive groups that can then readily interact with the positive charged uranium species.

4.2 Introduction

Uranium retention occurs predominantly at the bacterial cell surface since aqueous uranium species can readily interact with the outermost layers of bacteria. This is seen through the use of Transmission Electron Microscopy (TEM) in a number of documented cases. Numerous strains have displayed a capability to sequester uranium, whether through a process of biosorption or biomineralisation, at the cell surface. The Gram-positive strains *Bacillus sphaericus* JG-A12 and *Paenibacillus* sp. JG-TB8 sequestered uranium at the cell surface through a process of biosorption and biomineralisation, respectively (Merroun et al., 2005, Reitz et al., 2014). However, due to the poor resolution of the results obtained by TEM, it is difficult to distinguish whether this process happened at the outermost cell wall or whether it could be associated with other structures close to the cell surface. Uranium deposition onto the cell surface of the Gram-negative strains *Sphingomonas* sp. S15-S1 and *Rhodopseudomonas palustris* indicated uranium interactions with the outer membrane of the Gram-negative cell wall as well as with the cell surface membrane (Merroun et al., 2011, Llorens et al., 2012). Furthermore, the prolonged exposure of *Pseudomonas aeruginosa* J007 to uranium indicated a high tolerance to uranium due to its deposition onto the outer cell surface components (Choudhary and Sar, 2011).

Despite the large amount of evidence for uranium retention at the cell surface, the contribution of each cell surface structure and components to the mechanism of uranium removal is unknown. Many studies have investigated whole bacteria to sequester U(VI) from acidic environments. Understanding the individual role of each cell surface structure and how their macromolecular compositions aid in the retention of uranium is important in fully clarifying the biosorption and biomineralisation processes exhibited by whole bacteria. Previous studies have worked solely on whole cells and purified polymers commercially available (Barkleit et al., 2008, Barkleit et al., 2009, Barkleit et al., 2011). To date, no studies have been performed using cell surface structure isolates.

This work aimed to demonstrate the roles of cell wall and cell membrane structures from *Pseudomonas putida* 33015 and *Bacillus subtilis* 168 in uranium retention from acidic environments and compare them to the behaviour of whole cells. A comparison of the efficiency of the process was also made to whole *Deinococcus radiodurans* R1 cells as the cell wall and membrane from this strain could not be isolated (Chapter 3).

The amount of uranium removed by each cell surface structure was used to determine the maximum retention capacity, thus defining which structures are more influential in uranium removal. The speciation of U(VI) in solution depends on concentration, pH, ionic strength and temperature. Investigating uranium interactions with bacterial biomass within the pH range of pH 3 to 5.5 is important due to changes in uranium speciation and surface deprotonation of the bacterial biomass. At below pH 3, the bacterial cell surface has a neutral to positive charge due to protonation of functional groups (Harden and Harris, 1953, Fein et al., 1997, Borkowski et al., 2015). Additionally, the main species of uranium is the positively charged UO_2^{2+} ion. Therefore, at pH values below 3, it can be hypothesised that there are few interactions due to the positive charges of both reactants. ATR-FTIR was used to spectroscopically determine the interactions involved following uranium exposure. The novelty of this works resides in the fact that uranium interactions with bacteria have only been studied in a whole cell system or individual cell associated biopolymers. The results from this study will give insight into the specific role of bacterial cell wall and membrane structures in uranium retention and the processes involved.

4.3 Experimental procedures

4.3.1 Bacteria, growth conditions and cell fractionation

P. putida 33015, *D. radiodurans* R1 and *B. subtilis* 168 were cultured as described in section 3.3.1. Cell surface structures from *P. putida* 33015 and *B. subtilis* 168 were isolated as described in section 3.3.2.

4.3.2 Uranium biosorption and orthophosphate release

1 mg mL^{-1} of biomass was incubated with 0.5 mM uranium at pH 3 and 5.5 for 48 hours. Sub-samples were removed periodically to determine the rate of uranium removal as a function of time. To determine the maximum uranium biosorption and retention capacity of each cell fraction as a function of pH, 1 mg mL^{-1} of biomass was incubated with increasing concentrations of uranium (0.125 mM to 4 mM) at pH 3, 4.25 and 5.5 at 25 °C in the presence of 0.1 M NaCl. Following uranium biosorption, the biomass was removed from solution (10,000 *g*, 4 °C, 10 min) and the remaining uranium left within the supernatant was acidified using 1 % HNO_3 and analysed using a Spectro-Ciros-Vision ICP - AES. Instrument parameters were set at 1400 watts with a coolant flow of 12.00 litres/minute, auxiliary flow at 1.00 litre/minute, nebuliser flow at 0.85 litres/minute and a pump speed during analysis set at 1 mL/minute.

Orthophosphate released into the supernatant from the lysis of live cells and breakdown of cell surface structures was quantified using a modified ammonium molybdate method, as described previously (section 2.3.3) to determine any uranium retention by released orthophosphate.

4.3.3 Uranium precipitate characterisation by XRD

To determine whether any minerals were formed from the interactions of uranium with released orthophosphate, XRD patterns of the lyophilised biomass were recorded as described previously, section 2.3.7.

4.3.4 Uranium binding to biomass analysis using FT-IR

Biomass that had retained uranium was recovered by centrifugation (10,000 *g*, 4 °C, 10 min), washed three times using 0.1 M NaCl and lyophilised (Alpha 1-2 LD Plus freeze dryer). Measurements were obtained by Attenuated Total Reflectance (ATR) – FT-IR as described in section 3.3.4.

4.4 Results and Discussion

4.4.1 Uranium biosorption by bacterial biomass

The biosorption of uranium to bacterial biomass (q_e) was investigated as a function of time, pH and initial uranium concentration. The capacity, q_e, for both live cells and cell surface structures was calculated using the following equation;

$$q_e = \frac{(C_e - C) \times V}{m}$$ Equation 11

C_e and C are the uranium concentrations in solution before and after biomass interaction respectively, V is the reaction volume (mL) and m is the biomass weight (mg).

4.4.1.1 Uranium biosorption kinetics

A kinetics experiment was performed to determine the optimum uranium saturation time for concentration-dependent biosorption experiments. 1 mg mL^{-1} of live cells were incubated with 0.5 mM uranium at pH 3 and 5.5. Sub-samples were collected at timed intervals (up to 48 hours) and the remaining uranium quantified. Figure 36 shows the kinetics curve obtained up to two hours.

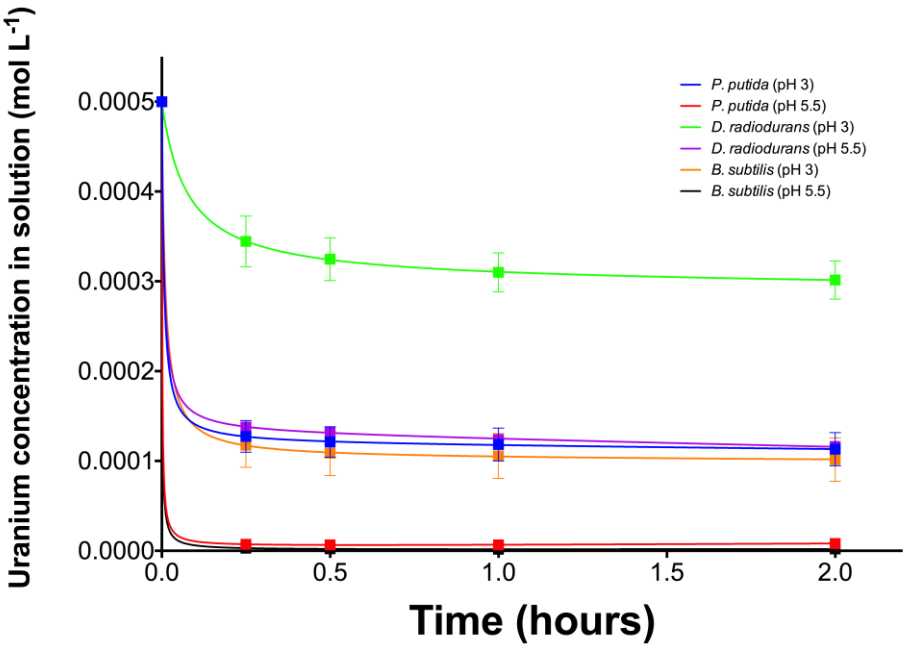

Figure 36. Kinetics of the uranium removal from solution using 1 mg mL^{-1} live cells as a function of time, with a starting uranium concentration of 0.5 mM.

Results indicated that maximum uranium binding with live cells occurred almost instantly, with little uranium removed thereafter from solution, by all three strains at

both pHs after two hours. There were small differences between the bacteria and pH range studied. The rate of removal at pH 5.5 was much faster for *P. putida* and *B. subtilis*, with most of the uranium removed within the first 10 minutes, compared to the two hours it took at pH 3. The rate of uranium retention of the strains investigated was similar to those of previous studies. Uranium biosorption to *Chlorella vulgaris* and *Acidithiobacillus ferrooxidans* both exhibited a pseudo-first order reaction with the majority of uranium removed in one hour (Amini et al., 2013, Romero-Gonzalez et al., 2016). The biosorption or uranium to *Citrobacter freudii* was described as a pseudo-second order reaction with uranium maximum retention observed after three hours (Xie et al., 2008). A faster rate of uranium retention was observed for *Micrococcus luteus* and a *Pseudomonas* strain in which maximum retention was observed within the first thirty minutes and was not given a reaction order (Nakajima and Tsuruta, 2004, Sar and D'Souza, 2001). The speed of this uranium retention was due to the metabolism-independent biosorption process, with electrostatic interactions between the positively charged U(VI) species and negatively charged functional groups within the bacterial biomass playing an important role in the biosorption of uranium from solution (Ferris and Beveridge, 1986, Reitz et al., 2014). The rate of removal by *D. radiodurans* within the experimental conditions studied was much slower, with removal still occurring after a 24-hour period. The maximum removal was observed after 48 hours and no further removal observed after this time period. Differences in cell surface structures of the three strains studied could affect the rate and amount of uranium removed between the strains due to differences in the functional groups responsible for uranium biosorption. Due to the fast nature of this process, it was difficult to fit the data to a reaction order, as evident in Appendix Figure 6 and Appendix Figure 7.

4.4.1.2 Uranium biosorption capacities

The biosorption capacity of live cells and cell surface structures to retain uranium from solution was studied by incubating 1 mg mL^{-1} biomass with solutions of increasing uranium concentration (0.125 – 4 mM) at pH 3, 4.25 and 5.5 for 48 hours at 30 °C. The results obtained for the live cells studied are found in Figure 37 and the fractions from isolates of both strains in Figure 38. For each data set, the equilibrium distribution constant of uranium between the aqueous solution and biomass was attempted by calculating the Langmuir and Freundlich distribution coefficients, Table 11 - Table 12. Langmuir and Freundlich isotherm fittings are displayed in Appendix Figure 8 - Appendix Figure 10.

For all cell types and cell surface structures studied, a higher removal of uranium from solution was observed as the pH of the solution increased from 3 to 5.5. The speciation of U(VI) in solution in the presence of 0.1 M NaCl varied as a function of pH, Appendix Table 6. At pH 3, the dominant U(VI) species in solution is the highly mobile UO_2^{2+} ion (~ 93 %) within the concentration range studied. At pH 4.25, UO_2^{2+} was still the dominant species, however its abundance decreased from 84.88 % to 64.28 % as the uranium concentration increased from 0.125 to 2 mM. Other species present included UO_2OH^+ and $(UO_2)_3(OH)_2^{2+}$, with the latter increasing to 21.35 % as the uranium concentration increased to 2 mM. At pH 5.5, there was a decrease in the amount of UO_2^{2+}. As the uranium concentration increased from 0.125 to 4 mM, the amount decreased from 6.67 to 0.66 %. The dominant species of uranium at pH 5.5 were $(UO_2)_3(OH)_5^+$ and $(UO_2)_4(OH)_7^+$, with the former decreasing and latter increasing as the uranium concentration increased in solution.

The pH range studied also had an effect on the speciation of functional groups on the bacterial cell surface and hence, affected the surface charge. The point of zero charge (pzc), at which the bacterial cell surface of whole *P. putida* and *B. subtilis* cells exhibit a net neutral charge, was calculated previously at pH 2.8 and 2.2 respectively (Harden and Harris, 1953, Fein et al., 1997, Borkowski et al., 2015). Therefore, at pH values higher than 3, the overall net-surface charge was negative due to deprotonation of functional groups on the surface

At pH 5.5 the predominant uranium species exhibited an overall positive charge within the uranium concentration range studied. Coupled with an increase in the number of deprotonated functional groups on the cell surface and isolated surface structures, it would be expected that there was a larger amount of uranium retained as the pH increased. Numerous studies have reported a higher biosorption capacity for whole cells at circumneutral pH. Similar findings using live *B. subtilis* were previously reported, suggesting a higher uranium retention from solution at pH 5 to 7 through complexation with the cell wall of live cells (Gorman-Lewis et al., 2005). However, no findings have been reported on purified cell wall isolates from this strain until this current study. Furthermore, three *Microbacterium* strains isolated from the Siberian radioactive waste depository Tomsk-7 in Russia (~ 230 mg U g^{-1} dry biomass) and two indigenous *Bacillus thuringiensis* strains (~ 400 mg U g^{-1} dry biomass) exhibited a higher uranium biosorption capacity as the pH of the solution increased towards circumneutral conditions

(Nedelkova et al., 2007, Pan et al., 2015). Similarly, the yeast *Saccharomyces cerevisiae* exhibited a higher uranium removal at pH 5.5, where approximately 80 % of 1 mg mL^{-1} U(VI) was removed from solution by 0.03 g L^{-1} dry biomass (Lu et al., 2013). It has been suggested that microbial phosphatase activity contributes to uranium sequestration at circumneutral pH within live cells through biomineralisation. However, due to the speed of this sequestration process with live cells, it was likely to be a process of biosorption because microbial phosphatase activity has been measured over a greater and significant period of time (Merroun et al., 2011, Reitz et al., 2014).

With regard to uranium biosorption as a function of cell type, the live cells of *B. subtilis* retained the largest quantity of uranium from solution within the pH range studied. At 2 mM, live *B. subtilis* cells retained 0.62, 0.93 and 1.80 mol U(VI) kg^{-1} biomass at pH 3, 4.25 and 5.5, respectively. This was substantially greater than live *P. putida* and cells that retained 0.59, 0.73 and 1.47 mol U(VI) kg^{-1} biomass and *D. radiodurans* that removed 0.47, 0.58 and 1.28 mol U(VI) kg^{-1} biomass from 2 mM U(VI) solution at pH 3, 4.25 and 5.5, respectively, Figure 37. Since the pzc values for *B. subtilis* and *P. putida* are 2.0 and 2.8, within the pH range studied, the net negative charge of the bacterial cell surface of *B. subtilis* will be greater than that for *P. putida*. This would result in a greater number of electrostatic interactions between deprotonated functional groups and positively charged U(VI) species in the former case. Furthermore, differences in the composition of the bacterial cell surface and differences in the number of functional groups could be attributed to differences in uranium retention as a function of cell type.

Uranium biosorption has been described in terms of interactions with phosphate, hydroxyl, carboxyl and amino groups (Newsome et al., 2014). The bacterial cell surface of *B. subtilis* is composed predominantly of polysaccharides, lipoteichoic acids and peptides, contributing to the increased number of phosphate hydroxyl, carboxyl and amino groups (Ahimou et al., 2007). The cell surface of *P. putida* contains large quantities of phospholipids and peptides, with the former increasing the number of ester groups and phosphate. Ester groups have not been shown to readily interact with uranium from solution in previous studies. However, phosphate readily interacts with uranium (Merroun et al., 2011, Luetke et al., 2012, Llorens et al., 2012). A lack of phosphate within the bacterial cell surface of *D. radiodurans*, as indicated by XPS (Figure 30) suggested a lack of uranium-phosphate surface interactions at the outermost layer

of *D. radiodurans*. This lack of reaction could be responsible for the decrease in uranium retention from solution by *D. radiodurans*.

Differences in uranium removal were observed as a function of cell surface structure in comparison to whole cells. Like whole cells, the cell wall isolates of *B. subtilis* sequestered a larger quantity of uranium from solution than *P. putida* cell wall isolates. *B. subtilis* cell wall isolates removed 0.66, 0.92 and 1.91 mol U(VI) kg^{-1} biomass at pH 3, 4.25 and 5.5 respectively from 2 mM uranium solution. This removal increased to 2.93 mol U(VI) kg^{-1} biomass following suspension in 4 mM uranium solution at pH 5.5. By comparison, *P. putida* cell wall isolates removed 0.66, 0.87 and 1.77 mol U(VI) kg^{-1} biomass at pH 3, 4.25 and 5.5 from 2 mM uranium solution, respectively, increasing to 2.22 mol U(VI) kg^{-1} biomass in the presence of 4 mM U(VI) at pH 5.5. However, both cell wall structures exhibited a higher uranium retention capability than that of whole cells, likely due to the increased number of uranium favourable functional groups associated with the cell walls, as the bacteria are no longer intact. Therefore there was a greater surface area for uranium biosorption with cell wall isolates. Furthermore, with intact cells, there was little or no interaction with the intracellular components that contribute towards the bacterial dry weight, resulting in differences of retention of uranium between samples.

Overall, both cell wall isolates exhibited a higher uranium biosorption capacity than that of whole cells, due to the increased concentration of uranium favourable groups in the cell wall structures. Cell wall isolation led to a greater surface area exposure for interactions with U(VI) species in comparison with whole cells. These results demonstrated that accounting for the removal of U(VI) from solution using whole cell dry weight underestimates the capacity of these organisms to sequester uranium by their cell wall. Intracellular components of whole cells contribute to the dry weight but may not contribute to the retention of uranium, and hence result in a lower uranium capacity per kg of biomass. Using the cell fractionation approach provides a better approximation of the retention capacity from whole cells, based on the direct contribution from key cell surface components deemed responsible for uranium biosorption.

Differences in uranium retention were observed with cell membrane isolates from both strains of bacteria compared to that observed in live cells and cell wall isolates. *P. putida* cell membrane isolates retained 0.54, 0.72 and 1.51 mol U(VI) kg^{-1} biomass at pH 3, 4.25

and 5.5 from 2 mM uranium solution, respectively. This retention capacity increased to 1.81 mol U(VI) kg^{-1} biomass following suspension in 4 mM uranium solution at pH 5.5. By comparison, *B. subtilis* cell membrane isolates retained 0.42, 0.57 and 1.30 mol U(VI) kg^{-1} biomass at pH 3, 4.25 and 5.5 from 2 mM uranium solution, increasing to 1.72 mol U(VI) kg^{-1} biomass in the presence of 4 mM U(VI) at pH 5.5. This decrease in uranium retention with both cell membrane isolates could be attributed to the decrease in the number of uranium favourable and reactive functional groups. The major constituents of the cell surface membranes are phospholipids, of which phosphate groups would biosorb uranium, while the lipid groups are unreactive and not uranium. A decrease in the concentration of uranium favourable groups from other cell surface biomolecules such as polysaccharides, that were present within whole cell and cell wall isolates, would decrease the retention capacity of cell membrane isolates in comparison.

In comparison to live cells, dead cells exhibited a larger capacity for uranium retention from solution within the pH range studied. The dead cells and lysate of *P. putida* retained 0.61, 0.87 and 1.76 mol U(VI) kg^{-1} biomass from 2 mM uranium solution at pH 3, 4.25 and 5.5, respectively. Similarly, the dead cells and lysate of *B. subtilis* retained 0.66, 0.91 and 1.76 mol U(VI) kg^{-1} biomass from 2 mM uranium solution. In the presence of 4 mM uranium at pH 5.5, the retention capacity of dead *P. putida* and *B. subtilis* cells increased to 2.14 and 2.54 mol U(VI) kg^{-1} biomass, respectively. The dead cells exhibited a higher retention than live cells, similar to previous studies comparing live and dead biomass (Lu et al., 2013). This was due to increase in the availability of functional groups within the cell that are exposed to uranium following cell lysis (Merroun et al., 2011, Choudhary and Sar, 2011). However, the uranium retention capacity was much higher with cell wall isolates, because there was concentration of functional groups associated with the cell wall within these isolates that have been well documented to accumulate uranium within a whole cell system.

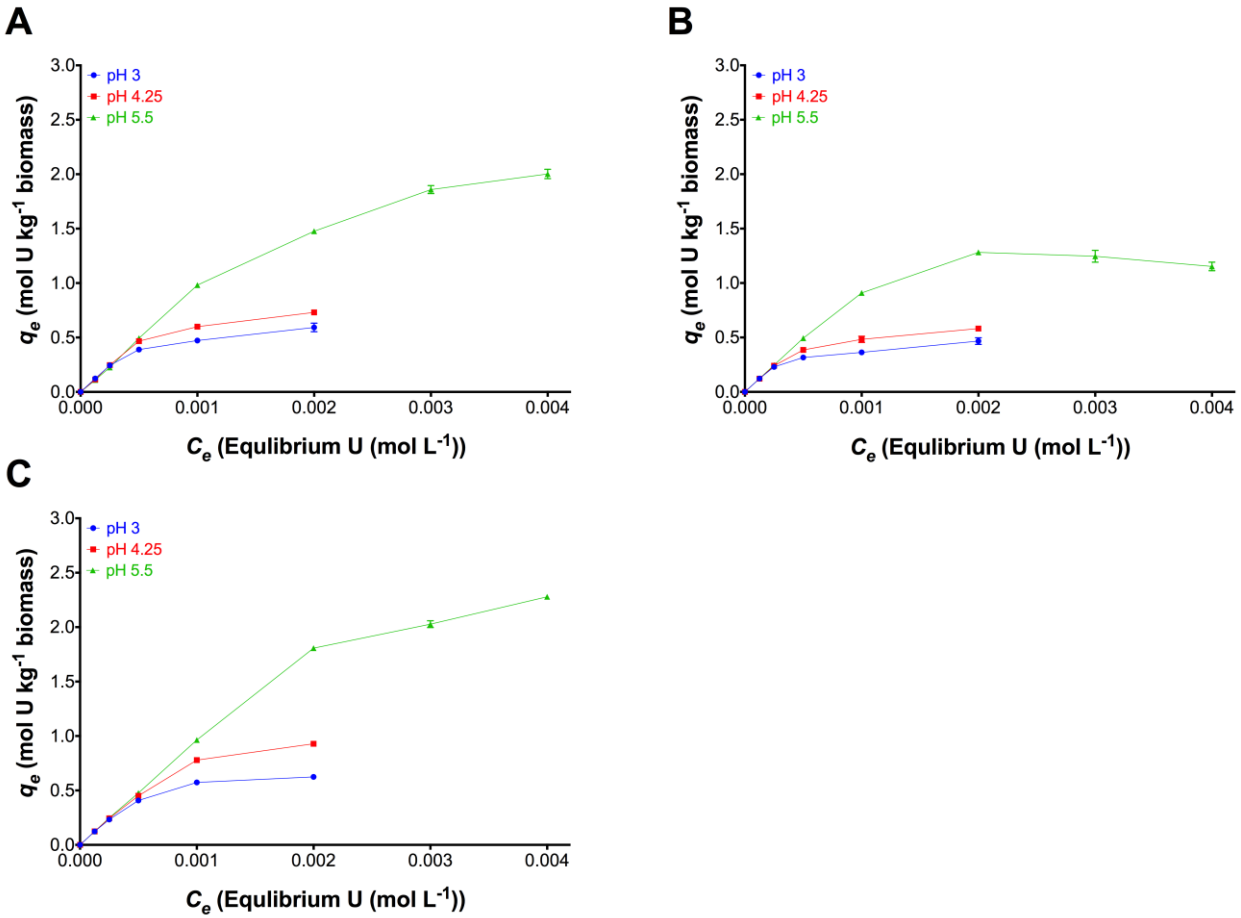

Figure 37. 48 hour uranium accumulation by 1 mg mL^{-1} live [A] *P. putida*, [B] *D. radiodurans* and [C] *B. subtilis* cells as a function of initial uranium concentration.

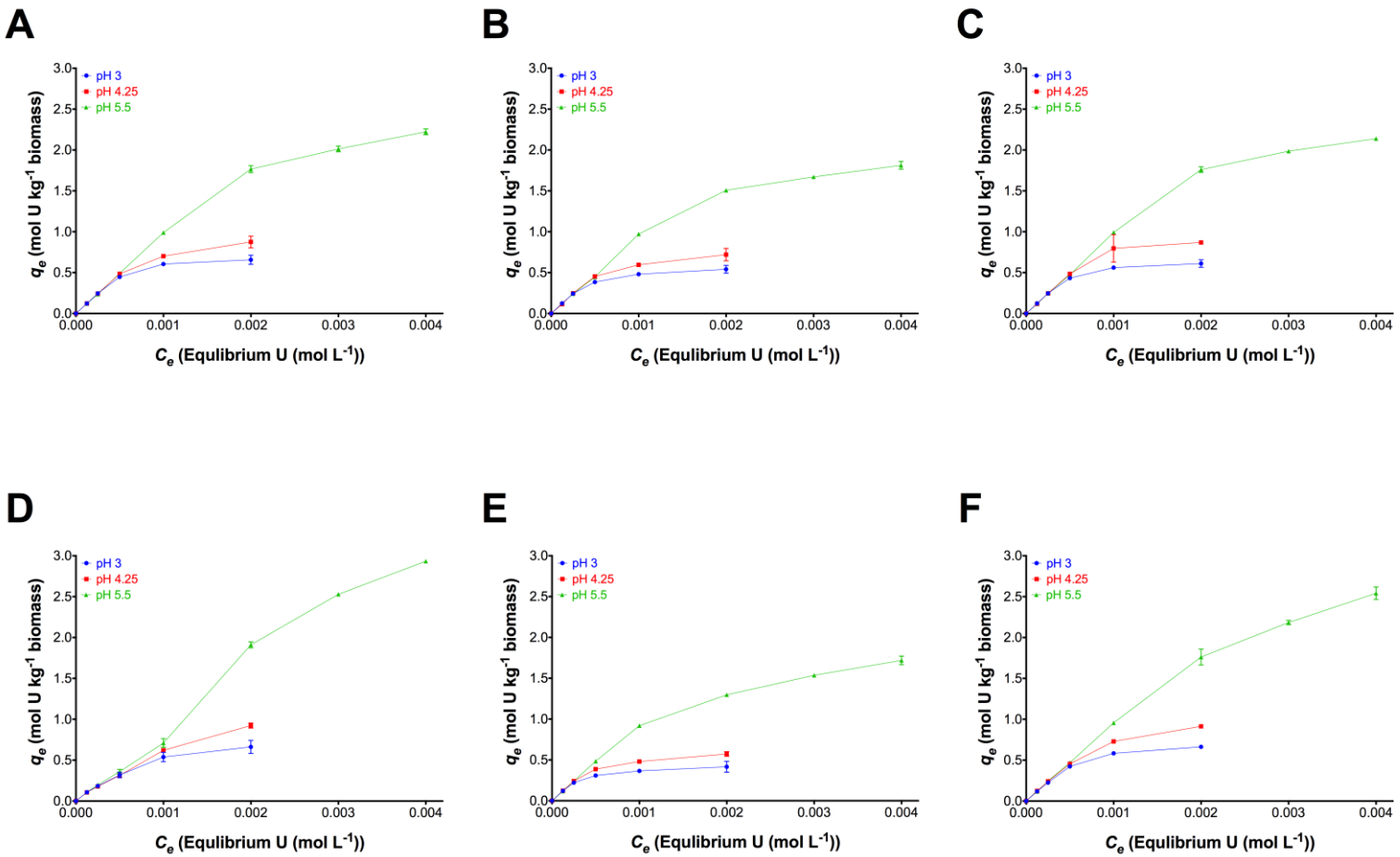

Figure 38. 48 hour uranium accumulation by 1 mg mL^{-1} of cell wall isolates, cell membrane isolates and dead cells from *P. putida* [A-C] and *B. subtilis* [D-F] as a function of initial uranium concentration.

The Langmuir isotherm was applied to the uranium biosorption data by plotting the inverse of C_e vs. q_e. The linear regression equation was applied to the Langmuir equation, Equation 12.

$$\frac{1}{q_e} = \frac{1}{K_L \times Q_{max}} \times \frac{1}{C_e} + \frac{1}{Q_{max}} \quad \text{Equation 12}$$

Using the linear regression in which the gradient (m) is $1/(K_L \times Q_{max})$ and the intercept (b) is $1/Q_{max}$, Q_{max}, K_L and K_D were calculated. Q_{max} was the maximum adsorption concentration of sorbate, K_L was the Langmuir constant and K_D the dissociation constant.

$$Q_{max} = \frac{1}{\mathbf{b}} \quad \text{Equation 13}$$

$$K_L = \frac{1}{\mathbf{m} \times Q_{max}} \quad \text{Equation 14}$$

$$K_D = K_L \times Q_{max} \quad \text{Equation 15}$$

Using these values, the moles of uranium accumulated per kilogram of biomass from an initial known concentration of uranium were calculated, Equation 16.

$$q_e = \frac{Q_{max} \times K_L \times C_e}{1 + K_L \times C_e} \quad \text{Equation 16}$$

The Freundlich constants were calculated by plotting the logarithmic form of C_e vs. q_e. The corresponding linear regression can be applied to the following equation, Equation 17, from which the n_i and the Freundlich constant (K_F) can be inferred.

$$\log(q_e) = n_i \log(C_e) + \log K_F \quad \text{Equation 17}$$

Using these values, the distribution constant from the Freundlich isotherm was calculated, Equation 18, in which C_{max} was the maximum uranium concentration used within the isotherm range studied.

$$K_D = K_F \times C_{max}^{n_i - 1} \quad \text{Equation 18}$$

Finally, the free energy change of adsorption, $\Delta G°$, was calculated where R was the universal gas constant (8.314 J mol^{-1} K^{-1}), T was temperature (Kelvin) and K_D was the equilibrium constant, Equation 19.

$$\Delta G° = -RT \ln K_D$$ Equation 19

The Langmuir and Freundlich isotherm constants calculated for each cell type and associated cell surface components, as a function of pH, are presented in Table 11 and Table 12, respectively.

Table 11. Constants obtained from Langmuir isotherms, at 298.15 K.

Fraction Type	pH	R^2	Q_{max} mol^{-1} kg	K_L L^{-1} mol	K_D K_L X Q_{max}	$\Delta G°$ $kJ\ mol^{-1}$
Pseudomonas putida live cells	3	0.989	0.934	1254.277	1171.783	-17.517
	4.25	0.986	1.967	510.700	1004.722	-17.136
	5.5	0.998	20.284	44.291	898.392	-16.858
Deinococcus radiodurans live cell	3	0.985	0.590	2176.516	1284.687	-17.745
	4.25	0.989	0.950	1207.043	1147.052	-17.464
	5.5	0.995	3.053	339.519	1036.699	-17.213
Bacillus subtilis live cell	3	0.995	1.127	1001.806	1128.796	-17.424
	4.25	0.998	2.440	432.566	1055.298	-17.257
	5.5	1.000	9.050	111.414	1008.268	-17.144
Pseudomonas putida cell wall	3	0.990	1.397	789.677	1102.901	-17.367
	4.25	0.995	2.322	453.368	1052.632	-17.251
	5.5	0.999	10.741	91.266	980.296	-17.075
Bacillus subtilis cell wall	3	0.998	1.020	929.648	948.137	-16.992
	4.25	0.993	1.403	635.853	892.299	-16.841
	5.5	0.996	6.588	130.435	859.254	-16.748
Pseudomonas putida cell membrane	3	0.987	0.875	1364.038	1193.175	-17.562
	4.25	0.985	1.875	53.684	100.644	-11.432
	5.5	0.999	4.686	21.678	101.585	-11.455
Bacillus subtilis cell membrane	3	0.987	0.553	231.157	127.747	-12.023
	4.25	0.989	0.919	127.324	117.069	-11.807
	5.5	0.998	5.339	181.951	971.440	-17.052
Pseudomonas putida dead cells	3	0.988	1.185	95.769	113.443	-11.729
	4.25	0.993	3.203	31.523	100.969	-11.440
	5.5	0.999	15.244	62.829	957.763	-17.017
Bacillus subtilis dead cells	3	0.995	1.327	79.314	105.274	-11.543
	4.25	0.998	2.249	46.904	105.496	-11.549
	5.5	0.999	25.063	37.827	948.047	-16.992

Table 12. Constants obtained from Freundlich isotherms, at 298.15 K.

Fraction Type	pH	R^2	n_i L kg^{-1}	K_F mol kg^{-1}	C_{max} mol L^{-1}	K_D $K_F X C_{max}^{n-1}$	$\Delta G°$ kJ mol^{-1}
Pseudomonas putida live cells	3	0.931	0.548	20.55	0.002	340.56	-14.70
	4.25	0.925	0.663	55.16	0.002	447.31	-15.38
	5.5	0.978	0.850	271.27	0.004	621.00	-16.21
Deinococcus radiodurans live cell	3	0.924	0.451	8.41	0.002	255.21	-13.74
	4.25	0.928	0.553	21.13	0.002	340.31	-14.45
	5.5	0.920	0.658	69.10	0.004	457.17	-15.18
Bacillus subtilis live cell	3	0.931	0.597	31.40	0.002	383.51	-14.75
	4.25	0.967	0.748	117.22	0.002	560.18	-15.69
	5.5	0.986	0.865	326.44	0.004	689.42	-16.20
Pseudomonas putida cell wall	3	0.915	0.614	37.41	0.002	411.65	-14.92
	4.25	0.955	0.719	91.94	0.002	526.79	-15.54
	5.5	0.983	0.867	329.46	0.004	685.12	-16.19
Bacillus subtilis cell wall	3	0.980	0.698	51.68	0.002	338.64	-14.44
	4.25	0.995	0.805	145.68	0.002	489.74	-15.35
	5.5	0.993	0.999	792.32	0.004	796.71	-16.56
Pseudomonas putida cell membrane	3	0.909	0.523	16.70	0.002	323.35	-14.33
	4.25	0.927	0.658	52.41	0.002	439.53	-15.09
	5.5	0.975	0.800	187.20	0.004	565.42	-15.71
Bacillus subtilis cell membrane	3	0.903	0.429	6.87	0.002	238.34	-13.57
	4.25	0.925	0.543	19.60	0.002	335.66	-14.42
	5.5	0.973	0.775	150.11	0.004	519.92	-15.50
Pseudomonas putida dead cells	3	0.908	0.581	28.02	0.002	379.86	-14.72
	4.25	0.941	0.744	111.84	0.002	548.27	-15.63
	5.5	0.981	0.863	315.21	0.004	672.72	-16.14
Bacillus subtilis dead cells	3	0.935	0.635	42.13	0.002	406.62	-14.89
	4.25	0.969	0.737	105.75	0.002	541.49	-15.60
	5.5	0.992	0.901	426.87	0.004	735.76	-16.36

Fitting the uranium biosorption data indicated discrepancies in the calculated values obtained from the Langmuir and Freundlich adsorption models to describe the equilibrium distribution of uranium with the aqueous solution and sorbent material within this experimental study. The uranium biosorption data indicated that the lysed cells of *B. subtilis* and associated cell wall isolates exhibited the highest uranium biosorption capacity (Figure 38D and Figure 38F). Fitting the uranium biosorption to both adsorption models indicated a better fit using the Langmuir model in comparison to the Freundlich model. The R^2 values

obtained from plotting the inverse of C_e vs. q_e (Langmuir-Table 11) were closer to 1 in comparison to those obtained from plotting the logarithmic form of C_e vs. q_e (Freundlich-Table 12).

However, examining the data obtained from the Langmuir adsorption model calculations, Table 11, revealed inaccuracies in the results obtained in comparison to those displayed within the raw data (Figure 37 - Figure 38). The maximum uranium retention (Q_{max}) calculations suggested that lysed *B. subtilis* cells and live *P. putida* cells had a higher uranium retention capacity, with a Q_{max} of 25.063 and 20.284 mol^{-1} kg at pH 5.5, respectively. This contradicted the uranium biosorption data.

The Langmuir constants (K_L) and Gibbs free energy values ($\Delta G°$) were calculated to determine which adsorption reactions were more spontaneous and energetically favourable. For the majority of the biomass isolates investigated, a greater K_L and more negative $\Delta G°$ were calculated for reactions that occurred at lower pH (barring the lysed cells of both strains and cell membrane isolates from *B. subtilis*). The calculated Q_{max}, K_L and $\Delta G°$ values suggested that were inaccuracies in the calculations associated with the Langmuir adsorption model that contradicted the uranium biosorption data. For all biomass investigated, the maximum uranium retention occurred at higher pH, with the cell wall isolates and lysed *B. subtilis* cells exhibiting greater uranium retention, Figure 37 and Figure 38. The $\Delta G°$ values obtained from this study were much higher than those of other studies investigating uranium biosorption to bacterial biomass. With the Langmuir model, the $\Delta G°$ values ranged from -11.4 to -17.6 kJ mol^{-1} within the pH range studied. Previous studies have reported lower values: -6.54 kJ mol^{-1} for whole *Citrobacter freudii* cells (Xie et al., 2008) and approximately -10 kJ mol^{-1} for whole *Chlorella vulgaris* cells (Amini et al., 2013).

The fitting of the uranium biosorption data to the Langmuir isotherm is based on a number of assumptions. The Langmuir isotherm assumes that all adsorption sites on the sorbent material are equivalent and that these sites hold only one sorbate molecule at a time, with no further interactions with adjacent sorbate molecules from the aqueous solution or on the surface. The bacterial cell surface is not a mono-adsorption site system, as it is rich in uranium interactive functional moieties, such as hydroxyl, phosphate, carboxyl and amino groups. Additionally, the uranium concentration range investigated should result in all available sites for biosorption being occupied by the sorbent material. This would cause a

plateau in the adsorption plot as the initial uranium concentration increases. This was apparent for the majority of cell types and associated surface structures investigated at pH 3 and 4.25. The adsorption plots for all biomass types investigated at pH 5.5 did not plateau, indicating that there was not enough uranium within the concentration range studied to saturate the binding sites on the cell structures. The speciation of uranium at the pH values investigated indicated that more than one species (and therefore more than one absorbing species) was present. Furthermore, there may be different binding affinities by functional groups for different uranium species due to deprotonation of functional groups within the pH range studied. Therefore, due to these limitations, inaccuracies in the results obtained from the calculations and corresponding Q_{max}, K_L and $\Delta G°$ values in comparison to the raw data obtained, the Langmuir adsorption model was deemed inadequate and could not be used to model the current biosorption data.

The Freundlich isotherm model was applied to the biosorption data, Table 12, as this absorption model assumed there was a heterogeneous adsorbent surface with multiple adsorption sites with different binding affinities for uranium within the pH and concentration range studied. The corresponding Freundlich constants, K_F, and $\Delta G°$ values correlated with the biosorption data that indicated the cell wall isolates and cell lysates of *B. subtilis* exhibited the greatest uranium retention capacity. However, the correlation coefficients, R^2, obtained (Appendix Figure 8 -Appendix Figure 10) showed that the Langmuir ($1/C_e$ vs. $1/q_e$- Table 11) adsorption isotherm model was a better fit than the Freundlich (Log C_e vs. Log q_e- Table 12) model.

Each model has its benefits and drawbacks. The Langmuir adsorption model can be applied to fit the data at pH 3 and 4.25 due to the saturation of adsorption sites on the surface of the biomass. However, the calculated results associated with the model were deemed inaccurate in comparison to the biosorption data. The Freundlich adsorption model was more suitable for the whole pH range studied as the bacterial cell surface and isolated structures have numerous types of binding sites. However, the calculated R^2 values were much smaller in comparison to those calculated using the Langmuir model. It can be assumed that the fitting of the biosorption data was inconclusive for the two adsorption models applied, but the Freundlich model complemented the raw biosorption data. The uranium quantification data suggested that the cell wall isolates from *B. subtilis* have the

greatest uranium retention capacity. However, an accurate Q_{max} cannot be determined for pH 5.5, due to the solubility of uranium at higher concentrations than 4 mM at this pH. Previous studies have successfully utilised the Langmuir and Freundlich adsorption isotherm for uranium binding within microbiological systems (Sar and D'Souza, 2001, Nakajima and Tsuruta, 2004, Xie et al., 2008, Amini et al., 2013, Romero-Gonzalez et al., 2016). The Q_{max} for a live *Pseudomonas* isolate was 312 and 263 mg U g^{-1} dry weight for sorption at pH 3 and 5, respectively (Sar and D'Souza, 2001) while the Freundlich K_F were calculated as 56.23 and 45.70. *Micrococcus luteus* retained a maximum of 385 mol U kg^{-1} dry weight at pH 3.5 (Nakajima and Tsuruta, 2004). The biosorption of uranium by *Chlorella vulgaris* indicated a Q_{max} of 165 mg U g^{-1} dry weight and K_F of 68.47 at pH 4 (Amini et al., 2013). A negative $\Delta G°$ of -9.51 kJ mol^{-1} was also calculated. Additionally, a $\Delta G°$ of -6.54 for *Citrobacter freudii* was obtained for cells that retained uranium from solution (Xie et al., 2008) suggested the interactions of uranium with the biomass used in this study were more favourable than previous studies.

4.4.2 Orthophosphate release during uranium removal

Orthophosphate release has been associated with uranium biomineralisation through the formation of uranium phosphate minerals. Orthophosphate released into the supernatant, following bacterial biomass interactions with uranium, was quantified to determine any differences in release as a function of cell fraction, pH and uranium concentration after 48 hours incubation. A possible source of orthophosphate was from the lysis of bacteria following cell death after being subject to unfavourable conditions for a long period of time (i.e. lack of nutrients and high salt content).

Results indicated differences in orthophosphate release as a function of fraction types, pH and uranium concentration. There were differences in orthophosphate release between the three strains of live bacteria, Figure 39. *B. subtilis* and *D. radiodurans* released far more orthophosphate into solution than *P. putida* after 48 hours. Interestingly, with all three strains, there was a higher release of orthophosphate into solution as the pH increased from 3 to 5.5, suggesting more intact cells at a lower pH. In the presence of increasing concentrations of uranium in solution, the amount of orthophosphate released decreased. There was no further quantifiable orthophosphate as the initial uranium concentration increased from 0.5 mM to 2 mM by all three strains over the pH range studied. Since the kinetics of the biosorption reaction occurred within the first 30 minutes using live cells (Figure 36), the uranium retained by phosphate moieties could prevent orthophosphate release from cell lysis. Alternatively, the differences in orthophosphate released could be due to precipitation as a uranium phosphate phase. A decrease in orthophosphate release, for example in the presence of 0.125 to 0.25 mM uranium, suggested that the uranium was accumulated by the released orthophosphate. The higher the uranium concentration the less orthophosphate was present in solution.

There were differences in the amount of released orthophosphate from the cell fractions of *P. putida* and *B. subtilis* in the control samples (Figure 40), compared to that released from live cells. There was less orthophosphate released from the cell wall isolates of either strain. Approximately 80 - 100 μM was released from *P. putida* cell wall isolates (pH 3 – 5.5) (Figure 40A) while approximately 55 – 20 μM (pH 3 – 5.5) were released by *B. subtilis* isolates (Figure 40B) with no uranium present. Interestingly, there was a higher amount of orthophosphate released at pH 3 than pH 5.5 from *B. subtilis* cell wall isolates. This

contradicted the trends observed from the cell wall isolates of *P. putida* and the live cells of *B. subtilis* where there was a greater amount of orthophosphate released at pH 5.5. This difference in the quantities of orthophosphate released between cell wall isolates and in comparison to live cells was due to two reasons; the differences in phosphate concentrations between the cell wall architecture of isolates (such as the presence of phosphate from outer membrane phospholipids in *P. putida* cell wall isolates) and the lack of other phosphate containing biomolecules that were released during the lysis of whole cells (i.e. from intracellular components). Similar to the trends observed with live cells, there was a decrease in orthophosphate quantified in solution as the uranium concentration increased, suggesting precipitation of uranium with released orthophosphate.

The release of orthophosphate from cell membrane isolates of *P. putida* (Figure 40C) and *B. subtilis* (Figure 40D) was greater than that from cell wall isolates. This difference was due to the presence of large quantities of phosphate from phospholipids of the cell membrane structure of both strains. A decrease in quantifiable orthophosphate in the presence of uranium in solution suggested that the cell membrane orthophosphate was a contributing factor to overall release in live cells, due to breakdown of cell membrane components over the incubation time from cell lysis.

There were slightly higher concentrations of orthophosphate release from the dead cells of *P. putida* (Figure 40E) and *B. subtilis* (Figure 40F) than from live cells. This increase was due to the greater amount of orthophosphate available following the lysis of the dead cells from the fractionation process, compared to the availability of orthophosphate within the phosphorylated biopolymers of intact live cells (Merroun et al., 2011). As a function of sample type and pH, the amount of orthophosphate in solution was considerably lower in the presence of uranium. It can be suggested that orthophosphate released that sequestered uranium from solution was not just from the lysis of whole cells and release from intracellular phosphorylated components, but also from the orthophosphate released from both the breakdown of cell wall and cell membrane components of the bacteria used within this study.

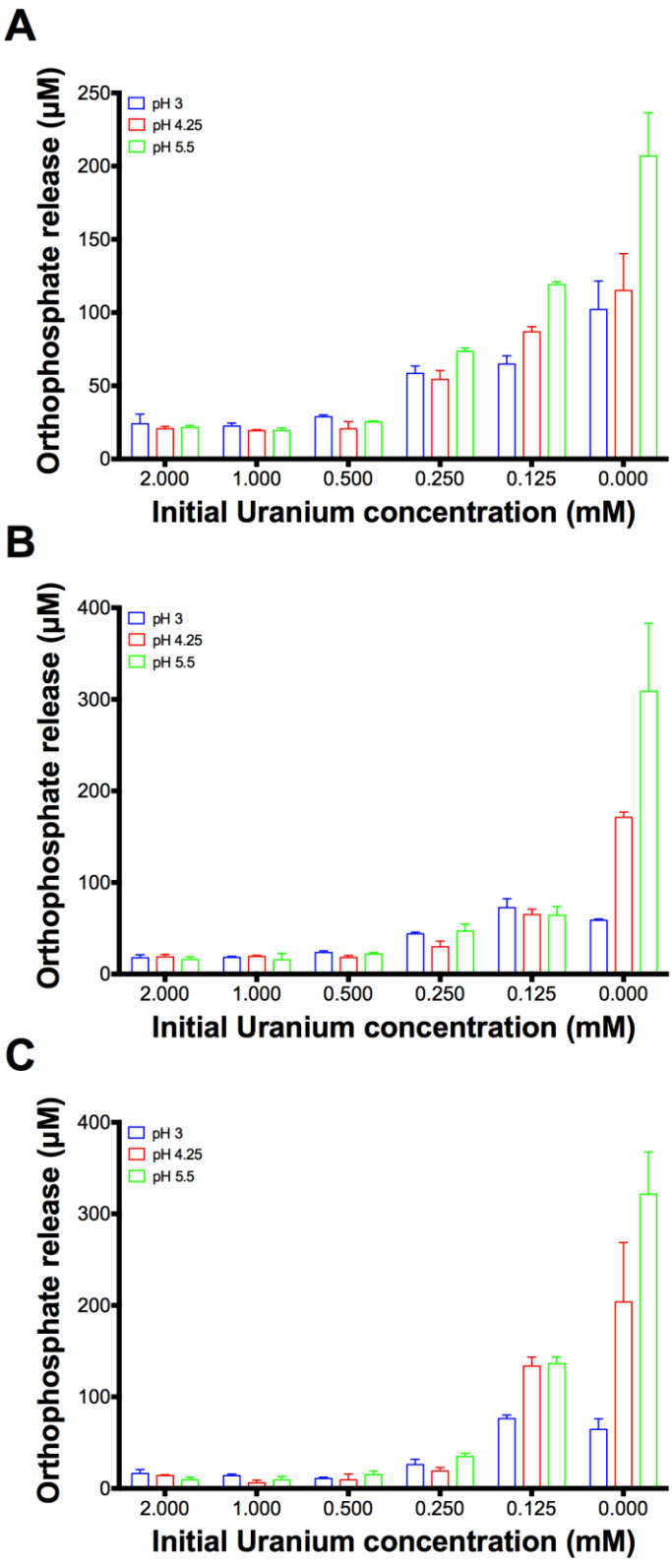

Figure 39. Orthophosphate release into the supernatant of [A] *P. putida*, [B] *D. radiodurans* and [C] *B. subtilis* live cells.

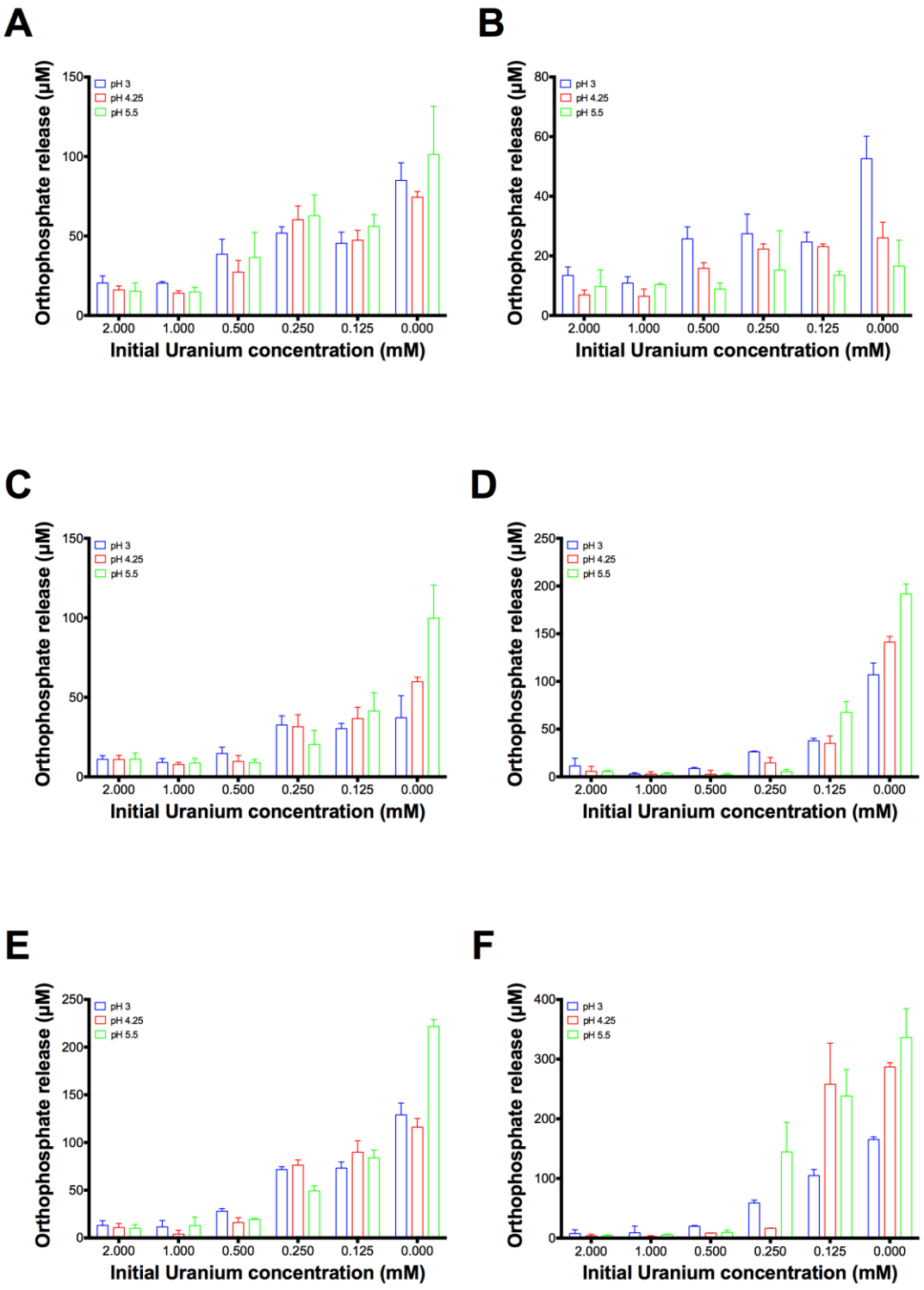

Figure 40. Orthophosphate release into the supernatant of the [A-B] cell wall, [C-D] cell membrane and [E-F] dead cells of *P. putida* and *B. subtilis*, respectively.

After exposing the cells to 4mM of uranium (pH 5.5) with 1 mg mL^{-1} of live cells and cell surface structures, lyophilised samples were analysed by XRD to elucidate any mineral structure from the interactions of uranium with released orthophosphate, Appendix Figure 11. This pH and concentration were analysed because, under this experimental condition, the live cells and cell surface structures investigated had retained the greatest amount of uranium and in turn the majority of phosphate from solution.

No clearly defined diffraction peaks were observed in any of the types that retained uranium. This could be attributed to an amorphous mineral phase with little structural ordering (Choudhary and Sar, 2011, Handley-Sidhu et al., 2014), suggesting that no significant mineral structure was formed from the released orthophosphate.

The kinetics of the reaction (Section 4.4.1.1) suggested that it was mainly a process of biosorption with negatively charged functional groups on the cell surface structures. Additional orthophosphate released following cell lysis and breakdown of cell surface contributed to the retention of uranium from solution. Previous studies have suggested that metabolic processes such as phosphatase activity were responsible for the precipitation of uranium mineral phases such as meta-autunite and uramphite (Merroun et al., 2011, Sousa et al., 2013, Reitz et al., 2014, Pan et al., 2015). Although orthophosphate was released from live cells, we suggest that phosphatase activity was not the major contributing factor responsible for uranium mineral formation due to the fast nature of the uranium retention exhibited by all biomass types.

4.4.3 ATR-FT-IR

4.4.3.1 Uranium interactions with bacterial biomass

ATR-FT-IR was used to investigate the binding of uranium with bacterial biomass as a function of pH and uranium concentration. The changes in adsorption band position provide identification of the functional groups of chemical molecules involved in uranium binding. Detailed band assignments and vibrational frequencies of each cell structure as a function of pH and uranium concentration are presented in Appendix Table 7 - Appendix Table 13. ATR-FT-IR spectra of biomass that retained uranium at pH 5.5 are displayed within the main body of text as the greatest changes in spectra were observed at this pH.

In all cell surface structures investigated, there was a broad and strong adsorption band in the 3700-3000 cm^{-1} region attributed to the O - H stretching vibrations of hydroxyl groups and N - H stretching of amino groups (Baker et al., 2014). It was likely that these groups were responsible for uranium biosorption and they have been reported previously in whole cell studies (Kazy et al., 2009, Choudhary and Sar, 2011). However, due to the broadness of this band and the contribution of water to the O-H stretching of this band, it was difficult to distinguish any noticeable differences in this band following uranium binding. Therefore it will not be discussed in detail.

4.4.3.2 Uranium interactions with whole *P. putida* cells

Figure 42 shows the FT-IR spectra of uranium biosorbed whole *P. putida* cells at pH 5.5. A shift in adsorption band position was observed corresponding to the vibrational symmetric stretching of CH_2 bonds from lipidic material of the outer and cell surface membrane of whole cells. The adsorption band shifts position slightly from 2856 - 2852 to 2860 cm^{-1} (pH 3 - 5.5) as whole cells were exposed to 2 mM uranium. An overall decrease in absorption intensity was observed in other absorption bands corresponding to lipidic material (~ 3000 - 2850 cm^{-1}) following uranium exposure at pH 5.5 (Baker et al., 2014, Shakirova et al., 2013, Merroun et al., 2003a, Kazy et al., 2008). At approximately 2958 (ν_{as} CH_3), 2918 (ν_{as} CH_2) and 2852 cm^{-1} (ν_s CH_2) the adsorption intensity decreased as the whole cells were exposed to 4 mM uranium. No changes in absorption band intensity were seen in cells exposed to uranium at pH 3 and 4.25. Uranium binding with components containing lipidic material within whole *P. putida* cells was further supported by the shift in absorption band position

and increase in intensity corresponding to the bending vibrations of CH_2 groups (Ojeda et al., 2008a, Jiang et al., 2004). This band shifted from 1451 - 1453 (pH 3-5.5) to 1457 cm^{-1} following interactions with concentrations of uranium up to 2 mM. Furthermore, the absorption intensity increased as the uranium concentration increased from 0 to 2 mM. A greater increase in adsorption intensity was also observed as the pH increased from 3 to 5.5. This suggested that there was favourable uranium binding with lipid containing biomolecules of the Gram-negative cell surface over the pH range studied, similar to that observed in previous studies (Pan et al., 2015, Choudhary and Sar, 2011).

Shifts in absorption band position corresponding to functional groups associated with proteins suggested differences in binding of uranium as a function of pH. Within the control samples the absorption band positions at 1408, 1399 and 1399 cm^{-1} at pH 3, 4.25 and 5.5, respectively, corresponded to the vibrational symmetric stretching of carboxyl groups. In the presence of concentrations of up to 2 mM uranium, these absorption bands shifted to 1413, 1388, and 1388 cm^{-1}, respectively. Shifts in adsorption band position following uranium binding at different pH were attributed to the differences in amount of uranium retained. The differences in uranium retention were due to the deprotonation behaviour of carboxyl groups. At pH 3, there was less uranium retention due to protonated carboxyl groups (Choudhary and Sar, 2011, Kazy et al., 2008, Theodorakopoulos et al., 2015).

Significant shifts in peak position and changes intensity were observed in the region of 1250-1000 cm^{-1} corresponding to functional groups associated with uranium interactions with polysaccharides and phosphorylated biomolecules, Figure 41, (Merroun et al., 2003a, Kazy et al., 2008, Choudhary and Sar, 2011, Lu et al., 2013, Pan et al., 2015, Theodorakopoulos et al., 2015). Slight shifts were observed in the absorption band associated with vibrational asymmetric stretching of phosphate groups. This band shifted from 1232, 1241 and 1239 cm^{-1} to the same wavenumber (1229 cm^{-1}) as the concentration of uranium in solution increased to 2 mM at pH 3, 4.25 and 5.5, respectively. A decrease in absorption intensity of this band was observed as whole cells retained more uranium, with a greater decrease observed as they retained more at pH 5.5. This suggested a greater affinity for uranium binding at pH 5.5 to phosphorylated biomolecules within whole *P. putida* cells. This was further supported by a significant shift in the absorption band position between 1087-1068 cm^{-1} attributed to the vibrational symmetric stretching of phosphate groups and

vibrations of carbon-containing groups associated with polysaccharides (Kazy et al., 2008, Choudhary and Sar, 2011, Lu et al., 2013). At pH 3, this absorption band shifts from 1073 to 1067 cm^{-1} as the whole cells are exposed to uranium at 2 mM, while at pH 4.25 and 5.5 this absorption band shifts from 1087 to 1068 cm^{-1}. The absorption intensity increased as the uranium concentration increased in solution within the pH range investigated.

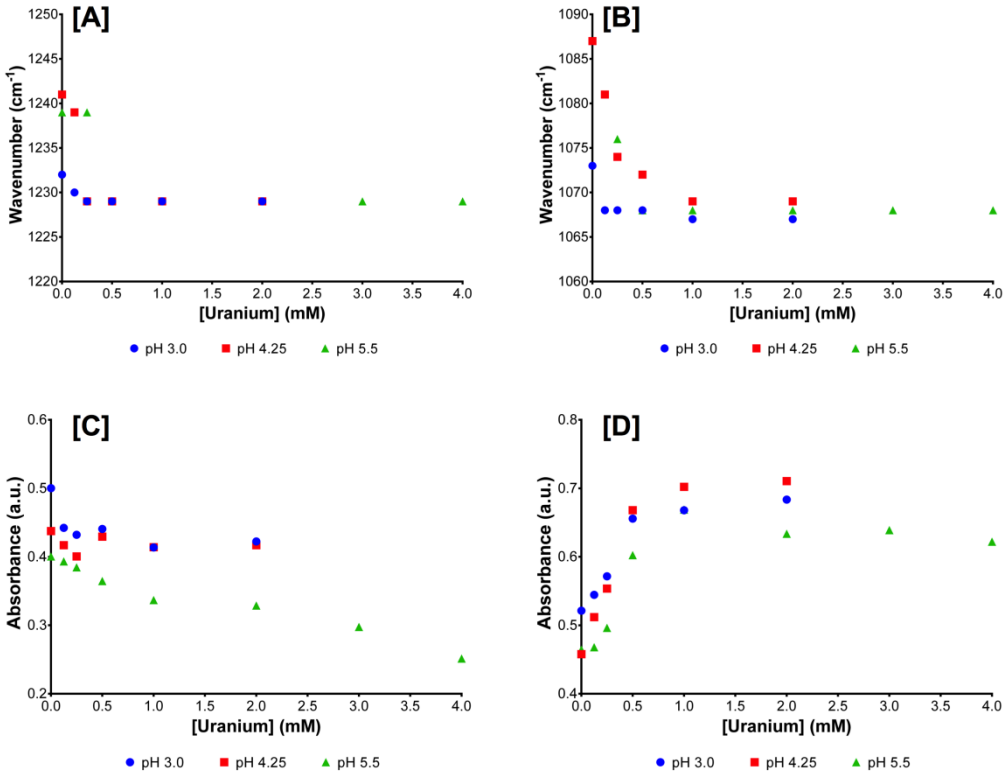

Figure 41. Changes in *P. putida* whole cell absorption band position [A-B] and intensity [C-D] for the ν_{as} (PO_2) and ν_s (PO_2), respectively, following uranium exposure.

The additional absorption band at 916 – 923 cm^{-1} corresponded to vibrations of the U-O ligand (Lumetta et al., 1999, Kazy et al., 2008, Choudhary and Sar, 2011, Barkleit et al., 2011, Lu et al., 2013, Pan et al., 2015, Theodorakopoulos et al., 2015) as the biomass retained uranium. An increase in absorption intensity relative to the amount of uranium retained from solution was observed. This absorption band was present in all samples that retained uranium from solution during this experimental study (Section 4.4.3.2-4.4.3.8).

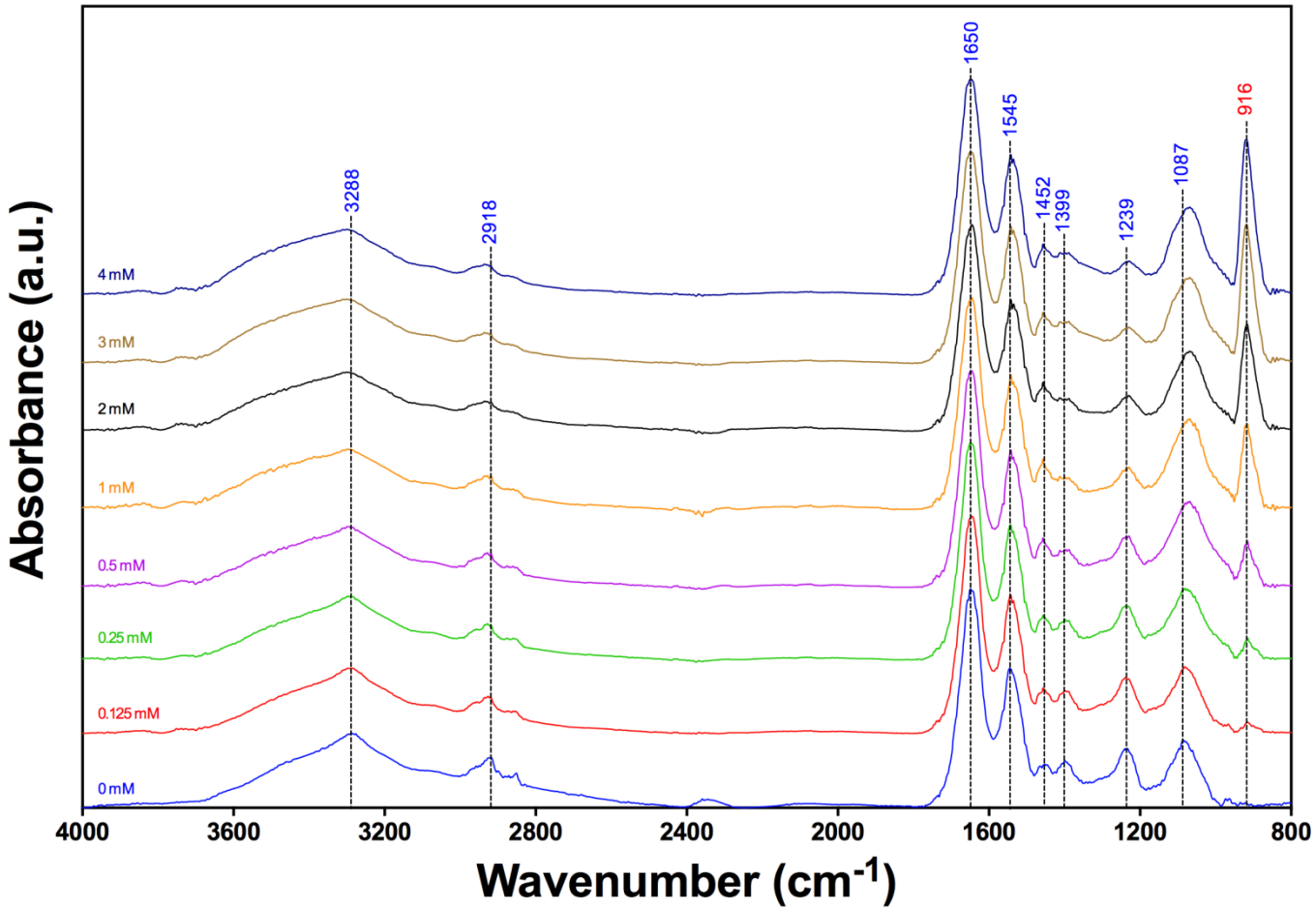

Figure 42. FTIR spectra of *P. putida* whole cells as a function of initial uranium concentration (pH 5.5, 0.1 M NaCl)

4.4.3.3 Uranium interactions with whole *D. radiodurans* cells

Fewer changes in absorption band position were observed for whole *D. radiodurans* cells that retained uranium in the pH range studied. This lack of change could be attributed to cell surface architecture, and a lower amount of uranium retained in the pH range studied compared to the *P. putida* and *B. subtilis* whole cells. Figure 44shows the FT-IR spectra of uranium biosorbed whole *D. radiodurans* cells at pH 5.5. An increase in absorption band intensity was observed in the range 1452 – 1457 cm^{-1} between pH 3 and 5.5 as the uranium exposure concentration increased. This absorption band corresponded to the δ_s (CH_2) from lipids and fatty acids, suggesting changes in availability of the functional group at the surface due to increased interactions with uranium. This was similar to that previously suggested following heavy metal exposure to *B. subtilis* cells resulted in an increase of lipoteichoic acid content (Ramstedt et al., 2014, Ojeda et al., 2008a, Jiang et al., 2004).

Shifts of the ν_s (COO^-) band suggested that there were uranium interactions with proteins in the cell surface (Pagnanelli et al., 2000, Choudhary and Sar, 2011). At pH 3, this absorption band position shifted from 1383 to 1387 cm^{-1} and increased in intensity as the uranium exposure concentration increased. At pH 4.25 and 5.5, this absorption band shifted from 1388 and 1399 cm^{-1} to 1387 and 1395 cm^{-1}, respectively, as the uranium exposure concentration increased. These differences in peak position shift and changes in absorption intensity between pH values suggest differences in protein - uranium binding at different pH. The protonation - deprotonation behaviour of the carboxyl groups within the pH range affected the amount of uranium retained by *D. radiodurans* and in turn by carboxyl groups on the cell surface.

No significant change in peak position was observed for the absorption band attributed to the ν_{as} (PO_2) (Baker et al., 2014, Ojeda and Dittrich, 2012). This lack of change could be attributed to there being no phosphate present within the outermost layer of the cell surface, in accordance with XPS data that indicated no phosphorus - containing compounds at the outermost region of the cell surface (Figure 30). The presence of the absorption band in the spectrum was due to the penetration of the infrared radiation source with intracellular phosphate constituents of the bacteria, which the uranium cannot readily interact with. The significant shift in absorption band position and intensity following uranium exposure was attributed to the ν_s (PO_2) and ν (C-O, C-O-C, C-C) bands, Figure 43 (Kazy et al., 2008, Choudhary and Sar, 2011, Lu et al., 2013). At pH 3,

this absorption band shifts position from 1073 to 1055 cm^{-1} and increased in absorption intensity as the uranium exposure concentration increased to 2 mM. Similarly, at pH 5.5, this absorption band shifted from 1079 to 1067 cm^{-1} and increased in intensity. Interestingly, at pH 4.25, no shift in peak position was observed, although the absorption intensity increased and slight changed in absorption band shape, as the concentration of uranium increased. As no changes were observed in the absorption band position corresponding to the ν_{as} (PO_2), the changes in absorption band position in this region were more reasonably ascribed to ν (C-O, C-O-C, C-C), rather than the ν_s (PO_2).

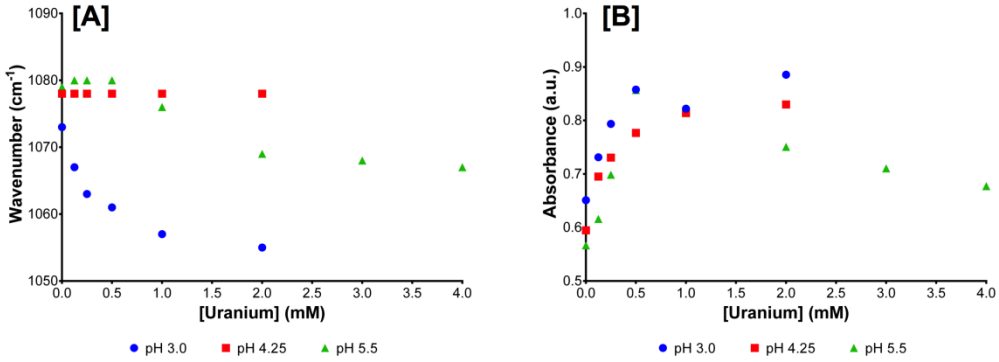

Figure 43. Changes in absorption band position [A] and intensity [B] for ν (C-O, C-O-C, and C-C) of whole *D. radiodurans* cells, following uranium exposure.

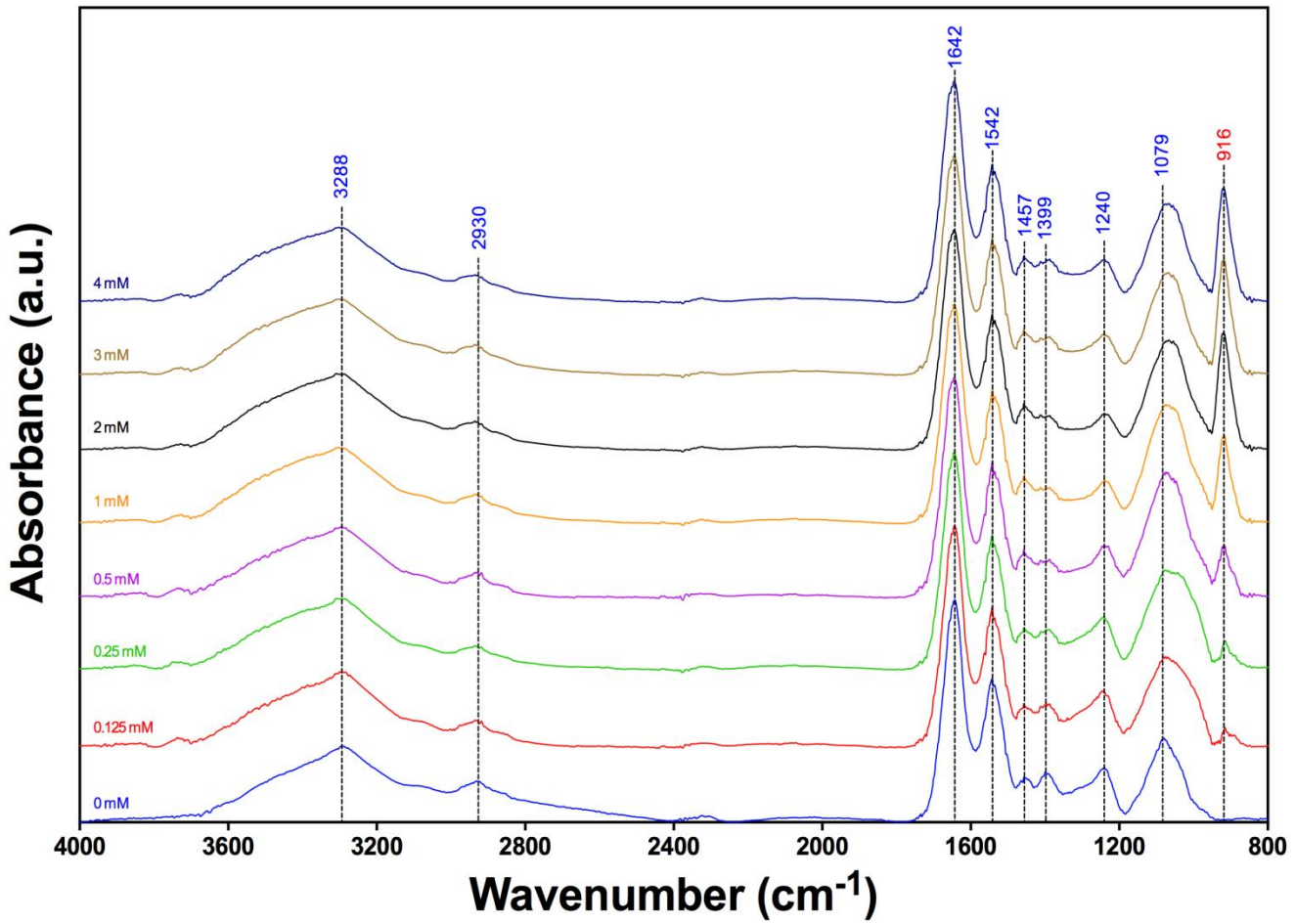

Figure 44. FTIR spectra of *D. radiodurans* whole cells as a function of initial uranium concentration (pH 5.5, 0.1 M NaCl)

4.4.3.4 Uranium interactions with whole *B. subtilis* cells

Figure 46 shows the FT-IR spectra of uranium biosorbed whole *B. subtilis* cells at pH 5.5. No shift in absorption band positions was observed within the region 3000 – 2850 cm^{-1} associated with lipidic functional groups of whole *B. subtilis* cells (Ojeda and Dittrich, 2012, Baker et al., 2014). However, there was a decrease in absorption intensity of the band associated with ν_{as} (CH_3) as the uranium exposure concentration increased for the pH range studied, more greatly at pH 5.5.

Changes in absorption band position for those associated with proteins suggested preferential binding at different pH in the range studied (Pagnanelli et al., 2000, Choudhary and Sar, 2011). There was a shift in the absorption band position from 1384, 1399 and 1399 cm^{-1} to 1387, 1387 and 1386 cm^{-1} at pH 3, 4.25 and 5.5, respectively, as the cells retained uranium from 2 mM solution, corresponding to the ν_s (COO^-). Furthermore, there was an overall decrease in intensity of this absorption band as the uranium exposure concentration increased; a greater decrease in absorption intensity was observed at pH 5.5 compared to pH 3 and 4.25. Additionally, the protein-associated absorption band corresponding to δ (N-H) at 1542 cm^{-1} decreased in intensity at pH 4.25 and 5.5 as the uranium exposure concentration increases to 2 mM. These changes in absorption intensity and peak position suggested differences in uranium binding to proteins within the pH range. Deprotonation of the protein associated functional groups and alterations in the secondary structure of cellular proteins allowed for greater uranium retention at higher pH (Kazy et al., 2009, Choudhary and Sar, 2011).

There were significant changes in absorption band position attributed to the ν_{as} (PO_2), Figure 45A (Merroun et al., 2003a, Kazy et al., 2008, Choudhary and Sar, 2011, Lu et al., 2013, Pan et al., 2015, Theodorakopoulos et al., 2015). A shift was observed from 1221, 1222 and 1229 cm^{-1} to 1213, 1214 and 1220 cm^{-1} at pH 3, 4.25 and 5.5, respectively, following uranium exposure at 2 mM. At pH 5.5, this absorption band shifts further to 1205 cm^{-1} following uranium exposure at 4 mM. Furthermore, there was a decrease in absorption intensity as the uranium concentration increased, with a greater decrease observed as the pH increases, Figure 45B. Similarly there were slight shifts in absorption band position corresponding to the ν_s (PO_2) and ν (C-O, C-O-C, C-C) (Kazy et al., 2008, Choudhary and Sar, 2011, Lu et al., 2013). At pH 4.25 and 5.5, the absorption band position shifted from 1060 and 1063 cm^{-1} to 1056 and 1055 cm^{-1}, respectively, as the uranium concentration increased. These shifts and changes in intensity indicated

binding of uranium to phosphate groups on the bacterial cell surface. Furthermore, due to shifts in peak positions and changes in absorption intensity corresponding to the ν_s (PO_2) and ν (C-O, C-O-C, C-C), the additional peak corresponding to the ν_s (PO_2) from DNA and phospholipids at approximately 976 cm^{-1} was masked at pH 3 and 4.25 following uranium retention.

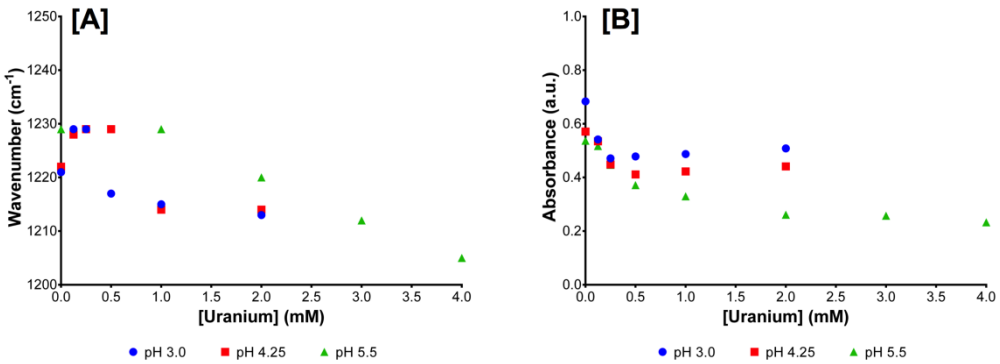

Figure 45. Changes in absorption band position [A] and intensity [B] for ν_{as} (PO_2) of whole *B. subtilis* cells, following uranium exposure.

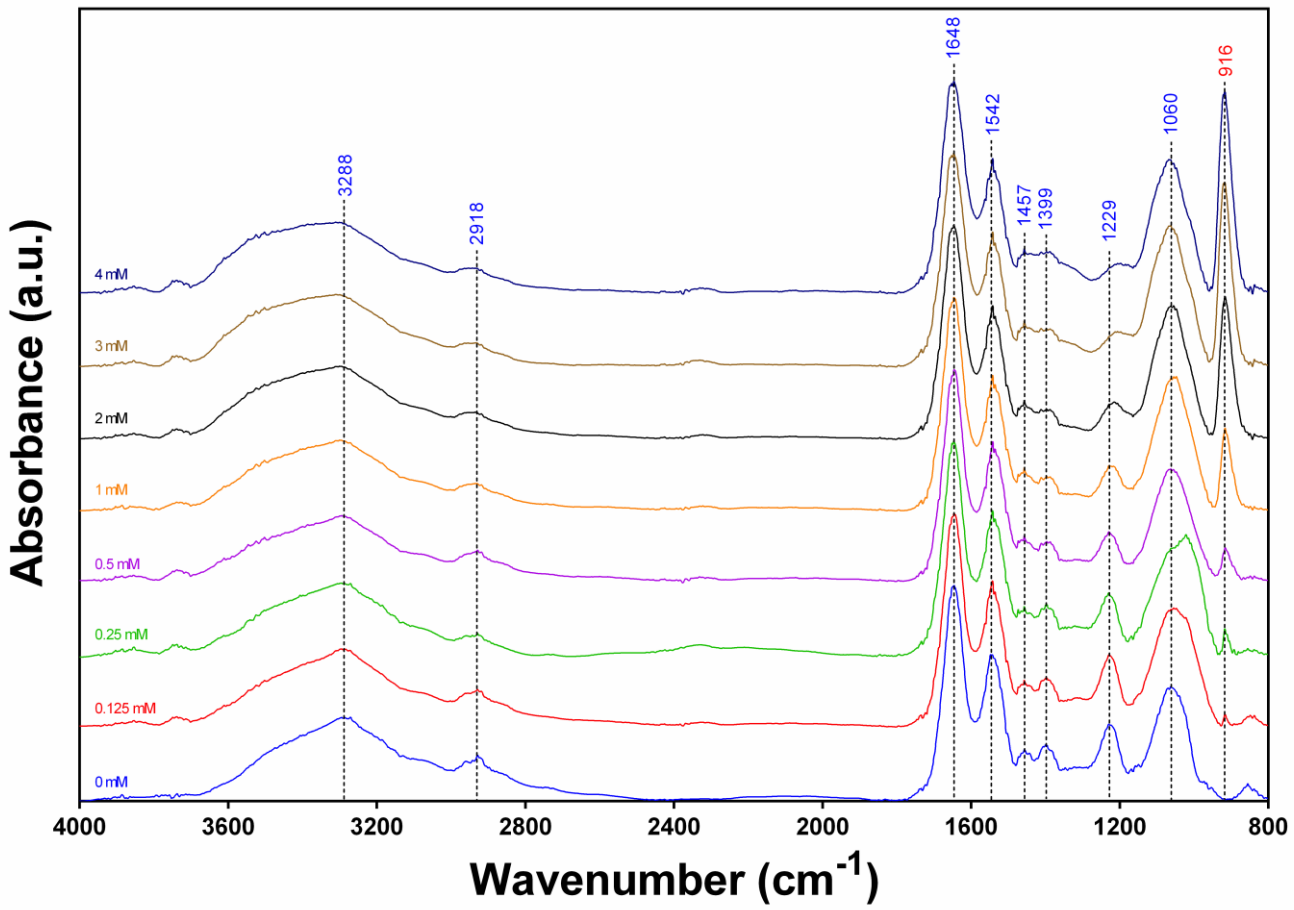

Figure 46. FTIR spectra of *B. subtilis* whole cells as a function of initial uranium concentration (pH 5.5, 0.1 M NaCl)

4.4.3.5 Uranium interactions with *P. putida* cell wall isolates

The interactions of cell wall isolates from *P. putida* with uranium from solution indicated a higher binding than that for whole cells. Analysing these interactions with ATR-FT-IR suggested similar mechanisms of removal since the isolates come from the outermost region of the cell where uranium can interact.

Figure 48 shows the FT-IR spectra of uranium biosorbed *P. putida* cells cell wall isolates at pH 5.5. Within the region of 3000 – 2850 cm^{-1}, which is populated by lipid-rich absorption bands, decreases in absorption intensity and slight shifts in absorption band position suggested that there was uranium binding with reactive groups of the Gram-negative cell wall outer membrane (Baker et al., 2014, Shakirova et al., 2013, Merroun et al., 2003a, Kazy et al., 2008). The absorption bands corresponding to the ν_{as} (CH_3), ν_{as} (CH_2) and ν_s (CH_2) of lipids and fatty acids decreased in intensity as the uranium exposure concentration increased within the pH range studied, Table 13. A greater decrease in absorbance intensity was observed at pH 4.25. This decrease suggested that reactive groups of the outer membrane interacted with uranium as its concentration increased. Furthermore, there was an increase in absorption intensity at approximately 1453 - 1457 cm^{-1} corresponding to the δ_s (CH_2) from lipids and fatty acids (Ojeda et al., 2008a, Jiang et al., 2004) as the uranium exposure concentration increased to 2 mM, supporting the idea of uranium interactions with components of the outer membrane.

Table 13. Changes in absorbance intensity for lipidic adsorption bands within the 3000-2850 cm^{-1} region.

	ν_{as} (CH_3)			ν_{as} (CH_2)			ν_s (CH_2)		
[U(VI)]	*pH 3*	*pH 4.25*	*pH 5.5*	*pH 3*	*pH 4.25*	*pH 5.5*	*pH 3*	*pH 4.25*	*pH 5.5*
0 mM	0.3242	0.3977	0.3677	0.4946	0.6498	0.5968	0.3030	0.4521	0.4063
2 mM	0.2620	0.2658	0.2549	0.3653	0.3931	0.3672	0.2088	0.2420	0.2224
Change	-0.0622	-0.1319	-0.1128	-0.1293	-0.2567	-0.2296	-0.0942	-0.2101	-0.1839

There were changes in absorption band shape and position within the range of 1420 – 1380 cm^{-1}. As the uranium exposure concentration increased within the pH range investigated, there was broadening of the peaks corresponding to the ν_s (COO^-). A greater broadening was observed at pH 5.5, indicating uranium binding with cell wall associated proteins anchored within the outer membrane (Pagnanelli et al., 2000, Choudhary and Sar, 2011).

Significant differences in absorption band position and intensity were observed in the region of 1250 – 1000 cm^{-1}, corresponding to the functional groups associated with phosphorylated biopolymers and carbohydrates within the Gram-negative cell wall, Figure 47, (Merroun et al., 2003a, Kazy et al., 2008, Choudhary and Sar, 2011, Lu et al., 2013, Pan et al., 2015, Theodorakopoulos et al., 2015, Barkleit et al., 2011). A broadening of the absorption band corresponding to the $\nu_{as}(PO_2)$ was observed, particularly at pH 5.5. This absorption band shifts from 1232 to 1228 cm^{-1} and decreased in absorption intensity. This broadening of the absorption band was also noticeable at pH 3 and 4.25, albeit with a lower decrease in absorption intensity. This suggested a preferential binding for phosphate groups within the Gram-negative cell wall, such as those found in phospholipids of the outer membrane, LPS and phosphorylated proteins.

Changes in absorption band position at 1077 cm^{-1} suggested uranium interactions with the functional groups, corresponding to the $\nu_s(PO_2)$ and ν (C-O, C-O-C, C-C) bands (Kazy et al., 2008, Choudhary and Sar, 2011, Lu et al., 2013). The band at 1077 cm^{-1} shifted to 1063 cm^{-1} at pH 3 and 1047 cm^{-1} at 4.25 and increased in absorption intensity as the uranium exposure concentration increased to 2 mM. No shift in absorption band position was observed at pH 5.5. Broadening of this peak happened at pH 4.25 and 5.5 as the uranium concentration increased and there was masking of an additional peak within the control spectra at 1151 cm^{-1}. Changes in absorption band position and shape were attributed to uranium interactions with phosphorylated biopolymers and polysaccharides, such as LPS, within the Gram-negative cell wall as previously demonstrated (Barkleit et al., 2008, Barkleit et al., 2011).

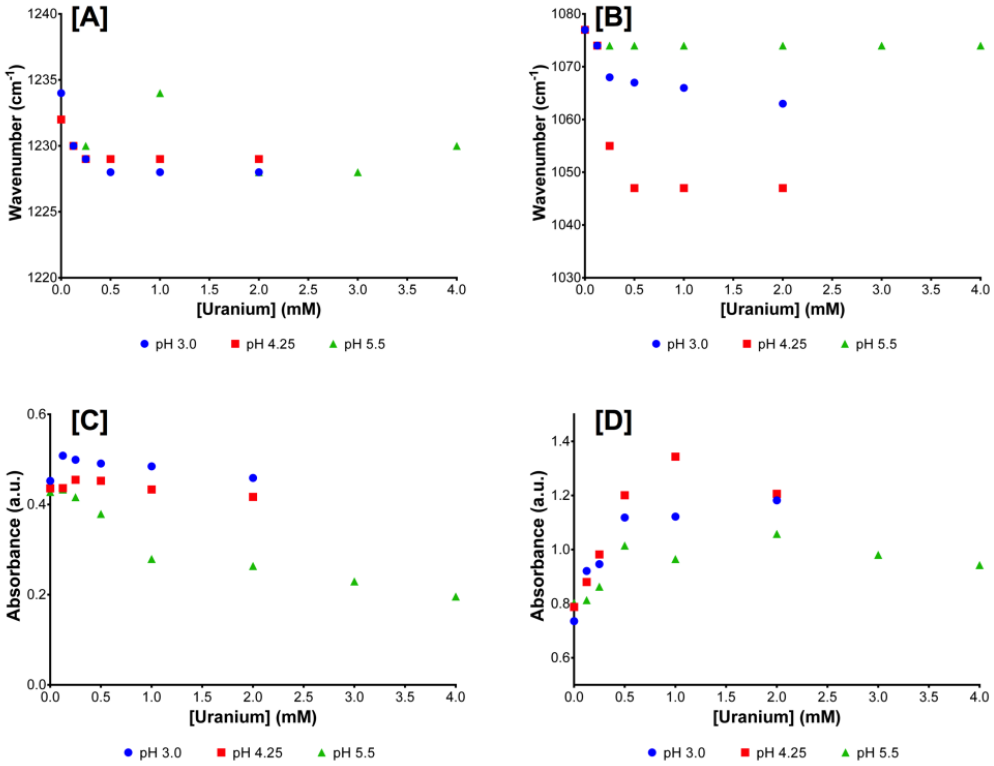

Figure 47. Changes in *P. putida* cell wall isolate absorption band position [A-B] and intensity [C-D] for the ν_{as} (PO_2) and ν_s (PO_2), respectively, following uranium exposure.

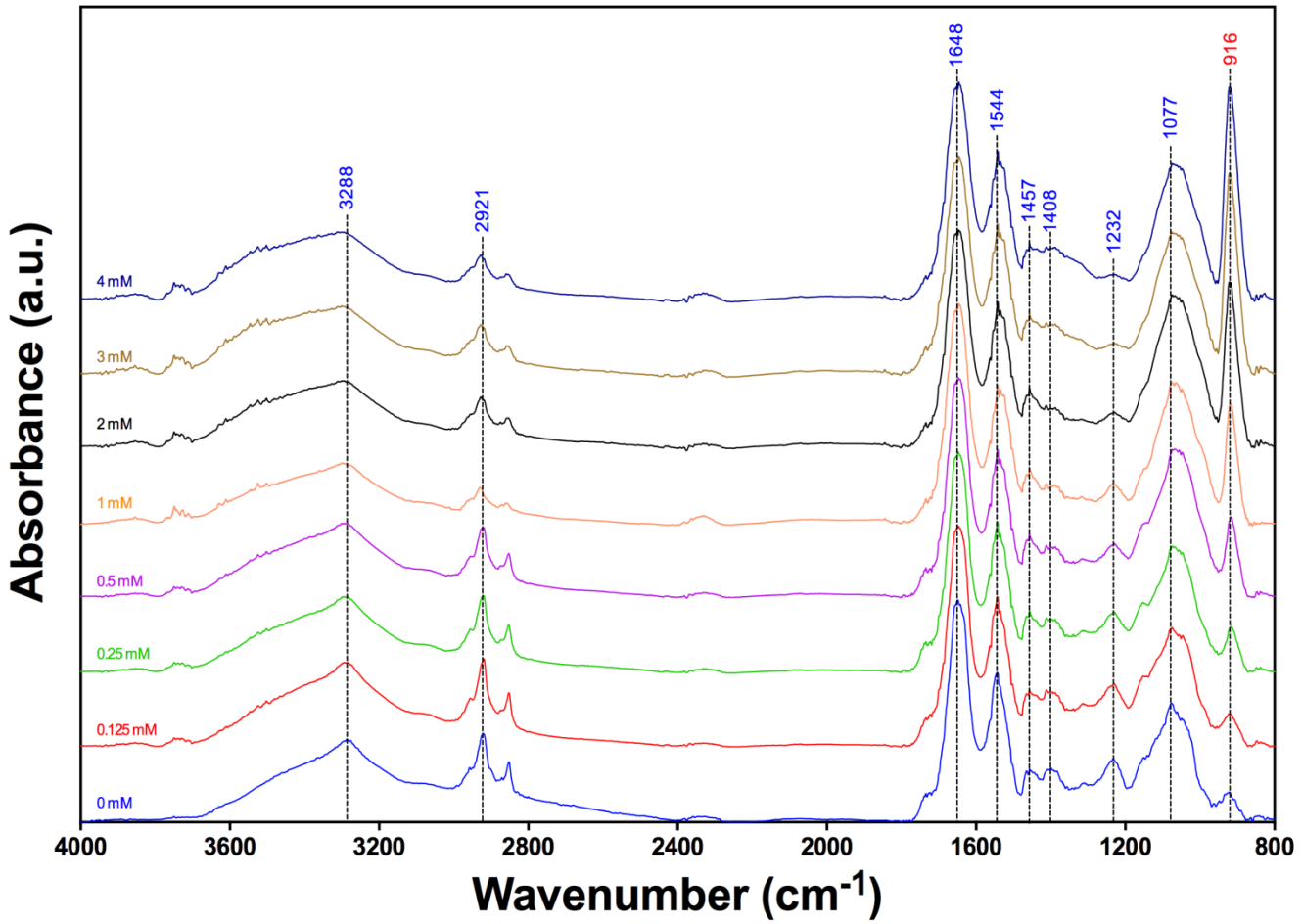

Figure 48. FTIR spectra of *P. putida* cell wall isolates as a function of initial uranium concentration (pH 5.5, 0.1 M NaCl)

4.4.3.6 Uranium interactions with *B. subtilis* cell wall isolates

Differences in absorption band position, shape and intensity associated with proteins, phosphorylated biopolymers and polysaccharides within the cell wall isolates were observed following uranium retention within the pH range investigated. Uranium retention was much higher with *B. subtilis* cell wall isolates than that for whole cells. Figure 50 shows the FT-IR spectra of uranium biosorbed whole *B. subtilis* cell wall isolates at pH 5.5. Following uranium retention, there was a broadening and disappearance of the shoulder at approximately 1740 cm^{-1} within the pH range studied, corresponding to the ν_s (C=O) either from the esters of lipids, carboxylic acids of proteins and carbonyl groups of polysaccharides (Baker et al., 2014, Alessi et al., 2014). This change in absorption intensity and broadening of the band was attributed to uranium binding the groups found within lipoteichoic acids, proteins and polysaccharides within the rich peptidoglycan layer of the *B. subtilis* cell wall.

Changes in absorption band shape between 1548 – 1542 cm^{-1} and 1420 – 1300 cm^{-1}, attributed to the δ (N-H) and the ν_s (COO^-) / ν (C-N), respectively, suggested alterations to the secondary protein structure following uranium interactions with the cell wall isolates (Pagnanelli et al., 2000, Choudhary and Sar, 2011). At pH 5.5, there was a large broadening of the δ (N-H) absorption band, resulting in a loss of definition. The Amide II peak (~1548 cm^{-1}) broadened significantly as the uranium concentration increased to 4 mM. Furthermore, at higher uranium concentrations, the broadening of peaks in the range 1420 – 1300 cm^{-1} supported uranium interactions with proteins occurred at pH 5.5. At pH 3 and 4.25, no changes in absorption band position, shape and intensity (compared to isolates not exposed to uranium) were observed. This suggested that there were fewer interactions with the functional groups associated with proteinaceous material at lower pH. Protonation of functional groups will hinder the binding of uranium, as evident in the uranium biosorption quantification. Hence no shift observed in the ATR-FT-IR spectra.

Significant differences were observed in cell wall isolates exposed to uranium at pH 3, 4.25 and 5.5, within the phosphate region, Figure 49. The ν_{as} (PO_2) band position shifted from 1215, 1221 and 1223 cm^{-1} to 1199, 1199 and 1207 cm^{-1} as the cell wall isolates retained uranium from 2mM solution at pH 3, 4.25 and 5.5, respectively. At 4 mM uranium, this absorption band broadened and shifted to 1195 cm^{-1} at pH 5.5. Furthermore, within the pH range studied, there was a decrease in absorption intensity

as the uranium concentration increased. Changes in this absorption band, corresponding to the ν_{as} (PO_2) frequency, suggested preferential interactions with phosphate groups within the cell wall isolates (Merroun et al., 2003a, Kazy et al., 2008, Choudhary and Sar, 2011, Lu et al., 2013, Pan et al., 2015, Theodorakopoulos et al., 2015, Barkleit et al., 2011). XPS analysis in this study and previous work indicated large quantities of phosphate within the Gram-positive cell wall that was attributed to the phosphodiester bonds of (lipo) teichoic acids (Ahimou et al., 2007) Broadening of this absorption band resulted in the disappearance of the band at approximately 1154 cm^{-1} as the cell wall isolates retained more uranium. No significant shift in absorption band corresponding to the ν (C-O, C-O-C, C-C) associated with polysaccharides was observed at pH 3 and 4.25 following uranium exposure (Kazy et al., 2008, Choudhary and Sar, 2011, Lu et al., 2013). However, this absorption band shifted position from 1052 to 1060 cm^{-1} when exposed to 4 mM uranium at pH 5.5. This shift in position suggested uranium interactions with polysaccharides at high uranium concentrations and towards neutral pH. Broadening of this absorption band, coupled with an increase in absorption intensity at ~ 918 cm^{-1} attributed to the ν $(U\text{-}O)_{ligand}$, caused a masking of the band at approximately 976 cm^{-1}.

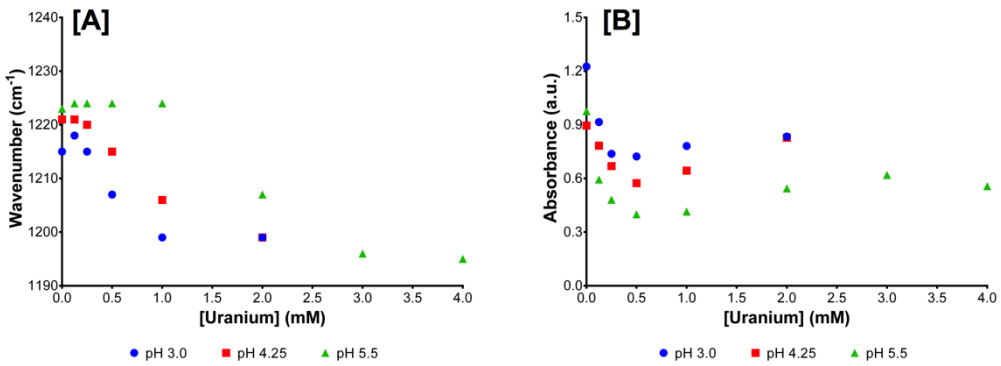

Figure 49. Changes in absorption band position [A] and intensity [B] for ν_{as} (PO_2) of *B. subtilis* cell wall isolates, following uranium exposure.

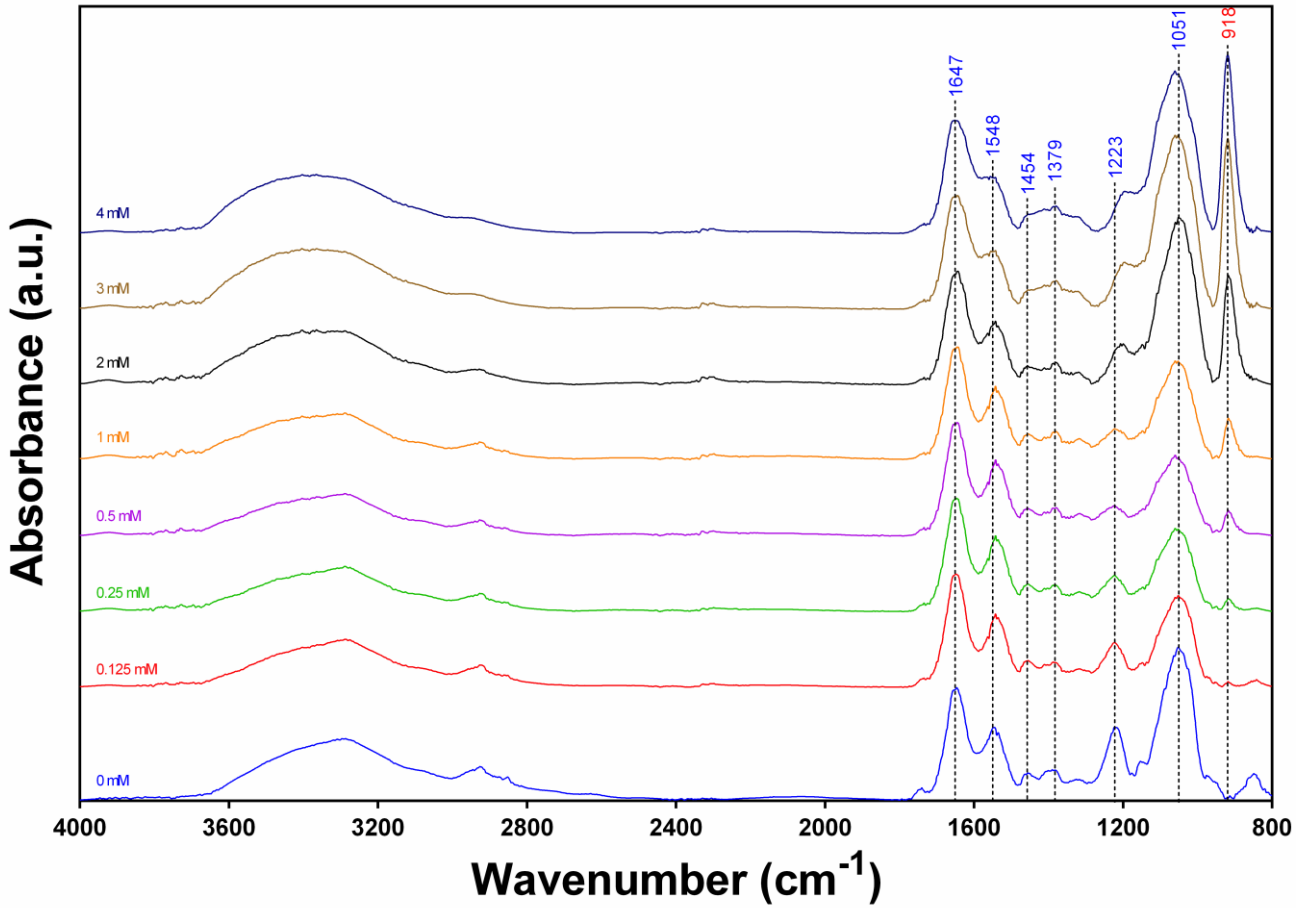

Figure 50. FTIR spectra of *B. subtilis* cell wall isolates as a function of initial uranium concentration (pH 5.5, 0.1 M NaCl)

4.4.3.7 Uranium interactions with *P. putida* cell membrane isolates

Interactions of cell membrane isolates from *P. putida* with uranium indicated a lower retention than for whole cells and cell wall isolates. The analysis of these interactions suggested different retention mechanisms from those for whole cells and cell wall isolates due to the different macromolecular composition of the cell membrane. *P. putida* whole cell, cell wall and cell surface membrane isolates contained similar amounts of hydrocarbon-like compounds, but with varying amounts of peptide and polysaccharide-like material, Table 7.

Figure 52 shows the FT-IR spectra of uranium biosorbed whole *P. putida* cell membrane isolates at pH 5.5. Similar to the cell wall isolates of *P. putida*, there was an overall decrease in absorption intensity corresponding to vibrations of lipid-associated molecules (Baker et al., 2014, Shakirova et al., 2013, Merroun et al., 2003a, Kazy et al., 2008), as the uranium concentration increased to 2 mM within the pH range investigated, Table 14. The greatest decrease following uranium retention was at pH 5.5. This was different to the behaviour of lipid-associated functional groups of cell wall isolates that exhibited a larger decrease in absorption intensity following exposure to uranium at 2 mM at pH 4.25. *P. putida* cell membrane isolates showed no substantial change in absorption band position at 1454 – 1456 cm^{-1}, corresponding to the δ_s (CH_2) from lipids and fatty acids. The shoulder at 1739 cm^{-1}, attributed to the ν_s (C=O) was less well defined as the cell membrane isolates retained more uranium from solution. As these adsorption bands are associated with the unreactive and non-polar lipidic material of the cell surface, changes in these adsorption bands should probably be attributed to the overall changes in membrane structure following uranium binding, rather than direct binding with lipidic material.

Table 14. Changes in absorbance intensity for lipidic adsorption bands within the 3000-2850 cm^{-1} region.

	ν_{as} (CH_3)			ν_{as} (CH_2)			ν_s (CH_2)		
[U(VI)]	*pH 3*	*pH 4.25*	*pH 5.5*	*pH 3*	*pH 4.25*	*pH 5.5*	*pH 3*	*pH 4.25*	*pH 5.5*
0 mM	0.3197	0.2944	0.3129	0.4191	0.4418	0.4900	0.2584	0.2672	0.2905
2 mM	0.2820	0.2964	0.2784	0.3503	0.3714	0.3591	0.2172	0.2342	0.2235
Change	-0.0377	**+0.002**	-0.0345	-0.0688	-0.0704	-0.1309	-0.0412	-0.033	-0.067

At pH 3, there was no change in absorption band position shape and intensity within the region ~1470 – 1300 cm^{-1} corresponding to various functional groups associated with lipids and proteins (Appendix Figure 22). Broadening of absorption bands in this region, in particular at 1391 cm^{-1}, occurred as the uranium exposure concentration increased at pH 4.25 and pH 5.5. The broadening of the absorption band attributed to the ν_s (COO^-) suggested interactions with uranium at higher pH. Deprotonation of carboxyl groups results in a greater number of uranium interactions. Additionally, uranium binding alters the secondary structure of proteins (Pagnanelli et al., 2000, Choudhary and Sar, 2011).

Significant shifts in absorption band position were observed within cell membrane isolates exposed to uranium in the pH range studied, corresponding to the ν_{as} (PO_2), Figure 51A. At pH 3, 4.25 and 5.5, the absorption band at 1232 cm^{-1} shifted to 1216, 1218 and 1226 cm^{-1}, respectively, as the membrane isolates retained uranium from 2 mM solution. At pH 5.5, this band shifted to 1216 cm^{-1} as the uranium exposure concentration increased to 4 mM. Furthermore, there was a significant shift in the absorption band position attributed to the ν_s (PO_2) and ν (C-O, C-O-C, C-C), Figure 51B. Within the pH range studied, this absorption band shifted from 1078 to 1055 cm^{-1} and increased in absorption intensity following uranium retention. Due to these changes in absorption band position and intensity, the band between 1157-1160 cm^{-1}, in the control spectra, became masked as the uranium exposure concentration increased. As there was a small amount of polysaccharide like material within the cell membrane isolates (14.71 %: Table 7), changes in the absorption band position were most likely to be because of uranium interactions with phosphate groups in phospholipids, the main constituent of bacterial cell surface membranes (Merroun et al., 2003a, Kazy et al., 2008, Choudhary and Sar, 2011, Lu et al., 2013, Pan et al., 2015, Theodorakopoulos et al., 2015, Barkleit et al., 2011).

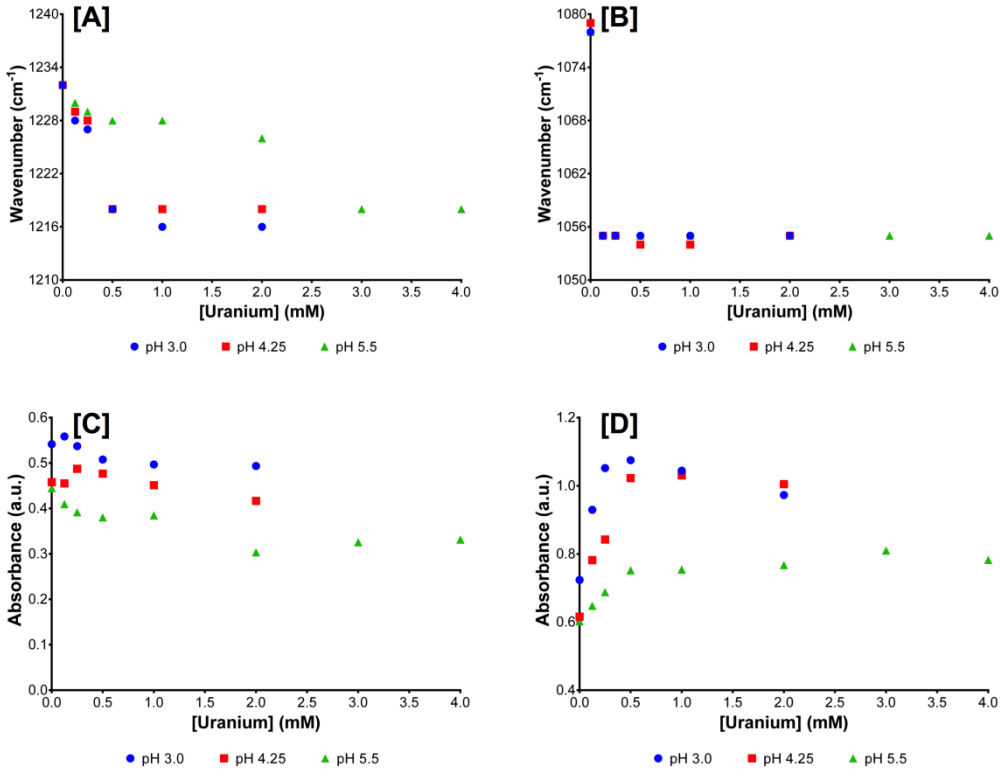

Figure 51. Changes in *P. putida* cell membrane isolate absorption band position [A-B] and intensity [C-D] for the ν_{as} (PO_2) and ν_s (PO_2), respectively.

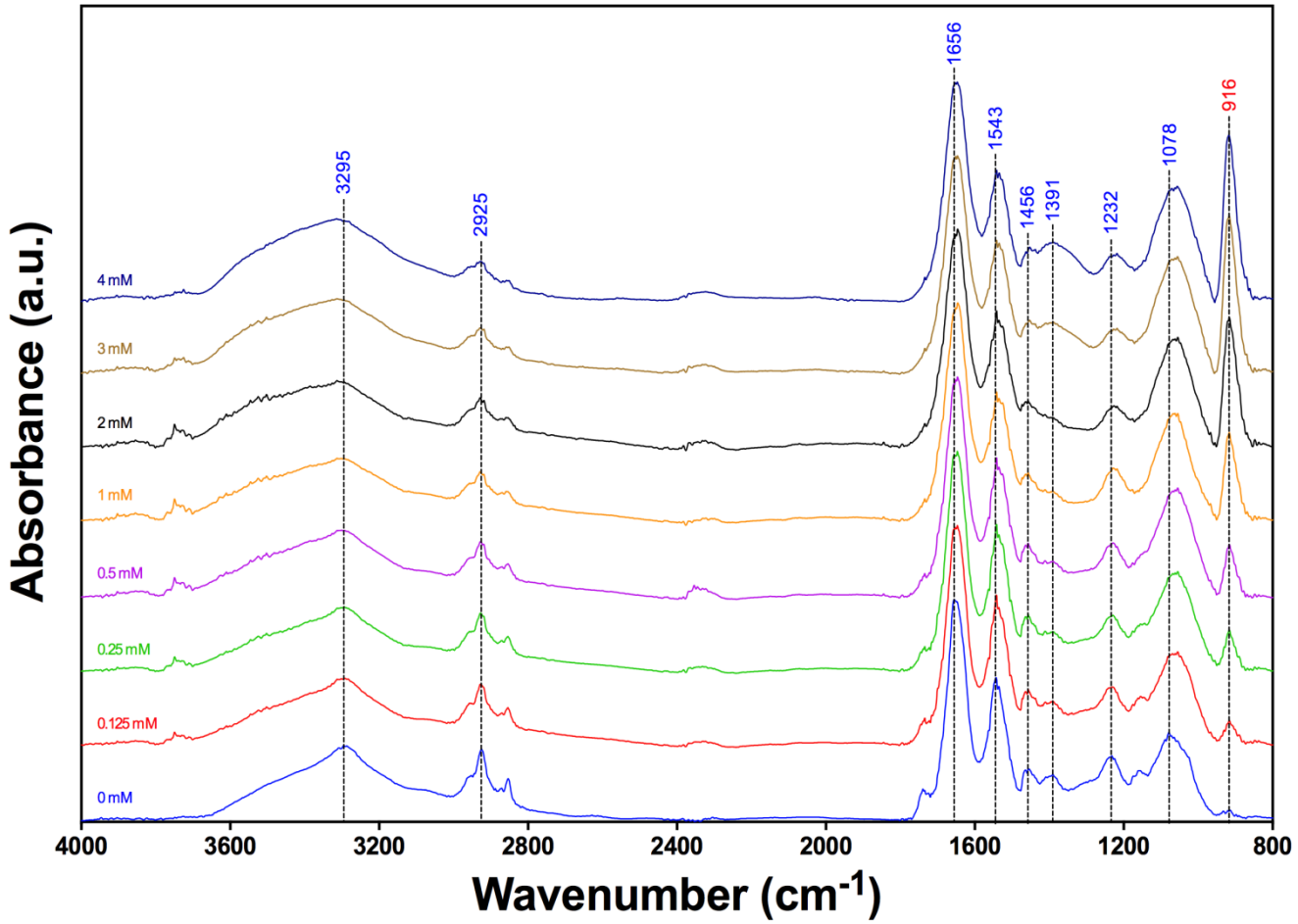

Figure 52. FTIR spectra of *P. putida* cell membrane isolates as a function of initial uranium concentration (pH 5.5, 0.1 M NaCl)

4.4.3.8 Uranium interactions with *B. subtilis* cell membrane isolates

The interaction of cell membrane isolates from *B. subtilis* with uranium gave similar levels of uranium retention as the cell membrane isolates from *P. putida*. XPS analysis indicated a similar macromolecular composition of membrane isolates from both bacteria, Table 7 and Table 9. Therefore, it was believed that there would be similar binding mechanisms between the two membrane isolates, which were different from those of whole cells and cell wall isolates from *B. subtilis*.

Figure 55 shows the FT-IR spectra of uranium biosorbed whole *B. subtilis* cell membrane isolates at pH 5.5.There were changes in the absorption bands within the lipidic adsorption band region of 3000 – 2850 cm^{-1}, Figure 53. Slight shifts in absorption band positions of the ν_{as} (CH_2) and ν_s (CH_2) were observed, in particularly at pH 5.5 where these bands shift from 2922 to 2926 and 2856 cm^{-1} to 2852 cm^{-1}, respectively, following uranium retention. The greatest change was the decrease in absorption band intensity within the pH range studied as the cell membrane isolates retained uranium. A greater decrease was observed at pH 5.5 as the uranium exposure concentration increased, Figure 53.

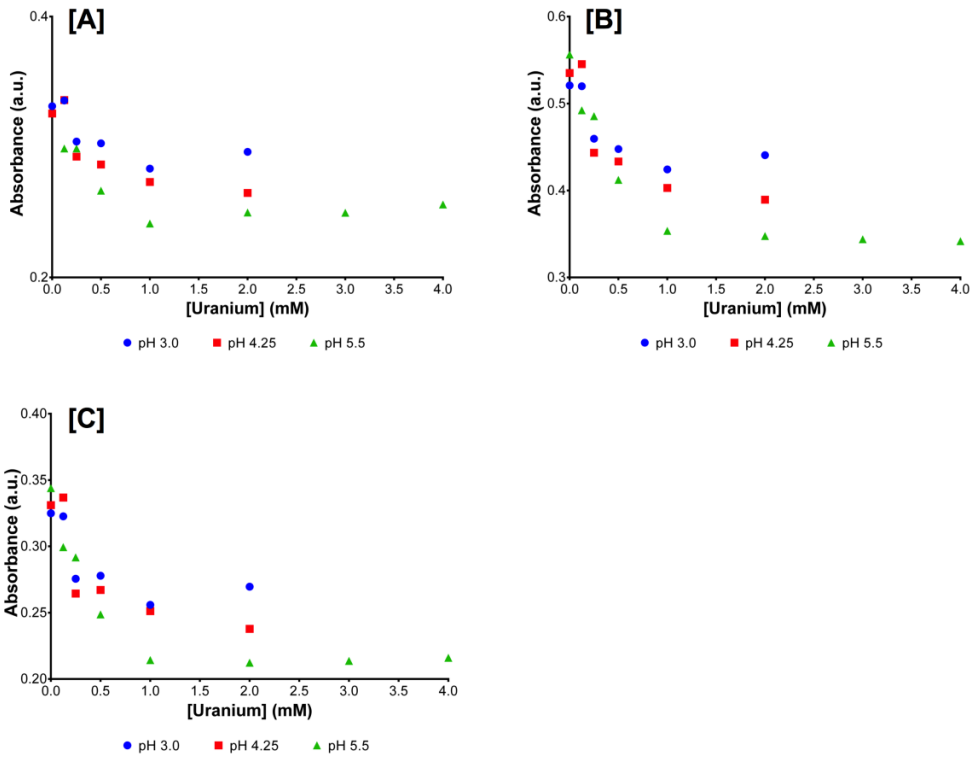

Figure 53. Changes in *B. subtilis* cell membrane isolate absorption band intensity for the ν_{as} (CH_3), ν_{as} (CH_2) and ν_s (CH_2), following uranium exposure.

This decrease in absorption intensity was similar to that of *P. putida* cell membrane isolates (Table 14) suggesting that changes in these adsorption bands were associated with the overall changes in membrane structure following uranium binding, rather than direct binding with lipid material. This was further supported by the broadening of ν_s (C=O) absorption band at 1739 cm^{-1}, attributed to carbon oxygen double bond within esters. There was broadening of this band as the uranium exposure concentration increased at pH 5.5, in comparison to little broadening at pH 3 and 4.25 (Baker et al., 2014, Shakirova et al., 2013, Merroun et al., 2003a, Kazy et al., 2008, Alessi et al., 2014).

At pH 5.5, there was a significant broadening of the ν_s (COO^-) absorption band at 1388 cm^{-1} as the membrane isolates retained uranium suggesting uranium interactions with membrane peptides and lipids (Pagnanelli et al., 2000, Choudhary and Sar, 2011). No change in absorption band shape was observed at pH 3 and little change at 4.25.

The greatest change in absorption band shape at all three pH values studied suggested favourable uranium interactions with phosphate groups as the membrane isolates retained uranium, Figure 54 (Merroun et al., 2003a, Kazy et al., 2008, Choudhary and Sar, 2011, Lu et al., 2013, Pan et al., 2015, Theodorakopoulos et al., 2015, Barkleit et al., 2011). The ν_{as} (PO_2) absorption band shifted from approximately 1226 cm^{-1} to 1224 cm^{-1} as the uranium exposure concentration increases to 2 mM at all pH values studied, suggesting favourable uranium interactions with phosphorylated groups, such as those found in phospholipids. This absorption band significantly changed in shape, broadened and decreased in intensity as the cell membrane isolates retained more uranium. Also, there was a large shift in position of the ν_s (PO_2) and ν (C-O, C-O-C, C-C) absorption bands. At pH 3 this band shifted from 1065 to 1058 cm^{-1} following exposure to 2 mM uranium. While at pH 4.25 and 5.5 the band shifted from 1071 to 1057 and 1058 cm^{-1}, respectively. As with *P. putida* cell membrane isolates, the broadening and shifts in the phosphate absorption bands masked the absorption band at 1176 cm^{-1} as cell membrane isolates retained more uranium.

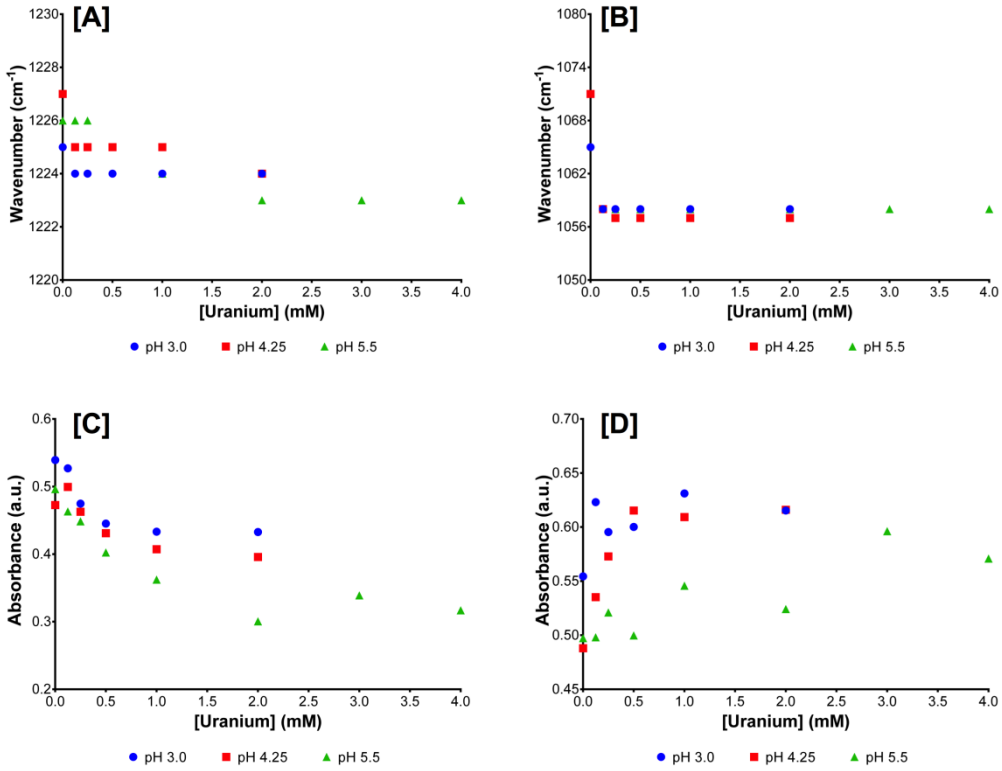

Figure 54. Changes in *B. subtilis* cell membrane isolate absorption band position [A-B] and intensity [C-D] for the ν_{as} (PO_2) and ν_s (PO_2), respectively, following uranium exposure.

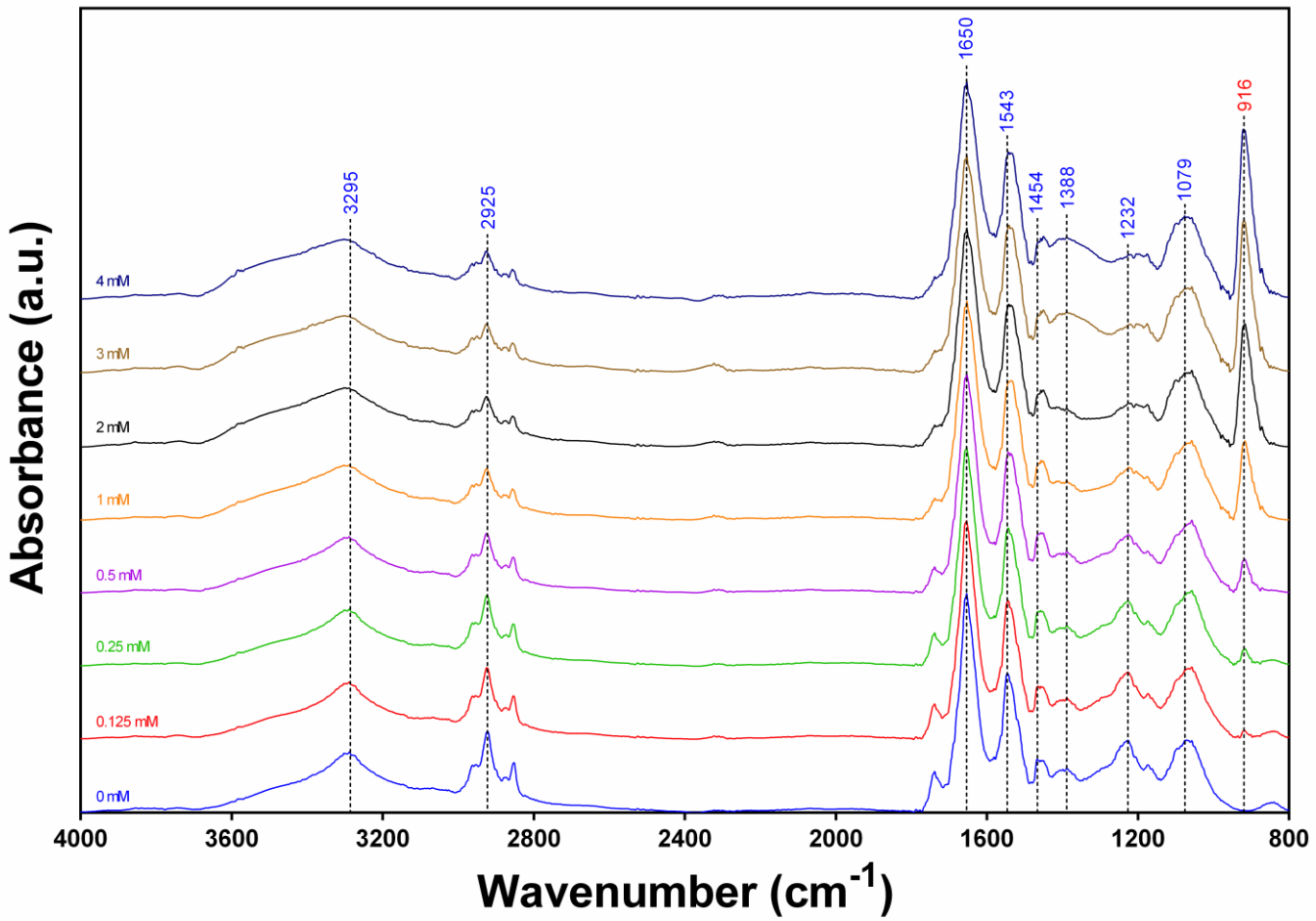

Figure 55. FTIR spectra of *B. subtilis* cell membrane isolates as a function of initial uranium concentration (pH 5.5, 0.1 M NaCl)

4.4.3.9 ATR-FT-IR Summary

The interactions of uranium with whole cells and cell surface structures, investigated by ATR-FT-IR, suggested that different mechanisms were involved in uranium retention due to the differences and abundance of functional groups associated with each cell surface structure. The presence of the broad and strong adsorption band between 3700 – 3000 cm^{-1} was attributed to O-H stretching vibrations of hydroxyl groups and N-H stretching of amino groups and were probably associated with uranium retention in all cell surface structures investigated (Baker et al., 2014, Kazy et al., 2009, Choudhary and Sar, 2011). Changes in absorption band position within the whole cells of the three bacteria studied suggested that phosphorylated biopolymers, amide and carboxyl groups from proteins and polysaccharides associated with the cell surface were responsible for uranium retention within the pH range studied. Changes in absorption band position corresponding to the ν_{as} (PO_2) of phosphate and broadening of the ν_s (COO^-) band from proteins were observed from whole *P. putida* and *B. subtilis* cells that retained uranium. These changes were more apparent at pH 5.5. Deprotonation of functional groups as the pH increased resulted in a greater retention of uranium from solution and hence, differences in adsorption band shape and position were observed.

A lack of phosphorylated biopolymers within the outermost layer of the cell surface of *D. radiodurans* explained why there was no shift in the ν_{as} (PO_2) absorption band position. This band was associated with intracellular phosphate components. Differences in the absorption band position, corresponding to the ν (C-O,C-O-C,C-C) were observed when whole *P. putida* and *D. radiodurans* cells retained uranium. No significant change in the absorption band position was observed following uranium exposure to whole *B. subtilis* cells, suggesting that the large quantities of peptidoglycan within the cell surface were not a major retainer of uranium from solution, apart from at pH 5.5. These results support the suggestion that role of phosphate and carboxyl groups from phosphorylated biomolecules and proteins at the surface of whole cells is important for uranium sequestration from solution, with preferential binding to different functional groups, depending on cell type. The results were comparable with other studies using FT-IR to investigate uranium interactions with whole cells that suggested that phosphate, carboxyl, hydroxyl and amino groups were the predominant functional groups responsible for uranium retention (Kazy et al., 2009, Choudhary and Sar, 2011, Pan et al., 2015, Lu et al., 2013, Theodorakopoulos et al., 2015). Furthermore,

other spectroscopic techniques, such as EXAFS and TRFLS, used to investigate uranium interactions with whole bacteria, suggested a similar process of uranium sequestration i.e. predominantly through phosphate groups (Renninger et al., 2004, Merroun et al., 2005, Merroun et al., 2011, Llorens et al., 2012, Morcillo et al., 2014, Reitz et al., 2014, Theodorakopoulos et al., 2015, Kelly et al., 2002).

It was suggested that there were different retention mechanisms involved between *P. putida* and *B. subtilis* cell wall isolates due to differences in cell wall architecture. It was suggested that biomolecules within the outer membrane of the Gram-negative cell wall of *P. putida* helped retain uranium from solution, but not through direct binding with lipids. This explained a decrease in intensity of the ν_{as} (CH_3), ν_{as} (CH_2) and ν_s (CH_2) absorption bands, associated with lipidic material, as the uranium exposure concentration increased. A higher decrease in intensity was observed at pH 4.25. In common with the whole cells, differences were observed in the absorption bands corresponding to phosphate groups, phosphorylated polymers and polysaccharides. This suggested that phosphate-containing molecules such as phospholipids from the outer membrane and phosphate-containing polysaccharides such as LPS were responsible for uranium retention within the Gram-negative bacterial cell wall. This was supported by previous studies suggesting that LPS retained uranium from solution using phosphate and carboxyl groups (Barkleit et al., 2008, Barkleit et al., 2011). Similar to whole *B. subtilis* cells, there was no significant shift in the absorption band corresponding to the ν (C-O,C-O-C,C-C) of polysaccharides following uranium binding to cell wall isolates, apart from at high concentrations of uranium at pH 5.5. This suggested that retention of uranium with the large quantities of peptidoglycan within the Gram-positive cell wall was a pH dependent process and occurred more frequently when exposed to high uranium concentrations. Potentiometric titrations of purified peptidoglycan revealed three pK_a values at 4.55, 6.31 and 9.56, corresponding to the carboxyl groups of glutamic acid, diaminopimelic acid and a combination of hydroxyl/amino groups, respectively (Barkleit et al., 2009). With only one pK_a value (4.55) reported within the pH range studied during this investigation (pH 3 – 5.5), it can be suggested that the net charge of the functional groups associated with polysaccharides within the cell wall isolate was positive at pH 3 and 4.25 due to protonation of corresponding functional groups. Therefore, this net positive charge would result in few electrostatic interactions with uranium at lower pH, explaining the lack of shift in ν (C-O,C-O-C,C-C) band position in the ATR-FT-IR spectra of cell wall isolates retaining uranium (Barkleit et al., 2009).

Shifts corresponding to changes in the ν_{as} (PO_2) absorption band position suggested that uranium interacted with phosphate groups within the Gram-positive cell wall, such as those in (lipo)teichoic acids and proteins associated with the phosphorylated cell wall. The latter was further confirmed by changes in the shape of the absorption bands associated with protein as the uranium exposure increased within the pH range studied. Broadening of the δ (N-H) and the ν_s (COO^-) absorption bands suggested favourable interactions with carboxyl groups associated with cell surface proteins. Conformational changes in protein structure following uranium binding probably contributed to changes in δ (N-H) adsorption band shape rather than those being due to uranium binding with amino groups. The pKa for amino groups is 9.0; hence within the pH range investigated, the amino groups exhibited a positive charge and would not bind positively charged U(VI) species. The interactions of uranium with the cell wall isolates of the Gram-negative *P. putida* and Gram-positive *B. subtilis* used in this study are represented in Figure 56.

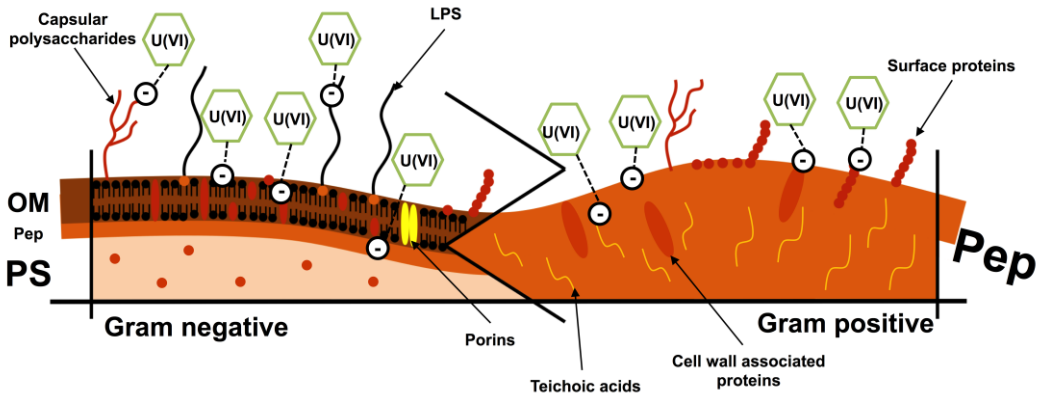

Figure 56: Uranium interactions with the cell wall isolates of *P. putida* (Gram-negative) and *B. subtilis* (Gram-positive). LPS: lipopolysaccharide OM: outer membrane, Pep: peptidoglycan, PS: Periplasmic space.

ATR-FT-IR spectra suggested that there were similar mechanisms of uranium binding for cell membrane isolates from *P. putida* and *B. subtilis* due to similarities in macromolecular composition. A decrease in absorption intensity corresponding to the ν_{as} (CH_3), ν_{as} (CH_2) and ν_s (CH_2) absorption bands occurred as both membrane isolates retained more uranium from solution. Lipids are unreactive and non-polar and would not directly bind uranium. Therefore, changes in these adsorption bands associated with lipids were attributed to the overall changes in membrane structure following uranium binding, rather than direct binding with lipidic material. Shifts and broadening of absorption bands corresponding to the ν_{as} (PO_2) and ν_s (PO_2) within both isolates suggested that there were favourable interactions with phosphate groups present

within the phospholipids of the cell surface membrane isolates. A larger shift at pH 5.5 suggests more favourable interactions towards more neutral conditions. Finally, the broadening of the protein absorption bands associated with carboxyl groups in both membrane isolates indicated that there were interactions with membrane associated proteins. The interactions of uranium with the cell membrane isolates used in this study are representative in Figure 57.

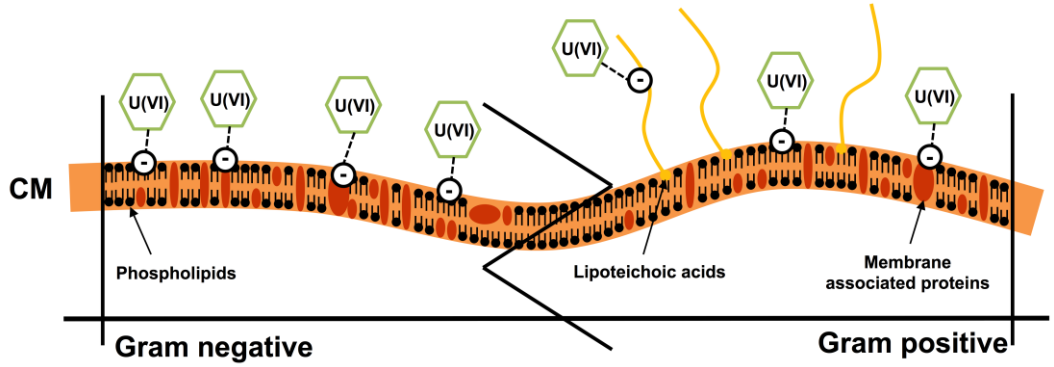

Figure 57. Uranium interactions with the cell membrane isolates of *P. putida* (Gram-negative) and *B. subtilis* (Gram-positive). CM: cell surface membrane

Overall, the ATR-FT-IR data suggested that numerous functional groups were associated with uranium retention and that retention was dependent on the cell surface structure and whether it was of Gram-negative or Gram-positive origin. The major functional groups associated with uranium binding were shown to be phosphate and carboxyl. The majority of cell surface structures contain available forms of these. However, the origin of these groups varies with structure type. Differences in uranium retention mechanisms were observed between the whole cells and cell wall isolates of the bacteria investigated. Due to similarities in macromolecular composition of the cell membrane isolates obtained from *P. putida* and *B. subtilis*, these isolates exhibited a similar mechanism of uranium retention. The most significant changes in absorption band position shifts, shape and intensity were at pH 5.5 for structures that retained uranium, supporting a pH-dependent biosorption process for uranium with the bacterial cell surface. This was due to a greater number of deprotonated groups at near-neutral pH, resulting in greater uranium retention. It is unknown how much uranium is retained by individual biomolecules (i.e. peptides, phospholipids and polysaccharides) or functional groups (i.e. phosphate, carboxyl and hydroxyl groups) present within each cell surface structure. To understand these specific mechanisms, extraction and purification of these biomolecules from the cell surface structures would be required.

4.5 Conclusions

The current work describes the ability of cell surface structures and their role in the biosorption of uranium. The differences in cell surface structure and whether they were of Gram-negative or Gram-positive origin had an influence on the biosorption of uranium. The preference for uranium biosorption of the structures investigated can be summarised as; *B. subtilis* cell wall isolates > *B. subtilis* dead cells > *B. subtilis* live cells > *P. putida* cell wall isolates > *P. putida* dead cells > *P. putida* live cells > *P. putida* cell membrane isolates > *B. subtilis* cell membrane isolates > *D. radiodurans* live cells.

The cell wall and lysed cells of *B. subtilis* exhibited the highest uranium biosorption capacity. ATR-FT-IR suggested that functional groups associated with proteins and phosphate-containing biomolecules of the cell wall mediated uranium binding. The cell walls and lysed cells of both strains exhibited a higher uranium capacity than live cells or cell surface membrane isolates of both strains. These results demonstrated that accounting for the removal of U(VI) from solution using whole cell dry weight underestimates the capacity of organisms to sequester uranium by their cell wall constituents. Intracellular components of whole cells contribute to the dry weight but may not contribute to the retention of uranium, and hence result in a lower uranium capacity per kg of biomass. Greater uranium retention was exhibited by all structures investigated as the pH increased. This confirmed the suggestion that the cell walls and associated biomolecules of many bacteria are the preferential binder for U(VI) from aqueous solutions, due to the increased concentration of functional moieties favourable for uranium binding, such as carboxyl and phosphate groups.

Further extraction of the macromolecular constituents of each cell surface component is required to fully understand the role of individual macromolecules involved in uranium biosorption at the cell surface. This could include protein and peptidoglycan extraction and purification from the cell walls of *B. subtilis* as well as protein and hydrocarbon extraction and purification from *P. putida* cell wall isolates. Overall, the functional groups associated with the cell walls of the Gram-positive and Gram-negative bacteria used in this study are appropriate remediators of uranium-contaminated aqueous environments.

Chapter 5: Tolerance and toxicity mechanisms exhibited by bacteria to withstand uranium.

5.1 Abstract

This work describes the effects tolerance, toxicity and survival mechanisms exhibited by *P. putida* 33015 and *D. radiodurans* R1 to withstand uranium during bacterial growth. The minimum inhibitory concentrations of U(VI) were determined by optical density measurements while cell viability and cellular activity were examined by flow cytometry. *P. putida* was able to grow in concentrations up to 0.5 mM at pH 5 and 7 while *D. radiodurans* could only tolerate concentrations up to 0.25 mM total U(VI) at pH 7. Fluorescein Diacetate-Propidium Iodide (FDA-PI) staining suggested a decrease in the number of viable cells as the U(VI) concentration in culture media increased for both strains investigated. 5-Cyano-2,3-ditolyl tetrazolium chloride (CTC) staining suggested a decrease in the respiratory activity of *P. putida* cells as the U(VI) concentration increased. Conversely, *D. radiodurans* exhibited an increase in respiratory activity as the U(VI) concentration increased, until toxicity was reached. Electron microscopy showed dense uranium precipitates located both at the surface and within the cells of both strains. *D. radiodurans* further exhibited precipitation external to the cell. This precipitation was linked to microbial phosphatase activity and subsequent orthophosphate release that readily interacted with the positively charged U(VI) species. High-Angle Annular Dark Field-Scanning Transmission Electron microscopy (HAADF-STEM) indicated the precipitation of uranium phosphate-like minerals by both strains. This study concurs with previous literature, in that Gram-negative bacteria were found to be more tolerant of higher uranium concentrations than Gram-positive strains and that microbial phosphatase activity and deposition of uranium minerals onto the cell surface is a tolerance mechanism to withstand uranium during growth.

5.2 Introduction

The interactions of uranium with bacteria have been well documented for numerous Gram-positive and Gram-negative strains (Macaskie et al., 1992, Macaskie et al., 2000, Merroun et al., 2006, Nedelkova et al., 2007, Merroun et al., 2011, Reitz et al., 2014). Several of these bacteria have been characterised and exhibited tolerance to uranium over a wide range of concentrations and at different pH. For example, the Gram-negative *Acidithiobacillus ferrooxidans* displayed a tolerance to uranium of up to 9 mM at pH 7 while the Gram-positive *Microbacterium oxydans* S15-M2 tolerated up to 4 mM at pH 7 (Merroun and Selenska-Pobell, 2001, Nedelkova et al., 2007). Many of these studies were conducted by resuspending live cells in fresh uranium solution, rather than the addition of uranium to growth media. This change to fresh uranium solution was not representative of bacterial growth or environmental conditions and only determined the ability of a thriving live bacterial culture to withstand uranium within the time period investigated. Therefore due to these experimental design issues, the effect of uranium on the growth of the bacteria is not fully understood.

A limited number of studies have investigated the growth of bacterial cultures and their subsequent viability and cellular activity in the presence of uranium. This was because of issues concerning the solubility of U(VI) species in complex culture media. Uranium precipitates from solution in the presence of phosphates and carbonates, with the solution pH is a governing factor in its solubility (Gavrilescu et al., 2009). The speciation and solubility of uranium within culture media was important since aqueous species are more toxic towards bacteria. For example, highly mobile species such as UO_2^{2+} readily displace essential ions and block functional groups on biomolecules (e.g. enzymes and nucleotides), inhibiting many metabolic processes (Sani et al., 2006). It is suggested that bacteria precipitates uranium at the cell surface and externally through microbial phosphatase activity as a tolerance mechanism within aerobic environments (Hu et al., 2005). Many Gram-negative and Gram-positive bacteria have exhibited this activity at varying levels. Few studies have tried to infer whether there is a significant difference between the tolerance of Gram-negative and Gram-positive bacteria to U(VI) and their ability to biomineralise uranium.

In this study, we have compared the growth of *P. putida* 33015 and *D. radiodurans* R1 and how both strains deal with uranium toxicity. Optical density measurements were performed in order to determine the minimum inhibitory concentrations (MIC) of

uranium. Flow cytometry was used to investigate the cell viability, respiratory and metabolic activity of proliferating cultures grown in the presence of increasing uranium concentration at different pH. With this information, it was used to help infer whether Gram-negative or Gram-positive bacteria are more susceptible to uranium. High Resolution-Transmission Electron Microscopy (HR-TEM) and High-Angle Annular Dark Field-Scanning Transmission Electron Microscopy (HAADF-STEM) were used to determine the localisation of uranium precipitates. Finally, acid phosphatase activity and orthophosphate release were quantified to assess the bacteria's capabilities to biomineralise uranium from culture media. If the bacteria exhibited acid phosphatase activity, it would be hypothesised that hydrolysed orthophosphate could precipitate uranium from solution as uranium phosphate minerals, reducing its solubility and subsequent toxicity.

5.3 Experimental Procedures

5.3.1 Bacteria and growth conditions

Two bacteria were used in this study; *Pseudomonas putida* 33015 (ATCC 33015) and *Deinococcus radiodurans* R1 (ATCC 13939) were obtained from LGC standards. *P. putida* 33015 was grown in sodium benzoate media (Appendix Table 14) for routine growth and in low phosphate media (LPM) (Appendix Table 15) for uranium sensitivity and toxicity experiments. For *D. radiodurans* R1, TYG media was used for routine growth (Appendix Table 16) whilst a modified LPM was used for uranium sensitivity and toxicity tests (Appendix Table 17). The LPMs used in this study were selected because the bacteria could be cultured in them and to minimise uranium precipitation with components of both culture media. Uranium speciation was calculated from the ionic and buffering components of each LPM using visual MINTEQ 3.1, Appendix Table 18 and Appendix Table 19.

5.3.2 Uranium sensitivity tests and MTC/MIC determination

To determine the maximum tolerance concentration (MTC) and minimum inhibitory concentration (MIC) of uranium, *P. putida* 33015 and *D. radiodurans* R1 were grown in their respective LPM containing increasing concentrations of uranium at pH 5, 7 and 9. LPM was supplemented using 0.1 M $UO_2(NO_3)_2 \bullet 6H_2O$ to the desired concentration and the pH altered using 10 % HCl and NaOH. The 0.1 M uranium stock solution was prepared by dissolving 5.15 g in 100 mL 1 % HNO_3 to prevent any precipitation of uranium during storage. Cells were incubated at 30 °C, shaken at 170 rpm for 48 hours and optical density measurements were taken at 600 nm at timed intervals to compare with non-inoculated media controls. Absorbance values were obtained using a microplate reader. The MTC was defined as the highest investigated U(VI) concentration in which bacterial growth was observed in LPM after a 24-hour period for *P. putida* 33015 and a 48-hour period for *D. radiodurans* R1. The MIC was defined as the lowest concentration at which complete cell growth was inhibited.

5.3.3 Cell viability and metabolic activity by flow cytometry

To measure the number of viable and metabolically active cells grown in the presence of uranium, flow cytometry was used. *P. putida* 33015 and *D. radiodurans* R1 were grown to late exponential phase as described previously (Section 5.3.2). Cells were harvested by centrifugation (10,000 rpm, 10 minutes, 4 °C) and washed 3 times using sterile

phosphate buffered saline (PBS, pH 7.4). Cells were subsequently diluted to ~ 1 x 10^6 cells mL^{-1} using PBS before the addition of any fluorescent stains.

To measure the number of viable cells, fluorescein diacetate (FDA, Acros Organics) and propidium iodide (PI, Invitrogen) were used. The FDA working solution was prepared by diluting the 1 mg mL^{-1} stock solution (dissolved in acetone and stored at -20 °C protected from light) in PBS. 0.1 mg mL^{-1} PI was prepared by dissolving the desired volume in PBS (stored at -20 °C protected from light). To 1 mL of cells, 20 µL of 0.1 mg mL^{-1} FDA working solution and 2 µL of 1 mg mL^{-1} PI were added sequentially, mixed and incubated at room temperature for 15 minutes protected from light, then analysed immediately. To measure the metabolic activity of cells, 3,3′-dihexyloxacarbocyanine iodide ($DiOC_6$, Invitrogen) was used. 20 µL of 10 µM stock solution (dissolved in PBS) was added to 1 mL of cells and incubated at room temperature for 15 minutes protected from light, then analysed immediately. A dead control was prepared by heating up live cells to 90 °C for 1 hour.

Stained cells were analysed using a BD Biosciences FACSCanto II Flow Cytometer equipped with 3 lasers (UV: 405 nm, Blue: 488 nm, Red: 630 nm) coupled with BD FACSDiva V6.3 software. Samples were analysed using a logarithmic scale at medium speed. FDA (FITC-A) and PI (PE-A) dual-stained cells were excited at 498 nm and 535 nm (blue laser), respectively; with emission recorded at 516 nm (green light) and 620 nm (red light), using 530/30 bandpass and 610 longpass filters respectively. $DiOC_6$ stained cells were excited at 482 nm (blue laser) and emission recorded at 504 nm (green light) using the 530/30 bandpass filter. Flow cytometry gates were applied using dead cells of both strains to calibrate the instrument for subsequent analysis, Appendix Figure 27 and Appendix Figure 28.

To measure the respiratory activity of cells, 5-Cyano-2,3-ditolyl tetrazolium chloride (CTC, Sigma) and SYTO® 24 green (Life Technologies) were used. 100 µL of 50 mM CTC (dissolved in ultra-high quality water) was added to 1 mL of cells, mixed and incubated at room temperature, protected from light for 30 minutes. Cells were harvested by centrifugation (10,000 rpm, 10 minutes, 4 °C), resuspended and fixed in 1 mL 1 % glutaraldehyde. Prior to analysis, 6 µL of a 1 in 50 working solution of SYTO® 24 green was added to the fixed cells. The SYTO® 24 green working solution was prepared by diluting 20 µL 0.5 mM SYTO® 24 green in 980 mL DMSO, protected from light.

Fixed and stained cells were analysed using a BD Biosciences FACSCalibur flow cytometer equipped with 2 lasers (Blue: 488 nm, Red: 635 nm). CTC stained cells (FL3-H) were excited at 450 nm (blue laser) and emission intensity recorded at 630 nm (red light) with a 585 bandpass filter while SYTO® 24 green stained cells (FL1-H) were excited at 490 nm (blue laser) and emission intensity recorded at 515 nm (blue/ green light) using a 530/30 bandpass filter. Only dual-stained cells were counted and taken into consideration to eliminate any interference from cell debris and any unbound stain. Non-specific staining wasn't observed with uranium precipitates within the cells, and therefore, no interference in the flow cytometric profiles was observed. Samples were analysed in a logarithmic scale at medium speed. Analysis was performed using BD CellQuest Pro software (Version 5.2.1). Comparison of control samples with single-stained and unstained cells were used to determine the FL1-H and FL3-H gates, Appendix Figure 29 and Appendix Figure 30.

5.3.4 Uranium localisation by HR-TEM/ HAADF-STEM/ EDX

P. putida 33015 and *D. radiodurans* R1 cells that accumulated uranium were grown to late exponential phase, harvested and washed with 0.1 M NaCl. Samples were prepared for Transmission Electron Microscopy (TEM) as described previously (Merroun et al., 2005). Washed cells (using 0.1 M cacodylate buffer, pH 7.4) were fixed in 0.1 M cacodylate buffer (pH 7.4) containing 2 % glutaraldehyde. Cells were fixed in 1 % OsO_4 in cacodylate buffer (60 minutes, 4 °C) before dehydration with ethanol and embedding in Spurr resin. 0.25 µm sections were placed on carbon coated copper grids and analysed using a Phillips CM 20 high-resolution TEM (200 kV acceleration voltage) equipped with Energy-dispersive X-ray (EDX) analysis (200 acceleration voltage with a 70 Å spot size). High-Angle Annular Dark Field-Scanning Transmission Electron Microscopy (HAADF-STEM) using a FEI TITAN G2 80-300, equipped with an EDX analyser, was used to gather elemental maps of uranium and phosphorus within the uranium-accumulated biomass. TEM sample holders were cleaned by plasma to prevent any contamination prior to STEM analysis.

5.3.5 Acid phosphatase activity and phosphate hydrolysis

To determine the acid phosphatase activity of the bacteria in the presence of uranium during growth, 50 µL of bacterial suspension was added to 50 µL of 4-Nitrophenyl phosphate solution (1 % w/v in 0.1 M $NaClO_4$). Samples were incubated at 30 °C shaking at 170 rpm for 30 minutes before the reaction was stopped by adding 200 µL 0.5 M

NaOH. The absorbance was measured at 405 nm with a microplate reader. A 300 µL 50 µM *p*-Nitrophenyl standard solution (prepared in 0.5 M NaOH) was used to calculate the specific activity in units mL^{-1}. One unit of acid phosphatase will hydrolyse 1 µmole of 4-nitrophenyl phosphate per minute at pH 4.8 at 37 °C as defined by the assay kit purchased from Sigma-Aldrich (CS0740). Orthophosphate released was quantified as described previously, Section 2.3.3.

5.4 Results and Discussion

5.4.1 Bacterial growth and uranium toxicity of *P. putida* 33015 and *D. radiodurans* R1

P. putida 33015 and *D. radiodurans* R1 were cultured in low phosphate media (LPM) in the presence of increasing uranium concentration at pH 5, 7 and 9. The pH values were representative of those found within natural environments and those with elevated uranium concentrations, such as those in acid and alkaline mine drainage (Beazley et al., 2007, Martinez et al., 2007, Chapon et al., 2012, Mondani et al., 2011, Bondici et al., 2013, Wolfaardt et al., 2008). *P. putida* 33015 growth was observed up to a concentration of 0.5 mM at pH 5 and 7, Figure 58. In the presence of 1 mM uranium, no noticeable growth was observed at either pH. A negative optical density was observed due to precipitation of media components at the higher uranium concentrations. Furthermore, no growth was observed within the time period investigated at pH 9, barring the control reaction where no uranium was present. Growth began following an extended lag phase of approximately 12 hours. Following this lag phase, the control growth experiment at pH 9 reached the stationary phase following 24 hours reaching a maximum OD_{600} of 0.139. This was substantially less than the control growth experiments at pH 5 and 7 where the maximum OD_{600} following a 24-hour cultivation was measured at 0.698 and 0.731, respectively.

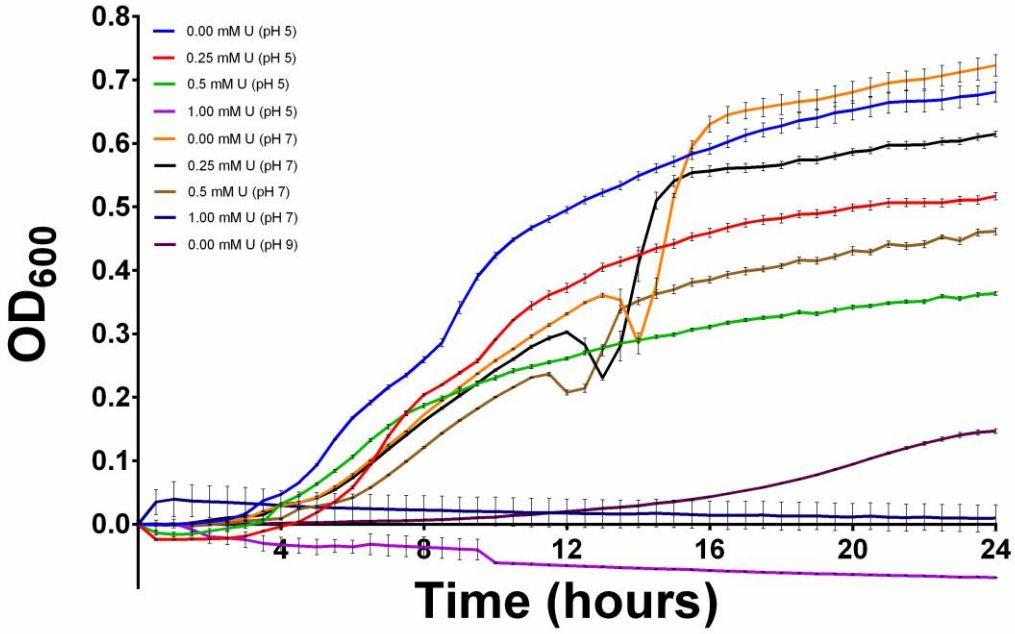

Figure 58. Growth curves of *P. putida* 33015 in LPM as a function of uranium solution concentration and pH.

Interestingly, the growth patterns observed within the 24-hour experimental growth period were different at pH 5 and 7. At pH 5, the initial log phase occurred between 4 and 11 hours for the growth experiments before slowly reaching the stationary phase towards the end of the 24-hour incubation. There was a slight decrease in growth rate at approximately 6-8 hours, suggesting that the cultures reach stationary phase. The maximum OD_{600} recorded at this time period was 0.698, 0.508 and 0.367 for cultures in the presence of 0.00, 0.25 and 0.5 mM U(VI), respectively. At pH 7, following an initial log growth phase of between approximately 4 and 11 hours, there was a small decrease in optical density, indicating cell death. This was followed by a noticeable increase in optical density in a secondary log phase for approximately 2 hours, reaching the stationary phase between 13 and 16 hours. The maximum OD_{600} recorded after 24 hours were 0.723, 0.615 and 0.462 in the presence of 0.00, 0.25 and 0.5 mM U(VI), respectively.

This secondary growth phase phenomenon, called *diauxie*, is characterised by a double growth cycle composed of two exponential phases separated by an intermediate stationary or death phase (Monod, 1949). This can occur when there is an initial utilisation of a primary carbon source within media composed of multiple sources. Once the primary carbon source has been fully consumed, the microbial system will adjust to use an alternate carbon source within the growth medium, hence the secondary log phase growth. Within the LPM, Trizma-base, peptone, glycerol and thiamine hydrochloride can be utilised as carbon sources. Glycerol is often used first rather than peptone and Trizma-base due to the simplicity of its molecular structure. Therefore, it is easier for the metabolising bacteria to break down. *P. putida* 33015 would have had to synthesise enzymes to break down the amino acids within peptone to use its carbon as a nutrient source. Trizma-base is commonly used as a buffering component in complex culture media, rather than a nutrient source. However, the presence of Trizma-base in growth media has been demonstrated to promote bacterial growth (Fábregas et al., 1993). Diauxic growth patterns have been well documented in many systems that have multiple carbon containing nutrient sources, in which simple carbon sources were used primarily for bacterial growth, such as glucose (Monod, 1949, Pelletier et al., 1994, Meredith and Woodard, 2005, Narang and Pilyugin, 2007).

The specific growth rates (μ) of these growth curves were calculated using their log phases by applying the following calculation, Equation 20. Specific growth rates for *P. putida* 33015 are shown in Table 15.

$$\boldsymbol{\mu} = 2.303 \times \frac{\log_{10} OD_{600}(end\ of\ \log phase) - \log_{10} OD_{600}(start\ of\ \log phase)}{Time(hours) at\ end\ of\ \log phase - Time(hours) at\ start\ of\ \log phase} \qquad \text{Equation 20}$$

Table 15. Specific growth rates (μ), maximum investigated tolerance concentration (MTC) and minimum inhibitory concentrations (MIC) for the growth *P. putida* 33015.

pH	[Total U(VI)] (mM)	Specific Growth Rate (μ)			MTC/MIC (mM)
5	0.00	0.632*	0.225#	0.327^	0.25/0.50
	0.25	0.421*	0.145#	0.303^	
	0.50		0.245^		
7	0.00	0.270*	0.571#	0.221^	0.25/0.50
	0.25	0.268*	0.506#	**0.229^**	
	0.50	0.249*	0.402#	0.218^	
9	0.00		0.189		0

*Primary log phase specific growth rate # Secondary log phase specific growth rate ^Total log phase specific growth rate

The specific growth rates obtained from the bacterial growth curves in the presence of uranium indicated different rates of growth at different times as a function of pH. The cultures exhibited a diauxic growth pattern in the presence of 0.00 - 0.25 mM U(VI) at pH 5 and between 0 - 0.5 mM U(VI) at pH 7. The primary log phase growth had a greater specific growth rate for cultures grown at pH 5, while the growth rate for the secondary growth phase was much greater than that for cultures grown at pH 7. This difference in growth rate could be attributed to a faster metabolism of the primary carbon source at pH 5 and of the secondary carbon source at pH 7 due to an increased availability arising from differences in uranium speciation within the LPM. Changes in uranium speciation were observed as a function of pH and uranium concentration. At pH 5, the culture media was dominated by positively charged species, such as UO_2^{2+}, $(UO_2)_2(OH)_2^{2+}$ and $(UO_2)_3(OH)_5^{+}$. At pH 7, $(UO_2)_3(OH)_5^{+}$ and $(UO_2)_4(OH)_7^{+}$ were the dominant species that reduced the solubility, resulting in uranium precipitation, Appendix Table 18. However, this speciation was only an estimate because the it was based on the assumption that no U(VI) carbonate species were formed in the culture media. This was due to limitations in the visual MINTEQ software. The overall specific growth rate was greater for cultures grown at pH 5, with decreasing growth rates as the uranium concentration increased in solution for both pH values. However, the overall optical density was greater at pH 7 for each uranium concentration tested. The decrease in specific growth rate and overall optical density as the uranium concentration increased within the culture media were both attributed to the inhibitory effect of uranium on the growth of bacteria (Nedelkova

et al., 2007). At 1 mM U(VI) there was no observable growth at pH 5 or 7. This is was due to the effect of uranium toxicity on the growing culture, preventing replication.

After a 24-hour growth period, the maximum tolerance concentration (MTC) and minimum inhibitory concentration (MIC) of U(VI) were determined. The MTC and MIC for U(VI) at pH 5 and 7 were 0.25 and 0.5 mM. However, the optical density of cultures grown at pH 7 was greater than those at pH 5. As described above, there were differences in U(VI) speciation at pH 5 and 7. This difference and the greater acidic conditions at pH 5 hindered bacterial growth within the time period investigated, decreasing the optical density.

D. radiodurans R1 growth was observed in the presence of U(VI) at pH 7 in LPM. Growth was only observed at pH 5 and 9 in the control experimental culture containing no uranium, Figure 59. Cell death was observed at pH 5 following a 24-hour incubation period with a maximum OD_{600} value of approximately 0.2. However, there was a prolonged lag phase for control cultures grown at pH 9, whereby the logarithmic phase started at approximately 40 hours, with a maximum OD_{600} of 0.1 mM within the time period investigated. The increased acidity (pH 5) and alkalinity (pH 9) of these culture media compared to cultures grown at pH 7 had an inhibitory effect on bacterial growth. Additionally, the differences in U(VI) species as a function of pH could would have a toxic effect on the bacteria.

Growth was observed in the presence of uranium at pH 7 only up to a concentration of 0.25 mM total U(VI). No bacterial growth was observed in the presence of 0.5 mM total U(VI) in *D. radiodurans* R1 specific LPM. Speciation using Visual MINTEQ (Appendix Table 19) of uranium in LPM showed that, at 0.05 mM total U(VI), the dominant U(VI) species were $(UO_2)_3(OH)_5^+$ and UO_2NTA^-. Nitrilotriacetic acid (NTA), though present in small concentrations (Appendix Table 17) chelated positively charged U(VI) species in solution. As the total U(VI) concentration increased, there was an increase in the concentrations of $(UO_2)_3(OH)_5^+$ and $(UO_2)_4(OH)_7^+$ and a decrease in UO_2NTA^-. As the chelated U(VI) species were not available, the amount of soluble U(VI) was calculated and the percentage of U(VI) species adjusted. The amount of soluble U(VI) was calculated as 0.033, 0.078 and 0.220 mM for cultures with 0.05, 0.10 and 0.25 mM total U(VI), respectively.

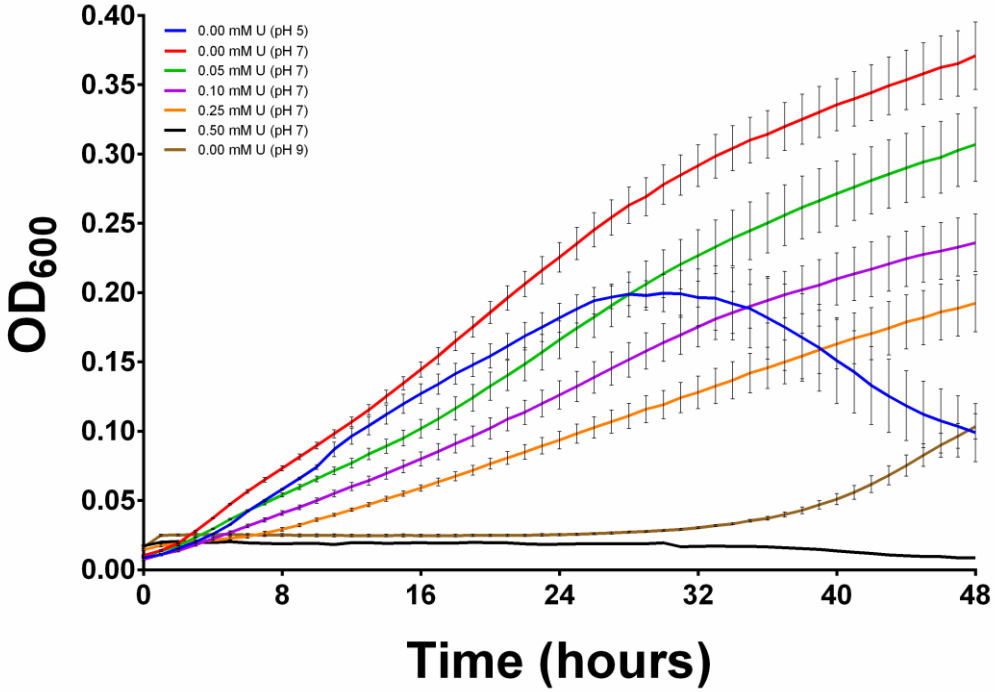

Figure 59. Growth curves of *D. radiodurans* R1 in LPM as a function of total uranium solution concentration at pH 7.

After 48 hours, the cultures grown in the presence of increasing U(VI) concentration never reached their stationary growth phase. As the concentration of U(VI) decreased in solution, the start of the retardation phase (the time at which the growth rate starts to decline) changed. This phase starts after approximately 24 for the control and is delayed to 28, 33 and 46 hours in the presence of 0.05, 0.10 and 0.25 mM U(VI), respectively. The maximum OD_{600} achieved by these cultures were 0.370, 0.307, 0.236 and 0.192 when grown in the presence of 0.00, 0.05, 0.10 and 0.25 mM total U(VI), respectively.

The specific growth rates, μ, decreased from 0.095 to 0.037 as the soluble U(VI) concentration increased from 0.00 to 0.22 mM, Table 16. The maximum OD_{600} and μ recorded for *D. radiodurans* R1 cultures was noticeably smaller than those obtained from *P. putida* 33015 cultures. These values were based on optical density recordings and cell size was not taken into consideration during these measurements. The diameter of *D. radiodurans* (approximately 1.5 – 3.5 µm) is reportedly greater than that of *P. putida* (0.5 - 1.0µm) (Hwang et al., 2008). Therefore, it can be suggested that it was the inhibitory effect of U(VI) that is responsible for differences in optical density and subsequent specific growth rates, μ. However, substantial EPS production has been documented for *P. putida* strains (Vilain et al., 2009, Steinberger and Holden, 2005, Kachlany et al., 2001, Matsui et al., 2003) in comparison to *D. radiodurans* (Battista,

1997). This could contribute to the differences in optical density of macromolecules that absorb light at the same wavelength. The MTC and MIC of cultures grown in LPM at pH 7 were 0.078 and 0.220 soluble U(VI).

Table 16. Specific growth rates (μ), maximum tolerance concentration (MTC) and minimum inhibitory concentrations (MIC) for the growth of *D. radiodurans* R1 grown in LPM.

pH	[Total U(VI)] (mM)	[Soluble U(VI)] (mM)	Specific Growth Rate (μ)	MTC/MIC (mM)
5	0.00	0.000	0.093	0.00
7	0.00	0.000	0.095	0.10/0.25
	0.05	0.033	0.057	
	0.10	0.078	0.054	
	0.25	0.220	0.037	
9	0.00	0.000	0.088	0.00

Numerous bacteria have been isolated from uranium-contaminated environments and their uranium tolerance investigated under a variety of experimental conditions. Previous studies indicate varying tolerance levels to uranium, Table 17. The uranium concentrations in which bacterial growth was observed ranged from 30 mM to 50 µM from those isolated from uranium-contaminated environments (Llorens et al., 2012, Theodorakopoulos et al., 2015). The MIC from the experimental data fell within this range, with the Gram-negative strain exhibiting a higher uranium tolerance than the Gram-positive strain represented in this study.

The inhibitory effect of uranium on the growth of bacteria is better documented for Gram-negative isolates than for those of Gram-positive origin, Table 17. The Gram-negative strains previously studied exhibited a higher tolerance to uranium than Gram-positive. A number of Gram-negative strains exhibited tolerance to uranium up to 30 mM at pH 7 (Llorens et al., 2012) and higher concentrations at lower pH (up to 2 mM at pH 5) than the Gram-positive isolates studied (Sousa et al., 2013, Kumar et al., 2011). The maximum documented uranium tolerance concentration for Gram-positive bacteria was 4 mM at pH 7 for *M. oxydans* S15-M2 (Nedelkova et al., 2007). Gram-positive cultures exhibiting tolerance at lower pH only could withstand concentrations up to 0.5 mM (Reitz et al., 2014, Sowmya et al., 2014, Martinez et al., 2007). The higher tolerance to U(VI) by Gram-negative bacteria (Table 17) compared to Gram-positive suggests an overall increased tolerance for Gram-negative isolates.

However, from all the previous studies compiled, there were no underlying experimental conditions and the growth and tolerance of the bacteria to uranium have

been investigated in various ways. Therefore, the experimental conditions are not directly comparable. The pH of the uranium-containing culture media and subsequent uranium speciation may affect the growth of the bacteria due to changes in availability and subsequent toxic effects of aqueous uranium species. For example, the Gram-negative *Serratia marcesecens* tolerated concentrations of 3.5 – 4 mM U(VI) at pH 7 but only 2 mM at pH 3.5, where more toxic uranyl ions were present (Kumar et al., 2013). This tolerance was investigated by resuspending freshly grown cells in solutions with varying uranium concentration, followed by transfer to agar plates to assess their ability to replicate following uranium exposure. This method has been commonly used to determine the MIC of various bacteria (Luetke et al., 2012, Theodorakopoulos et al., 2015, Martinez et al., 2007, Suzuki and Banfield, 2004, Sowmya et al., 2014). LPM agar-containing uranium has also been investigated to determine the inhibitory concentrations for various strains (Nedelkova et al., 2007, Lopez-Fernandez et al., 2014). However, the growth and uranium exposure conditions are not replicated following transfer to agar plates, such as pH and uranium concentration within aqueous media. Investigating the growth of the bacterial biomass within liquid growth media containing uranium, will give a more accurate interpretation of the growth and sustainability of bacteria in the presence of uranium in aqueous environments. Additionally, using a low phosphate liquid culture will limit the formation uranium precipitates with culture media components. Therefore, one can really assess the toxicity of uranium based on an initial concentration added rather than the toxicity to precipitated uranium species.

Table 17. Documented cases of uranium tolerance from bacteria isolated from different environments.

Bacteria	Origin	Maximum observed growth	Method	Reference
		Gram-negative		
Cupriavidus metallidurans CH34	Metal processing factory, Belgium	< 30 mM (pH 7)	OD_{600}	(Llorens et al., 2012)
Acidithiobacillus ferrooxidans	Uranium waste mine piles, Johanngeorgenstadt, Germany.	9 mM (pH 7)	CFU counting on agar	(Merroun and Selenska-Pobell, 2001)
Serratia marcesecens	Sandstone uranium deposits, Domiasiat, India	3.5 – 4 mM (pH 7) 0.1 – 2 mM (pH 3.5)	CFU counting on agar	(Kumar et al., 2013)
Rhodanobacter A2-61	Urgeiriça Mine, Portugal	2 mM (pH 5)	CFU counting on agar	(Sousa et al., 2013)
Pseudomonas putida	Heavy metal tolerant strain	1.7 mM (pH 8) < 1 mM (pH 5 and 7)	OD_{600}	(Ruggiero et al., 2005) This study
Rhodopseudomonas palustris	Lab culture	1 mM (pH 7.5)	OD_{600}	(Llorens et al., 2012)
Acinetobacter sp. YU-SS-SB-29	Someshwara beach, Mangalore, India	0.5 mM (pH 4)	CFU counting on agar	(Sowmya et al., 2014)
Pseudomonas aeruginosa J007	Mine water tank of, Uranium Corporation of India Ltd, Jaduguda, India	0.42 mM (pH 4)	CFU counting on agar	(Choudhary and Sar, 2011)
Rahnella sp. Y9602	(DOE) Oak Ridge Field Research Center (ORFRC)	0.2 mM (pH 5)	CFU counting on agar	(Martinez et al., 2007)
Pseudomonas sp.	Cold Test Pit South (CTPS), Idaho National Laboratory (INL)	0.1 – 0.15 mM (pH 7)	Protein estimation	(VanEngelen et al., 2010)
Pseudomonas fluorescens	Granitic rock aquifers at Äspö Hard Rock Laboratory, Sweden	< 0.1 mM (pH 7 - 8)	CFU counting on agar	(Luetke et al., 2012)
		Gram-positive		
Microbacterium oxydans S15-M2.	Siberian radioactive waste depository Tomsk-7, Russia.	4 mM (pH 7)	CFU counting on agar	(Nedelkova et al., 2007)
Deinococcus radiodurans	Lab culture	2.5 mM (pH 8) < 0.5 mM (pH 7)	OD_{600}	(Ruggiero et al., 2005) This study
Paenibacillus sp. JG-TB8	Uranium mining waste pile ‘‘Haberland’’ Saxony, Germany	0.5 mM (pH 3 - 6)	Live/Dead staining	(Reitz et al., 2014)
Arthrobacter ilicis	Midnite mine, Stevens County, Washington.	0.34 mM (pH 4)	CFU counting on agar	(Suzuki and Banfield, 2004)
Bacillus sp. Y9-2	(DOE) Oak Ridge Field Research Center (ORFRC)	0.2 mM (pH 5)	CFU counting on agar	(Martinez et al., 2007)
Microbacterium sp. A9	Chernobyl trench T22 soil	> 0.05 mM (pH 5)	CFU counting on agar	(Theodorakopoulos et al., 2015)

5.4.1.1 Flow Cytometry

Previous studies predominantly focused on determining the inhibitory effect of U(VI) on bacterial growth using plate counting methods, rather than understanding the viability and activity of proliferating cells grown in the presence of uranium. Flow cytometry was used to determine the toxic effect of U(VI) on the cell viability and metabolic activity of *P. putida* 33015 and *D. radiodurans* R1. Flow cytometry measurements take into account 10,000 individual events (cells) within the growth media. The cells were diluted to approximately the same concentration before stains were added to ensure the same proportion of cells to stain, supporting reliability and accuracy within the measurements taken. This method was based on a previous study by Lopez-Fernandez et al. (2014).

To investigate the cell viability, cells were harvested at late exponential-prestationary phase and dual-stained with Fluorescein Diacetate (FDA) and Propidium Iodide (PI) to distinguish the proportion of live (Q4) and dead cells (Q1), respectively. Cells that had retained both stains (Q2) were classed as dead since they were membrane damaged, allowing PI to accumulate and be retained within the cells through DNA intercalation. Unstained cells and cellular rests (Q3) were not taken into account, Figure 60. Following a 24-hour incubation period, flow cytometry measurements indicated that approximately 76 % of the *P. putida* cells grown in the absence of U(VI) at pH 5 were alive. As the U(VI) concentration in solution increased to 0.50 mM U(VI), the number of viable cells decreased to 18 %. At pH 7, the number of viable cells decreased further, from 79 to 12 % as the U(VI) concentration increased to 0.50 mM. Statistical analysis suggested a significant difference in the number of viable cells as the uranium concentration increased for both pH 5 and 7. However, there was no significant difference between the numbers of viable cells at these different pH values when the uranium concentration in LPM was the same (unpaired *t*-Tests, Table 18). For *D. radiodurans,* the U(VI) tolerance concentration was lower but the number of viable cells was greater. The number of viable cells grown in the absence of U(VI) at pH 7 was approximately 89 %. As the total U(VI) concentration increased to 0.25 mM U(VI), the number of viable cells slightly decreased to only 74 %, until toxicity was reached. This decrease in cell viability was not as noticeable as the decrease observed for *P. putida* cells and not deemed statistically significant, according to Kruskal-Wallis analysis, Table 18. However cells subject to 0.5 mM would not be expected to be viable cells as they were unable to tolerate this concentration during bacterial growth. This data showed

that there was a correlation between U(VI) concentration in culture media and cell viability for both bacteria.

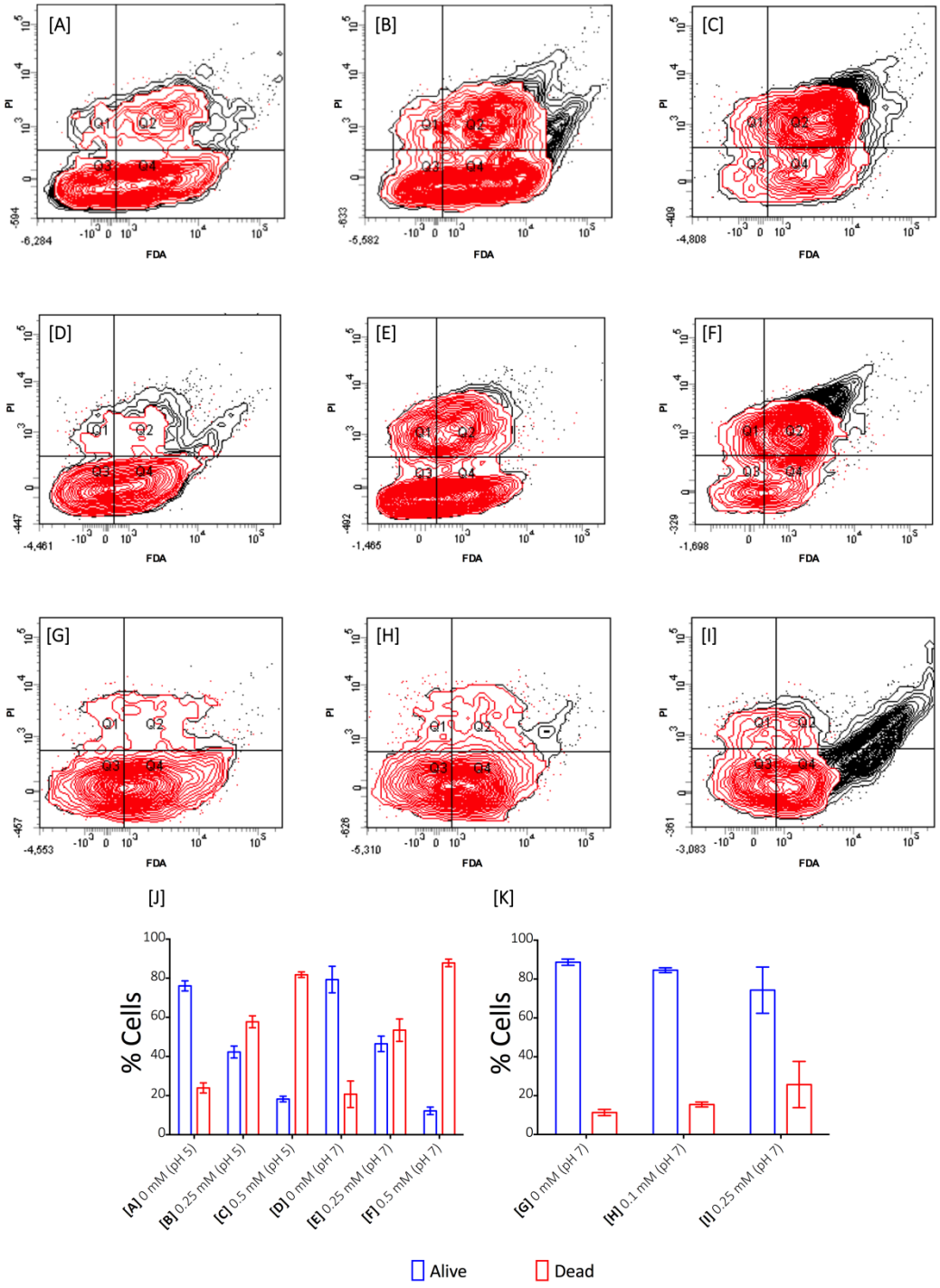

Figure 60. The effect of uranium concentration and solution pH on the cell viability of *P. putida* 33015 and *D. radiodurans* R1 using FDA and PI staining. Flow cytometric scatterplots of *P. putida* dual stained cells at 0 mM [A], 0.25 mM [B] and 0.5 mM [C] at pH 5 and 0 mM [D], 0.25 mM [E] and 0.5 mM [F] at pH 7 and *D. radiodurans* dual stained cells at 0 mM [G], 0.1 mM [H] and 0.25 mM [I] at pH 7 are represented.

To investigate metabolic activity, cells from the U(VI) growth experiments were washed and stained with $DiOC_6$, a lipophilic dye used to stain the cell membrane of respiring cells (Rottenberg and Wu, 1998). The percentage of metabolically active cells (P3/CLS ACTIV) was determined from the flow cytometry histogram plots of $DiOC_6$ stained cells, Figure 61. No correlation was observed between the metabolic activity of *P. putida* cultures as a function of culture pH or U(VI) concentration when using $DiOC_6$ to stain the cells. Interestingly, as the concentration of U(VI) increased in LPM from 0.00 mM to 0.25 mM, the amount of metabolically active *D. radiodurans* cells increased from 23 to 46 %. Kruskal-Wallis analysis indicated a significant difference in the number of metabolically active cells as the U(VI) concentration increased in culture media, Table 18. This increase in metabolic activity of the living cultures was to overcome the toxic effects of increased uranium concentrations.

To confirm this increase in metabolically active *D. radiodurans* cells at higher U(VI) concentration in LPM, and to determine whether there was any correlation between the U(VI) concentration in LPM and *P. putida* metabolic activity, late-exponential phase cells were washed and stained with 5-cyano- 2,3-ditolyl-tetrazolium chloride (CTC). Respiring cells absorb CTC via the electron transport chain and reduce it to an insoluble, red fluorescent formazan product (Rodriguez et al., 1992). The concentration of this product was proportional to the number of respiring cells. Cells were counterstained with SYTO 24 green to ensure that no cellular debris was included during measurements. From the histogram plots, the percentage of active cells was calculated using the gated region for inactive cells (M1), Figure 62. For *P. putida* cultures grown at pH 5, there was a slight decrease in the respiratory activity as the U(VI) concentration increased in LPM. In the presence of no uranium, 96 % of the cells are respiratory active. This decreased to approximately 91 % as the U(VI) concentration increased to 0.50 mM. A greater decrease was observed at pH 7. The percentage of respiratory active cells decreased from 93 to 70 % as the U(VI) increased from 0.00 to 0.50 mM. This difference suggested that the pH of LPM and uranium speciation had an effect on the respiratory activity, with U(VI) concentration in solution having a more noticeable effect at neutral pH. Statistical analysis suggested that there was no significant difference in the number of respiratory active cells as the uranium concentration increased for pH 5 but that there was a significant difference at pH 7. There was also a significant difference between the numbers of viable cells at the different pH values with a fixed uranium concentration in LPM, Table 18. The respiratory activity for *D. radiodurans* cultures increased as the U(VI)

concentration increased in culture media, from 85 to 97 % as the total U(VI) concentration increased from 0.00 to 0.25 mM. However, Kruskal-Wallis analysis suggested that there was no significant difference in the number of respiratory active cells in the U(VI) concentration range studied, Table 18. This increase was comparable to the CTC/SYTO green flow cytometry measurements that indicated an increase in respiratory activity due to increased metabolic activity, Figure 61.

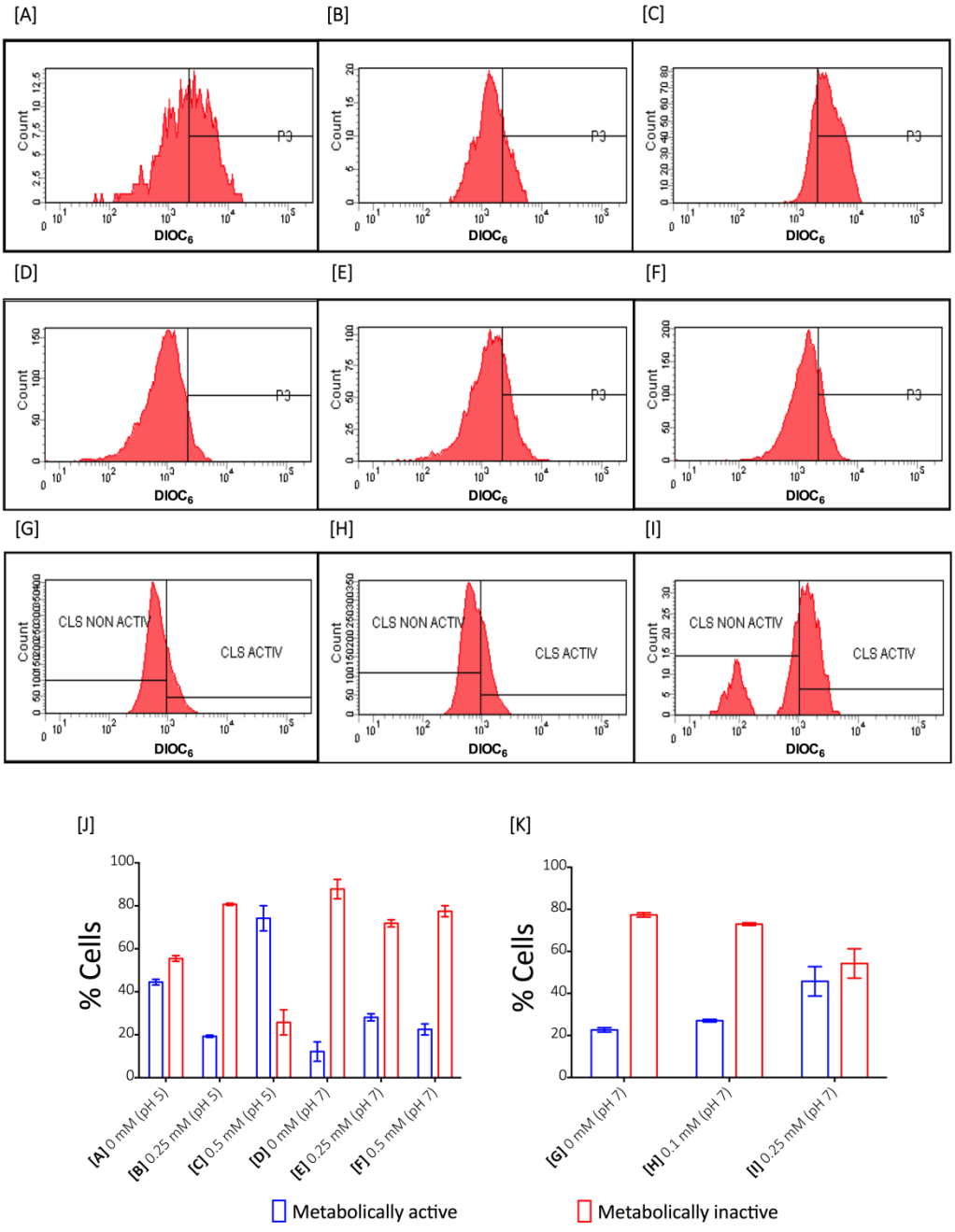

Figure 61. The effect of uranium concentration and solution pH on the metabolic activity of *P. putida* 33015 and *D. radiodurans* R1 using $DIOC_6$ staining. Flow cytometric scatterplots of *P. putida* stained cells at 0 mM [A], 0.25 mM [B] and 0.5 mM [C] at pH 5 and 0 mM [D], 0.25 mM [E] and 0.5 mM [F] at pH 7 and *D. radiodurans* stained cells at 0 mM [G], 0.1 mM [H] and 0.25 mM [I] at pH 7 are represented.

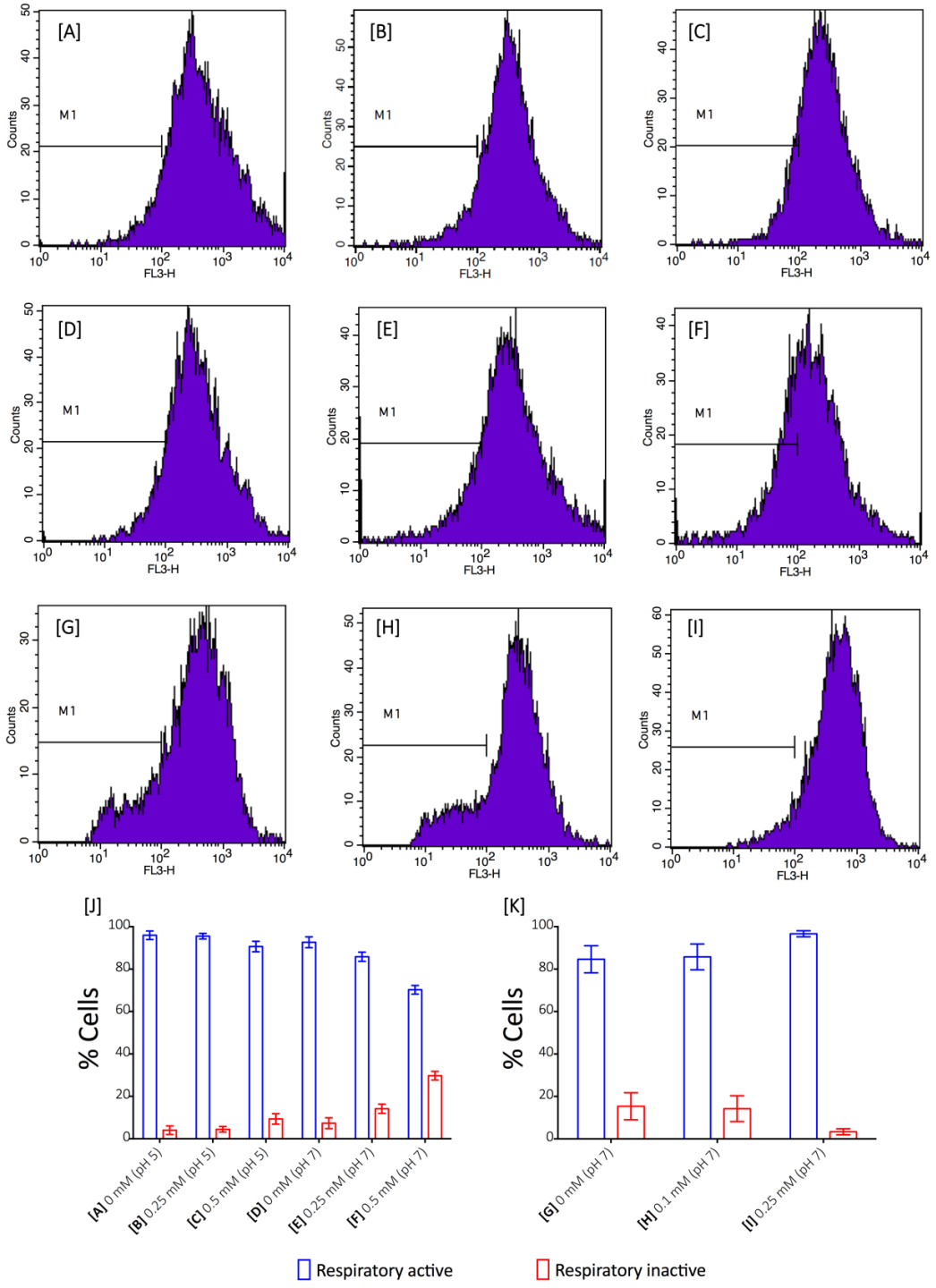

Figure 62. The effect of uranium concentration and solution pH on the respiratory and metabolic activity of *P. putida* 33015 and *D. radiodurans* R1 using CTC/SYTO 24 green staining. Flow cytometric histogram plots of *P. putida* dual stained cells at 0 mM [A], 0.25 mM [B] and 0.5 mM [C] at pH 5 and 0 mM [D], 0.25 mM [E] and 0.5 mM [F] at pH 7 and *D. radiodurans* dual stained cells at 0 mM [G], 0.1 mM [H] and 0.25 mM [I] at pH 7 are represented.

Table 18. Summary of the significance tests performed on flow cytometric data. The appropriate significance test was chosen based on the number of repeats available for each parameter investigated. All tests were performed using a 0.05 significance level (α).

Culture Conditions	Statistical Test	Null Hypothesis (H_0)	P-value	Decision
Cell Viability (FDA-PI staining)				
P. putida (0.0 mM U)	Paired T-Test	There is no difference between the number of viable cells at pH 5 and 7 at the given uranium concentration	0.5997	Accept H_0
P. putida (0.25 mM U)	Unpaired T-Test (Equal Variances)		0.4918	Accept H_0
P. putida (0.5 mM U)	Unpaired T-Test (Equal Variances)		0.0712	Accept H_0
P. putida (pH 5)	Kruskal-Wallis	There is no difference between number of viable cells within the U(VI) concentration range studied	0.0273	Reject H_0
P. putida (pH 7)	Kruskal-Wallis		0.0051	Reject H_0
P. putida (pH 5-7)	Kruskal-Wallis		0.0018	Reject H_0
D. radiodurans (pH 7)	Kruskal-Wallis		0.4298	Accept H_0
Metabolic Activity ($DIOC_6$ staining)				
P. putida (0.0 mM U)	Unpaired T-Test (Equal Variances)	There is no difference between the number of metabolically active cells at pH 5 and 7 at the given uranium concentration	0.0018	Reject H_0
P. putida (0.25 mM U)	Unpaired T-Test (Equal Variances)		0.0078	Reject H_0
P. putida (0.5 mM U)	Unpaired T-Test (Equal Variances)		8.144E-05	Reject H_0
P. putida (pH 5)	Kruskal-Wallis	There is no difference between number of metabolically active cells within the U(VI) concentration range studied	0.0273	Reject H_0
P. putida (pH 7)	Kruskal-Wallis		0.0539	Accept H_0
P. putida (pH 5-7)	Kruskal-Wallis		0.0033	Reject H_0
D. radiodurans (pH 7)	Kruskal-Wallis		0.0390	Reject H_0
Respiratory Activity (CTC-SYTO green staining)				
P. putida (0.0 mM U)	Paired T-Test	There is no difference between the number of respiring cells at pH 5 and 7 at the given uranium concentration	0.0569	Accept H_0
P. putida (0.25 mM U)	Paired T-Test		0.0036	Reject H_0
P. putida (0.5 mM U)	Unpaired T-Test (Equal Variances)		4.962E-05	Reject H_0
P. putida (pH 5)	Kruskal-Wallis	There is no difference between number of respiring cells within the U(VI) concentration range studied	0.1765	Accept H_0
P. putida (pH 7)	Kruskal-Wallis		0.0005	Reject H_0
P. putida (pH 5-7)	Kruskal-Wallis		0.0001	Reject H_0
D. radiodurans (pH 7)	Kruskal-Wallis		0.1787	Accept H_0

Overall, the optical density and flow cytometry data obtained from the bacterial growth experiments indicated varying U(VI) tolerance levels, viability and activity responses for both bacteria studied. Kruskal-Wallis and *t*-tests indicated that the majority of the results were statistically significant, with $\alpha = 0.05$, suggesting that uranium concentration and pH had a significant effect on cell viability and cellular activity.

The representative Gram-negative isolate used within this study (*P. putida* 33015) exhibited a greater tolerance to higher U(VI) concentrations over a greater pH range than the Gram-positive isolate (*D. radiodurans* R1) used within this study. Subsequent viability studies suggested that for both strains, higher U(VI) concentration in culture media reduced the number of viable cells, with *P. putida* 33015 exhibiting a greater decline following a 24-hour growth period. CTC staining suggested a positive correlation with the decrease in respiratory activity and a decrease in cell viability as the U(VI) concentration increased for *P. putida*. At pH 7, this decrease in the number of respiratory active cells was greater, Figure 63. The calculated correlation coefficients (*r*) for cultures grown at pH 5 and 7 were 0.367 and 0.860, respectively, indicating a stronger positive relationship between the number of viable and respiratory active cells at pH 7. However, *D. radiodurans* cultures demonstrate a negative correlation. As the cell viability decreased, respiratory activity and metabolic activity increased, Figure 64. The calculated *r* indicated a stronger negative relationship between the number of viable cells and the number of metabolic active cells ($r = -0.698$) compared to the number of respiratory active cells ($r = -0.237$).

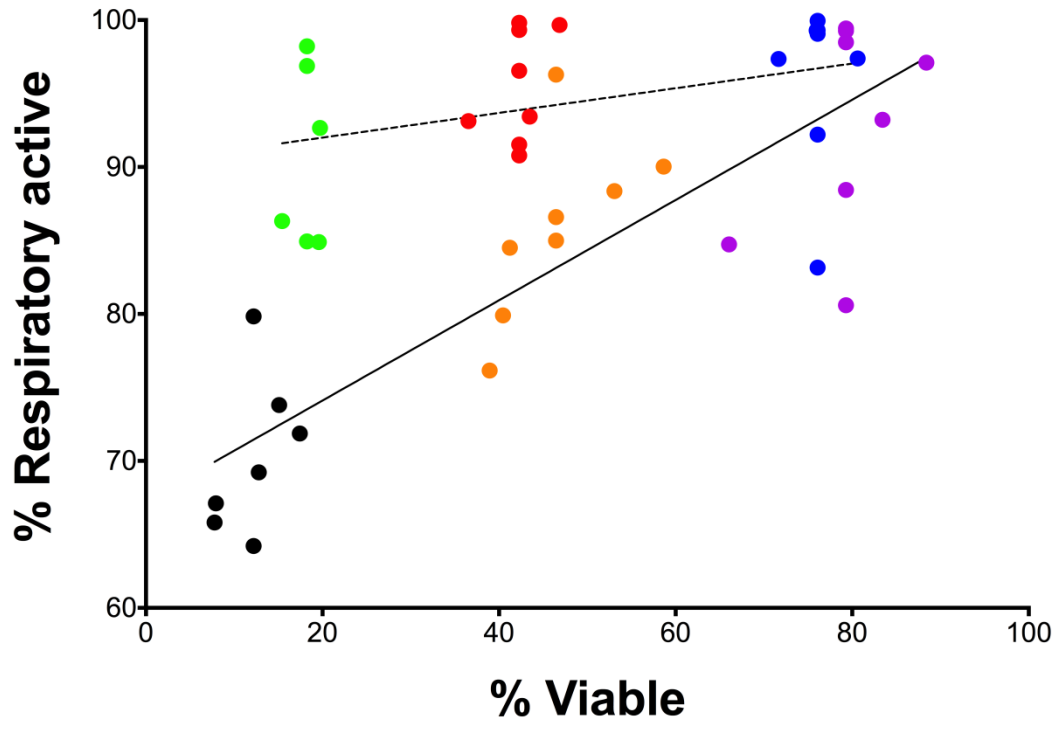

Figure 63. Pearson correlation of the % viable *P. putida* 33015 cells vs. % respiratory active cells. The dashed line applies to cultures at pH 5 grown with 0 mM (blue), 0.25 mM (red) and 0.5 mM (green) U(VI). The solid line applies to cultures at pH 7 grown with 0 mM (purple), 0.25 mM (orange) and 0.5 mM (black) U(VI).

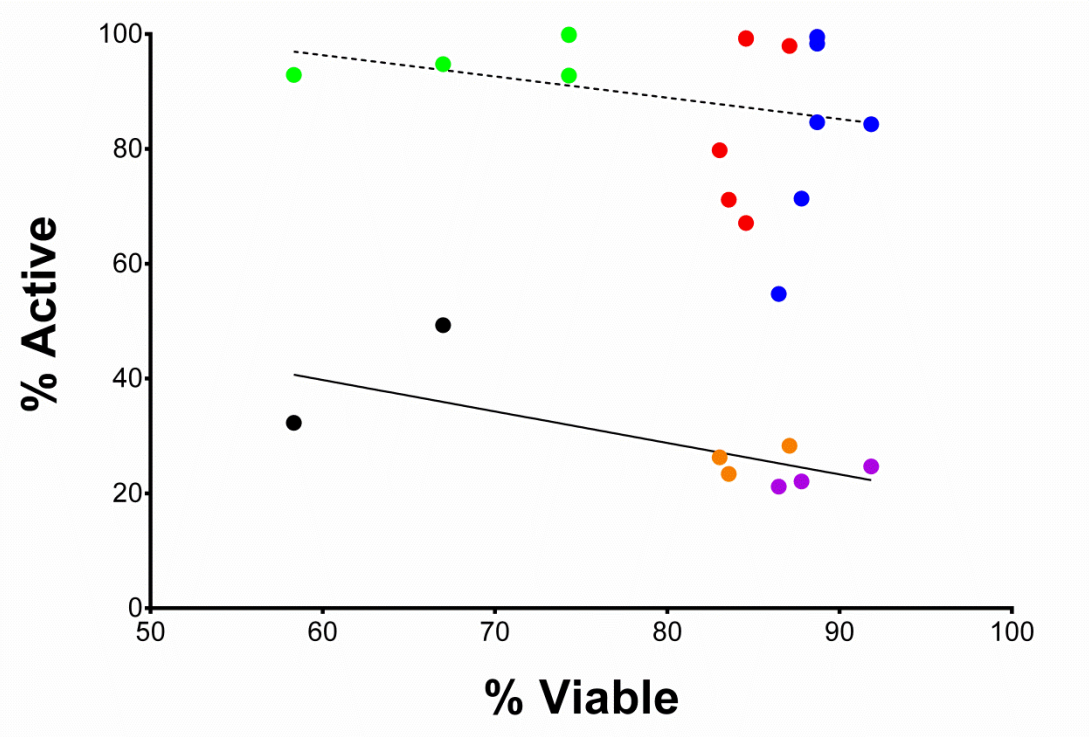

Figure 64. Pearson correlation of the % viable *D. radiodurans* R1 cells vs. % active cells grown at pH 7. The dashed line applies to CTC-SYTO green stained cells grown with 0 mM (blue), 0.1 mM (red) and 0.25 mM (green) U(VI). The solid line applies to $DIOC_6$ stained cells grown with 0 mM (purple), 0.1 mM (orange) and 0.25 mM (black) U(VI).

The toxicity of U(VI) to the bacteria may arise from the interactions of uranium with bacterial components, hindering metabolic processes and subsequent growth. The highly mobile uranyl ion can displace essential ions in cellular sites and block functional groups, such as those found in enzymes, polynucleotides and nutrient transport systems. This can disrupt cell organelles and compromise membrane integrity, resulting in cell lysis (Sani et al., 2006). For example, UO_2^{2+} has been shown to displace Ca^{2+} in pyrroloquinoline quinone (PQQ), a cofactor for many bacterial dehydrogenases that are essential for growth. The binding to PQQ and Ca^{2+} displacement can considerably diminish cell function in *Pseudomonas aeruginosa* PAO1 (VanEngelen et al., 2011, Burbank et al., 2015). Interestingly, there was a greater decrease in the number of viable and respiring *P. putida* 33015 cells grown in the presence of increasing concentrations of U(VI) at pH 7 than at pH 5. According to the speciation calculations, no UO_2^{2+} species were present at pH 7, but they should be present at pH 5 (Appendix Table 18). This suggested that the other U(VI) species, such as $(UO_2)_4(OH)_7^+$, exhibited a greater toxicity to *P. putida* 33015. Following U(VI) exposure to *Desulfovibrio alaskensis* G20, the genes responsible for DNA repair, rRNA methylation, regulation of transcription and membrane transport were disrupted, inhibiting protein synthesis (Li et al., 2014). However, up-regulation of the genes responsible for outer membrane protein and LPS biosynthesis occurred following U(VI) exposure to *Caulobacter crescentus* (Hu et al., 2005). Following uranium exposure, the bacteria can exhibit an increased oxidative stress. This is due to the formation of reactive oxygen species, such as highly mobile superoxide radicals that can easily interact with and damage essential biomolecules such as DNA, proteins and lipidic material (Imlay, 2003). The oxidative stress hinders the metabolic activity of cells while maintaining the viability through not damaging cell surface components (Sepulveda-Medina et al., 2015). To overcome this issue bacterial superoxide dismutase (SOD) converts ROS into O_2 and H_2O_2, the latter of which is broken down by catalase, thus acting as a tolerance mechanism. The genes responsible for this activity are up-regulated in *Caulobacter crescentus* following U(VI) exposure (Slade and Radman, 2011, Hu et al., 2005). *D. radiodurans* exhibit this activity at high levels of radiation damage, coupled with DNA repair mechanisms (Slade and Radman, 2011).

Furthermore, the production of extra polymeric substances and extracellular-cell surface uranium precipitation has been documented as a tolerance mechanism within aerobic environments. The bacteria present within the outermost layers of biofilms exhibited a greater respiratory activity to cope with the detoxification of U(VI) through the

precipitation of uranium minerals on the surface or extracellularly (Krawczyk-Baersch et al., 2008). Similarly, the liberation of phosphates external to the cell precipitates uranium, decreasing the amount of toxic U(VI) species in solution (Suzuki and Banfield, 2004, Theodorakopoulos et al., 2015).

Overall, from the tolerance and toxicity studies undertaken, it was suggested that *P. putida* exhibited a greater tolerance to higher uranium concentrations and over a greater pH range compared to *D. radiodurans.* The number of viable cells decreased more rapidly as the uranium concentration increased, while differences in metabolic activity were observed by both strains within the tolerated uranium concentration range. With these results, it could be suggested that Gram-negative bacteria exhibit a greater tolerance compared to Gram-positive bacteria.

5.4.2 Uranium biomineralisation by the live cells of *P. putida* 33015 and *D. radiodurans* R1

5.4.2.1 Uranium localisation by electron microscopy

HR-TEM and HAADF-STEM were used to determine the localisation of uranium following exposure. Micrographs of thin sections of *P. putida* 33015 and *D. radiodurans* R1 cells exposed to U(VI) solution (pH 7) are shown in Figure 65 and Figure 66. Cells were analysed following exposure to U(VI) in 0.1 M $NaClO_4$ rather than LPM to avoid any interferences with growth media and U(VI) precipitation. Accumulation of electron dense precipitates were located at the surface and within the cells for *P. putida* 33015 cells exposed to 0.5 mM U(VI) for 24 hours, Figure 65A, B, D and E.

Precipitates located at the cell surface were needle-like in structure and protruded through the cell wall. A cell that precipitated uranium at the cell wall had fewer intracellular accumulates than those that did not precipitate uranium at the cell surface. These cells have large amounts of intracellular precipitates. Intracellular uranium accumulation with polyphosphate bodies has been documented for numerous Gram-negative strains such as *Acidithiobacillus ferrooxidans* (Merroun et al., 2003b), *Sphingomonas* species S15-S1 (Merroun et al., 2006) and various *Pseudomonas* strains (Renninger et al., 2004, Kazy et al., 2009, Choudhary and Sar, 2011). EDX analysis of exposed cells confirmed the presence of uranium and phosphorus associated with these dense precipitates, Figure 65C and F. The presence of osmium was due to the sample preparation process, copper due to the TEM sample holder and silicon came from

sample impurities. EDX elemental-distribution mapping of uranium and phosphorus (Figure 65G and H) showed that the precipitates were composed of both elements. The existence of this uranium-phosphorus interaction was further supported by ATR-FT-IR analysis of *P. putida* 33015 whole cells and cell wall isolates that indicated phosphate and peptides were involved in uranium interactions, Figure 42 and Figure 48.

D. radiodurans R1 cells showed precipitates that predominantly located at the cell surface with small amounts of intracellular and extracellular accumulation, Figure 66A, B, D and E. Two distinct layers of uranium precipitates were observed at the cell surface of *D. radiodurans* R1. The cell surface of *D. radiodurans* is composed of five layers; the interior cell surface membrane, the rigid peptidoglycan layer, the main compartmental and hexagonal layers consisting of lipids, peptides and polysaccharides and a characteristic outer membrane that aids the movement of substances in and out of the cell (Thornley et al., 1965, Slade and Radman, 2011). The different layers will have different binding affinities for uranium, hence the two distinct layers formed. The amount of intracellular precipitates exhibited by *D. radiodurans* R1 was less than those from *P. putida* 33015. *D. radiodurans* stores polyphosphate granules as a nutrient source and for nucleic acid synthesis at times of oxidative stress (Slade and Radman, 2011). The thick multi-layer boundary of the *D. radiodurans* cells would prevent large quantities of intracellular accumulation, while the polyphosphate granules would chelate any uranium that passes this boundary. EDX and elemental-distribution mapping confirmed the presence of uranium and phosphorus within the precipitates formed by *D. radiodurans* R1, Figure 66C, F-H. Interestingly, this result differed from the XPS wide and high resolution scans obtained for whole *D. radiodurans* R1 cells (Figure 31). These results suggested that no phosphorus was present within the outermost surface layer. However, the X-ray penetration depth with XPS is only approximately 1-10 nm. The *D. radiodurans* cell envelope is approximately 150 nm thick (Slade and Radman, 2011). Therefore, it could be suggested that phosphate interactions will occur with the lower layers of the cell envelope and XPS analysis is from an unreactive outermost layer. Furthermore, ATR-FT-IR analysis pointed to interactions with phosphates and carbohydrates due to changes in adsorption band positions corresponding to the ν_s (PO_2) and ν (C-O), following exposure to uranium (Figure 45).

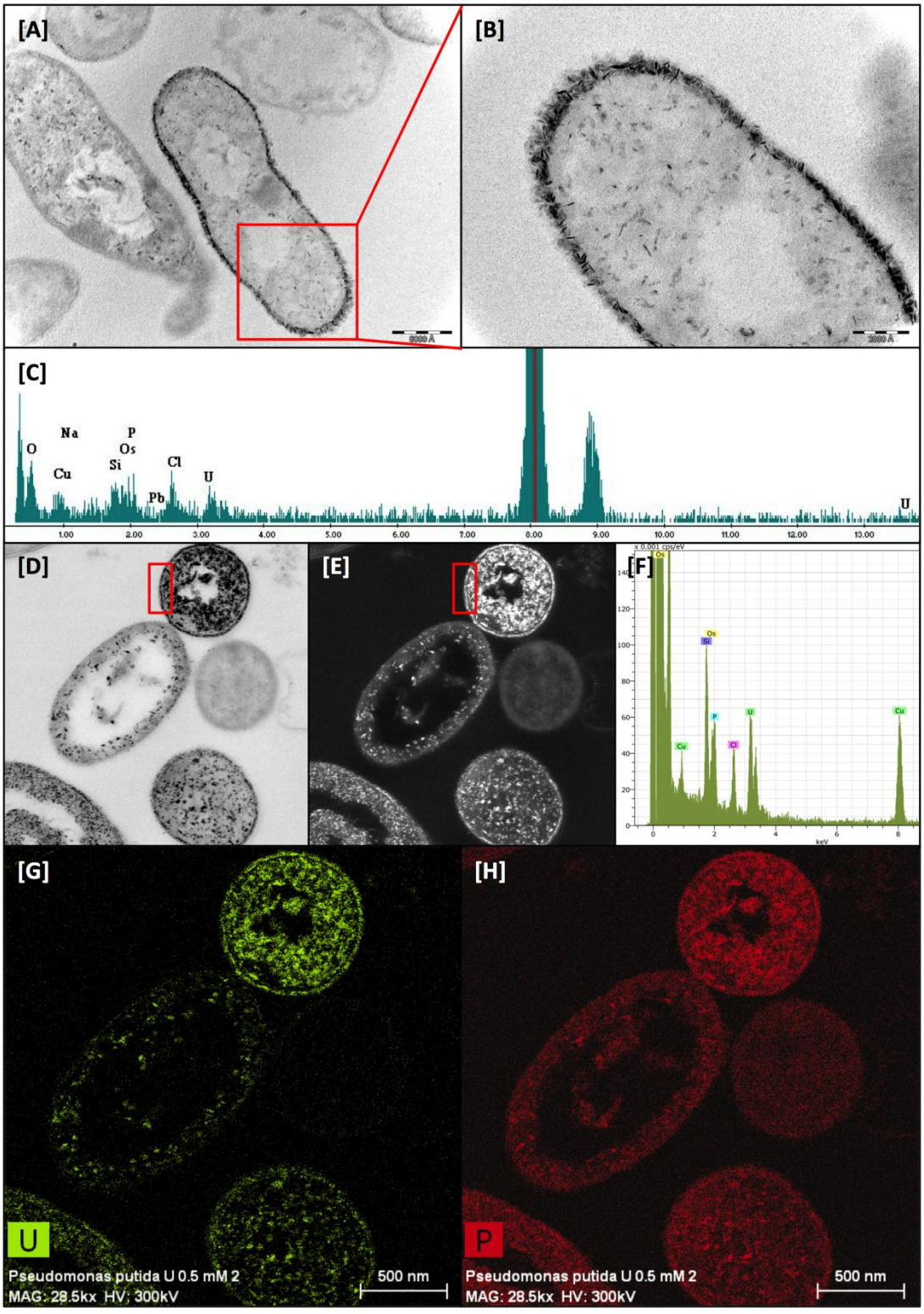

Figure 65. High Resolution-Transmission Electron micrographs of thin sections of *P. putida* cells treated with 0.5 mM uranium [A, B, D, E] coupled with EDX spectra [C, F]. Scanning Transmission Electron Microscopy-High Angle Annular Dark-Field (STEM-HAADF) micrographs of the same treated cells with uranium [G] and phosphorus [H] elemental mapping.

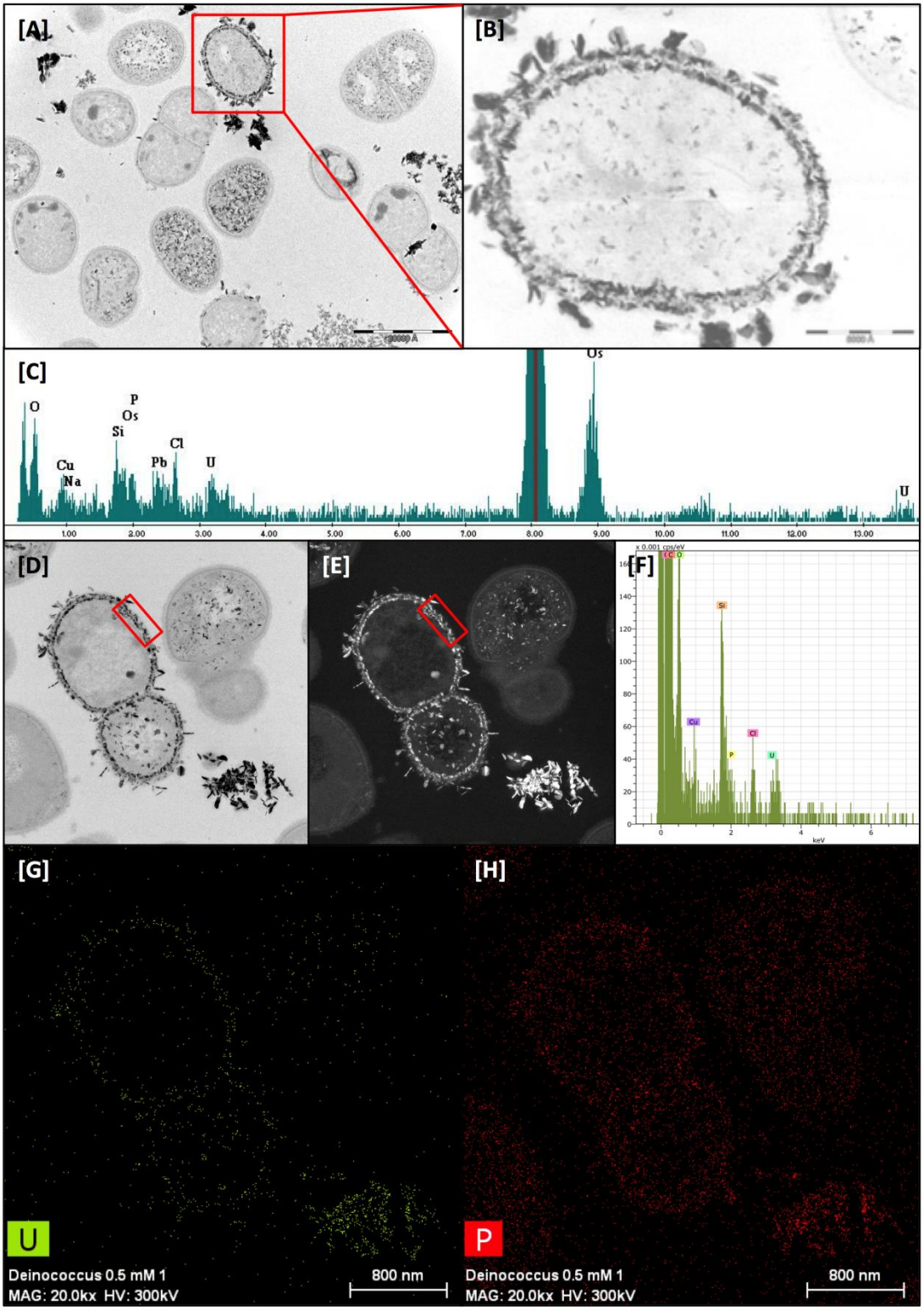

Figure 66. High Resolution-Transmission Electron micrographs of thin sections of D. radiodurans cells treated with 0.5 mM uranium [A, B, D, E] coupled with EDX spectra [C, F]. Scanning Transmission Electron Microscopy-High Angle Annular Dark-Field (STEM-HAADF) micrographs of the same treated cells with uranium [G] and phosphorus [H] elemental mapping.

From the TEM micrographs obtained, cells of *P. putida* 33015 displayed greater quantities of intracellular accumulate than *D. radiodurans* R1 following incubation with U(VI) at pH 7, Figure 65 and Figure 66. However, this was based on only one replicate. TEM sample preparation requires thin slices of fixed cell cultures. The angle at which the cells are fixed and hence the angle of slicing could give inaccuracies in the perception of uranium deposition onto the bacteria. For example, the cells could appear to have accumulated large quantities of uranium internally even if the accumulation occurred at the cell surface and the fixing and slicing of cells along the surface gave the impression of internal accumulation. Multiple repeats of TEM analysis would be required to properly determine whether this process occurred and hence if the internal accumulation of uranium by *P. putida* was an anomaly or due to inaccuracies with cell fixing and slicing. Due to limitations in access to instrumentation, the measurements could not be repeated.

The *D. radiodurans* R1 cell wall is thicker than that of *P. putida* 33015 and is composed of large quantities of peptidoglycan and other polysaccharides and peptides (Slade and Radman, 2011). This outer boundary, composed of multiple layers, likely prevented intracellular precipitation. The needle-like uranium precipitates located at the cell surface of *P. putida* 33015 protruded through the cell wall. This protrusion could cause punctures in the cell surface, resulting in greater amounts of intracellular accumulation. There was a greater decline in the number of viable *P. putida* cells than *D. radiodurans* cells when the U(VI) concentration in culture media is approximately the same at pH 7, Figure 60. The larger number of membrane-damaged *P. putida* cells in comparison to *D. radiodurans* cells may correlate to the amount of intracellular accumulation within both strains. This could suggest that the intracellular accumulation of uranium was due to the cell lysis of membrane-damaged or dead cells and that the precipitation onto the surface is an initial tolerance mechanism of live cells to deal with uranium exposure. The punctures caused by the deposition of needle-like precipitates onto the *P. putida* cell surface could result in PI accumulation and inferred cell death. The intracellular accumulation of damaged cells would cause a decrease in metabolic activity and subsequent death due to the toxic effects that U(VI) species have on metabolic processes within the cell.

Needle-like nano-crystals were observed extracellularly following U(VI) exposure to *D. radiodurans* R1 cells at pH 7. This has been previously documented for *D. radiodurans*

cells at low pH that precipitated U(VI) crystals as chernikovite, a uranium-phosphate mineral, following cell lysis (Suzuki and Banfield, 2004). Overall, electron microscopy revealed precipitation of uranium at the cell surface and within the cells for both strains. *D. radiodurans* further exhibited precipitation external to the cell. Elemental mapping suggested the formation of phosphorus barring minerals.

5.4.2.2 Uranium biomineralisation through microbial phosphatase activity

Orthophosphate within LPM was quantified before and after inoculation with *P. putida* 33015 and *D. radiodurans* R1, Figure 67. A significant decrease in orthophosphate in *P. putida* 33015 cultures grown without U(VI) at pH 5 and 7 was observed, due to consumption for growth, Figure 67A. Significantly less orthophosphate was observed in non-inoculated media containing U(VI) at pH 5 and 7. At pH 5, there was an increase in the amount of orthophosphate following microbial growth in the presence of 0.25 and 0.50 mM U(VI). At pH 7, there was a decrease in orthophosphate release in the presence of 0.25 mM U(VI) and an increase in release at 0.5 mM U(VI).

No significant difference in orthophosphate concentrations was observed in non-inoculated media for *D. radiodurans* growth containing increasing concentrations of U(VI), Figure 67B. Following growth, there was a decrease in total orthophosphate in solution. A small decrease in orthophosphate in solution was observed as the U(VI) concentration in solution increased. The amount of orthophosphate remaining appeared to decrease proportionally to the increase in biomass concentration quantified by optical density experiments, Figure 59, suggesting the decline in orthophosphate in the media was due to consumption for bacterial growth.

Increases in orthophosphate concentrations within the supernatant can be explained in a number of ways. Cell lysis following uranium exposure liberated inorganic phosphate from phosphorylated biopolymers that can be subsequently broken down to contribute to an increase in total orthophosphate in solution (Merroun et al., 2011). Furthermore, phosphatase and exopolyphosphatase activity can liberate inorganic phosphate outside the cell for extracellular uranium precipitation (Theodorakopoulos et al., 2015). The acid phosphatase based assay was used on live *P. putida* 33015 and *D. radiodurans* R1 cells investigated within a range of acidic pH, Figure 68. A greater phosphatase activity was documented for both strains as the pH of the culture solution decreased. *D. radiodurans* R1 exhibited a greater amount of phosphatase activity compared to the same concentration of *P. putida* 33015 cells.

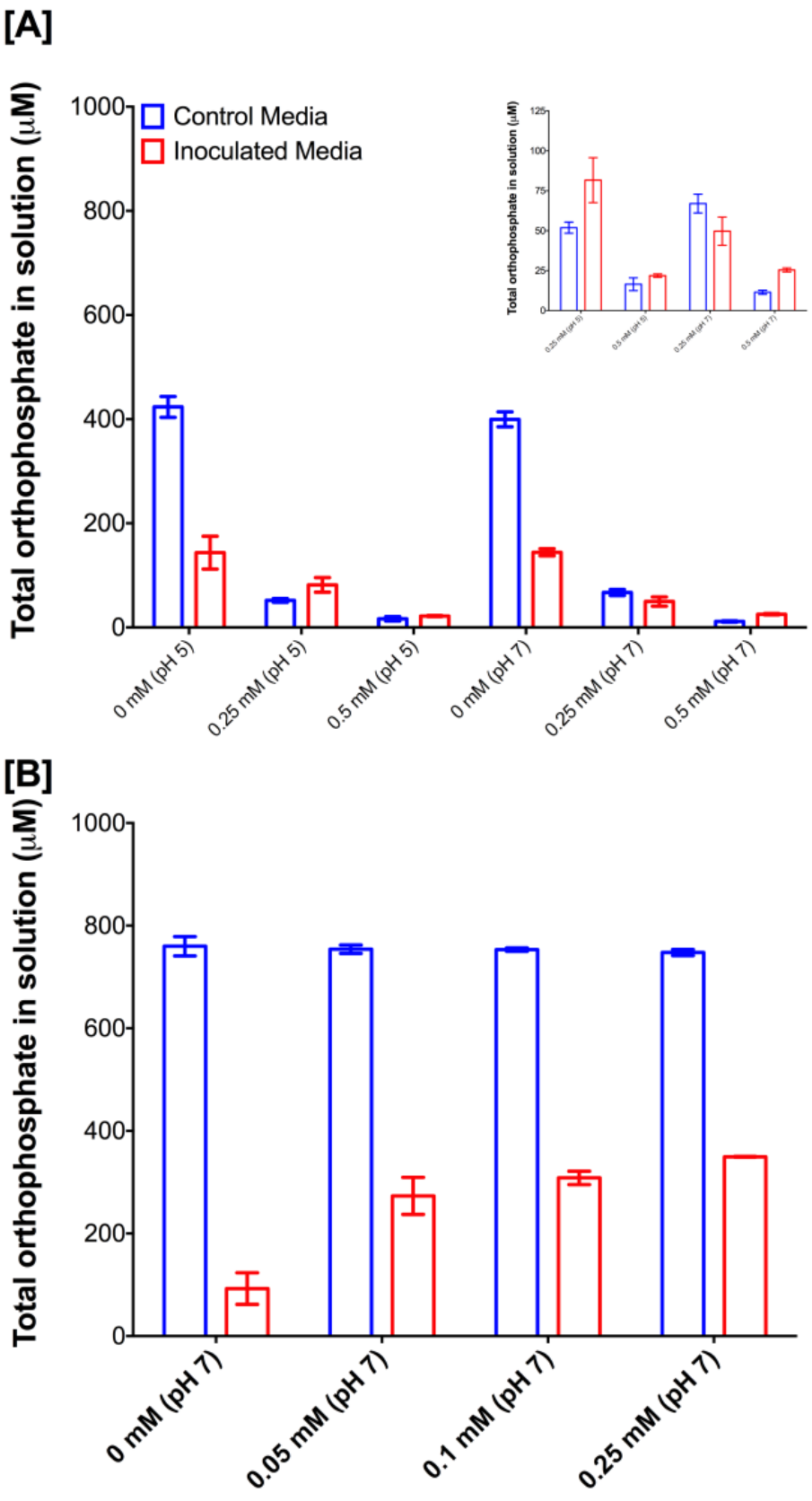

Figure 67. Changes in total orthophosphate concentrations in growth media containing different uranium concentrations following 48 hour bacterial of *P. putida* 33015 [A] and *D. radiodurans* R1 [B].

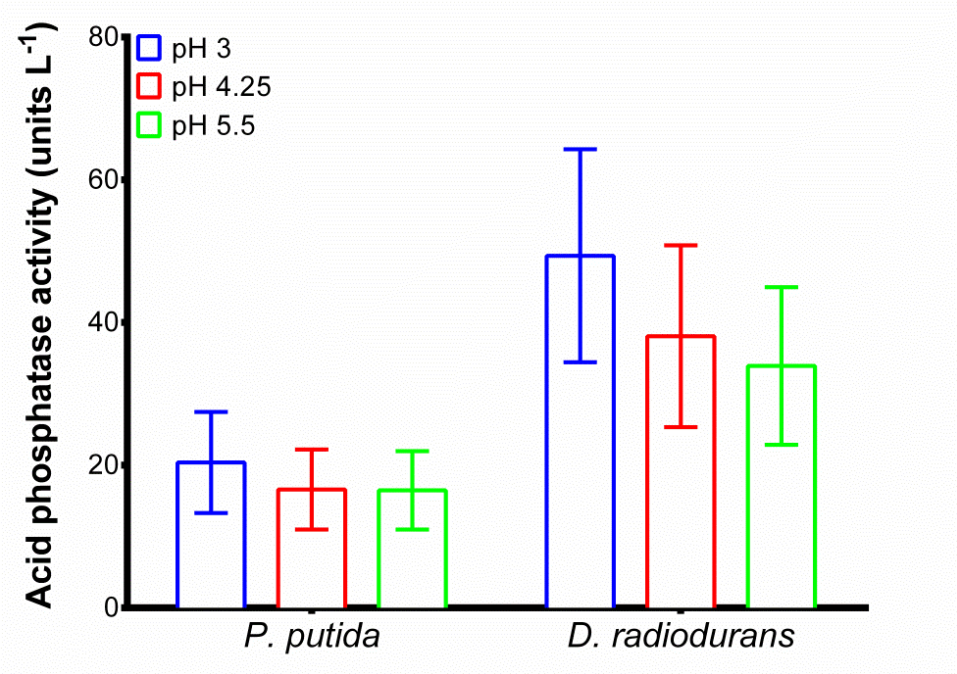

Figure 68. Acidic phosphatase activity of cells of *P. putida* 33015 and *D. radiodurans* R1 cells incubated in 0.1 M NaCl for 48 h at pH 3, 4.25 and 5.5.

The precipitation of uranium can occur through the interactions with orthophosphates either through cell lysis or via microbial phosphatase activity for both Gram-negative and Gram-positive bacteria (Macaskie et al., 2000, Merroun et al., 2006, Nedelkova et al., 2007, Beazley et al., 2007, Martinez et al., 2007, Merroun et al., 2011, Reitz et al., 2014). These studies suggested that the precipitation of uranium via phosphatase activity was greater in the region of higher acidic pH to circumneutral conditions. Interestingly, *P. putida* 33015 and *D. radiodurans* R1 exhibited a greater phosphatase activity at lower pH than previously documented cases. The work of Merroun et al. (2011) found that a high level of phosphatase activity at pH 3 was exhibited by *Sphingomonas* sp. S15-S1 when uranium precipitated as a meta-autunite phase ($Ca(UO_2)_2(PO_4)_2 \bullet 4(H_2O)$). However, this activity increased as the solution pH increased. As the pH of the solution increased to 7 in this study (used for TEM studies), HPO_4^{2-} is the dominant orthophosphate species while $(UO_2)_3(OH)^{5+}$ and $(UO_2)_4(OH)^{7+}$ are the dominant uranium species. Membrane-bound phosphatase activity has been associated with the liberation of hydrogen phosphates for uranium precipitation and deposition onto the cell surface by Gram-negative bacteria (Macaskie et al., 1992b, Jeong et al., 1997). At circumneutral pH, a *Citrobacter* species was shown to initially accumulate uranium with phosphate groups on LPS. This nucleation allowed large deposits of enzymatically liberated uranyl phosphates to be deposited onto the cell surface without

diminishing cell function, thus acting as a U(VI) tolerance mechanism (Macaskie et al., 2000). Naturally occurring microbial phosphatase activity was exhibited by *Bacillus* and *Rahnella* strains isolated from the subsurface soils at the US Department of Energy's (DOE) Oak Ridge Field Research Center (ORFRC) (Martinez et al., 2007). Phosphatase activity was documented through the implementation of an external organic phosphate source. This same activity was documented for *Bacillus* and *Sphingomonas* species when no external organic phosphate source was added and it was suggested that this organic phosphate was from the lysis of dead cells (Merroun et al., 2011).

Few studies have implemented the use of bacteria to remediate uranium in up-scaled *ex-situ* biotechnologies. Most application studies have focused on the *in-situ* remediation of uranium mill tailing sites. There is an opportunity for the development of bioreactor technologies to remediate uranium-contaminated waters (Jelinek and Sorg, 1988, Campbell et al., 2015). A recent study has investigated and implemented *Acidithiobacillus ferrooxidans* strains within an *ex-situ* bioreactor technology (Romero-Gonzalez et al., 2016). The bioreactor was developed to harness the power of live cells that were able to remove 60 % of 100 mg L^{-1} uranium from simulated mine water. The capabilities of both strains in this study to grow in the presence of uranium, in particularly *P. putida* 33015 that can grow at different pH, makes them ideal for use in up-scaled *ex-situ* bioremediation systems where the culture pH and uranium concentrations are known. Furthermore, both strains have exhibited an ability to sequester uranium through biosorption (Figure 36). This ability would be useful, as over time, the bacteria within the bioreactor would die, switching from a process of biomineralisation to biosorption to sequester uranium from solution.

5.5 Conclusions

This study described the abilities of *P. putida* 33015 and *D. radiodurans* R1 to tolerate U(VI) during bacterial growth and how the cultures cope with it's toxic effects. This was achieved through growth experiments, flow cytometry, electron microscopy and phosphatase assessment. Results indicated that *P. putida* 33015 exhibited a greater tolerance to higher concentrations of uranium over a wider pH range (up to 0.25 mM at pH 5 and 7) in comparison to *D. radiodurans* R1 that only tolerated a maximum of 0.25 mM at pH 7. Flow cytometry measurements indicated that, as the U(VI) concentration in growth media increased, there was a decrease in the number of viable cells for both strains studied. Cellular activity staining suggested a decrease in

respiratory activity by *P. putida* cultures as the U(VI) concentration increased while *D. radiodurans* exhibited an increase in metabolic activity under the same culture conditions until it's MIC was reached.

Electron microscopy revealed deposition of uranium minerals on the cell surface and within the cells for both strains. *D. radiodurans* further exhibited precipitation external to the cell. Elemental mapping suggested that phosphorus-bearing uranium minerals were formed. Phosphatase activity and orthophosphate release were demonstrated for both strains suggesting that this activity was responsible for uranium precipitation. It is suggested that the precipitation of U(VI) species on the cell surface and in its external environment is a mechanism to cope with the toxicity of the radioactive material. The intracellular accumulation would result in U(VI) interactions with essential biomolecules responsible for bacterial growth, decreasing cell viability and cellular activity from cell lysis and inhibition of metabolic processes. At higher concentrations of uranium or at low pH where the bacterial growth wasn't favourable or cell death, biosorption to the bacterial biomass present likely occurred. However, further HR-TEM would be required to confirm this fully since problems with slicing and fixing mean that the results presented here may not be fully representative of the cells analysed.

Both this study and previous literature indicated that Gram-negative bacteria are more tolerant of U(VI) species. However, the results obtained in this study were only from one Gram-negative and Gram-positive strain. Furthermore, no single defined experimental procedure has been utilised throughout previous literature to determine the MIC of U(VI) and the culture conditions would need to be uniform to accurately support this argument. Further work is therefore required to confirm this suggestion. This includes the characterisation of the inhibitory effect of U(VI) on the bacterial growth of further Gram-negative and positive strains investigated, in the same manner as in this study to confirm this difference in susceptibility, and help elucidate their contribution to uranium biosorption and biomineralisation.

Chapter 6: Final conclusions and further work.

6.1 Conclusions

Biosorption and biomineralisation are processes exhibited by bacteria to sequester uranium from contaminated waters. The majority of studies have focused on a whole cell system. The role of the bacterial cell surface and other structures involved in these processes are not fully understood due to the complexity of these components, making it difficult to consider for their use and application in remediation, extraction and reuse of uranium. Therefore, the aim of this study was, to deconstruct the bacterial cell and characterise the specific roles of microbial cell surface components in U(VI) biomineralisation and biosorption from aerobic environments. This was achieved in order to determine the specific processes involved with bacterial extra polymeric substances (Chapter 2) and bacterial cell surface structures (Chapter 4). These processes were then investigated within live cells to therefore assess how these U(VI) interactions affected cell viability and metabolic activity (Chapter 5).

The contributions of cell components were investigated in a number of ways in order to provide a comprehensive study of the physiochemical and biological processes involved in uranium biosorption and biomineralisation. This included utilising model biomolecules representative of bacterial components as well as extracting and purifying those from whole cells that have been suggested to be responsible for uranium retention. A combination of analytical, microscopy and spectroscopic techniques were employed to characterise cell surface structures and their subsequent interactions with uranium.

Bacterial extra polymeric substances (EPS) have been associated with the extracellular precipitation of uranium. Extracellular DNA (eDNA) was chosen as a representative biomolecule to investigate the uranium interactions within complex macromolecular EPS. The results showed that it is a key contributor to the biomineralisation of uranium within EPS. ATR-FT-IR analysis indicated that the complexation and precipitation of uranium with eDNA was predominantly mediated by negatively charged phosphate moieties. Uranium and eDNA quantification indicated that a higher percentage of precipitates were formed at low pH due to the increased availability of both phosphate and nitrogenous bases (likely due to alterations to the eDNA structure) and the uranium speciation in solution. Between mildly acidic and circumneutral pH, acid phosphatase liberated phosphate (ePO_4) from eDNA to mineralise uranium. XRD confirmed that the minerals formed belonged to the uranium phosphate family, with a structure similar to the mineral $(UO_2HPO_4)•xH_2O$ (ICDD PDF# 00-037-0373). SEM-EDX and XPS confirmed the

incorporation of impurities from the enzymatic hydrolysis of eDNA, while the latter suggested that the minerals formed were mainly in the +6 oxidation state. The quantification of uranium and ePO_4 revealed that the stoichiometry of the reaction at pH 5 was 3 : 1 $H_2PO_4^-$: $(UO_2)_3(OH)_5^+$ and that the difference in the recorded molar ratio of 3.5 : 1 was due to the overestimation of ePO_4 removed by uranium and not by other residual material left over from the enzymatic hydrolysis of eDNA.

The biosorption of uranium with bacteria is governed by the interactions with functional groups on the cell surface. Bacterial cell surface structures were isolated from whole cells in order to determine the specific roles and capabilities of those responsible for uranium biosorption. The cell wall and membrane from *P. putida* 33015 and *B. subtilis* 168 were successfully isolated from whole cells using a combination of a French pressure cell and differential centrifugation. *D. radiodurans* R1 could not be fractionated despite the numerous cell disruption techniques explored, and therefore, only whole cells were characterised. XPS analysis of isolated structures indicated that the Gram-negative *P. putida* cell wall was composed of mainly peptide (47 %) and hydrocarbon-like material (32 %) while the cell wall isolated from the Gram-positive *B. subtilis* was composed mainly of a combination of both peptides and polysaccharides (both at 42 %). The composition of cell surface membranes from both bacteria indicated a similar macromolecular composition and were both composed mainly of peptides and lipids.

Uranium biosorption experiments were designed to determine which cell surface structure exhibited the greatest biosorption capacity at pH 3, 4.25 and 5.5, the pH range at which there were changes in the protonation-deprotonation behaviour of cell surface structures and changes in U(VI) speciation as a function of pH. Differences in cell surface structure and whether they were of Gram-negative or Gram-positive origin had an influence on the biosorption of uranium. The preference for uranium biosorption of the structures investigated can be summarised as; *B. subtilis* cell wall isolates > *B. subtilis* dead cells > *B. subtilis* live cells > *P. putida* cell wall isolates > *P. putida* dead cells > *P. putida* live cells > *P. putida* cell membrane isolates > *B. subtilis* cell membrane isolates > *D. radiodurans* live cells. These results confirmed the assumption that the cell walls of bacteria are the preferential binder for U(VI) species in acidic conditions. The deprotonation of functional groups and a subsequent increase in their availability as the pH increased resulted in an increased uranium biosorption capacity for each cell surface structure within the pH range studied. ATR-FT-IR suggested that hydroxyl, amino,

carboxyl and phosphate groups, those present within proteins and phosphorylated biopolymers, were responsible for the biosorption of U(VI) for each cell surface structure investigated.

Finally, the processes involved in uranium biosorption and biomineralisation using extracted cell surface components and biomolecules representative of EPS were investigated to assess how these uranium interactions affected the viability and metabolic activity of live *P. putida* 33015 and *D. radiodurans* R1 cells. This study supported previous literature that suggested that Gram-negative bacteria exhibit a higher tolerance to uranium than Gram-positive strains bacteria. *P. putida* had a greater tolerance to uranium (up to 0.5 mM between pH 5 and 7) compared to *D. radiodurans* (up to 0.25 mM at pH 7). Flow cytometry indicated a direct link with the concentration of U(VI) and cell viability; as the U(VI) concentration in growth media increased, there was a decrease in the cell viability of both bacteria investigated. A decrease in respiratory activity of *P. putida* cells was observed as the U(VI) concentration increased. *D. radiodurans* exhibited an increase in respiratory activity until cell toxicity was reached. Within the concentration range investigated in which the cells were still alive, both strains precipitated uranium onto the cell surface and internally. *D. radiodurans* further precipitated uranium externally. This precipitation was suggested to be due to microbial phosphatase activity.

High-angle annular dark field-scanning transmission electron microscopy (HAADF-STEM) indicated that the precipitates formed were a type of uranium phosphate. These results suggest that at low concentrations of U(VI) and toward circumneutral pH, live cells were likely to retain uranium either through biosorption with negatively charged moieties on the bacterial cell surface or through the precipitation of enzymatically generated uranium phosphate minerals tethered to the cell or within EPS as a tolerance mechanism to cope with uranium toxicity. At higher concentrations of uranium or at low pH where the bacterial growth is not favourable or cell death, biosorption to the bacterial biomass present occurs.

In conclusion, the work presented in this thesis has deconstructed the bacterial cell surface and investigated the specific roles of cell surface structures and representative biomolecules in the biosorption and biomineralisation of U(VI) from aqueous environments. The use of bacteria for the remediation of uranium-contaminated waters is being studied more and more frequently. Understanding the contribution of these

components in comparison to whole cells is fundamental in understanding the mechanistic processes involved in biosorption and biomineralisation and for their application in the remediation, extraction and reuse of uranium.

6.2 Further work

Uranium complexation, precipitation and biomineralisation with eDNA as a representative biopolymer of EPS was investigated. Further work is needed to provide the coordination environment of the precipitated eDNA-uranium complexes and the uranium phosphate minerals formed using hydrolysed ePO_4 to clearly identify the interactions involved in eDNA complexation and mineral formation within bacterial EPS. Ideally, this could be achieved using XAS in which the structural environment of the uranium precipitates and minerals can be determined by EXAFS. Additionally, XANES could be employed to further elucidate the multiple oxidation states exhibited by uranium minerals formed using ePO_4 and abiotic phosphate (aPO_4). Further assessment of other biomolecules present within EPS (such as sugar acids including uronic and pyruvic acid) and their interactions with uranium could give insight into the other processes involved in uranium biomineralisation with bacterial EPS.

The bacterial cell surface was deconstructed into the individual cell surface structures associated with uranium biosorption, i.e. cell wall and cell membrane isolates. Due to the macromolecular complexity of these structures from both strains investigated, it was difficult to distinguish the contribution of certain types of biomolecules and functional groups responsible for the biosorption of U(VI) species. Therefore, further work should aim to identify the contribution of biomolecules within the cell surface structures. Extraction of biomolecules (i.e. protein and peptidoglycan extraction and purification from the cell walls of *B. subtilis* as well as protein and hydrocarbon extraction and purification from *P. putida* cell wall isolates) is required to fully understand the role of individual macromolecules involved in uranium biosorption at the cell surface. A combination of functional groups was shown to be responsible for uranium biosorption. Further work could include blocking the availability of certain functional groups with site-specific ions prior to future uranium biosorption experiments. This could help determine the retention of uranium by specific moieties on the bacterial cell surface and help contribute towards calculating the mass balance of the uranium biosorption process. The method used in this study isolated cell wall and membrane structures prior to uranium biosorption investigations. Further work could

aim to further develop the cell fractionation process of cells that have accumulated uranium to determine the specific retention of uranium by cell structures within a whole cell system and help determine the mass balance for uranium retained by the structures of whole bacteria.

Finally, work conducted using live cells within this study supported previous literature that suggested that Gram-negative bacteria exhibit a higher tolerance to uranium than Gram-positive bacteria. The advantage of the results obtained in this study are that the growth conditions and experimental procedure used to investigate uranium tolerance and toxicity mechanisms were more accurate than those of previous studies in which no single defined experimental procedure was utilised. Therefore, to further support this difference in susceptibility between Gram-negative and Gram-positive bacteria, characterisation of further bacteria in the same manner as this study would be required.

References.

ABD EL-SABOUR, M. F. 2007. Remediation and bioremediation of uranium contaminated soils. *Electronic Journal of Environmental, Agricultural and Food Chemistry,,* 6**,** 2009-2023.

ABDELOUAS, A., LUTZE, W. & NUTTALL, H. E. 1999. Oxidative dissolution of uraninite precipitated on Navajo sandstone. *Journal of Contaminant Hydrology,* 36**,** 353-375.

AHIMOU, F., BOONAERT, C. J. P., ADRIAENSEN, Y., JACQUES, P., THONART, P., PAQUOT, M. & ROUXHET, P. G. 2007. XPS analysis of chemical functions at the surface of Bacillus subtilis. *Journal of Colloid and Interface Science,* 309**,** 49-55.

AKSU, Z., SAG, Y. & KUTSAL, T. 1992. The biosorption of copper(II) by *c-vulgaris* and *z-ramigera*. *Environmental Technology,* 13**,** 579-586.

AKYUZ, T., AKYUZ, S., CAGLAR, H. & CAGLAR, N. 2008. FT-IR, EDXRF analysis of the Mardin-Mazidag phosphate deposit of Turkey and relations between phosphate, uranium and fluorine. *Asian Journal of Chemistry,* 20**,** 4085-4091.

ALESSI, D. S., LEZAMA-PACHECO, J. S., STUBBS, J. E., JANOUSCH, M., BARGAR, J. R., PERSSON, P. & BERNIER-LATMANI, R. 2014. The product of microbial uranium reduction includes multiple species with U(IV)-phosphate coordination. *Geochimica Et Cosmochimica Acta,* 131**,** 115-127.

ALEX, S. & DUPUIS, P. 1989. FT-IR and Raman Investigation of Cadmium Binding to DNA. *Inorganica Chimica Acta,* 157**,** 271-281.

ALLEN, G. C., TUCKER, P. M. & TYLER, J. W. 1982. Oxidation of uranium-dioxide at 298-degrees-k studied by using x-ray photo-electron spectroscopy. *Journal of Physical Chemistry,* 86**,** 224-228.

ALLESEN-HOLM, M., BARKEN, K. B., YANG, L., KLAUSEN, M., WEBB, J. S., KJELLEBERG, S., MOLIN, S., GIVSKOV, M. & TOLKER-NIELSEN, T. 2006. A characterization of DNA release in *Pseudomonas aeruginosa* cultures and biofilms. *Molecular Microbiology,* 59**,** 1114-1128.

ALRAKABI, M., SINGH, G., BHALLA, A., KUMAR, S., SRIVASTAVA, A., RAI, B., SINGH, N., SHAHI, J. S. & MEHTA, D. 2012. Study of uranium contamination of ground water in Punjab state in India using X-ray fluorescence technique. *Journal of Radioanalytical and Nuclear Chemistry,* 294**,** 221-227.

AMINI, M., YOUNESI, H. & BAHRAMIFAR, N. 2013. Biosorption of U(VI) from Aqueous Solution by *Chlorella vulgaris*: Equilibrium, Kinetic, and Thermodynamic Studies. *Journal of Environmental Engineering,* 139**,** 410-421.

APPLETON, J. D. 2007. Radon: Sources, health risks, and hazard mapping. *Ambio,* 36**,** 85-89.

APPUKUTTAN, D., RAO, A. S. & APTE, S. K. 2006. Engineering of *Deinococcus radiodurans* R1 for bioprecipitation of uranium from dilute nuclear waste. *Applied and Environmental Microbiology,* 72**,** 7873-7878.

ASUVATHRARNAN, R., GNANASEKAR, K. I., CLINSHA, P. C., RAVINDRAN, T. R. & KUTTY, K. V. G. 2015. Investigations on the charge compensation on Ca and U substitution in $CePO_4$ by using XPS, XRD and Raman spectroscopy. *Ceramics International,* 41**,** 3731-3739.

BABKINA, S. S. & ULAKHOVICH, N. A. 2005. Complexing of heavy metals with DNA and new bioaffinity method of their determination based on amperometric DNA-based biosensor. *Analytical Chemistry,* 77**,** 5678-5685.

BAKER, M. J., TREVISAN, J., BASSAN, P., BHARGAVA, R., BUTLER, H. J., DORLING, K. M., FIELDEN, P. R., FOGARTY, S. W., FULLWOOD, N. J., HEYS, K. A., HUGHES, C., LASCH, P., MARTIN-HIRSCH, P. L., OBINAJU, B., SOCKALINGUM, G. D., SULE-SUSO, J., STRONG, R. J., WALSH, M. J., WOOD, B. R., GARDNER, P. & MARTIN, F. L. 2014. Using Fourier transform IR spectroscopy to analyze biological materials. *Nature Protocols,* 9**,** 1771-1791.

BARKLEIT, A., FOERSTENDORF, H., LI, B., ROSSBERG, A., MOLL, H. & BERNHARD, G. 2011. Coordination of uranium(VI) with functional groups of bacterial lipopolysaccharide studied by EXAFS and FT-IR spectroscopy. *Dalton transactions,* 40**,** 9868-9876.

BARKLEIT, A., MOLL, H. & BERNHARD, G. 2008. Interaction of Uranium(VI) with lipolysaccharide. *Dalton transactions,* 21**,** 2879-2886.

BARKLEIT, A., MOLL, H. & BERNHARD, G. 2009. Complexation of uranium(VI) with peptidoglycan. *Dalton Transactions***,** 5379-5385.

BATTISTA, J. R. 1997. Against all odds: The survival strategies of *Deinococcus radiodurans*. *Annual Review of Microbiology,* 51**,** 203-224.

BEAZLEY, M. J., MARTINEZ, R. J., SOBECKY, P. A., WEBB, S. M. & TAILLEFERT, M. 2007. Uranium Biomineralization As a Result of Bacterial Phosphatase Activity: Insights From Bacterial Isolates From a Contaminated Subsurface. *Environmental science & technology,* 41**,** 5701-5707.

BEAZLEY, M. J., MARTINEZ, R. J., SOBECKY, P. A., WEBB, S. M. & TAILLEFERT, M. 2009. Nonreductive Biomineralization of Uranium(VI) Phosphate Via Microbial Phosphatase Activity in Anaerobic Conditions. *Geomicrobiology Journal,* 26**,** 431-441.

BEAZLEY, M. J., MARTINEZ, R. J., WEBB, S. M., SOBECKY, P. A. & TAILLEFERT, M. 2011. The effect of pH and natural microbial phosphatase activity on the speciation of uranium in subsurface soils. *Geochimica Et Cosmochimica Acta,* 75**,** 5648-5663.

BELITZ, K., FRAM, M. S. & JOHNSON, T. D. 2015. Metrics for Assessing the Quality of Groundwater Used for Public Supply, CA, USA: Equivalent-Population and Area. *Environmental Science & Technology,* 49**,** 8330-8338.

BENARD, P., LOUER, D., DACHEUX, N., BRANDEL, V. & GENET, M. 1994. $U(UO_2)((PO_4)_2$, a new mixed-valence uranium orthophosphate - ab-initio structure determination from powder diffraction data and optical and X-ray photoelectro spectra. *Chemistry of Materials,* 6**,** 1049-1058.

BENZERARA, K., MIOT, J., MORIN, G., ONA-NGUEMA, G., SKOURI-PANET, F. & FERARD, C. 2011. Significance, mechanisms and environmental implications of microbial biomineralization. *Comptes Rendus Geoscience,* 343**,** 160-167.

BERNIER-LATMANI, R., VEERAMANI, H., VECCHIA, E. D., JUNIER, P., LEZAMA-PACHECO, J. S., SUVOROVA, E. I., SHARP, J. O., WIGGINTON, N. S. & BARGAR, J. R. 2010. Non-uraninite Products of Microbial U(VI) Reduction. *Environmental Science & Technology,* 44**,** 9456-9462.

BEVERIDGE, T. J. 1988. Wall Ultrastructure How Little We Know. *Actor, P., Et Al. (Ed.). Antibiotic Inhibition of Bacterial Cell Surface Assembly and Function; American Society for Microbiology Conference, Philadelphia, Pennsylvania, USA, May 17-20, 1987. Xxii+657p. American Society for Microbiology: Washington, D.C., USA. Illus***,** 3-20.

BONDICI, V. F., LAWRENCE, J. R., KHAN, N. H., HILL, J. E., YERGEAU, E., WOLFAARDT, G. M., WARNER, J. & KORBER, D. R. 2013. Microbial communities in low permeability, high pH uranium mine tailings: characterization and potential effects. *Journal of Applied Microbiology,* 114**,** 1671-1686.

BORKOWSKI, A., SZALA, M. & CLAPA, T. 2015. Adsorption Studies of the Gram-Negative Bacteria onto Nanostructured Silicon Carbide. *Applied Biochemistry and Biotechnology,* 175**,** 1448-1459.

BORROK, D. M. & FEIN, J. B. 2005. The impact of ionic strength on the adsorption of protons, Pb, Cd, and Sr onto the surfaces of Gram negative bacteria: testing non-electro static, diffuse, and triple-layer models. *Journal of Colloid and Interface Science,* 286**,** 110-126.

BOYANOV, M. I., FLETCHER, K. E., KWON, M. J., RUI, X., O'LOUGHLIN, E. J., LOFFLER, F. E. & KEMNER, K. M. 2011. Solution and Microbial Controls on the Formation of Reduced U(IV) Species. *Environmental Science & Technology,* 45**,** 8336-8344.

BOYD, V. C., O.M.; PAPAS, K.K. 2008. Limitations in the Use of Fluorescein Diacetate/Propidium Iodide (FDA/PI) and Cell Permeable Nucleic Acid Stains for Viability Measurements of Isolated Islets of Langerhans. *Curr Trends Biotechnol Pharm.,* 2**,** 66–84.

BUCK, E. C., BROWN, N. R. & DIETZ, N. L. 1996. Contaminant uranium phases and leaching at the Fernald site in Ohio. *Environmental Science & Technology,* 30**,** 81-88.

BURA, R., CHEUNG, M., LIAO, B., FINLAYSON, J., LEE, B. C., DROPPO, I. G., LEPPARD, G. G. & LISS, S. N. 1998. Composition of extracellular polymeric substances in the activated sludge floc matrix. *Water Science and Technology,* 37**,** 325-333.

BURBANK, K. A., WALKER, R. A. & PEYTON, B. M. 2015. A molecular level mechanism for uranium (VI) toxicity through Ca^{2+} displacement in pyrroloquinoline quinone-dependent bacterial dehydrogenase. *Journal of Inorganic Biochemistry,* 149**,** 59-67.

BURNETT, P. G., HEINRICH, H., PEAK, D., BREMER, P. J., MCQUILLAN, A. J. & DAUGHNEY, C. J. 2006. The effect of pH and ionic strength on proton adsorption by the thermophilic bacterium *Anoxybacillus flavithermus*. *Geochimica Et Cosmochimica Acta,* 70**,** 1914-1927.

CAMPBELL, K. M., GALLEGOS, T. J. & LANDA, E. R. 2015. Biogeochemical aspects of uranium mineralization, mining, milling, and remediation. *Applied Geochemistry,* 57**,** 206-235.

CECAL, A., HUMELNICU, D., RUDIC, V., CEPOI, L., GANJU, D. & COJOCARI, A. 2012. Uptake of uranyl ions from uranium ores and sludges by means of *Spirulina platensis, Porphyridium cruentum* and *Nostok linckia* alga. *Bioresource Technology,* 118**,** 19-23.

CHAPON, V., PIETTE, L., VESVRES, M.-H., COPPIN, F., LE MARREC, C., CHRISTEN, R., THEODORAKOPOULOS, N., FEVRIER, L., LEVCHUK, S., MARTIN-GARIN, A., BERTHOMIEU, C. & SERGEANT, C. 2012. Microbial diversity in contaminated soils along the T22 trench of the Chernobyl experimental platform. *Applied Geochemistry,* 27**,** 1375-1383.

CHOUDHARY, S. & SAR, P. 2011. Uranium biomineralization by a metal resistant Pseudomonas aeruginosa strain isolated from contaminated mine waste. *Journal of Hazardous Materials,* 186**,** 336-343.

CHOUDHARY, S. & SAR, P. 2015. Interaction of uranium (VI) with bacteria: potential applications in bioremediation of U contaminated oxic environments. *Reviews in Environmental Science and Bio-Technology,* 14**,** 347-355.

CHOY, C. C., KORFIATIS, G. P. & MENG, X. 2006. Removal of depleted uranium from contaminated soils. *Journal of Hazardous Materials,* 136**,** 53-60.

CLAESSENS, J., VAN LITH, Y., LAVERMAN, A. M. & VAN CAPPELLEN, P. 2006. Acid-base activity of live bacteria: Implications for quantifying cell wall charge. *Geochimica Et Cosmochimica Acta,* 70**,** 267-276.

COMTE, S., GUIBAUD, G. & BAUDU, M. 2006. Relations between extraction protocols for activated sludge extracellular polymeric substances (EPS) and EPS complexation properties Part I. Comparison of the efficiency of eight EPS extraction methods. *Enzyme and Microbial Technology,* 38**,** 237-245.

DALLA VECCHIA, E. C., VEERAMANI, H., SUVOROVA, E. I., WIGGINTON, N. S., BARGAR, J. R. & BERNIER-LATMANI, R. 2010. U(VI) reduction by spores of *Clostridium acetobutylicum*. *Research in Microbiology,* 161**,** 765-771.

DAS, N. 2010. Recovery of precious metals through biosorption - A review. *Hydrometallurgy,* 103**,** 180-189.

DAS, T., KROM, B. P., VAN DER MEI, H. C., BUSSCHER, H. J. & SHARMA, P. K. 2011. DNA-mediated bacterial aggregation is dictated by acid-base interactions. *Soft Matter,* 7**,** 2927-2935.

DAS, T., SEHAR, S. & MANEFIELD, M. 2013. The roles of extracellular DNA in the structural integrity of extracellular polymeric substance and bacterial biofilm development. *Environmental Microbiology Reports,* 5**,** 778-786.

DISPIRITO, A. A. & TUOVINEN, O. H. 1982. Uranous ion oxidation and carbon-dioxide fixation by Thiobacillus-ferrooxidans. *Archives of Microbiology,* 133**,** 28-32.

DITTRICH, M. & SIBLER, S. 2005. Cell surface groups of two picocyanobacteria strains studied by zeta potential investigations, potentiometric titration, and infrared spectroscopy. *Journal of Colloid and Interface Science,* 286**,** 487-495.

DOBSON, R. S. & BURGESS, J. E. 2007. Biological treatment of precious metal refinery wastewater: A review. *Minerals Engineering,* 20**,** 519-532.

DOZOL, M., HAGEMANN, R., HOFFMAN, D. C., ADLOFF, J. P., VONGUNTEN, H. R., FOOS, J., KASPRZAK, K. S., LIU, Y. F., ZVARA, I., ACHE, H. J., DAS, H. A., HAGEMANN, R. J. C., HERRMANN, G., KAROL, P., MAENHAUT, W., NAKAHARA, H., SAKANOUE, M., TETLOW, J. A., BARO, G. B., FARDY, J. J., BENES, P., ROESSLER, K., ROTH, E., BURGER, K., STEINNES, E., KOSTANSKI, M. J., PEISACH, M., LILJENZIN, J. O., ARAS, N. K., MYASOEDOV, B. F. & HOLDEN, N. E. 1993. Radionuclide Migration In Groundwaters - Review Of The Behavior Of Actinides - (Technical Report). *Pure and Applied Chemistry,* 65**,** 1081-1102.

DUFF, M. C., HUNTER, D. B., BERTSCH, P. M. & AMRHEIN, C. 1999. Factors influencing uranium reduction and solubility in evaporation pond sediments. *Biogeochemistry,* 45**,** 95-114.

DUFRENE, Y. F. & ROUXHET, P. G. 1996. X-ray photoelectron spectroscopy analysis of the surface composition of *Azospirillum brasilense* in relation to growth conditions. *Colloids and Surfaces B-Biointerfaces,* 7**,** 271-279.

DUFRENE, Y. F., VANDERWAL, A., NORDE, W. & ROUXHET, P. G. 1997. X-ray photoelectron spectroscopy analysis of whole cells and isolated cell walls of gram-positive bacteria: Comparison with biochemical analysis. *Journal of Bacteriology,* 179**,** 1023-1028.

DUGUID, J. G., BLOOMFIELD, V. A., BENEVIDES, J. M. & THOMAS, G. J. 1995. Raman spectroscopy of DNA-Metal complexes .2. The thermal denaturation of DNA in the presence of Sr^{2+}, Ba^{2+}, Mg^{2+}, Ca^{2+}, Mn^{2+}, Co^{2+}, Ni^{2+}, and Cd^{2+}. *Biophysical Journal,* 69**,** 2623-2641.

EBOIGBODIN, K. E. & BIGGS, C. A. 2008. Characterization of the extracellular polymeric substances produced by *Escherichia coli* using infrared spectroscopic, proteomic, and aggregation studies. *Biomacromolecules,* 9**,** 686-695.

EL ARBI, A., GHORBAL, S., DELACROIX-BUCHET, A. & BOUIX, M. 2011. Assessment of the dynamics of the physiological states of *Lactococcus lactis* ssp cremoris SK11 during growth by flow cytometry. *Journal of Applied Microbiology,* 111**,** 1205-1211.

FÁBREGAS, J., VÁZQUEZ, V., CABEZAS, B. & OTERO, A. 1993. Tris not only controls the pH in microalgal cultures, but also feeds bacteria. *Journal of Applied Phycology,* 5**,** 543-545.

FANG, L. C., CAI, P., CHEN, W. L., LIANG, W., HONG, Z. N. & HUANG, Q. Y. 2009. Impact of cell wall structure on the behavior of bacterial cells in the binding of copper and cadmium. *Colloids and Surfaces a-Physicochemical and Engineering Aspects,* 347**,** 50-55.

FANG, L. C., HUANG, Q. Y., WEI, X., LIANG, W., RONG, X. M., CHEN, W. L. & CAI, P. 2010. Microcalorimetric and potentiometric titration studies on the adsorption of copper by extracellular polymeric substances (EPS), minerals and their composites. *Bioresource Technology,* 101**,** 5774-5779.

FEIN, J. B., BOILY, J. F., YEE, N., GORMAN-LEWIS, D. & TURNER, B. F. 2005. Potentiometric titrations of *Bacillus subtilis* cells to low pH and a comparison of modeling approaches. *Geochimica Et Cosmochimica Acta,* 69**,** 1123-1132.

FEIN, J. B., DAUGHNEY, C. J., YEE, N. & DAVIS, T. A. 1997. A chemical equilibrium model for metal adsorption onto bacterial surfaces. *Geochimica Et Cosmochimica Acta,* 61**,** 3319-3328.

FERRIS, F. G. & BEVERIDGE, T. J. 1986. Site specificity of metallic ion binding in Escherichia-coli k-12 lipopolysaccharide. *Canadian Journal of Microbiology,* 32**,** 52-55.

FINLAY, J. A., ALLAN, V. J. M., CONNER, A., CALLOW, M. E., BASNAKOVA, G. & MACASKIE, L. E. 1999. Phosphate release and heavy metal accumulation by biofilm-immobilized and chemically-coupled cells of a *Citrobacter* sp. pre-grown in continuous culture. *Biotechnology and Bioengineering,* 63**,** 87-97.

FINNERAN, K. T., HOUSEWRIGHT, M. E. & LOVLEY, D. R. 2002. Multiple influences of nitrate on uranium solubility during bioremediation of uranium-contaminated subsurface sediments. *Environmental Microbiology,* 4**,** 510-516.

FLETCHER, K. E., BOYANOV, M. I., THOMAS, S. H., WU, Q. Z., KEMNER, K. M. & LOFFLER, F. E. 2010. U(VI) Reduction to Mononuclear U(IV) by *Desulfitobacterium* Species. *Environmental Science & Technology,* 44**,** 4705-4709.

FOWLE, D. A., FEIN, J. B. & MARTIN, A. M. 2000. Experimental study of uranyl adsorption onto *Bacillus subtilis*. *Environmental Science & Technology,* 34**,** 3737-3741.

FRANCIS, C. W., TIMPSON, M. E., LEE, S. Y., ELLESS, M. P. & WILSON, J. H. 1998. The use of carbonate lixiviants to remove uranium from uranium-contaminated soils. *Journal of Radioanalytical and Nuclear Chemistry,* 228**,** 15-20.

GADD, G. M. 1993. Interactions of fungi with toxic metals. *New Phytologist,* 124**,** 25-60.

GARIDEL, P., BLUME, A. & HUBNER, W. 2000. A Fourier transform infrared spectroscopic study of the interaction of alkaline earth cations with the negatively charged phospholipid 1,2-dimyristoyl-sn-glycero-3-phosphoglycerol. *Biochimica Et Biophysica Acta-Biomembranes,* 1466**,** 245-259.

GAVRILESCU, M., PAVEL, L. V. & CRETESCU, I. 2009. Characterization and remediation of soils contaminated with uranium. *Journal of Hazardous Materials,* 163**,** 475-510.

GEHRKE, T., TELEGDI, J., THIERRY, D. & SAND, W. 1998. Importance of extracellular polymeric substances from *Thiobacillus ferrooxidans* for bioleaching. *Applied and Environmental Microbiology,* 64**,** 2743-2747.

GORBY, Y. A. & LOVLEY, D. R. 1992. Enzymatic uranium precipitation. *Environmental Science & Technology,* 26**,** 205-207.

GORMAN-LEWIS, D., ELIAS, P. E. & FEIN, J. B. 2005. Adsorption of aqueous uranyl complexes onto *Bacillus subtilis* cells. *Environmental Science and Technology,* 39**,** 4906-4912.

GROOTAERT, C., BOON, N., ZEKA, F., VANHOECKE, B., BRACKE, M., VERSTRAETE, W. & VAN DE WIELE, T. 2011. Adherence and viability of intestinal bacteria to differentiated Caco-2 cells quantified by flow cytometry. *Journal of Microbiological Methods,* 86**,** 33-41.

HA, J., GELABERT, A., SPORMANN, A. M. & BROWN, G. E., JR. 2010. Role of extracellular polymeric substances in metal ion complexation on *Shewanella oneidensis*: Batch uptake, thermodynamic modeling, ATR-FTIR, and EXAFS study. *Geochimica Et Cosmochimica Acta,* 74**,** 1-15.

HAAS, J. R., DICHRISTINA, T. J. & WADE, R. 2001. Thermodynamics of U(VI) sorption onto *Shewanella putrefaciens*. *Chemical Geology,* 180**,** 33-54.

HAAS, J. R. & NORTHUP, A. 2004. Effects of aqueous complexation on reductive precipitation of uranium by *Shewanella putrefaciens*. *Geochemical Transactions,* 5**,** 41-48.

HAMMES, F., BERNEY, M. & EGLI, T. 2011. Cultivation-independent Assessment of Bacterial Viability. *High Resolution Microbial Single Cell Analytics,* 124**,** 123-150.

HANDLEY-SIDHU, S., HRILJAC, J. A., CUTHBERT, M. O., RENSHAW, J. C., PATTRICK, R. A. D., CHARNOCK, J. M., STOLPE, B., LEAD, J. R., BAKER, S. & MACASKIE, L. E. 2014. Bacterially Produced Calcium Phosphate Nanobiominerals: Sorption Capacity, Site Preferences, and Stability of Captured Radionuclides. *Environmental Science & Technology,* 48**,** 6891-6898.

HARDEN, V. P. & HARRIS, J. O. 1953. The isoelectric point of bacterial cells. *Journal of Bacteriology,* 65**,** 198-202.

HE, Z. Q. & HONEYCUTT, C. W. 2005. A modified molybdenum blue method for orthophosphate determination suitable for investigating enzymatic hydrolysis of organic phosphates. *Communications in Soil Science and Plant Analysis,* 36**,** 1373-1383.

HU, P., BRODIE, E. L., SUZUKI, Y., MCADAMS, H. H. & ANDERSEN, G. L. 2005. Whole-genome transcriptional analysis of heavy metal stresses in *Caulobacter crescentus*. *Journal of Bacteriology,* 187**,** 8437-8449.

HWANG, G., BAN, Y. M., LEE, C. H., CHUNG, C. H. & AHN, I. S. 2008. Adhesion of *Pseudomonas putida* NCIB 9816-4 to a naphthalene-contaminated soil. *Colloids and Surfaces B-Biointerfaces,* 62**,** 91-96.

IKEDA, A., HENNIG, C., TSUSHIMA, S., TAKAO, K., IKEDA, Y., SCHEINOST, A. C. & BERNHARD, G. 2007. Comparative study of uranyl(VI) and -(V) carbonato complexes in an aqueous solution. *Inorganic Chemistry,* 46**,** 4212-4219.

IMLAY, J. A. 2003. Pathways of oxidative damage. *Annual Review of Microbiology,* 57**,** 395-418.

JACKSON, S. T. & NUZZO, R. G. 1995. DETERMINING HYBRIDIZATION DIFFERENCES FOR AMORPHOUS-CARBON FROM THE XPS C-1S ENVELOPE. *Applied Surface Science,* 90**,** 195-203.

JELINEK, R. T. & SORG, T. J. 1988. Operating a small full-scale ion exchange system for uranium removal. *American Water Works Association Journal,* 80**,** 79-83.

JEONG, B. C., HAWES, C., BONTHRONE, K. M. & MACASKIE, L. E. 1997. Localization of enzymically enhanced heavy metal accumulation by *Citrobacter* sp. and metal accumulation in vitro by liposomes containing entrapped enzyme. *Microbiology-Uk,* 143**,** 2497-2507.

JIANG, W., SAXENA, A., SONG, B., WARD, B. B., BEVERIDGE, T. J. & MYNENI, S. C. B. 2004. Elucidation of functional groups on gram-positive and gram-negative bacterial surfaces using infrared spectroscopy. *Langmuir,* 20**,** 11433-11442.

JOHNSON, N. R. & HILL, J. E. 2011. High-Throughput Measurement and Classification of Organic P in Environmental Samples. *Jouranl of Visualised Experiments***,** 1-3.

JROUNDI, F., MERROUN, M. L., ARIAS, J. M., ROSSBERG, A., SELENSKA-POBELL, S. & GONZALEZ-MUNOZ, M. T. 2007. Spectroscopic and microscopic characterization of uranium biomineralization in *Myxococcus xanthus*. *Geomicrobiology Journal,* 24**,** 441-449.

KACHLANY, S. C., LEVERY, S. B., KIM, J. S., REUHS, B. L., LION, L. W. & GHIORSE, W. C. 2001. Structure and carbohydrate analysis of the exopolysaccharide capsule of *Pseudomonas putida* G7. *Environmental Microbiology,* 3**,** 774-784.

KAMNEV, A. A., ANTONYUK, L. P., MATORA, L. Y., SEREBRENNIKOVA, O. B., SUMAROKA, M. V., COLINA, M., RENOU-GONNORD, M. F. & IGNATOV, V. V. 1999. Spectroscopic characterization of cell membranes and their constituents of the plant-associated soil bacterium Azospirillum brasilense. *Journal of Molecular Structure,* 481**,** 387-393.

KAZY, S. K., D'SOUZA, S. F. & SAR, P. 2009. Uranium and thorium sequestration by a *Pseudomonas* sp.: Mechanism and chemical characterization. *Journal of Hazardous Materials,* 163**,** 65-72.

KAZY, S. K., SAR, P. & D'SOUZA, S. F. 2008. Studies on uranium removal by the extracellular polysaccharide of a *Pseudomonas aeruginosa* strain. *Bioremediation Journal,* 12**,** 47-57.

KEASLING, J. D. & HUPF, G. A. 1996. Genetic manipulation of polyphosphate metabolism affects cadmium tolerance in *Escherichia coli*. *Applied and Environmental Microbiology,* 62**,** 743-746.

KELLY, S. D., KEMNER, K. M., FEIN, J. B., FOWLE, D. A., BOYANOV, M. I., BUNKER, B. A. & YEE, N. 2002. X-ray absorption fine structure determination of pH-dependent U-bacterial cell wall interactions. *Geochimica Et Cosmochimica Acta,* 66**,** 3855-3871.

KENNEY, J. P. L. & FEIN, J. B. 2011a. Cell Wall Reactivity of Acidophilic and Alkaliphilic Bacteria Determined by Potentiometric Titrations and Cd Adsorption Experiments. *Environmental Science & Technology,* 45**,** 4446-4452.

KENNEY, J. P. L. & FEIN, J. B. 2011b. Importance of extracellular polysaccharides on proton and Cd binding to bacterial biomass: A comparative study. *Chemical Geology,* 286**,** 109-117.

KHIJNIAK, T. V., SLOBODKIN, A. I., COKER, V., RENSHAW, J. C., LIVENS, F. R., BONCH-OSMOLOVSKAYA, E. A., BIRKELAND, N. K., MEDVEDEVA-LYALIKOVA, N. N. & LLOYD, J. R. 2005. Reduction of uranium(VI) phosphate during growth of the thermophilic bacterium *Thermoterrabacterium ferrireducens*. *Applied And Environmental Microbiology,* 71**,** 6423-6426.

KNOX, A. S., BRIMON, R. L., KAPLAN, D. I. & PALLER, M. H. 2008. Interactions among phosphate amendments, microbes and uranium mobility in contaminated sediments. *Science of the Total Environment,* 395**,** 63-71.

KOBAN, A., GEIPEL, G., ROSSBERG, A. & BERNHARD, G. 2004. Uranium(VI) complexes with sugar phosphates in aqueous solution. *Radiochimica Acta,* 92**,** 903-908.

KORNBERG, A., RAO, N. N. & AULT-RICHE, D. 1999. Inorganic polyphosphate: A molecule of many functions. *Annual Review of Biochemistry,* 68**,** 89-125.

KRAWCZYK-BAERSCH, E., GROSSMANN, K., ARNOLD, T., HOFMANN, S. & WOBUS, A. 2008. Influence of uranium (VI) on the metabolic activity of stable multispecies biofilms studied by oxygen microsensors and fluorescence microscopy. *Geochimica Et Cosmochimica Acta,* 72**,** 5251-5265.

KRAWCZYK-BARSCH, E., LUTKE, L., MOLL, H., BOK, F., STEUDTNER, R. & ROSSBERG, A. 2015. A spectroscopic study on U(VI) biomineralization in cultivated *Pseudomonas fluorescens* biofilms isolated from granitic aquifers. *Environmental Science and Pollution Research,* 22**,** 4555-4565.

KULKARNI, S., BALLAL, A. & APTE, S. K. 2013. Bioprecipitation of uranium from alkaline waste solutions using recombinant *Deinococcus radiodurans*. *Journal of Hazardous Materials,* 262**,** 853-61.

KUMAR, R., ACHARYA, C. & JOSHI, S. R. 2011. Isolation and Analyses of Uranium Tolerant *Serratia marcescens* Strains and Their Utilization for Aerobic Uranium U(VI) Bioadsorption. *Journal of Microbiology,* 49**,** 568-574.

KUMAR, R., NONGKHLAW, M., ACHARYA, C. & JOSHI, S. R. 2013. Uranium (U)-Tolerant Bacterial Diversity from U Ore Deposit of Domiasiat in North-East India and Its Prospective Utilisation in Bioremediation. *Microbes and Environments,* 28**,** 33-41.

KUSHWAHA, S., SREEDHAR, B. & PADMAJA, P. 2012. XPS, EXAFS, and FTIR As Tools To Probe the Unexpected Adsorption-Coupled Reduction of U(VI) to U(V) and U(IV) on *Borassus flabellifer*-Based Adsorbents. *Langmuir,* 28**,** 16038-16048.

LANGLEY, S. & BEVERIDGE, T. J. 1999. Effect of O-side-chain-lipopolysaccharide chemistry on metal binding. *Applied and Environmental Microbiology,* 65**,** 489-498.

LEE, S. Y., BAIK, M. H. & CHOI, J. W. 2010. Biogenic Formation and Growth of Uraninite (UO_2). *Environmental Science & Technology,* 44**,** 8409-8414.

LENHART, J. J., CABANISS, S. E., MACCARTHY, P. & HONEYMAN, B. D. 2000. Uranium(VI) complexation with citric, humic and fulvic acids. *Radiochimica Acta,* 88**,** 345-353.

LEVY-BOOTH, D. J., CAMPBELL, R. G., GULDEN, R. H., HART, M. M., POWELL, J. R., KLIRONOMOS, J. N., PAULS, K. P., SWANTON, C. J., TREVORS, J. T. & DUNFIELD, K. E. 2007. Cycling of extracellular DNA in the soil environment. *Soil Biology & Biochemistry,* 39**,** 2977-2991.

LI, X. K., ZHANG, H., MA, Y. T., LIU, P. & KRUMHOLZ, L. R. 2014. Genes required for alleviation of uranium toxicity in sulfate reducing bacterium *Desulfovibio alaskensis* G20. *Ecotoxicology,* 23**,** 726-733.

LIU, J. H., VAN DEN BERGHE, S. & KONSTANTINOVIC, M. J. 2009. XPS spectra of the U^{5+} compounds KUO_3, $NaUO_3$ and $Ba_2U_2O_7$. *Journal of Solid State Chemistry,* 182**,** 1105-1108.

LLORENS, I., UNTEREINER, G., JAILLARD, D., GOUGET, B., CHAPON, V. & CARRIERE, M. 2012. Uranium Interaction with Two Multi-Resistant Environmental Bacteria: *Cupriavidus metallidurans* CH34 and *Rhodopseudomonas palustris*. *Plos One,* 7.

LLOYD, J. R., LEANG, C., MYERSON, A. L. H., COPPI, M. V., CUIFO, S., METHE, B., SANDLER, S. J. & LOVLEY, D. R. 2003. Biochemical and genetic characterization of PpcA, a periplasmic c-type cytochrome in *Geobacter sulfurreducens*. *Biochemical Journal,* 369**,** 153-161.

LLOYD, J. R. & MACASKIE, L. E. 2000. Bioremediation of radionuclide-containing wastewaters. *Environmental Microbe-Metal Interactions***,** 277-327.

LLOYD, J. R. & RENSHAW, J. C. 2005. Microbial transformations of radionuclides: Fundamental mechanisms and biogeochemical implications. *Metal Ions in Biological Systems, Vol 44,* 44**,** 205-240.

LOPEZ-FERNANDEZ, M., FERNANDEZ-SANFRANCISCO, O., MORENO-GARCIA, A., MARTIN-SANCHEZ, I., SANCHEZ-CASTRO, I. & LARBI MERROUN, M. 2014. Microbial communities in bentonite formations and their interactions with uranium. *Applied Geochemistry,* 49**,** 77-86.

LOVLEY, D. R. & PHILLIPS, E. J. P. 1992. Reduction of uranium by *Desulfovibrio-desulfuricans*. *Applied and Environmental Microbiology,* 58**,** 850-856.

LOVLEY, D. R., PHILLIPS, E. J. P., GORBY, Y. A. & LANDA, E. R. 1991. Microbial reduction of uranium. *Nature,* 350**,** 413-416.

LOVLEY, D. R., WIDMAN, P. K., WOODWARD, J. C. & PHILLIPS, E. J. P. 1993. Reduction of uranium by cytochrome-C(3) of *Desulfovibrio-vulgaris*. *Applied and Environmental Microbiology,* 59**,** 3572-3576.

LU, X., ZHOU, X.-J. & WANG, T.-S. 2013. Mechanism of uranium(VI) uptake by *Saccharomyces cerevisiae* under environmentally relevant conditions: Batch, HRTEM, and FTIR studies. *Journal of Hazardous Materials,* 262**,** 297-303.

LUETKE, L., MOLL, H. & BERNHARD, G. 2012. Insights into the uranium(VI) speciation with *Pseudomonas fluorescens* on a molecular level. *Dalton Transactions,* 41**,** 13370-13378.

LUMETTA, G. J., MCNAMARA, B. K., RAPKO, B. M. & HUTCHISON, J. E. 1999. Complexation of uranyl ion by tetrahexylmalonamides: an equilibrium modeling and infrared spectroscopic study. *Inorganica Chimica Acta,* 293**,** 195-205.

LUO, W. & GU, B. 2011. Dissolution of Uranium-Bearing Minerals and Mobilization of Uranium by Organic Ligands in a Biologically Reduced Sediment. *Environmental Science & Technology,* 45**,** 2994-2999.

MACASKIE, L. E., BONTHRONE, K. M., YONG, P. & GODDARD, D. T. 2000. Enzymically mediated bioprecipitation of uranium by a *Citrobacter* sp.: a concerted role for exocellular lipopolysaccharide and associated phosphatase in biomineral formation. *Microbiology-Uk,* 146**,** 1855-1867.

MACASKIE, L. E., EMPSON, R. M., CHEETHAM, A. K., GREY, C. P. & SKARNULIS, A. J. 1992. Uranium bioaccumulation by a *Citrobacter* sp. as a result of enzymatically mediated growth of polycrystalline HUO_2PO_4. *Science,* 257**,** 782-784.

MADIGAN, M. T. M., J.M.; DUNLAP, P.V.; CLARK, D.P; BROCK, T. 2008. *Brock Biology of Microorganisms*, Pearson.

MARKICH, S. J. 2002. Uranium speciation and bioavailability in aquatic systems: an overview. *TheScientificWorldJournal,* 2**,** 707-29.

MARTINEZ, R. J., BEAZLEY, M. J., TAILLEFERT, M., ARAKAKI, A. K., SKOLNICK, J. & SOBECKY, P. A. 2007. Aerobic uranium (VI) bioprecipitation by metal-resistant bacteria isolated from radionuclide- and metal-contaminated subsurface soils. *Environmental Microbiology,* 12**,** 9.

MARTINEZ, R. J., WU, C. H., BEAZLEY, M. J., ANDERSEN, G. L., CONRAD, M. E., HAZEN, T. C., TAILLEFERT, M. & SOBECKY, P. A. 2014. Microbial Community Responses to Organophosphate Substrate Additions in Contaminated Subsurface Sediments. *Plos One,* 9.

MARVASI, M., VISSCHER, P. T. & MARTINEZ, L. C. 2010. Exopolymeric substances (EPS) from *Bacillus subtilis*: polymers andgenes encoding their synthesis. *FEMS Microbiology,* 313**,** 1-9.

MASON, C. F. V. 1997. Carbonate leaching of uranium from contaminated soils. *Environmental Science & Technology,* 31**,** 2707-2711.

MATSUI, K., ISHII, N. & KAWABATA, Z. 2003. Release of extracellular transformable plasmid DNA from *Escherichia coli* cocultivated with algae. *Applied and Environmental Microbiology,* 69**,** 2399-2404.

MEREDITH, T. C. & WOODARD, R. W. 2005. Identification of GutQ from *Escherichia col*i as a D-arabinose 5-phosphate isomerase. *Journal of Bacteriology,* 187**,** 6936-6942.

MERROUN, M., NEDELKOVA, M., ROSSBERG, A., HENNIG, C. & SELENSKA-POBELL, S. 2006. Interaction mechanisms of bacterial strains isolated from extreme habitats with uranium. *Radiochimica Acta,* 94**,** 723-729.

MERROUN, M. L. 2007. Interactions between Metals and Bacteria: Fundamental and Applied Research. *In:* MENDEZ-VILAS, A. (ed.) *Communicating Current Research and Educational Topics and Trends in Applied Microbiology.* Badajoz: Formatex.

MERROUN, M. L., GEIPEL, G., NICOLAI, R., HEISE, K. H. & SELENSKA-POBELL, S. 2003a. Complexation of uranium (VI) by three eco-types of *Acidithiobacillus ferrooxidans* studied using time-resolved laser-induced fluorescence spectroscopy and infrared spectroscopy. *Biometals,* 16**,** 331-339.

MERROUN, M. L., HENNIG, C., ROSSBERG, A., REICH, T. & SELENSKA-POBELL, S. 2003b. Characterization of U(VI)-*Acidithiobacillus ferrooxidans* complexes using EXAFS, transmission electron microscopy, and energy-dispersive X-ray analysis. *Radiochimica Acta,* 91**,** 583-591.

MERROUN, M. L., NEDELKOVA, M., OJEDA, J. J., REITZ, T., LOPEZ FERNANDEZ, M., ARIAS, J. M., ROMERO-GONZALEZ, M. & SELENSKA-POBELL, S. 2011. Bio-precipitation of uranium by two bacterial isolates recovered from extreme environments as estimated by potentiometric titration, TEM and X-ray absorption spectroscopic analyses. *Journal of Hazardous Materials,* 197**,** 1-10.

MERROUN, M. L., RAFF, J., ROSSBERG, A., HENNIG, C., REICH, T. & SELENSKA-POBELL, S. 2005. Complexation of uranium by cells and S-layer sheets of *Bacillus sphaericus* JG-A12. *Applied and Environmental Microbiology,* 71**,** 5532-5543.

MERROUN, M. L. & SELENSKA-POBELL, S. 2001. Interactions of three eco-types of *Acidithiobacillus ferrooxidans* with U(VI). *Biometals,* 14**,** 171-179.

MERROUN, M. L. & SELENSKA-POBELL, S. 2008. Bacterial interactions with uranium: An environmental perspective. *Journal of Contaminant Hydrology,* 102**,** 285-295.

MISHRA, B., BOYANOV, M., BUNKER, B. A., KELLY, S. D., KEMNER, K. M. & FEIN, J. B. 2010. High- and low-affinity binding sites for Cd on the bacterial cell walls of *Bacillus subtilis* and *Shewanella oneidensis*. *Geochimica Et Cosmochimica Acta,* 74**,** 4219-4233.

MISRA, C. S., APPUKUTTAN, D., KANTAMREDDI, V. S. S., RAO, A. S. & APTE, S. K. 2012. Recombinant *D. radiodurans* cells for bioremediation of heavy metals from acidic/neutral aqueous wastes. *Bioengineered,* 3**,** 44-48.

MONDANI, L., BENZERARA, K., CARRIERE, M., CHRISTEN, R., MAMINDY-PAJANY, Y., FEVRIER, L., MARMIER, N., ACHOUAK, W., NARDOUX, P., BERTHOMIEU, C. & CHAPON, V. 2011. Influence of Uranium on Bacterial Communities: A Comparison of Natural Uranium-Rich Soils with Controls. *Plos One,* 6.

MONOD, J. 1949. The growth of bacterial cultures. *Annual Review of Microbiology,* 3**,** 371-394.

MORCILLO, F., GONZALEZ-MUNOZ, M. T., REITZ, T., ROMERO-GONZALEZ, M. E., ARIAS, J. M. & MERROUN, M. L. 2014. Biosorption and Biomineralization of U(VI) by the Marine Bacterium *Idiomarina loihiensis* MAH1: Effect of Background Electrolyte and pH. *Plos One,* 9.

MORIWAKI, H., KOIDE, R., YOSHIKAWA, R., WARABINO, Y. & YAMAMOTO, H. 2013. Adsorption of rare earth ions onto the cell walls of wild-type and lipoteichoic acid-defective strains of *Bacillus subtilis*. *Applied Microbiology and Biotechnology,* 97**,** 3721-3728.

NAKAJIMA, A. & TSURUTA, T. 2004. Competitive biosorption of thorium and uranium by *Micrococcus luteus*. *Journal of Radioanalytical and Nuclear Chemistry,* 260**,** 13-18.

NARANG, A. & PILYUGIN, S. S. 2007. Bacterial gene regulation in diauxic and non-diauxic growth. *Journal of Theoretical Biology,* 244**,** 326-348.

NEDELKOVA, M., MERROUN, M. L., ROSSBERG, A., HENNIG, C. & SELENSKA-POBELL, S. 2007. *Microbacterium* isolates from the vicinity of a radioactive waste depository and their interactions with uranium. *Fems Microbiology Ecology,* 59**,** 694-705.

NEU, M. P., BOUKHALFA, H. & MERROUN, M. L. 2010. Biomineralization and biotransformations of actinide materials. *Mrs Bulletin,* 35**,** 849-857.

NEVIN, K. P. & LOVLEY, D. R. 2000. Potential for nonenzymatic reduction of Fe(III) via electron shuttling in subsurface sediments. *Environmental Science & Technology,* 34**,** 2472-2478.

NEWSOME, L., MORRIS, K. & LLOYD, J. R. 2014. The biogeochemistry and bioremediation of uranium and other priority radionuclides. *Chemical Geology,* 363**,** 164-184.

NEWSOME, L., MORRIS, K., SHAW, S., TRIVEDI, D. & LLOYD, J. R. 2015a. The stability of microbially reduced U(IV); impact of residual electron donor and sediment ageing. *Chemical Geology,* 409**,** 125-135.

NEWSOME, L., MORRIS, K., TRIVEDI, D., BEWSHER, A. & LLOYD, J. R. 2015b. Biostimulation by Glycerol Phosphate to Precipitate Recalcitrant Uranium(IV) Phosphate. *Environmental Science & Technology,* 49**,** 11070-11078.

NIELSEN, K. M., JOHNSEN, P. J., BENSASSON, D. & DAFFONCHIO, D. 2007. Release and persistence of extracellular DNA in the environment. *Environmental Biosafety Research,* 6**,** 37-53.

OJEDA, J. J. & DITTRICH, M. 2012. Fourier transform infrared spectroscopy for molecular analysis of microbial cells. *Methods in molecular biology (Clifton, N.J.),* 881**,** 187-211.

OJEDA, J. J., ROMERO-GONZALEZ, M. E., BACHMANN, R. T., EDYVEAN, R. G. J. & BANWART, S. A. 2008a. Characterization of the cell surface and cell wall chemistry of drinking water bacteria by combining XPS, FTIR spectroscopy, modeling, and potentiometric titrations. *Langmuir,* 24**,** 4032-4040.

OJEDA, J. J., ROMERO-GONZALEZ, M. E. & BANWART, S. A. 2009. Analysis of Bacteria on Steel Surfaces Using Reflectance Micro-Fourier Transform Infrared Spectroscopy. *Analytical Chemistry,* 81**,** 6467-6473.

OJEDA, J. J., ROMERO-GONZALEZ, M. E., POURAN, H. M. & BANWART, S. A. 2008b. In situ monitoring of the biofilm formation of *Pseudomonas putida* on hematite using flow-cell ATR-FTIR spectroscopy to investigate the formation of inner-sphere bonds between the bacteria and the mineral. *Mineralogical Magazine,* 72**,** 101-106.

OMOIKE, A. & CHOROVER, J. 2004. Spectroscopic study of extracellular polymeric substances from *Bacillus subtilis*: Aqueous chemistry and adsorption effects. *Biomacromolecules,* 5**,** 1219-1230.

ORELLANA, R., LEAVITT, J. J., COMOLLI, L. R., CSENCSITS, R., JANOT, N., FLANAGAN, K. A., GRAY, A. S., LEANG, C., IZALLALEN, M., MESTER, T. & LOVLEY, D. R. 2013. U(VI) Reduction by Diverse Outer Surface c-Type Cytochromes of *Geobacter sulfurreducens*. *Applied and Environmental Microbiology,* 79**,** 6369-6374.

PAGNANELLI, F., PAPINI, M. P., TORO, L., TRIFONI, M. & VEGLIO, F. 2000. Biosorption of metal ions on *Arthrobacter sp.*: Biomass characterization and biosorption modeling. *Environmental Science & Technology,* 34**,** 2773-2778.

PAN, X. H., CHEN, Z., CHEN, F. B., CHENG, Y. J., LIN, Z. & GUAN, X. 2015. The mechanism of uranium transformation from U(VI) into nano-uramphite by two indigenous *Bacillus thuringiensis* strains. *Journal of Hazardous Materials,* 297**,** 313-319.

PANAK, P. J., KNOPP, R., BOOTH, C. H. & NITSCHE, H. 2002. Spectroscopic studies on the interaction of U(VI) with Bacillus sphaericus. *Radiochimica Acta,* 90**,** 779-783.

PARIKH, S. J. & CHOROVER, J. 2006. ATR-FTIR spectroscopy reveals bond formation during bacterial adhesion to iron oxide. *Langmuir,* 22**,** 8492-8500.

PATERSON-BEEDLE, M., READMAN, J. E., HRILJAC, J. A. & MACASKIE, L. E. 2010. Biorecovery of uranium from aqueous solutions at the expense of phytic acid. *Hydrometallurgy,* 104**,** 524-528.

PELLETIER, G., FRENETTE, M. & VADEBONCOEUR, C. 1994. Transport of mannose by an inducible phosphoenolpyruvate - fructose phosphotransferase system in *Streptococcus-salivarius*. *Microbiology-Uk,* 140**,** 2433-2438.

PIETRAMELLARA, G., ASCHER, J., BORGOGNI, F., CECCHERINI, M. T., GUERRI, G. & NANNIPIERI, P. 2009. Extracellular DNA in soil and sediment: fate and ecological relevance. *Biology and Fertility of Soils,* 45**,** 219-235.

PINCHUK, G. E., AMMONS, C., CULLEY, D. E., LI, S. W., MCLEAN, J. S., ROMINE, M. F., NEALSON, K. H., FREDRICKSON, J. K. & BELIAEV, A. S. 2008. Utilization of DNA as a Sole Source of Phosphorus, Carbon, and Energy by *Shewanella* spp.: Ecological and Physiological Implications for Dissimilatory Metal Reduction. *Applied and environmental microbiology,* 74**,** 1198-1208.

PIROG, T. P., KOVALENKO, M. A., KUZMINSKAYA, Y. V. & VOTSELKO, S. K. 2004. Physicochemical properties of the microbial exopolysaccharide ethapolan synthesized on a mixture of growth substrates. *Microbiology,* 73**,** 14-18.

PLETTE, A. C. C., VANRIEMSDIJK, W. H., BENEDETTI, M. F. & VANDERWAL, A. 1995. pH dependent charging behavior of isolated cell-walls of a gram-positive soil bacterium. *Journal of Colloid and Interface Science,* 173**,** 354-363.

PRIESTER, J. H., OLSON, S. G., WEBB, S. M., NEU, M. P., HERSMAN, L. E. & HOLDEN, P. A. 2006. Enhanced exopolymer production and chromium stabilization in *Pseudomonas putida* unsaturated biofilms. *Applied and Environmental Microbiology,* 72**,** 1988-1996.

RAMSTEDT, M., LEONE, L., PERSSON, P. & SHCHUKAREV, A. 2014. Cell Wall Composition of *Bacillus subtilis* Changes as a Function of pH and Zn^{2+} Exposure: Insights from Cryo-XPS Measurements. *Langmuir,* 30**,** 4367-4374.

RAY, A. E., BARGAR, J. R., SIVASWAMY, V., DOHNALKOVA, A. C., FUJITA, Y., PEYTON, B. M. & MAGNUSON, T. S. 2011. Evidence for multiple modes of uranium immobilization by an anaerobic bacterium. *Geochimica Et Cosmochimica Acta,* 75**,** 2684-2695.

REITZ, T., ROSSBERG, A., BARKLEIT, A., SELENSKA-POBELL, S. & MERROUN, M. L. 2014. Decrease of U(VI) Immobilization Capability of the Facultative Anaerobic Strain *Paenibacillus* sp JG-TB8 under Anoxic Conditions Due to Strongly Reduced Phosphatase Activity. *Plos One,* 9.

RENNINGER, N., KNOPP, R., NITSCHE, H., CLARK, D. S. & KEASLING, J. D. 2004. Uranyl precipitation by *Pseudomonas aeruginosa* via controlled polyphosphate metabolism. *Applied and Environmental Microbiology,* 70**,** 7404-7412.

RIEGER, A. M., HALL, B. E., LE THUONG, L., SCHANG, L. M. & BARREDA, D. R. 2010. Conventional apoptosis assays using propidium iodide generate a significant number of false positives that prevent accurate assessment of cell death. *Journal of Immunological Methods,* 358**,** 81-92.

RODRIGUEZ, G. G., PHIPPS, D., ISHIGURO, K. & RIDGWAY, H. F. 1992. Use of a fluorescent redox probe for direct visualization of actively respiring bacteria. *Applied and Environmental Microbiology,* 58**,** 1801-1808.

ROH, Y., LEE, S. R., CHOI, S. K., ELLESS, M. P. & LEE, S. Y. 2000. Physicochemical and mineralogical characterization of uranium-contaminated soils. *Soil & Sediment Contamination,* 9**,** 463-486.

ROMERO-GONZALEZ, M., NWAOBI, B., HUFTON, J. M. & GILMOUR, D. J. 2016. Ex-situ bioremediation of U(VI) from contaminated mine water using *Acidithiobacillus ferrooxidans* strains. *Frontiers in Environmental Science,* 4.

ROSSBACH, S., WILSON, T. L., KUKUK, M. L. & CARTY, H. A. 2000. Elevated zinc induces siderophore biosynthesis genes and a zntA-like gene in *Pseudomonas fluorescens*. *Fems Microbiology Letters,* 191**,** 61-70.

ROTTENBERG, H. & WU, S. L. 1998. Quantitative assay by flow cytometry of the mitochondrial membrane potential in intact cells. *Biochimica Et Biophysica Acta-Molecular Cell Research,* 1404**,** 393-404.

ROUXHET, P. G., MOZES, N., DENGIS, P. B., DUFRENE, Y. F., GERIN, P. A. & GENET, M. J. 1994. Application of X-ray photoelectron-spectroscopy to microorganisms. *Colloids and Surfaces B-Biointerfaces,* 2**,** 347-369.

RUGGIERO, C. E., BOUKHALFA, H., FORSYTHE, J. H., LACK, J. G., HERSMAN, L. E. & NEU, M. P. 2005. Actinide and metal toxicity to prospective bioremediation bacteria. *Environmental Microbiology,* 7**,** 88-97.

RUI, X., KWON, M. J., O'LOUGHLIN, E. J., DUNHAM-CHEATHAM, S., FEIN, J. B., BUNKER, B., KEMNER, K. M. & BOYANOV, M. I. 2013. Bioreduction of Hydrogen Uranyl Phosphate: Mechanisms and U(IV) Products. *Environmental Science & Technology,* 47**,** 5668-5678.

SALOME, K. R., GREEN, S. J., BEAZLEY, M. J., WEBB, S. M., KOSTKA, J. E. & TAILLEFERT, M. 2013. The role of anaerobic respiration in the immobilization of uranium through biomineralization of phosphate minerals. *Geochimica Et Cosmochimica Acta,* 106**,** 344-363.

SANI, R. K., PEYTON, B. M. & DOHNALKOVA, A. 2006. Toxic effects of uranium on *Desulfovibrio desulfuricans* G20. *Environmental Toxicology and Chemistry,* 25**,** 1231-1238.

SAR, P. & D'SOUZA, S. F. 2001. Biosorptive uranium uptake by a *Pseudomonas* strain: characterization and equilibrium studies. *Journal of Chemical Technology and Biotechnology,* 76**,** 1286-1294.

SENKO, J. M., ISTOK, J. D., SUFLITA, J. M. & KRUMHOLZ, L. R. 2002. In-situ evidence for uranium immobilization and remobilization. *Environmental Science & Technology,* 36**,** 1491-1496.

SENKO, J. M., MOHAMED, Y., DEWERS, T. A. & KRUMHOLZ, L. R. 2005a. Role for Fe(III) minerals in nitrate-dependent microbial U(IV) oxidation. *Environmental Science & Technology,* 39**,** 2529-2536.

SENKO, J. M., SUFLITA, J. M. & KRUMHOLZ, L. R. 2005b. Geochemical controls on microbial nitrate-dependent U(IV) oxidation. *Geomicrobiology Journal,* 22**,** 371-378.

SEPULVEDA-MEDINA, P., KATSENOVICH, Y., MUSARAMTHOTA, V., LEE, M., LEE, B., DUA, R. & LAGOS, L. 2015. The effect of uranium on bacterial viability and cell surface morphology using atomic force microscopy in the presence of bicarbonate ions. *Research in Microbiology,* 166**,** 419-427.

SHAKIROVA, L., GRUBE, M., GOODACRE, R., GAVARE, M., AUZINA, L. & ZIKMANIS, P. 2013. FT-IR spectroscopic investigation of bacterial cell envelopes from *Zymomonas mobilis* which have different surface hydrophobicities. *Vibrational Spectroscopy,* 64**,** 51-57.

SHELOBOLINA, E. S., KONISHI, H., XU, H. & RODEN, E. E. 2009. U(VI) Sequestration in Hydroxyapatite Produced by Microbial Glycerol 3-Phosphate Metabolism. *Applied and Environmental Microbiology,* 75**,** 5773-5778.

SINGH, G., SENGOER, S. S., BHALLA, A., KUMAR, S., DE, J., STEWART, B., SPYCHER, N., GINN, T. M., PEYTON, B. M. & SANI, R. K. 2014. Reoxidation of Biogenic Reduced Uranium: A Challenge Toward Bioremediation. *Critical Reviews in Environmental Science and Technology,* 44**,** 391-415.

SLADE, D. & RADMAN, M. 2011. Oxidative Stress Resistance in *Deinococcus radiodurans*. *Microbiology and Molecular Biology Reviews,* 75**,** 133-+.

SLEYTR, U. B. 1997. Basic and applied S-layer research: An overview. *Fems Microbiology Reviews,* 20**,** 5-12.

SMITH, T. J. & FOSTER, S. J. 1995. Characterization of the involvement of 2 compensatory autolysins in mother cell-lysis during sporulation of *Bacillus-subtilis*-168. *Journal of Bacteriology,* 177**,** 3855-3862.

SMITH, T. J. & FOSTER, S. J. 1997. Autolysins during sporulation of *Bacillus subtilis* 168. *Fems Microbiology Letters,* 157**,** 141-147.

SOUSA, T., CHUNG, A. P., PEREIRA, A., PIEDADE, A. P. & MORAIS, P. V. 2013. Aerobic uranium immobilization by *Rhodanobacter* A2-61 through formation of intracellular uranium-phosphate complexes. *Metallomics,* 5**,** 390-397.

SOWMYA, S., REKHA, P. D. & ARUN, A. B. 2014. Uranium(VI) bioprecipitation mediated by a phosphate solubilizing *Acinetobacter* sp YU-SS-SB-29 isolated from a high natural background radiation site. *International Biodeterioration & Biodegradation,* 94**,** 134-140.

STEINBERGER, R. E. & HOLDEN, P. A. 2005. Extracellular DNA in single- and multiple-species unsaturated biofilms. *Applied and Environmental Microbiology,* 71**,** 5404-5410.

SUTHERLAND, I. W. 2001. Biofilm exopolysaccharides: a strong and sticky framework. *Microbiology-Uk,* 147**,** 3-9.

SUZUKI, Y. & BANFIELD, J. F. 1999. Geomicrobiology of Uranium. *Reviews in Mineralogy <D>,* 38**,** 393-432.

SUZUKI, Y. & BANFIELD, J. F. 2004. Resistance to, and accumulation of, uranium by bacteria from a uranium-contaminated site. *Geomicrobiology Journal,* 21**,** 113-121.

SUZUKI, Y., KELLY, S. D., KEMNER, K. M. & BANFIELD, J. F. 2002. Radionuclide contamination - Nanometre-size products of uranium bioreduction. *Nature,* 419**,** 134-134.

TAKAHASHI, Y., KONDO, K., MIYAJI, A., WATANABE, Y., FAN, Q., HONMA, T. & TANAKA, K. 2014. Recovery and Separation of Rare Earth Elements Using Salmon Milt. *Plos One,* 9.

TAY, J. H., LIU, Q. S. & LIU, Y. 2001. The role of cellular polysaccharides in the formation and stability of aerobic granules. *Letters in Applied Microbiology,* 33**,** 222-226.

TAYLOR, D. L. & WANG, Y. L. 1989. Fluorescence microscopy of living cells in culture. Part B. Quantitative fluorescence microscopy - imaging and spectroscopy. *Methods in Cell Biology,* 30**,** i-xiv, 1-503.

THEODORAKOPOULOS, N., CHAPON, V., COPPIN, F., FLORIANI, M., VERCOUTER, T., SERGEANT, C., CAMILLERI, V., BERTHOMIEU, C. & FEVRIER, L. 2015. Use of combined microscopic and spectroscopic techniques to reveal interactions between uranium and *Microbacterium* sp A9, a strain isolated from the Chernobyl exclusion zone. *Journal of Hazardous Materials,* 285**,** 285-293.

THOMAS, R. A. P. & MACASKIE, L. E. 1996. Biodegradation of tributyl phosphate by naturally occurring microbial isolates and coupling to the removal of uranium from aqueous solution. *Environmental Science & Technology,* 30**,** 2371-2375.

THORNLEY, M. J., HORNE, R. W. & GLAUERT, A. M. 1965. Fine Structure Of *Micrococcus radiodurans*. *Archiv Fur Mikrobiologie,* 51**,** 267-&.

UESHIMA, M., GINN, B. R., HAACK, E. A., SZYMAILOWSKI, J. E. S. & FEIN, F. B. 2008. Cd adsorption onto *Pseudomonas putida* in the presence and absence of extracellular polymeric substances. *Geochimica Et Cosmochimica Acta,* 72**,** 5885-5895.

USA-EPA 2014. Federal actions to address the impact of uranium contamination in the Navajo nation.

VAN DER MEI, H. C., DE VRIES, J. & BUSSCHER, H. J. 2000. X-ray photoelectron spectroscopy for the study of microbial cell surfaces. *Surface Science Reports,* 39**,** 3-24.

VANENGELEN, M. R., FIELD, E. K., GERLACH, R., LEE, B. D., APEL, W. A. & PEYTON, B. M. 2010. UO_2^{2+} speciation determines uranium toxicity and bioaccumulation in an environmental *Pseudomonas* sp isolate. *Environmental Toxicology and Chemistry,* 29**,** 763-769.

VANENGELEN, M. R., SZILAGYI, R. K., GERLACH, R., LEE, B. D., APEL, W. A. & PEYTON, B. M. 2011. Uranium Exerts Acute Toxicity by Binding to Pyrroloquinoline Quinone Cofactor. *Environmental Science & Technology,* 45**,** 937-942.

VANVEEN, H. W., ABEE, T., KORTSTEE, G. J. J., KONINGS, W. N. & ZEHNDER, A. J. B. 1993. Characterization of 2 phosphate-transport systems in *Acinetobacter-johnsonii* 210a. *Journal of Bacteriology,* 175**,** 200-206.

VILAIN, S., PRETORIUS, J. M., THERON, J. & BROZEL, V. S. 2009. DNA as an adhesin: *Bacillus cereus* requires extracellular DNA to form biofilm. *Applied Environmental Microbiology,* 75**,** 2861-2868.

VINCENT, J. B., CROWDER, M. W. & AVERILL, B. A. 1992. Hydrolysis of phosphate monoesters - a biological problem with multiple chemical solutions. *Trends in Biochemical Sciences,* 17**,** 105-110.

VOLESKY, B. 2001. Detoxification of metal-bearing effluents: biosorption for the next century. *Hydrometallurgy,* 59**,** 203-216.

WALL, J. D. & KRUMHOLZ, L. R. 2006. Uranium Reduction. *The Annual Review of Microbiology,* 60**,** 149-166.

WANG, J. & CHEN, C. 2009. Biosorbents for heavy metals removal and their future. *Biotechnology Advances,* 27**,** 195-226.

WEI, X., FANG, L. C., CAI, P., HUANG, Q. Y., CHEN, H., LIANG, W. & RONG, X. M. 2011. Influence of extracellular polymeric substances (EPS) on Cd adsorption by bacteria. *Environmental Pollution,* 159**,** 1369-1374.

WELLMAN, D. M., CATALANO, J. G., ICENHOWER, J. P. & GAMERDINGER, A. P. 2005. Synthesis and characterization of sodium meta-autunite, $NaUO_2PO_4 \bullet 3H_2O$. *Radiochimica Acta,* 93**,** 393-399.

WINDER, C. L., DUNN, W. B., SCHULER, S., BROADHURST, D., JARVIS, R., STEPHENS, G. M. & GOODACRE, R. 2008. Global metabolic profiling of *Escherichia coli* cultures: An evaluation of methods for quenching and extraction of intracellular metabolites. *Analytical Chemistry,* 80**,** 2939-2948.

WINGENDER, J., NEU, T. R. & FLEMMING, H. C. 1999. *Microbial Extracellular Polymeric Substances: Characterization, Structure, and Function.,* Berlin, Springer.

WOLFAARDT, G. M., HENDRY, M. J. & KORBER, D. R. 2008. Microbial distribution and diversity in saturated, high pH, uranium mine tailings, Saskatchewan, Canada. *Canadian Journal of Microbiology,* 54**,** 932-940.

XIE, S., YANG, J., CHEN, C., ZHANG, X., WANG, Q. & ZHANG, C. 2008. Study on biosorption kinetics and thermodynamics of uranium by *Citrobacter freudii*. *Journal of Environmental Radioactivity,* 99**,** 126-133.

YAGOUBI, S., RENARD, C., ABRAHAM, F. & OBBADE, S. 2013. Molten salt flux synthesis and crystal structure of a new open-framework uranyl phosphate $Cs-3(UO_2)_2(PO_4)O_2^-$: Spectroscopic characterization and cationic mobility studies. *Journal of Solid State Chemistry,* 200**,** 13-21.

YANG, J., DONG, F. Q., DAI, Q. W., LIU, M. X., NIE, X. Q., ZHANG, D., MA, J. L. & ZHOU, X. 2015. Biosorption of Radionuclide Uranium by *Deinococcus Radiodurans*. *Spectroscopy and Spectral Analysis,* 35**,** 1010-1014.

YUE, Z. B., LI, Q., LI, C. C., CHEN, T. H. & WANG, J. 2015. Component analysis and heavy metal adsorption ability of extracellular polymeric substances (EPS) from sulfate reducing bacteria. *Bioresource Technology,* 194**,** 399-402.

YUNG, M. C. & JIAO, Y. 2014. Biomineralization of Uranium by PhoY Phosphatase Activity Aids Cell Survival in *Caulobacter crescentus*. *Applied and Environmental Microbiology,* 80**,** 4795-4804.

ZHOU, P. & GU, B. H. 2005. Extraction of oxidized and reduced forms of uranium from contaminated soils: Effects of carbonate concentration and pH. *Environmental Science & Technology,* 39**,** 4435-4440.

Appendices.

Appendix Table 1. Uranium speciation as a function of solution pH at 298.15 K. 0.1 M NaCl was used as the background electrolyte solution and 0.5 mM $UO_2(NO_3)_2.6H_2O$ was used as the source of U(VI). Calculations were made with Visual MINTEQ 3.1.

	% of total					
Species	pH 2	pH 3	pH 4	pH 5	pH 6	pH 7
UO_2^{2+}	94.898	94.337	84.749	15.015	0.367	
$UO_2NO_3^+$	0.034	0.035	0.031		0.984	
UO_2OH^+	0.025	0.252	2.27	4.027		0.197
$(UO_2)_2(OH)_2^{2+}$		0.079	6.393	20.106	1.199	0.048
$(UO_2)_3(OH)_5^+$			0.084	47.166	68.762	54.855
$(UO_2)_4(OH)_7^+$				7.84	27.925	44.512
$(UO_2)_3(OH)_7^-$						0.122
$(UO_2)_3(OH)_4^{2+}$			0.079	4.418	0.644	0.051
$(UO_2)_2OH^{3+}$	0.023	0.226	1.827	0.573		
$UO_2Cl_{2\ (aq)}$	0.015	0.016	0.014			
$UO_2(OH)_3^-$						0.02
$UO_2(OH)_{2\ (aq)}$				0.039	0.094	0.189
UO_2Cl^+	5.004	5.055	4.55	0.808	0.02	

Appendix Table 2. Uranium speciation as a function of background electrolyte concentration at 298.15 K. NaCl was used as the background electrolyte and 0.5 mM $UO_2(NO_3)_2.6H_2O$ was used as the source of U(VI) at pH 5. Calculations were made with Visual MINTEQ 3.1.

	% of total				
Species	1000 mM	100 mM	10 mM	1 mM	0 mM
UO_2^{2+}	16.33	15.015	9.549	7.742	7.277
UO_2OH^+	3.977	4.027	3.912	3.827	3.8
$(UO_2)_2(OH)_2^{2+}$	20.483	20.106	14.335	12.109	11.508
$(UO_2)_3(OH)_5^+$	40.876	47.166	57.594	61.154	62.08
$(UO_2)_4(OH)_7^+$	6.365	7.84	10.734	11.873	12.188
$(UO_2)_3(OH)_4^{2+}$	4.216	4.418	3.531	3.107	2.986
$(UO_2)_2OH^{3+}$	0.671	0.573	0.202	0.125	0.108
$UO_2(OH)_{2\ (aq)}$	0.031	0.039	0.044	0.046	0.047
$UO_2Cl_{2\ (aq)}$	0.149				
UO_2Cl^+	6.897	0.808	0.092		

Appendix Table 3. Uranium speciation as a function of solution concentration at 298.15 K. 0.1 M NaCl was used as the background electrolyte solution and $UO_2(NO_3)_2.6H_2O$ was used as the source of U(VI) at pH 5. Calculations were made with Visual MINTEQ 3.1.

	% of total					
Species	0.0625 mM	0.125 mM	0.25 mM	0.5 mM	1 mM	2 mM
UO_2^{2+}	43.467	32.041	22.351	15.015	9.835	6.333
UO_2OH^+	11.67	8.6	5.998	4.027	2.635	1.694
$(UO_2)_2(OH)_2^{2+}$	21.092	22.915	22.294	20.106	17.227	14.252
$(UO_2)_3(OH)_5^+$	17.948	28.735	38.978	47.166	52.813	56.031
$(UO_2)_4(OH)_7^+$	1.081	2.551	4.826	7.84	11.484	15.654
$(UO_2)_3(OH)_4^{2+}$	1.679	2.689	3.649	4.418	4.952	5.263
$(UO_2)_2OH^{3+}$	0.6	0.652	0.635	0.573	0.492	0.408
$UO_2(OH)_{2\ (aq)}$	0.112	0.083	0.058	0.039	0.025	0.016
UO_2Cl^+	2.342	1.726	1.203	0.808	0.528	0.339

Appendix Table 4. Uranium sequestration by eDNA as a function of % removal of reactant products, μg mL^{-1} removal and μg U mg^{-1} eDNA

pH	% Uranium removal	% eDNA removal	μg mL^{-1} uranium removed	μg mL^{-1} eDNA removed	μg U mg^{-1} eDNA
2	95.30 ± 0.40	99.99 ±0.24	113.40 ± 0.48	999.85 ± 1.99	113.42 ± 0.48
3	88.63 ± 1.50	93.36 ± 1.28	105.47 ± 1.78	933.57 ± 10.47	111.74 ± 2.11
4	88.20 ± 0.72	92.28 ± 2.62	104.96 ± 0.86	922.80 ± 21.41	113.80 ± 2.89
5	42.57 ± 3.34	31.74 ± 13.98	50.66 ± 3.98	317.39 ± 131.75	267.99 ± 189.85
6	-	25.23 ± 3.77	-	252.29 ± 30.75	-
7	-	9.77 ± 7.05	-	97.69 ± 57.58	-
NaCl conc. (mM)	**% Uranium removal**	**% eDNA removal**	**μg mL^{-1} uranium removed**	**μg mL^{-1} eDNA removed**	**μg U mg^{-1} eDNA**
1	56.28 ± 2.27	36.77 ± 6.85	66.97 ± 2.70	367.75 ± 55.92	254.89 ± 46.66
0.1	42.57 ± 3.34	31.74 ± 13.97	50.66 ± 3.98	317.39 ± 131.75	267.99 ± 189.85
0.01	21.69 ± 9.91	16.44 ± 2.08	25.81 ± 11.79	164.40 ± 17.01	158.60 ± 65.16
0.001	20.11 ± 8.71	10.78 ± 2.43	23.93 ± 10.37	107.82 ± 19.81	230.01 ± 99.63
0	10.63 ± 7.57	13.68 ± 4.11	12.65 ± 9.00	136.80 ± 33.60	98.16 ± 67.05
Initial uranium conc. (mM)	**% Uranium removal**	**% eDNA removal**	**μg mL^{-1} uranium removed**	**μg mL^{-1} eDNA removed**	**μg U mg^{-1} eDNA**
2	74.97 ± 4.24	96.15 ± 1.81	356.86 ± 20.16	961.52 ± 14.81	371.23 ± 19.14
1	59.37 ± 7.38	37.00 ± 5.92	168.35 ± 53.91	370.03 ± 48.33	370.79 ± 57.44
0.5	42.57 ± 3.34	31.74 ± 13.97	50.66 ± 3.98	317.39 ± 131.75	267.99 ± 189.85
0.25	44.20 ± 11.90	26.10 ± 0.54	26.30 ± 7.08	261.00 ± 4.37	100.80 ± 23.57
0.125	37.63 ± 2.49	21.16 ± 6.68	11.19 ± 0.74	211.55 ± 54.50	57.08 ± 15.67
0.0625	40.03 ± 6.00	16.25 ± 3.43	5.95 ± .089	162.47 ± 28.04	37.70 ± 8.21
Initial DNA conc. (mg mL^{-1})	**% Uranium removal**	**% eDNA removal**	**μg mL^{-1} uranium removed**	**μg mL^{-1} eDNA removed**	**μg U mg^{-1} eDNA**
2	64.51 ± 6.94	15.99 ± 15.31	77.85 ± 8.26	319.89 ± 250.07	428.57 ± 278.31
1	42.57 ± 3.34	31.74 ± 13.97	50.66 ± 3.98	317.39 ± 131.75	267.99 ± 189.85
0.5	42.44 ± 2.92	47.81 ± 5.86	50.51 ± 3.47	239.06 ± 23.93	213.38 ± 25.76
0.25	37.19 ± 4.25	67.99 ± 7.16	44.26 ± 5.05	169.98 ± 14.62	262.45 ± 36.43

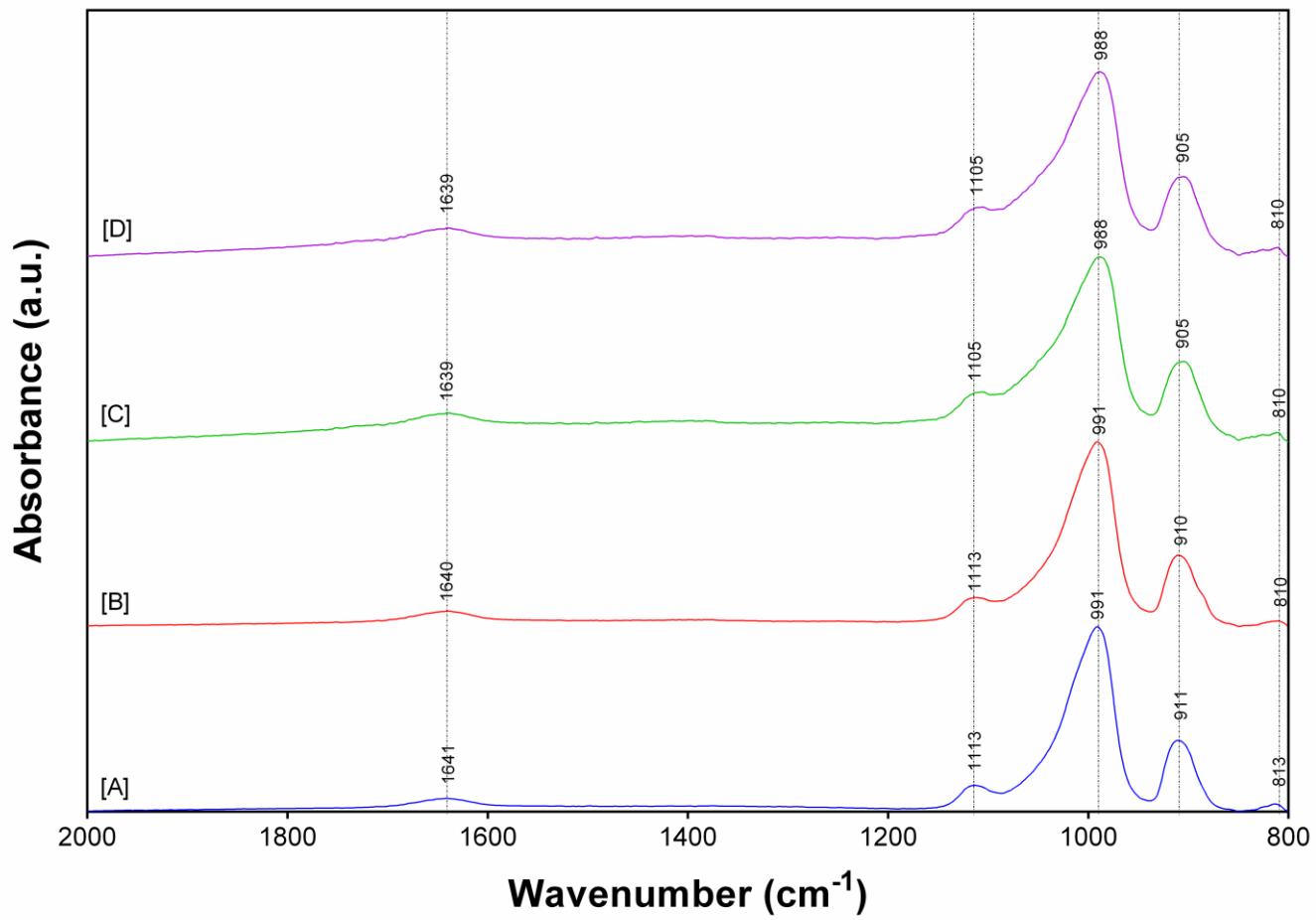

Appendix Figure 1. FT-IR spectra of minerals formed from the interaction of ePO_4 with uranium at increasing molar ratios; 1.8 : 1 [A], 3.8 : 1 [B], 7.5 : 1 [C] and 15 : 1 [D] $H_2PO_4^-$: $(UO_2)_3(OH)_5^+$ within the region 2000 – 800 cm^{-1}.

Appendix Table 5. *d*-spacing values corresponding to the minerals formed within this study and other uranium phosphate minerals showing similar homologies.

1.8:1 aPO_4: $(UO_2)_3(OH)_5^+$ (This study)			1.8:1 ePO_4: $(UO_2)_3(OH)_5^+$ (This study)			$Ca(UO_2)_2(PO_4)_2 \bullet 3H_2O$ (ICDD PDF# 00-039-1351)	$Ca(UO_2)_2(PO_4)_2(H_2O)_6$ (ICDD PDF# 04-012-5106)	$(UO_2HPO_4)\bullet xH_2O$ (ICDD PDF# 00-037-0373)	$(UO_2)_3\bullet(PO_4)_2\bullet 4H_2O$ (ICDD PDF# 00-064-0815)
2 θ	*d*-spacing	*I*/*I*0, %	2 θ	*d*-spacing	*I*/*I*0, %	*d*-spacing	*d*-spacing	*d*-spacing	*d*-spacing
4.81	**8.45**	**55.54**	**4.81**	**8.45**	**49.17**	**8.46**	**8.4**	**8.35**	**8.441**
7.6	5.35	53.09	7.58	5.37	47.79	5.39	5.359	-	-
8.30	**4.91**	**80.13**	**8.33**	**4.88**	**77.07**	**4.941**	**4.921**	**-**	**-**
9.52	4.27	42.83	9.52	4.27	48.62	4.271	4.246	4.24	4.242
-	-	-	-	-	-	4.233	4.2	3.97	4.179
11.20	3.63	45.28	11.19	3.64	43.37	3.62	3.596	-	3.625
11.74	**3.47**	**100.00**	**11.75**	**3.46**	**100.00**	**3.495**	**3.48**	**3.52**	**-**
12.67	**3.21**	**65.64**	**12.64**	**3.22**	**59.94**	**3.233**	**3.215**	**3.18**	**3.29**
13.95	2.92	39.41	13.97	2.92	40.33	2.93	2.919	2.91	-
16.24	2.51	26.71	16.59	2.46	37.02	2.513	2.5	2.507	2.51
16.57	2.46	35.50	16.63	2.45	41.71	2.47	2.461	2.435	2.438
17.24	2.37	32.41	17.24	2.37	33.98	2.372	2.361	2.39	-
18.22	2.24	29.15	-	-	-	2.245	2.236	2.256	2.259
18.52	**2.20**	**45.93**	**18.52**	**2.20**	**49.72**	**2.209**	**2.2**	**2.205**	**-**
19.16	2.13	36.97	19.15	2.13	36.19	2.139	2.129	2.123	-
20.03	2.04	30.46	-	-	-	2.041	2.03		-
21.72	1.88	25.73	21.74	1.88	33.15	1.888	1.881	1.868	1.87
23.46	1.74	31.43	-	-	-	1.739	1.74	1.729	
23.96	1.71	24.92	24.05	1.70	33.15	1.71	1.704	-	-
25.45	1.61	25.97	-	-	-	1.601	1.61	-	-
26.30	1.56	27.52	-	-	-	1.566	1.566	-	-
26.74	1.53	28.50	-	-	-	1.527	1.53	1.538	-

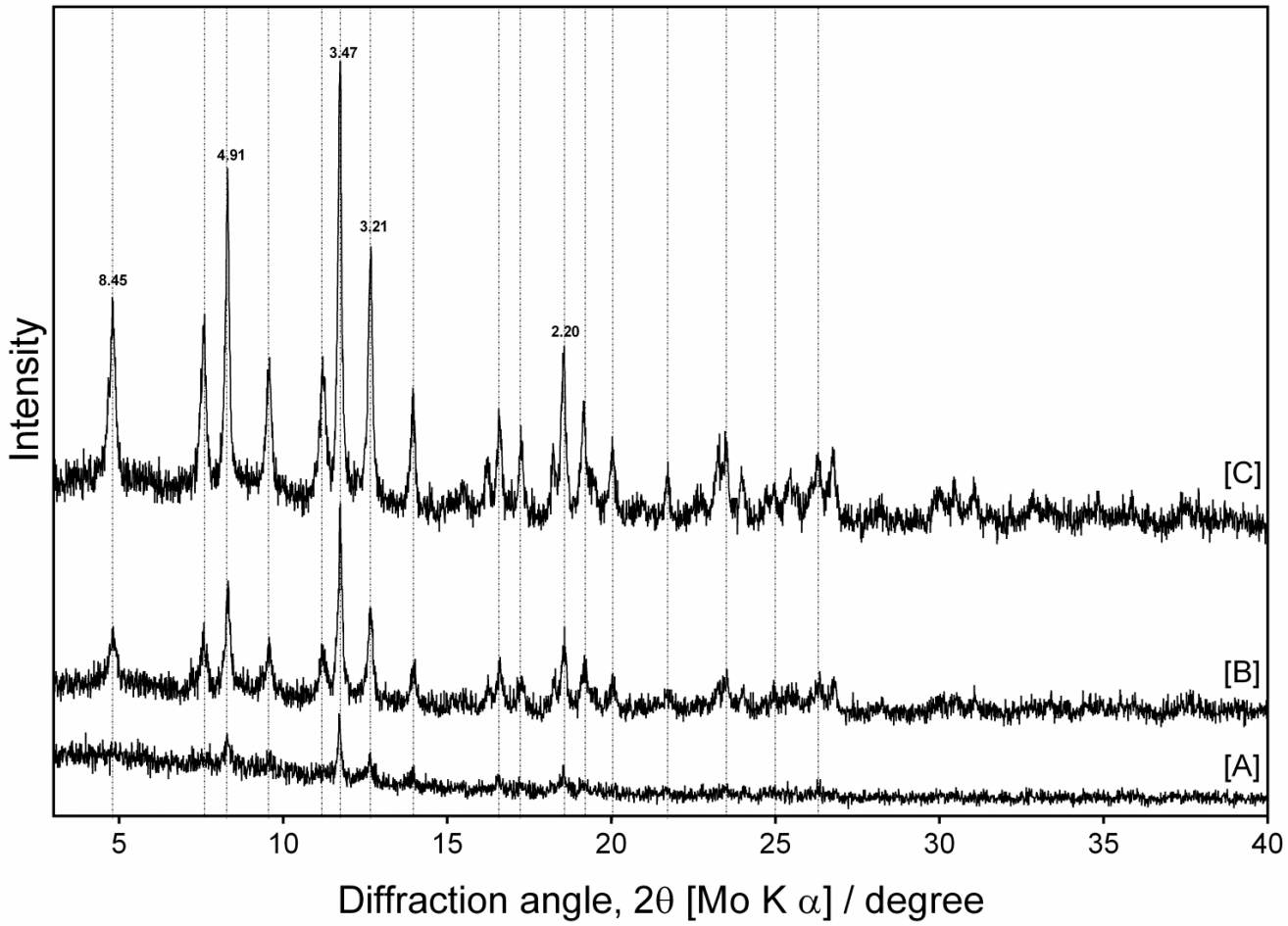

Appendix Figure 2. XRD patterns of uranium precipitates at molar ratios of [A] 1.8:1, [B] 3.8:1 and [C] 7.5:1 uranium: aPO_4 (pH 5).

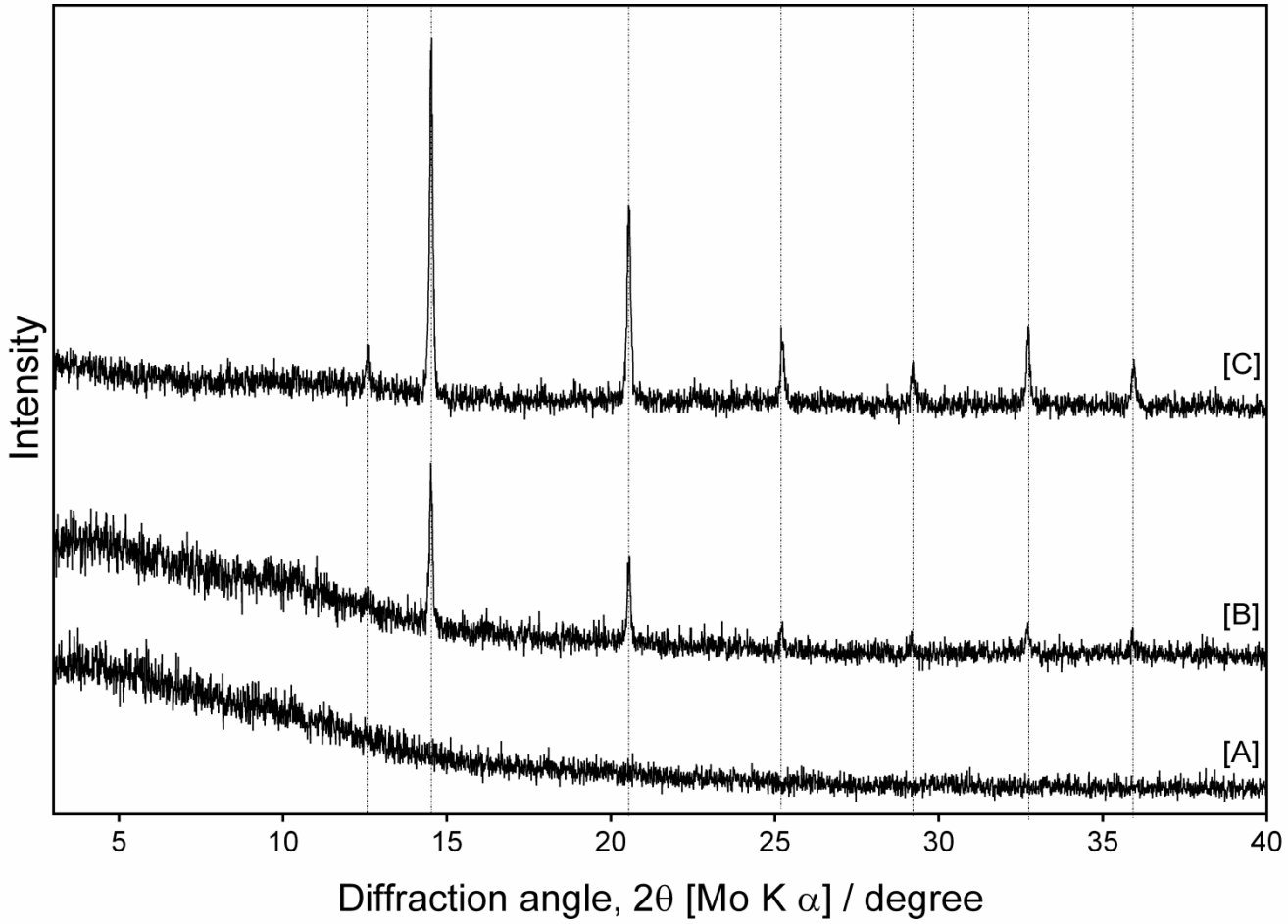

Appendix Figure 3. XRD patterns of [A] lyophilised eDNA, [B] uranium biosorbed DNA and [C] following the reaction of eDNA with acid phosphatase while in the presence of uranium (pH 5)

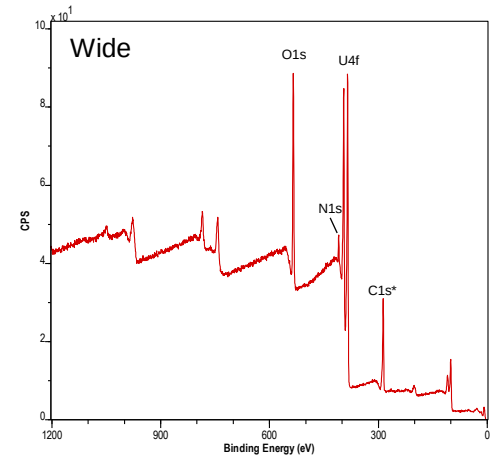

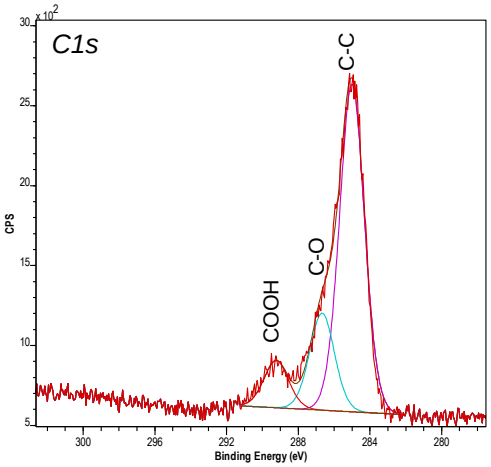

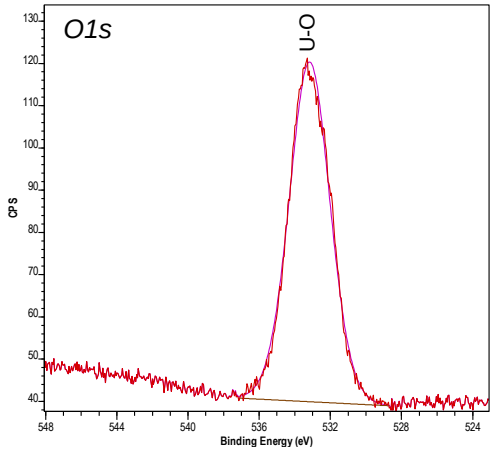

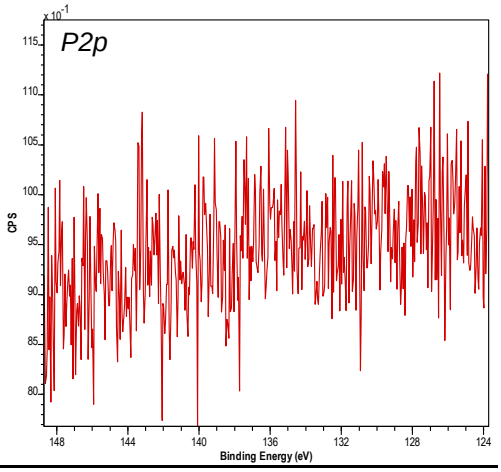

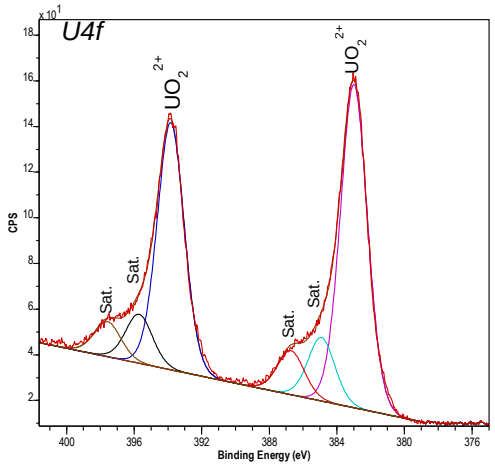

Position (eV)	FWHM	% Area	Assignment
	C 1s		
285	1.612	69.45	C-C, H*
286.67	1.612	20.57	C-O*
289.23	1.612	9.98	COOH*
	O 1s		
533.17	2.591	100	U-O, N-O
	U 4f		
382.99	1.855	42.61	UO_2^{2+}, U-O
384.89	1.855	8.43	Satellite
386.7	1.855	5.83	Satellite
393.84	1.855	32.41	UO_2^{2+}, U-O
395.68	1.855	6.27	Satellite
397.52	1.855	4.45	Satellite

Appendix Figure 4. XPS spectra of $UO_2(NO_3)_2.6H_20$

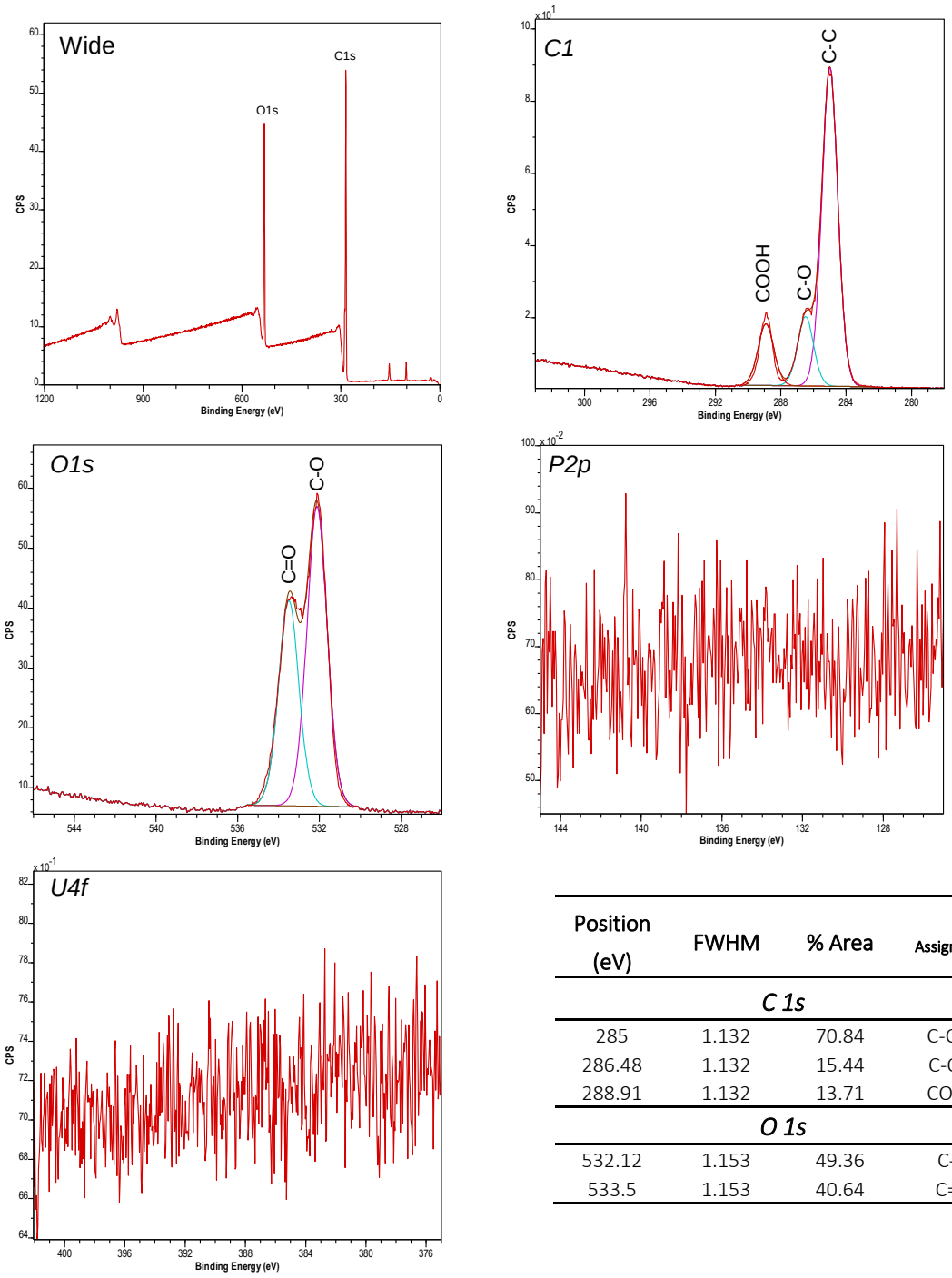

Position (eV)	FWHM	% Area	Assignment
	C 1s		
285	1.132	70.84	C-C, H
286.48	1.132	15.44	C-O-C
288.91	1.132	13.71	COOH
	O 1s		
532.12	1.153	49.36	C-O
533.5	1.153	40.64	C=O

Appendix Figure 5. XPS spectra of carbon tape used in this experimental study.

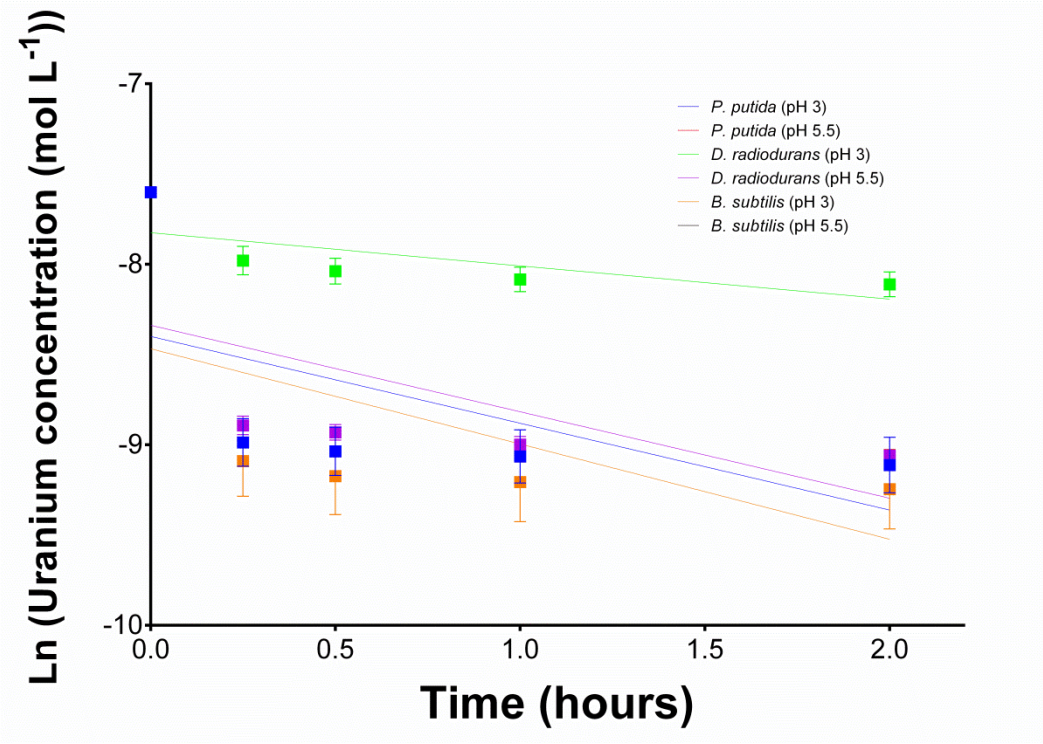

Appendix Figure 6. First order reaction fitting of whole cell uranium sorption data.

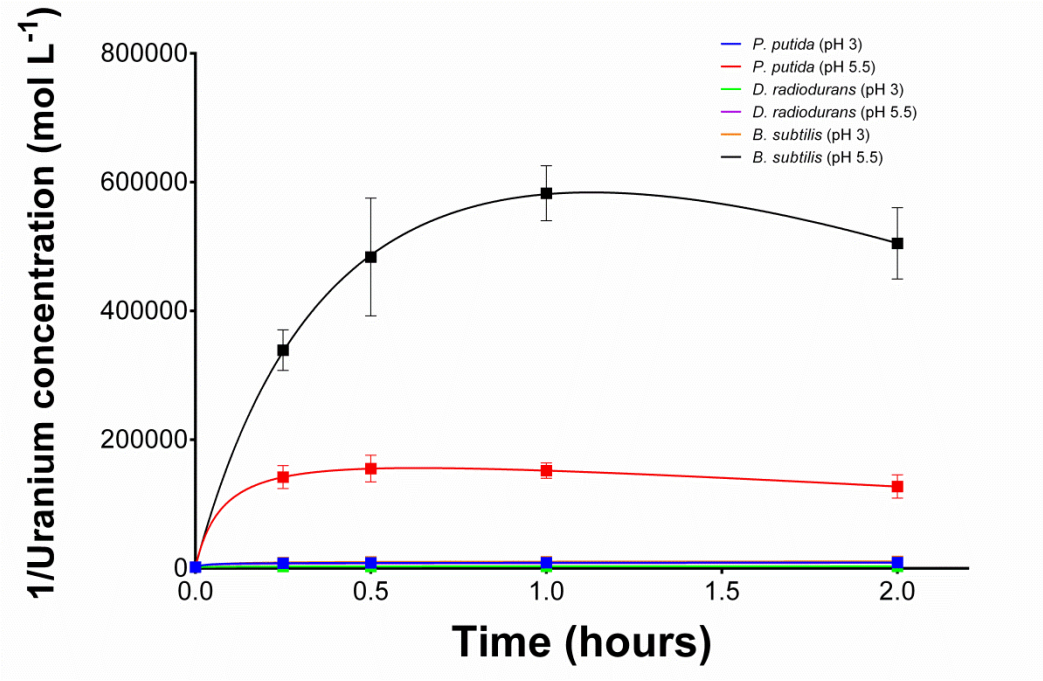

Appendix Figure 7. Second order reaction fitting of whole cell uranium sorption data.

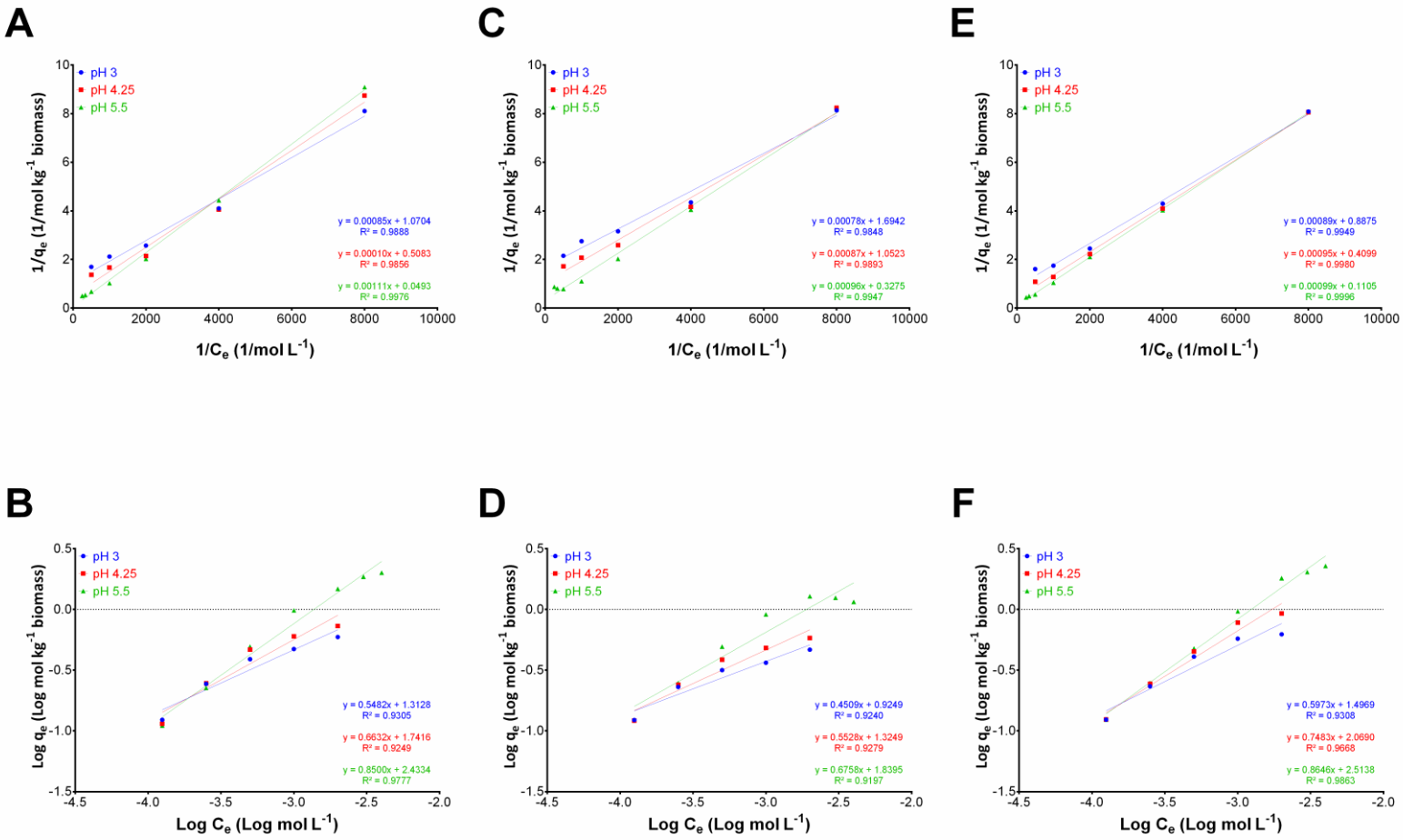

Appendix Figure 8.Langmuir and Freundlich isotherms of the uranium adsorption onto live cells of *P. putida* [A,B], *D. radiodurans* [C,D] and *B. subtilis* [E,F].

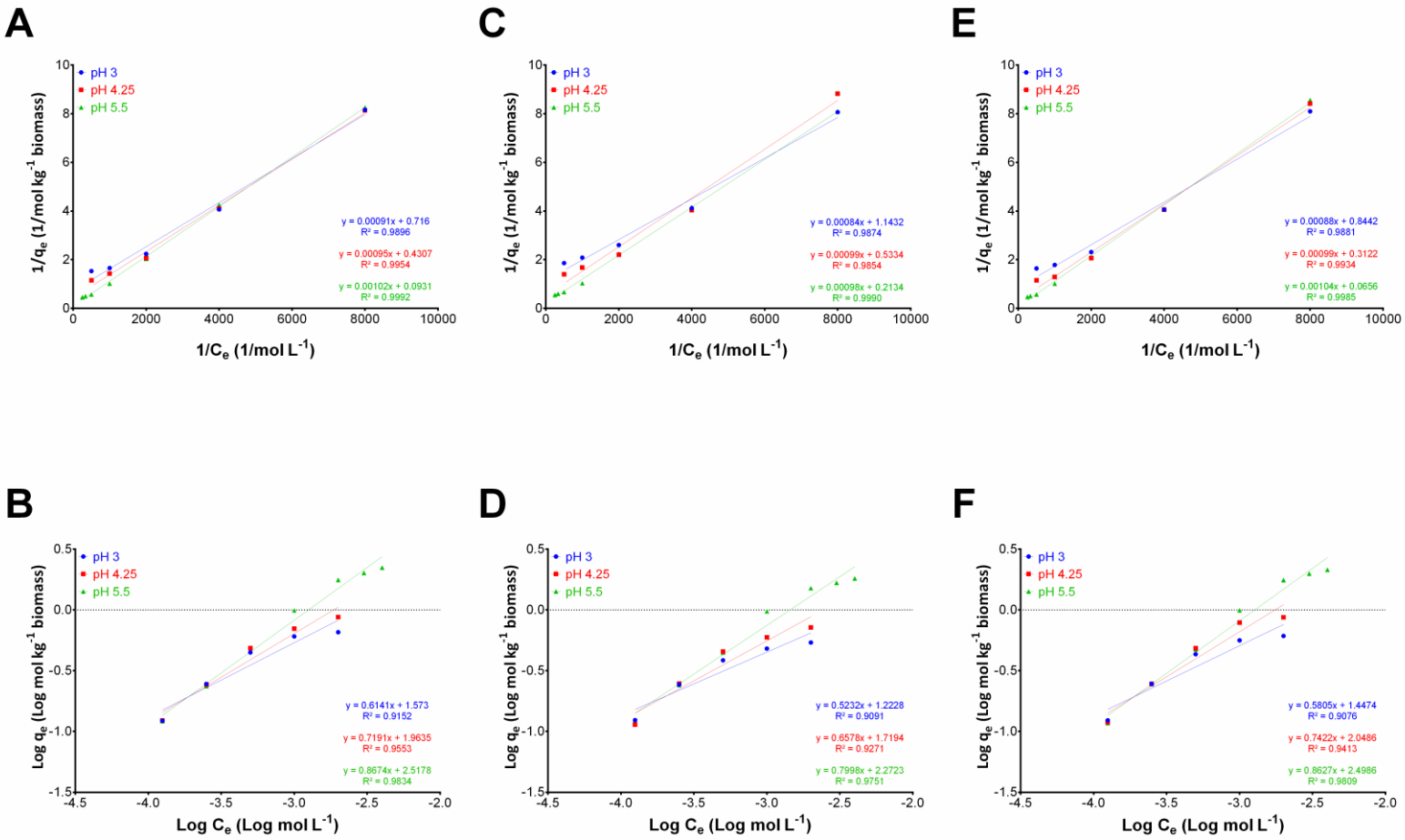

Appendix Figure 9.Langmuir and Freundlich isotherms of the uranium adsorption onto *P. putida* cell wall isolates [A,B], membrane isolates [C,D] and dead cells [E,F].

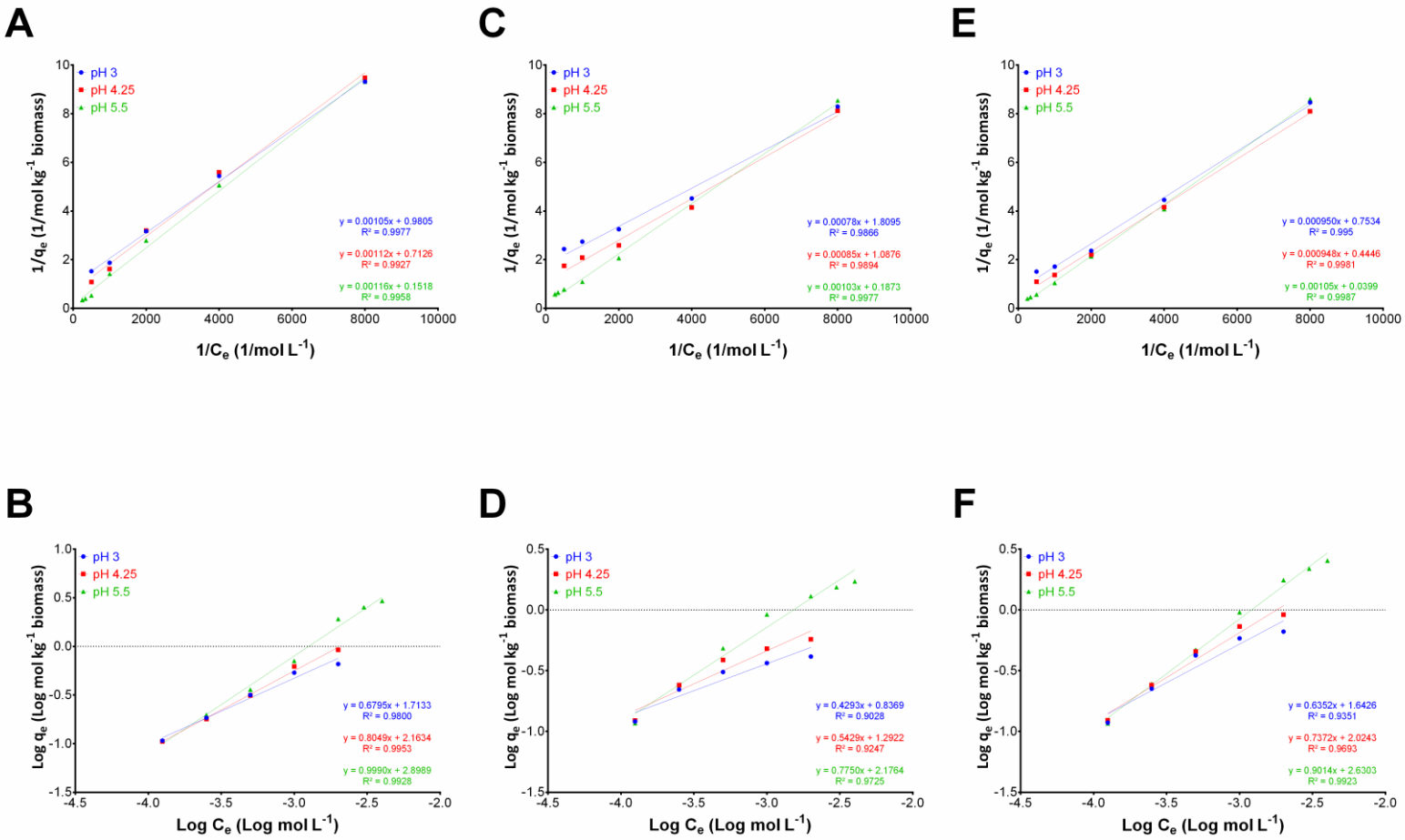

Appendix Figure 10. Langmuir and Freundlich isotherms of the uranium adsorption onto *B. subtilis* cell wall isolates [A,B], membrane isolates [C,D] and dead cells [E,F].

Appendix Table 6. Uranium, nitrate, sodium and chloride speciation as a function of uranium concentration and pH of solution at 298.15 K. 0.1 M NaCl was used as the background electrolyte solution and $UO_2(NO_3)_2.6H_2O$ was used as the source of U(VI). Calculations were made with Visual MINTEQ 3.1.

		% total concentration																
Component	Species	0.125 mM			0.25 mM			0.5 mM			1 mM			2 mM			3 mM	4 mM
		pH 3	pH 4.25	pH 5.5	pH 3	pH 4.25	pH 5.5	pH 3	pH 4.25	pH 5.5	pH 3	pH 4.25	pH 5.5	pH 3	pH 4.25	pH 5.5	pH 5.5	pH 5.5
UO_2^{2+}	UO_2^{2+}	93.44	84.88	6.67	93.36	80.63	4.26	93.20	80.63	2.69	92.88	64.28	1.69	92.26	52.81	1.05	0.80	0.66
	UO_2Cl^+	6.21	5.65	0.44	6.20	5.36	0.28	6.18	5.36	0.18	6.15	4.26	0.11	6.08	3.49	0.07	0.05	0.04
	$UO_2NO_3^+$	0.02	0.01		0.03	0.03		0.06	0.03		0.12	0.09		0.25	0.14			
	UO_2OH^+	0.24	3.81	5.32	0.24	3.61	3.39	0.23	3.61	2.14	0.23	2.87	1.34	0.23	2.35	0.84	0.63	0.52
	$(UO_2)_2(OH)_2^{2+}$	0.02	4.68	9.13	0.04	8.43	7.44	0.07	8.43	5.93	0.14	21.35	4.66	0.28	28.66	3.62	3.11	2.79
	$(UO_2)_3(OH)_5^+$		0.08	65.09		0.26	67.65		0.26	68.13		2.07	67.00		4.52	64.68	62.90	61.48
	$(UO_2)_4(OH)_7^+$			11.06			14.67			18.66		0.09	22.99		0.31	27.63	30.46	32.52
	$(UO_2)_3(OH)_4^{2+}$		0.04	2.05		0.15	2.13		0.15	2.15		1.16	2.11		2.55	2.05	1.99	1.95
	$(UO_2)_2OH^{3+}$	0.06	0.83	0.09	0.11	1.50	0.07	0.23	1.50	0.06	0.45	3.82	0.05	0.89	5.16	0.04	0.03	0.03
	$UO_2Cl_{2\ (aq)}$	0.03	0.02		0.03	0.02		0.03	0.02		0.02	0.02		0.02	0.01			
	$UO_2(OH)_{2\ (aq)}$			0.16			0.10			0.06			0.04			0.03	0.02	0.02
NO_3^-	NO_3^-	97.94	97.94	97.95	97.93	97.94	97.95	97.92	97.94	97.95	97.89	97.91	97.95	97.84	97.89	97.95	97.95	97.95
	$UO_2NO_3^+$				0.02	0.01		0.03	0.01		0.06	0.04		0.12	0.07			
	$NaNO_{3\ (aq)}$	2.05	2.05	2.05	2.05	2.05	2.05	2.05	2.05	2.05	2.05	2.05	2.05	2.04	2.04	2.05	2.05	2.05
Na^+	Na^+	96.41	96.40	96.40	96.40	96.40	96.40	96.40	96.40	96.39	96.39	96.39	96.38	96.37	96.36	96.36	96.33	96.30
	$NaCl_{(aq)}$	3.59	3.59	3.59	3.59	3.59	3.59	3.59	3.59	3.59	3.58	3.59	3.59	3.57	3.58	3.58	3.58	3.58
	$NaNO_{3\ (aq)}$							0.02		0.02	0.03	0.03	0.03	0.06	0.06	0.06	0.09	0.12
Cl^-	Cl^-	96.40	96.40	96.41	96.40	96.40	96.41	96.39	96.40	96.41	96.37	96.38	96.41	96.34	96.37	96.41	96.42	96.42
	UO_2Cl^+				0.01			0.02			0.05	0.03		0.09	0.05			
	$NaCl_{(aq)}$	3.59	3.59	3.59	3.59	3.59	3.59	3.59	3.59	3.59	3.58	3.59	3.59	3.57	3.58	3.59	3.58	3.58

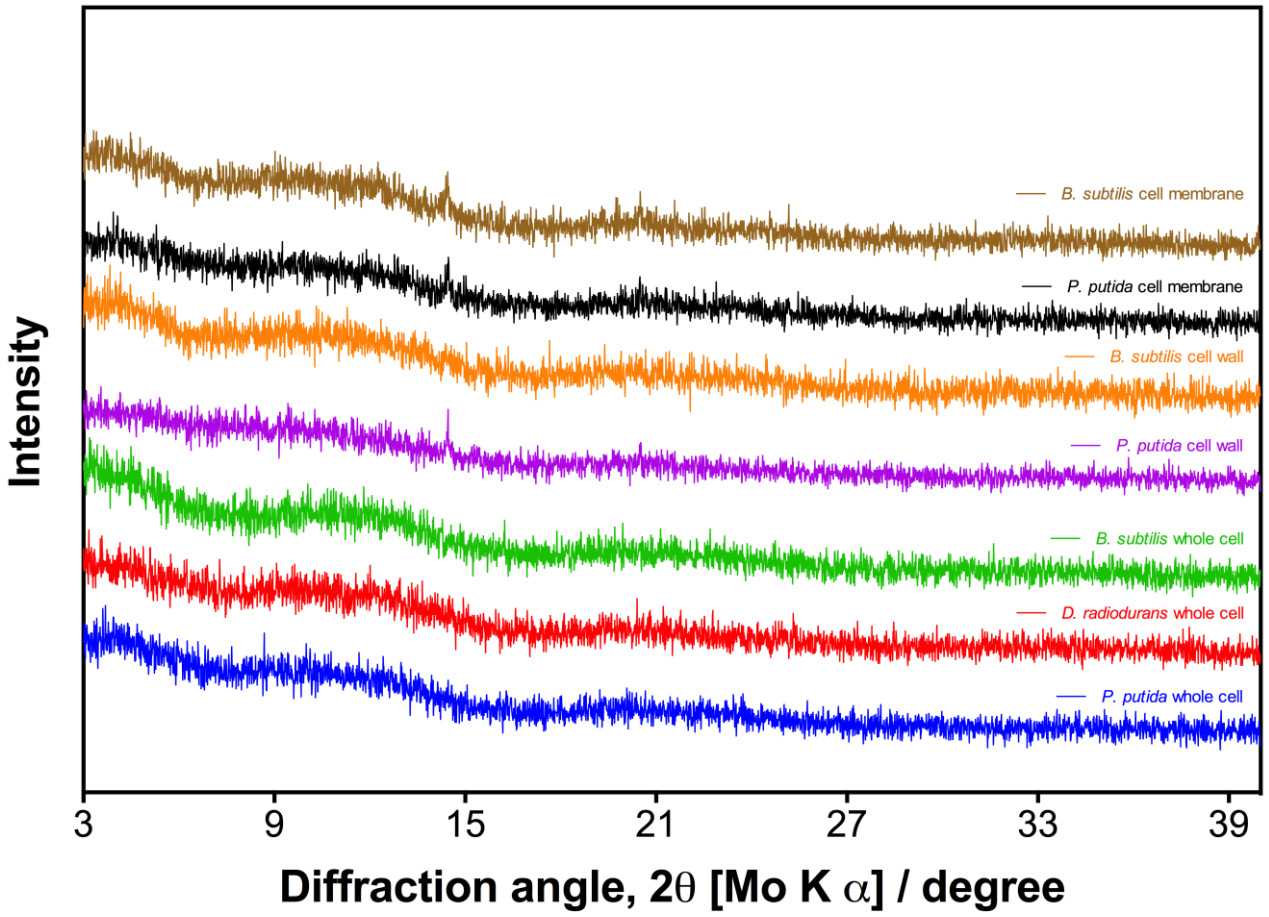

Appendix Figure 11. XRD diffraction patterns following the interaction of 4 mM uranium (pH 5.5) with 1 mg mL^{-1} biomass.

Allocation			ν (O-H)	ν_{as} (CH_3)	ν_{as} (CH_2)	ν_s (CH_2)	ν (C=O)	δ (N-H)	δ_s (CH_2), ν (C-N)	δ_s (CH_2), ν_s (COO-)	ν_{as} (PO_2)	ν_s (PO_2); ν (C-OH, C-0-C, C-C)	ν (U-O)
0 mM	pH 3	σ (cm^{-1})	**3288**	**2958**	**2927**	**2856**	**1648**	**1543**	**1451**	**1408** **1386**	**1232**	**1073**	**-**
		I (a.u.)	0.4699	0.2486	0.2841	0.1716	1.5000	0.8669	0.2669	0.1989 0.1921	0.5002	0.5213	-
	pH 4.25	σ (cm^{-1})	**3295**	**2957**	**2926**	**2852**	**1650**	**1545**	**1453**	**1399**	**1241**	**1087**	**-**
		I (a.u.)	0.4586	0.2256	0.2668	0.1670	1.5000	0.9601	0.3026	0.3090	0.4376	0.4579	-
	pH 5.5	σ (cm^{-1})	**3288**	**2958**	**2918**	**2852**	**1650**	**1545**	**1452**	**1399**	**1239**	**1087**	**-**
		I (a.u.)	0.5138	0.2858	0.3454	0.2385	1.5000	0.9574	0.2996	0.3245	0.4006	0.4645	-
0.125 mM	pH 3	σ (cm^{-1})	**3294**	**-**	**2928**	**2860**	**1644**	**1541**	**1457**	**1412** **1388**	**1230**	**1068**	**916**
		I (a.u.)	0.4834	-	0.2855	0.1806	1.5000	0.8760	0.2905	0.2385 0.2328	0.4423	0.5445	0.1049
	pH 4.25	σ (cm^{-1})	**3295**	**2956**	**2926**	**2858**	**1644**	**1543**	**1457**	**1407** **1390**	**1239**	**1081**	**917**
		I (a.u.)	0.4723	0.2336	0.2621	0.1673	1.4998	0.9443	0.3220	0.2820 0.2898	0.4170	0.5119	0.1101
	pH 5.5	σ (cm^{-1})	**3295**	**2955**	**2926**	**2854**	**1644**	**1543**	**1457**	**1398**	**1239**	**1081**	**916**
		I (a.u.)	0.4572	0.2264	0.2643	0.1628	1.4995	0.9643	0.3241	0.3029	0.3933	0.4680	0.0894
0.25 mM	pH 3	σ (cm^{-1})	**3294**	**-**	**2929**	**2860**	**1652**	**1541**	**1457**	**1413** **1388**	**1229**	**1068**	**916**
		I (a.u.)	0.4368	-	0.2734	0.1788	1.5000	0.8807	0.3128	0.2333 0.2210	0.4322	0.5716	0.2081
	pH 4.25	σ (cm^{-1})	**3294**	**2956**	**2928**	**2859**	**1645**	**1542**	**1457**	**1412** **1388**	**1229**	**1074**	**916**
		I (a.u.)	0.4536	0.2373	0.2756	0.1721	1.5000	0.9026	0.3173	0.2432 0.2424	0.4005	0.5536	0.1935
	pH 5.5	σ (cm^{-1})	**3295**	**2956**	**2928**	**2860**	**1651**	**1542**	**1457**	**1397**	**1239**	**1076**	**916**
		I (a.u.)	0.4523	0.2269	0.2625	0.1635	1.5000	0.9413	0.3216	0.2885	0.3846	0.4962	0.1652
0.5 mM	pH 3	σ (cm^{-1})	**3294**	**-**	**2928**	**2860**	**1644**	**1541**	**1457**	**1413** **1388**	**1229**	**1068**	**916**
		I (a.u.)	0.4663	-	0.2907	0.1931	1.5000	0.8797	0.3469	0.2544 0.2405	0.4407	0.6558	0.3328
	pH 4.25	σ (cm^{-1})	**3296**	**2956**	**2927**	**2860**	**1646**	**1542**	**1457**	**1413** **1388**	**1229**	**1072**	**920**
		I (a.u.)	0.4683	0.2606	0.2823	0.1994	1.5000	0.9361	0.3940	0.2768 0.2755	0.4294	0.6681	0.4031
	pH 5.5	σ (cm^{-1})	**3295**	**2956**	**2928**	**2860**	**1646**	**1542**	**1457**	**1412** **1388**	**1229**	**1068**	**916**
		I (a.u.)	0.4299	0.2150	0.2504	0.1567	1.5000	0.9562	0.3539	0.2653 0.2726	0.3646	0.6024	0.3320
1 mM	pH 3	σ (cm^{-1})	**3294**	**-**	**2929**	**2860**	**1645**	**1541**	**1457**	**1413** **1388**	**1229**	**1067**	**922**
		I (a.u.)	0.4441	-	0.2744	0.1743	1.5000	0.8950	0.3513	0.2455 0.2335	0.4137	0.6680	0.4116
	pH 4.25	σ (cm^{-1})	**3296**	**2956**	**2928**	**2860**	**1645**	**1542**	**1457**	**1413** **1388**	**1229**	**1069**	**921**
		I (a.u.)	0.4624	0.2613	0.2803	0.2004	1.4993	0.9409	0.4131	0.2861 0.2857	0.4140	0.7021	0.4987
	pH 5.5	σ (cm^{-1})	**3295**	**2956**	**2928**	**2860**	**1645**	**1542**	**1457**	**1412** **1388**	**1229**	**1068**	**916**
		I (a.u.)	0.4617	0.2497	0.2786	0.1884	1.5000	0.9744	0.3958	0.2736 0.2652	0.3368	0.6690	0.6372
2 mM	pH 3	σ (cm^{-1})	**3294**	**-**	**2928**	**2860**	**1646**	**1542**	**1457**	**1413** **1388**	**1229**	**1067**	**923**
		I (a.u.)	0.4339	-	0.2779	0.1790	1.5000	0.9202	0.3800	0.2809 0.2737	0.4224	0.6835	0.4836
	pH 4.25	σ (cm^{-1})	**3295**	**2955**	**2928**	**2861**	**1645**	**1542**	**1457**	**1413** **1388**	**1229**	**1069**	**922**
		I (a.u.)	0.4638	0.2781	0.2941	0.2135	1.4998	0.9620	0.4409	0.3112 0.3129	0.4170	0.7105	0.5815
	pH 5.5	σ (cm^{-1})	**3299**	**2955**	**2928**	**2861**	**1645**	**1542**	**1457**	**1412** **1388**	**1229**	**1068**	**917**
		I (a.u.)	0.4896	0.2745	0.2882	0.2169	1.5000	0.9912	0.4227	0.3132 0.3074	0.3288	0.6336	0.8203
3 mM	pH 5.5	σ (cm^{-1})	**3299**	**2955**	**2928**	**2861**	**1647**	**1542**	**1457**	**1412** **1388**	**1229**	**1068**	**918**
		I (a.u.)	0.4899	0.2460	0.2569	0.1774	1.4988	0.9935	0.4035	0.3355 0.3367	0.2976	0.6389	1.0049
4 mM	pH 5.5	σ (cm^{-1})	**3299**	**2955**	**2928**	**2861**	**1646**	**1542**	**1457**	**1412** **1388**	**1229**	**1068**	**918**
		I (a.u.)	0.4695	0.2170	0.2255	0.1456	1.4959	0.9854	0.3699	0.3091 0.3083	0.2514	0.6220	1.0858

Appendix Table 7. Infrared adsorption bands of uranium accumulated *P. putida* live cells and their functional groups.

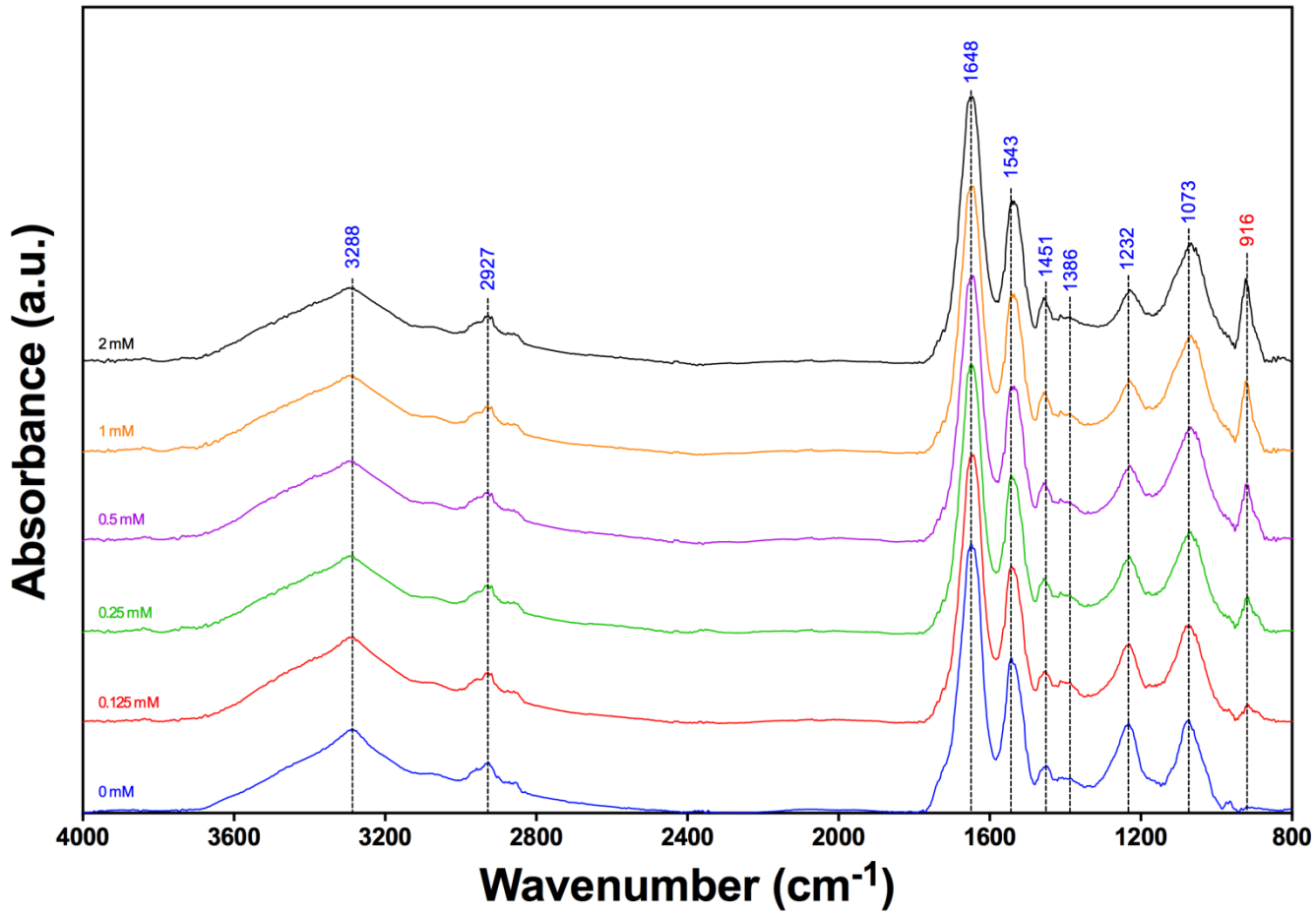

Appendix Figure 12. FTIR spectra of *P. putida* whole cells as a function of initial uranium concentration (pH 3, 0.1 M NaCl)

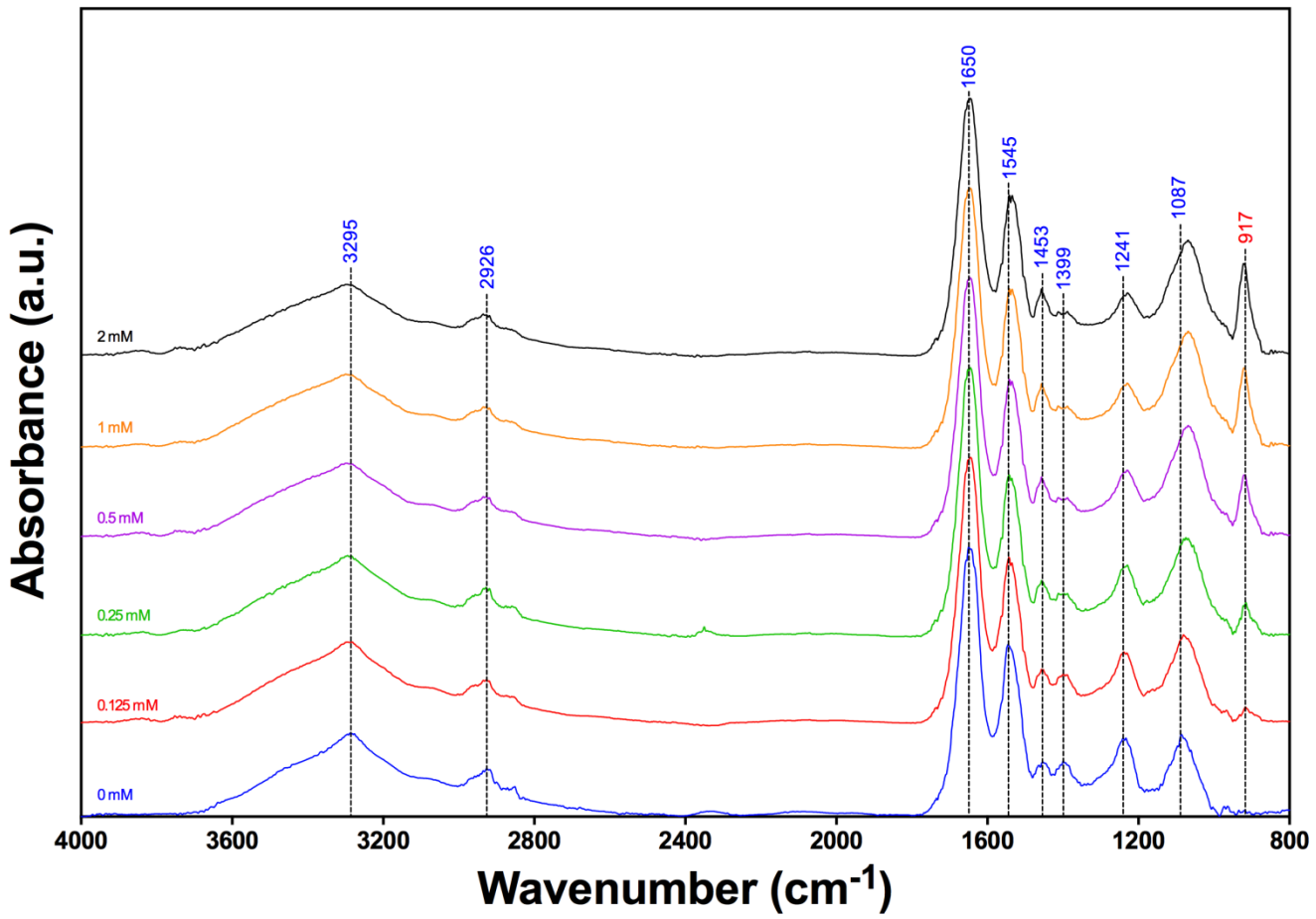

Appendix Figure 13. FTIR spectra of *P. putida* whole cells as a function of initial uranium concentration (pH 4, 0.1 M NaCl)

Allocation			ν (O-H)	ν_{as} (CH_3)	ν_{as} (CH_2)	ν (C=O)	δ (N-H)	δ_s (CH_2), ν (C-N)	δ_s (CH_2), ν_s (COO-)	ν_{as} (PO_2)	ν_s (PO_2); ν (C-OH, C-0-C, C-C)	ν (U-O)
0 mM	pH 3	σ (cm^{-1})	**3288**	**2957**	**2935**	**1642**	**1542**	**1452**	**-**	**1383**	**1241**	**1073**	**-**
		I (a.u.)	0.5486	0.2902	0.3071	1.5000	0.8728	0.2621	-	0.2130	0.4173	0.6510	-
	pH 4.25	σ (cm^{-1})	**3288**	**-**	**2928**	**1642**	**1542**	**1456**	**-**	**1388**	**1241**	**1078**	**-**
		I (a.u.)	0.5438	-	0.2610	1.5000	0.9517	0.3002	-	0.3079	0.3667	0.5946	-
	pH 5.5	σ (cm^{-1})	**3288**	**-**	**2930**	**1642**	**1542**	**1457**	**-**	**1399**	**1240**	**1079**	**-**
		I (a.u.)	0.5143	-	0.2780	1.5000	0.9673	0.3055	-	0.3390	0.3715	0.5668	-
0.125 mM	pH 3	σ (cm^{-1})	**3288**	**-**	**2935**	**1646**	**1542**	**1457**	**1412**	**1387**	**1239**	**1067**	**917**
		I (a.u.)	0.5579	-	0.2371	1.5000	0.8927	0.2983	0.2577	0.2638	0.4361	0.7313	0.1378
	pH 4.25	σ (cm^{-1})	**3287**	**-**	**2927**	**1646**	**1543**	**1452**	**-**	**1387**	**1240**	**1078**	**916**
		I (a.u.)	0.5584	-	0.2297	1.5000	0.9001	0.3063	-	0.2843	0.3792	0.6951	0.1158
	pH 5.5	σ (cm^{-1})	**3292**	**-**	**2930**	**1644**	**1542**	**1457**	**-**	**1397**	**1240**	**1080**	**916**
		I (a.u.)	0.5138	-	0.1860	1.5000	0.9534	0.3042	-	0.2996	0.3808	0.6159	0.1405
0.25 mM	pH 3	σ (cm^{-1})	**3288**	**-**	**2935**	**1645**	**1542**	**1457**	**1412**	**1387**	**1239**	**1063**	**922**
		I (a.u.)	0.5068	-	0.2129	1.4977	0.8865	0.3002	0.2441	0.2498	0.4220	0.7936	0.2298
	pH 4.25	σ (cm^{-1})	**3286**	**-**	**2925**	**1647**	**1543**	**1452**	**-**	**1387**	**1239**	**1078**	**917**
		I (a.u.)	0.5779	-	0.2593	1.4992	0.8788	0.3144	-	0.2584	0.3777	0.7307	0.2017
	pH 5.5	σ (cm^{-1})	**3292**	**-**	**2929**	**1646**	**1542**	**1457**	**-**	**1395**	**1240**	**1080**	**915**
		I (a.u.)	0.5041	-	0.1888	1.4993	0.9389	0.3171	-	0.2997	0.3841	0.6985	0.2273
0.5 mM	pH 3	σ (cm^{-1})	**3288**	**-**	**2935**	**1645**	**1542**	**1457**	**1412**	**1387**	**1239**	**1061**	**923**
		I (a.u.)	0.5134	-	0.2242	1.4988	0.9079	0.3250	0.2593	0.2628	0.4326	0.8578	0.3382
	pH 4.25	σ (cm^{-1})	**3285**	**-**	**2925**	**1647**	**1543**	**1452**	**-**	**1387**	**1239**	**1078**	**923**
		I (a.u.)	0.5459	-	0.2448	1.5000	0.8687	0.3265	-	0.2471	0.3700	0.7768	0.3269
	pH 5.5	σ (cm^{-1})	**3294**	**-**	**2929**	**1646**	**1542**	**1457**	**-**	**1396**	**1240**	**1080**	**916**
		I (a.u.)	0.4970	-	0.1865	1.5000	0.9316	0.3440	-	0.2665	0.3649	0.8570	0.3685
1 mM	pH 3	σ (cm^{-1})	**3287**	**-**	**2936**	**1646**	**1542**	**1454**	**1412**	**1387**	**1239**	**1057**	**923**
		I (a.u.)	0.5607	-	0.2449	1.5000	0.8605	0.3047	0.2364	0.2420	0.3793	0.8220	0.3483
	pH 4.25	σ (cm^{-1})	**3287**	**-**	**2925**	**1647**	**1543**	**1452**	**-**	**1387**	**1239**	**1078**	**923**
		I (a.u.)	0.5447	-	0.2357	1.4997	0.8703	0.3357	-	0.2542	0.3707	0.8138	0.4101
	pH 5.5	σ (cm^{-1})	**3297**	**-**	**2929**	**1646**	**1542**	**1457**	**-**	**1395**	**1240**	**1076**	**917**
		I (a.u.)	0.5242	-	0.2145	1.4994	0.9182	0.3443	-	0.2559	0.3082	0.8176	0.6092
2 mM	pH 3	σ (cm^{-1})	**3287**	**-**	**2935**	**1646**	**1542**	**1457**	**1412**	**1387**	**1239**	**1055**	**923**
		I (a.u.)	0.5326	-	0.2264	1.4993	0.9050	0.3336	0.2716	0.2773	0.4230	0.8856	0.4239
	pH 4.25	σ (cm^{-1})	**3287**	**-**	**2927**	**1647**	**1543**	**1452**	**-**	**1387**	**1239**	**1078**	**923**
		I (a.u.)	0.5584	-	0.2460	1.4981	0.8654	0.3486	-	0.2620	0.3602	0.8299	0.4799
	pH 5.5	σ (cm^{-1})	**3297**	**-**	**2929**	**1646**	**1542**	**1457**	**-**	**1395**	**1240**	**1069**	**921**
		I (a.u.)	0.5234	-	0.2030	1.4977	0.9291	0.3283	-	0.2415	0.2592	0.7507	0.8007
3 mM	pH 5.5	σ (cm^{-1})	**3297**	**-**	**2929**	**1646**	**1542**	**1457**	**-**	**1395**	**1240**	**1068**	**922**
		I (a.u.)	0.5288	-	0.2217	1.4992	0.9414	0.3275	-	0.2723	0.2951	0.7104	0.7934
4 mM	pH 5.5	σ (cm^{-1})	**3300**	**-**	**2929**	**1646**	**1542**	**1457**	**-**	**1395**	**1240**	**1067**	**921**
		I (a.u.)	0.5157	-	0.1921	1.5000	0.9437	0.3270	-	0.2945	0.2978	0.6773	0.7781

Appendix Table 8. Infrared adsorption bands of uranium accumulated *D. radiodurans* whole cells and their functional groups.

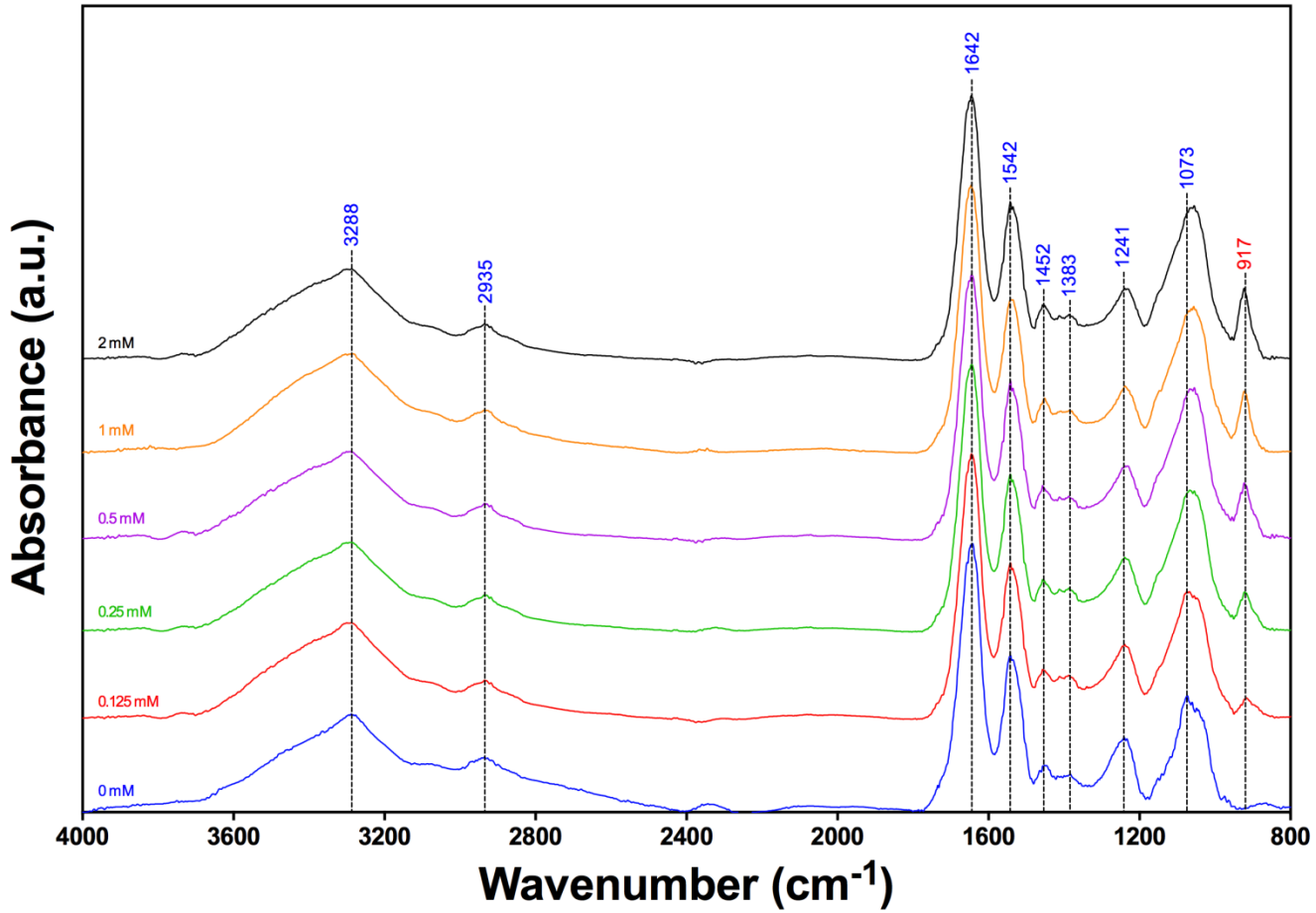

Appendix Figure 14. FTIR spectra of *D. radiodurans* whole cells as a function of initial uranium concentration (pH 3, 0.1 M NaCl)

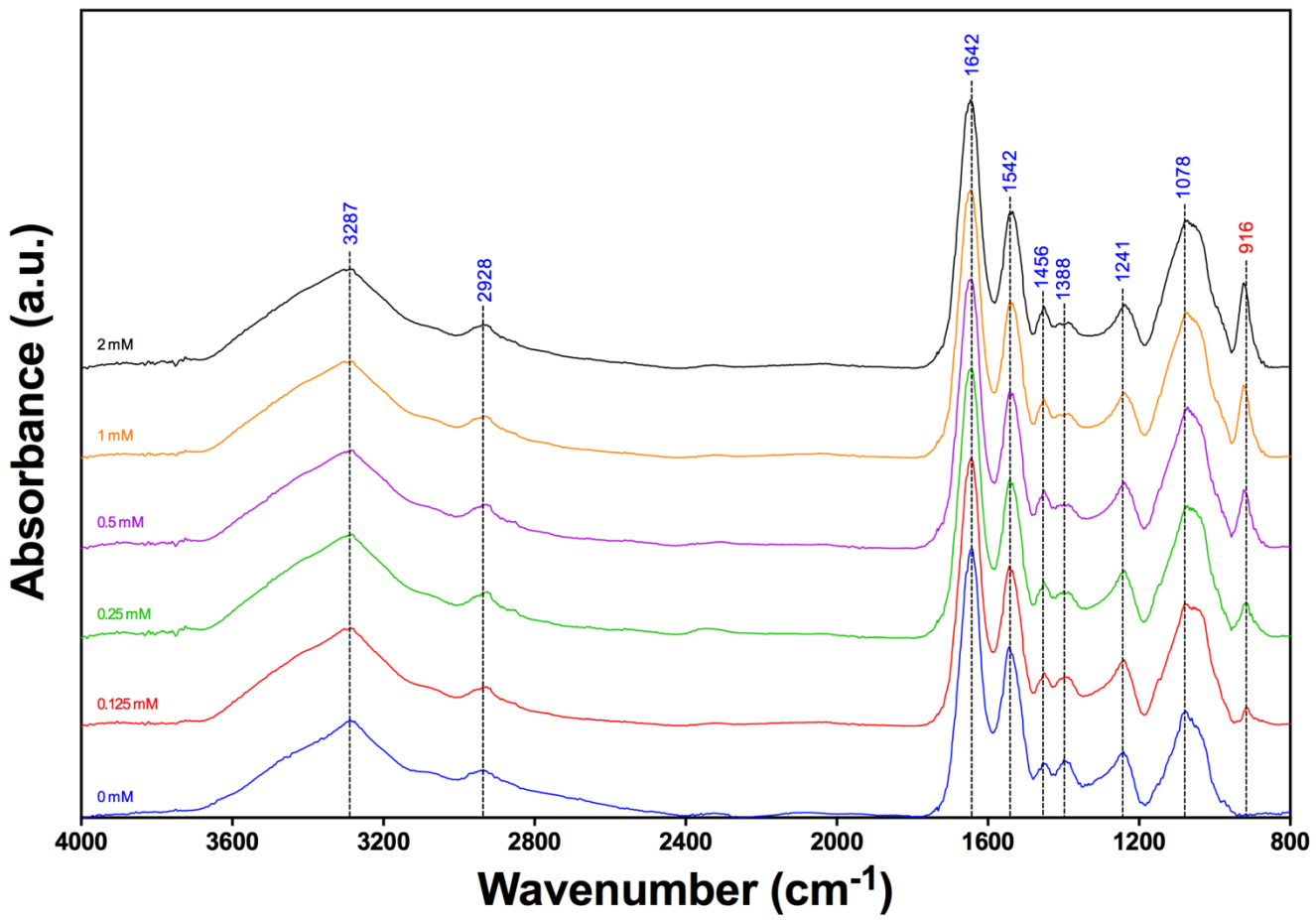

Appendix Figure 15. FTIR spectra of *D. radiodurans* whole cells as a function of initial uranium concentration (pH 4.25, 0.1 M NaCl)

Allocation			ν (O-H)	ν_{as} (CH_3)	ν_{as} (CH_2)	ν (C=O)	δ (N-H)	δ_s (CH2), ν (C-N)	δ_s (CH_2), ν_s (COO-)	ν_{as} (PO_2)	ν_s (PO_2); ν (C-OH, C-0-C, C-C)	ν_s (PO_2)	ν (U-O)
0 mM	pH 3	σ (cm^{-1})	**3294**	**-**	**2928**	**1648**	**1543**	**1457**	**1384**	**1221**	**1060**	**964**	**-**
		I (a.u.)	0.5110	-	0.3132	1.5000	0.8951	0.2734	0.2213	0.6837	1.0560	0.1668	-
	pH 4.25	σ (cm^{-1})	**3288**	**-**	**2918**	**1648**	**1542**	**1457**	**1399**	**1222**	**1060**	**963**	**-**
		I (a.u.)	0.5719	-	0.3207	1.5000	1.0791	0.3493	0.3931	0.5712	0.9012	0.1359	-
	pH 5.5	σ (cm^{-1})	**3296**	**2958**	**2929**	**1647**	**1543**	**1457**	**1399**	**1229**	**1063**	**-**	**-**
		I (a.u.)	0.5803	0.2769	0.3204	1.4997	1.0173	0.3580	0.3930	0.5373	0.7961	-	-
0.125 mM	pH 3	σ (cm^{-1})	**3294**	**-**	**2929**	**1646**	**1542**	**1457**	**1387**	**1229**	**1055**	**-**	**916**
		I (a.u.)	0.5811	-	0.2584	1.5000	0.9756	0.3452	0.3016	0.5419	0.8249	-	0.0859
	pH 4.25	σ (cm^{-1})	**3294**	**-**	**2918**	**1646**	**1542**	**1457**	**1397**	**1228**	**1055**	**-**	**916**
		I (a.u.)	0.6150	-	0.2220	1.5000	1.0326	0.3348	0.3498	0.5350	0.9116	-	0.0870
	pH 5.5	σ (cm^{-1})	**3296**	**2957**	**2929**	**1646**	**1542**	**1457**	**1396**	**1229**	**1055**	**-**	**916**
		I (a.u.)	0.5569	0.2510	0.2760	1.4982	1.0290	0.3419	0.3570	0.5174	0.8411	-	0.1050
0.25 mM	pH 3	σ (cm^{-1})	**3294**	**-**	**2929**	**1646**	**1540**	**1457**	**1383**	**1229**	**1057**	**-**	**917**
		I (a.u.)	0.5389	-	0.2595	1.5000	0.9245	0.3532	0.2718	0.4715	0.8144	-	0.1857
	pH 4.25	σ (cm^{-1})	**3294**	**-**	**2918**	**1646**	**1542**	**1457**	**1396**	**1229**	**1055**	**-**	**917**
		I (a.u.)	0.5650	-	0.2023	1.5000	0.9874	0.3491	0.3202	0.4483	0.8027	-	0.1972
	pH 5.5	σ (cm^{-1})	**3296**	**2957**	**2929**	**1647**	**1542**	**1457**	**1396**	**1229**	**1021**	**-**	**917**
		I (a.u.)	0.5133	0.1487	0.1671	1.5000	1.0182	0.3529	0.3658	0.4471	0.8512	-	0.1980
0.5 mM	pH 3	σ (cm^{-1})	**3294**	**-**	**2929**	**1646**	**1542**	**1457**	**1386**	**1229** **1217**	**1058**	**-**	**921**
		I (a.u.)	0.5229	-	0.2149	1.4986	0.9553	0.3534	0.2460	0.4791 0.4785	1.0106	-	0.3159
	pH 4.25	σ (cm^{-1})	**3294**	**-**	**2918**	**1646**	**1542**	**1457**	**1388**	**1229**	**1056**	**-**	**917**
		I (a.u.)	0.4817	-	0.1735	1.5000	0.9770	0.3555	0.2808	0.4113	0.8560	-	0.3064
	pH 5.5	σ (cm^{-1})	**3296**	**2956**	**2929**	**1646**	**1542**	**1457**	**1396**	**1229**	**1063**	**-**	**916**
		I (a.u.)	0.4812	0.2189	0.2427	1.4973	0.9985	0.3429	0.3037	0.3713	0.8078	-	0.2611
1 mM	pH 3	σ (cm^{-1})	**3294**	**-**	**2929**	**1646**	**1542**	**1457**	**1387**	**1215**	**1062**	**-**	**922**
		I (a.u.)	0.4958	-	0.1970	1.4976	0.9475	0.3560	0.2460	0.4874	1.0818	-	0.4561
	pH 4.25	σ (cm^{-1})	**3294**	**-**	**2918**	**1647**	**1542**	**1457**	**1387**	**1228** **1214**	**1055**	**-**	**922**
		I (a.u.)	0.5004	-	0.2219	1.4989	0.9514	0.3416	0.2357	0.4106 0.4224	1.0406	-	0.5206
	pH 5.5	σ (cm^{-1})	**3296**	**2956**	**2929**	**1646**	**1542**	**1457**	**1396**	**1229**	**1054**	**-**	**917**
		I (a.u.)	0.5047	0.2002	0.2067	1.4985	0.9584	0.3161	0.2560	0.3298	0.9465	-	0.5885
2 mM	pH 3	σ (cm^{-1})	**3294**	**-**	**2929**	**1646**	**1542**	**1457**	**1387**	**1213**	**1063**	**-**	**923**
		I (a.u.)	0.5092	-	0.2055	1.4966	0.9586	0.3682	0.2618	0.5085	1.1094	-	0.4987
	pH 4.25	σ (cm^{-1})	**3294**	**-**	**2918**	**1647**	**1542**	**1457**	**1387**	**1228** **1214**	**1056**	**-**	**922**
		I (a.u.)	0.5000	-	0.2158	1.5000	0.9430	0.3364	0.2459	0.4215 0.4413	1.0772	-	0.6267
	pH 5.5	σ (cm^{-1})	**3296**	**2956**	**2929**	**1647**	**1542**	**1457**	**1396**	**1228** **1220**	**1055**	**-**	**916**
		I (a.u.)	0.5185	0.1990	0.1991	1.4986	0.9434	0.2844	0.2222	0.2561 0.2613	0.9409	-	1.0033
3 mM	pH 5.5	σ (cm^{-1})	**3296**	**2956**	**2929**	**1647**	**1542**	**1457**	**1396**	**1225** **1212**	**1056**	**-**	**917**
		I (a.u.)	0.5135	0.1818	0.1806	1.4991	0.9541	0.3350	0.2791	0.2300 0.2576	0.9745	-	1.2964
4 mM	pH 5.5	σ (cm^{-1})	**3296**	**2956**	**2929**	**1646**	**1542**	**1457**	**1396**	**1205**	**1055**	**-**	**917**
		I (a.u.)	0.5161	0.2008	0.1997	1.4994	0.9634	0.3369	0.3140	0.2328	0.9298	-	1.4274

Appendix Table 9. Infrared adsorption bands of uranium accumulated *B. subtilis* whole cells and their functional groups.

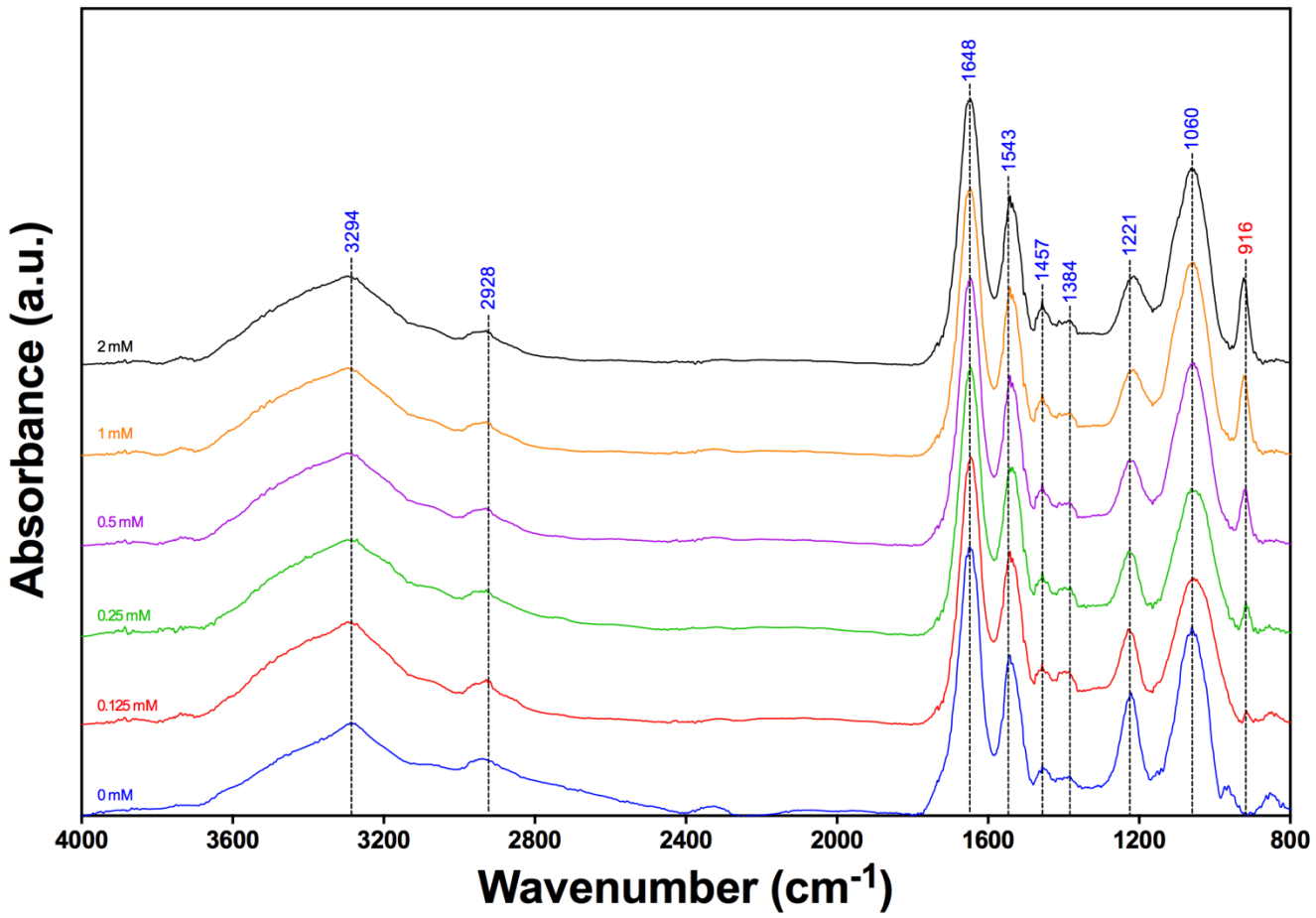

Appendix Figure 16. FTIR spectra of *B. subtilis* whole cells as a function of initial uranium concentration (pH 3, 0.1 M NaCl)

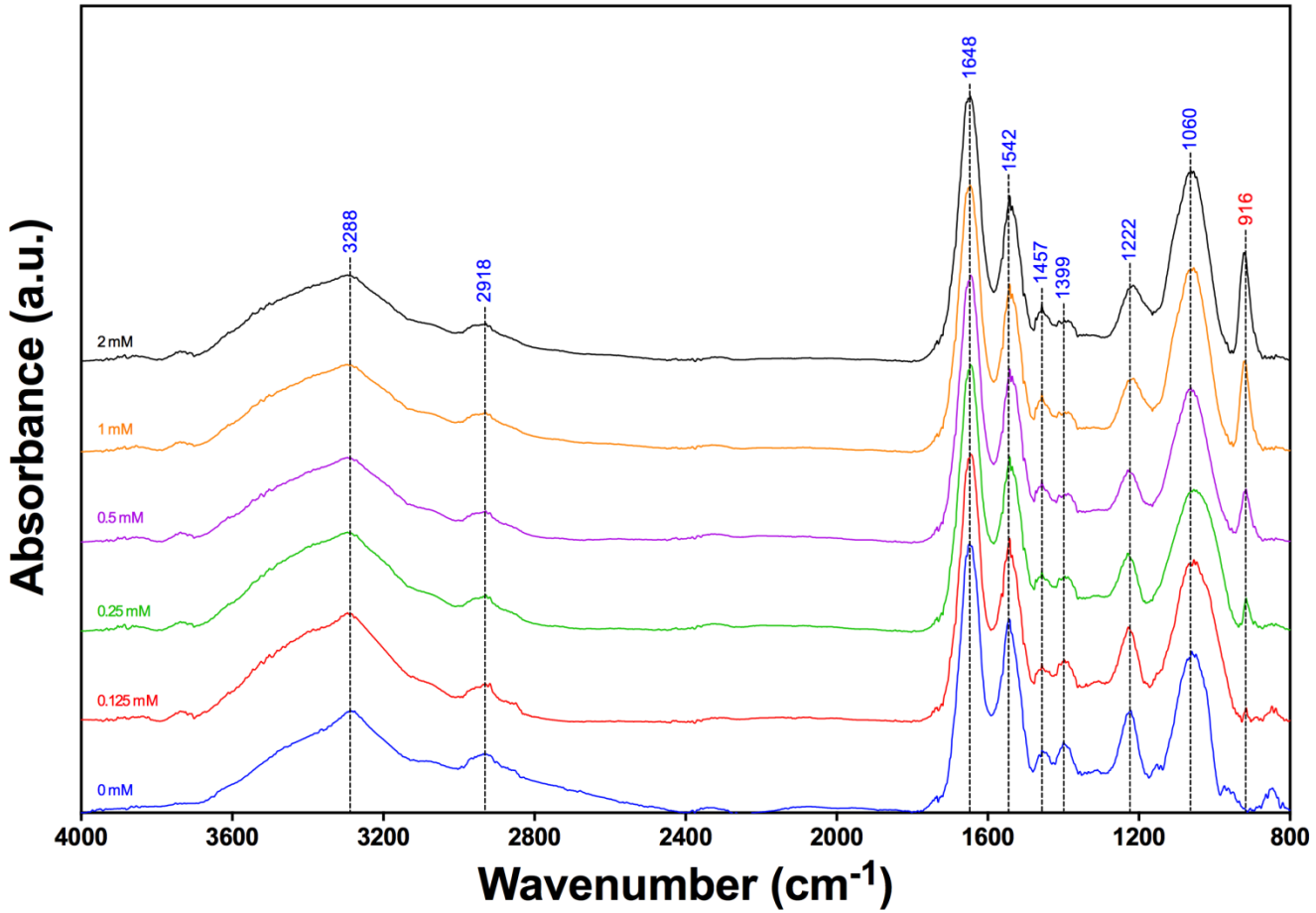

Appendix Figure 17. FTIR spectra of *B. subtilis* whole cells as a function of initial uranium concentration (pH 4.25, 0.1 M NaCl)

Allocation			ν (O-H)	ν_{as} (CH_3)	ν_{as} (CH_2)	ν_s (CH_2)	ν_s (C=O)	ν (C=O)	δ (N-H)	δ_s (CH_2), ν (C-N)	ν_s (COO-), δ (CH_2/CH_3)	ν_{as} (PO_2), ν (-COOH)	ν_s (PO_2); ν (C-OH, C-0-C, C-C)	ν (U-O)
0 mM	pH 3	σ (cm^{-1})	3292	2956	2923	2853	1723	1648	1544	1453	1410	1234	1151 1077	916
		I (a.u.)	0.6187	0.3242	0.4946	0.3030	0.2391	1.5000	0.9227	0.3354	0.3074	0.4525	0.3759 0.7356	0.1579
	pH 4.25	σ (cm^{-1})	-	2957	2919	2852	1734	1648	1543	1457	1400	1232	1151 1077	921
		I (a.u.)	-	0.3977	0.6498	0.4521	0.2027	1.5000	0.9875	0.3527	0.3399	0.4361	0.4039 0.7881	0.1863
	pH 5.5	σ (cm^{-1})	-	2957	2921	2852	1734	1648	1544	1457	1408	1232	1151 1077	921
		I (a.u.)	-	0.3667	0.5968	0.4063	0.1938	1.5000	1.0094	0.3575	0.3550	0.4279	0.4365 0.8028	0.2045
0.125 mM	pH 3	σ (cm^{-1})	3292	2956	2925 2919	2852	1723	1647	1542	1457	1412	1230	1153 1074	916
		I (a.u.)	0.5423	0.2811	0.4465 0.4525	0.2738	0.2824	1.4994	0.9326	0.3486	0.2919	0.5085	0.4650 0.9212	0.2399
	pH 4.25	σ (cm^{-1})	-	2955	2919	2852	1734	1647	1542	1457	1412	1230	1153 1074	915
		I (a.u.)	-	0.2911	0.4932	0.3155	0.2266	1.4999	1.0054	0.4045	0.3571	0.4364	0.4734 0.8803	0.2906
	pH 5.5	σ (cm^{-1})	-	2955	2919	2852	1734	1647	1541	1457	1411	1230	1152 1074	916
		I (a.u.)	-	0.3364	0.6014	0.3749	0.2058	1.5000	1.0033	0.3970	0.3921	0.4335	0.4850 0.8134	0.2262
0.25 mM	pH 3	σ (cm^{-1})	3292	2956	2927 2919	2852	1723	1646	1542	1457	1412	1229	1153 1068	916
		I (a.u.)	0.5256	0.3018	0.4546 0.4519	0.2838	0.2773	1.4994	0.9578	0.3744	0.2936	0.4994	0.4949 0.9466	0.3579
	pH 4.25	σ (cm^{-1})		2955	2919	2852	1734	1647	1542	1457	1412	1229	1153 1055	916
		I (a.u.)		0.2969	0.4773	0.3057	0.2169	1.5000	0.9650	0.4030	0.3338	0.4549	0.5254 0.9824	0.3743
	pH 5.5	σ (cm^{-1})	-	2955	2920	2852	1734	1647	1541	1457	1411	1230	1153 1074	916
		I (a.u.)	-	0.3024	0.5281	0.3324	0.2155	1.4999	1.0113	0.4342	0.3780	0.4164	0.4818 0.8630	0.3229
0.5 mM	pH 3	σ (cm^{-1})	3292	2956	2927 2919	2851	1723	1647	1542	1457	1412	1228	1153 1067	923
		I (a.u.)	0.5769	0.3222	0.4744 0.4701	0.2959	0.2747	1.5000	0.9685	0.4254	0.3152	0.4910	0.6221 1.1186	0.5504
	pH 4.25	σ (cm^{-1})	-	2956	2919	2853	1734	1647	1542	1457	1412	1229	1153 1047	922
		I (a.u.)	-	0.2704	0.4030	0.2549	0.2276	1.4748	0.9531	0.4299	0.3201	0.4526	0.6209 1.2012	0.6016
	pH 5.5	σ (cm^{-1})	-	2955	2920	2852	1734	1647	1541	1457	1411	1229	1147 1074 1069	916
		I (a.u.)	-	0.2935	0.4864	0.3128	0.2150	1.4998	1.0022	0.4519	0.3662	0.3791	0.5181 1.0150 1.0141	0.5620
1 mM	pH 3	σ (cm^{-1})	3292	2956	2927 2920	2851	1723	1647	1542	1457	1412	1228	1153 1066	923
		I (a.u.)	0.5022	0.2716	0.3823 0.3573	0.2103	0.2999	1.4957	0.9737	0.4539	0.3163	0.4848	0.6361 1.1221	0.7331
	pH 4.25	σ (cm^{-1})	-	2956	2919	2852	1734	1646	1542	1457	1412	1229	1153 1047	923
		I (a.u.)	-	0.2806	0.4262	0.2597	0.2269	1.5000	0.9948	0.4718	0.3380	0.4334	0.6889 1.3436	0.8408
	pH 5.5	σ (cm^{-1})	-	2951	2930	2860	1734	1647	1541	1457	1411	1234	1147 1074 1064	918
		I (a.u.)	-	0.1827	0.2590	0.1530	0.1849	1.5000	0.9391	0.3950	0.2828	0.2793	0.3826 0.9654 0.9652	0.8198
2 mM	pH 3	σ (cm^{-1})	3292	2956	2928 2920	2851	1723	1647	1542	1457	1412	1228	1152 1063	923
		I (a.u.)	0.5440	0.2620	0.3860 0.3653	0.2088	0.2710	1.4991	0.9885	0.4745	0.3497	0.4590	0.6734 1.1821	0.8226
	pH 4.25	σ (cm^{-1})	-	2956	2919	2852	1734	1646	1542	1457	1412	1229	- 1047	923
		I (a.u.)	-	0.2658	0.3931	0.2420	0.2369	1.5000	1.0267	0.5008	0.3616	0.4169	- 1.2062	0.9697
	pH 5.5	σ (cm^{-1})	-	2950	2928	2860	1734	1646	1541	1457	1411	1228	1147 1074	921
		I (a.u.)	-	0.2549	0.3672	0.2224	0.1952	1.4960	1.0014	0.4378	0.3109	0.2638	0.4430 1.0581	1.1443
3 mM	pH 5.5	σ (cm^{-1})	-	2950	2928	2860	1734	1646	1541	1457	1411	1228	1147 1074	921
		I (a.u.)	-	0.2541	0.3565	0.2098	0.2116	1.4955	1.0274	0.4368	0.3675	0.2296	0.3872 0.9808	1.3784
4 mM	pH 5.5	σ (cm^{-1})	-	2950	2927	2860	1734	1646	1541	1457	1411	1230	1147 1074	921
		I (a.u.)	-	0.2443	0.3262	0.1981	0.1877	1.4950	1.0192	0.4096	0.3820	0.1960	0.3406 0.9431	1.4612

Appendix Table 10. Infrared adsorption bands of uranium accumulated *P. putida* cell wall isolates and their functional groups

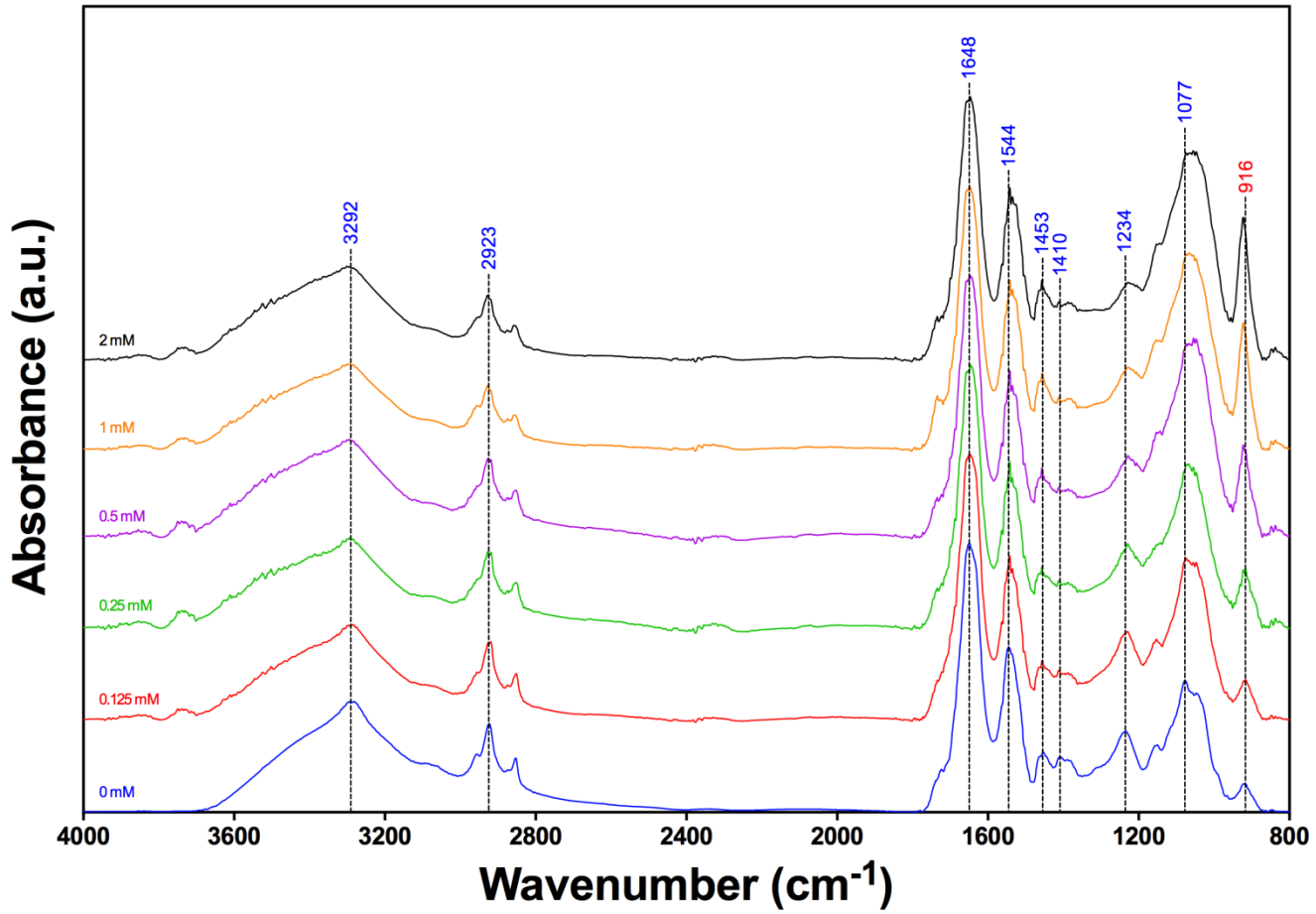

Appendix Figure 18. FTIR spectra of *P. putida* cell wall isolates as a function of initial uranium concentration (pH 3, 0.1 M NaCl)

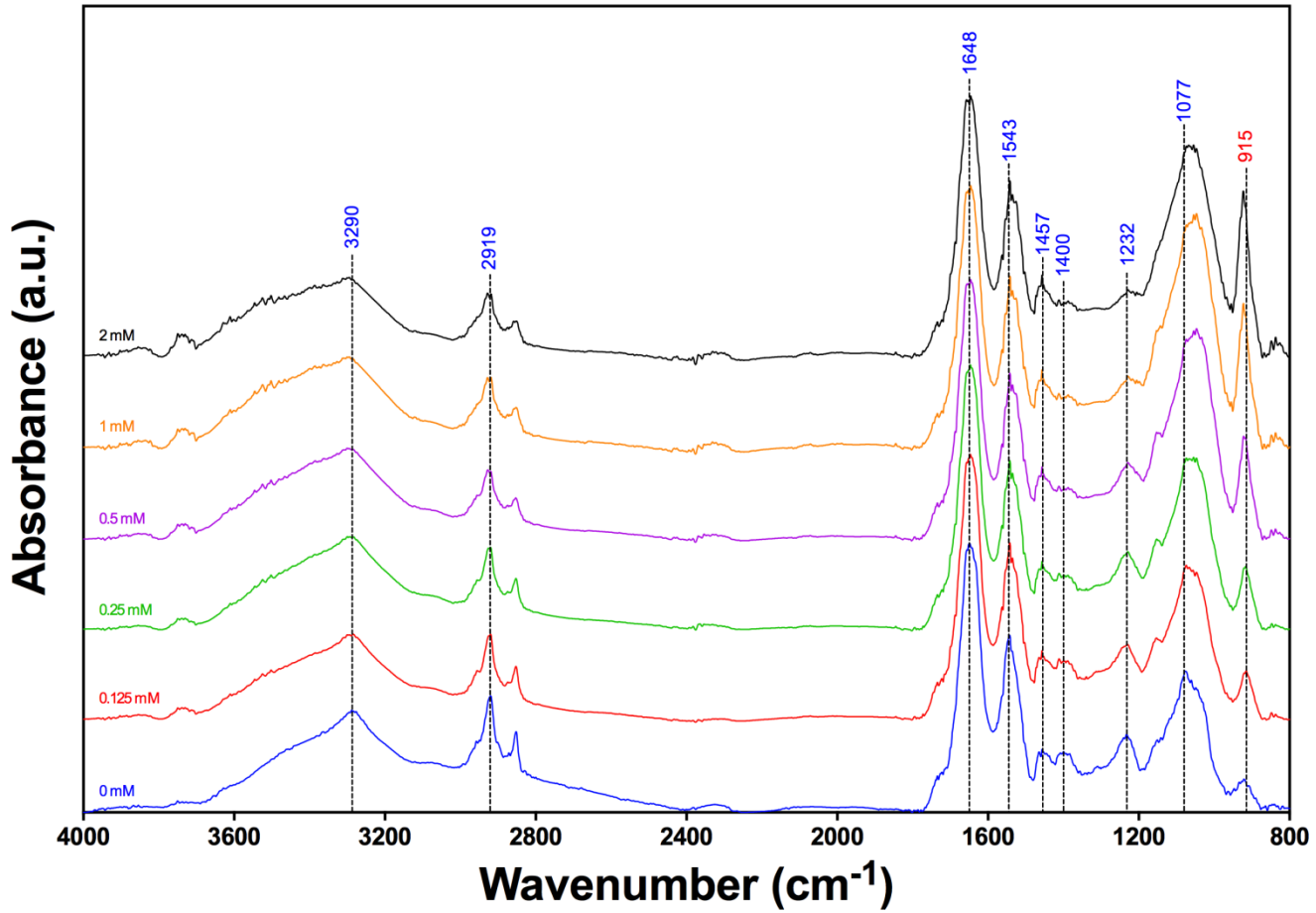

Appendix Figure 19. FTIR spectra of *P. putida* cell wall isolates as a function of initial uranium concentration (pH 4.25, 0.1 M NaCl)

Allocation			ν_s (C=O)	ν (C=O)	δ (N-H)	δ_s (CH_2), ν (C-N)	ν_s (COO-), δ (CH_2/CH_3)	ν_{as} (PO_2)	ν_s (PO_2); ν (C-OH, C-0-C, C-C)		ν_s (PO_2)	ν (U-O)
0 mM	pH 3	σ (cm^{-1})	**1724**	**1647**	**1548**	**1454**	**1379**	**1326**	**1215**	**-**	**1051**	**-**	**-**
		I (a.u.)	0.2612	1.4979	0.8559	0.3257	0.3436	0.2489	1.2260	-	2.7044	-	-
	pH 4.25	σ (cm^{-1})	**1739**	**1647**	**1545**	**1455**	**1384**	**1318**	**1221**	**1154**	**1052**	**976**	**-**
		I (a.u.)	0.1715	1.5000	0.9473	0.3585	0.3628	0.2627	0.8961	0.4665	1.7813	0.2919	-
	pH 5.5	σ (cm^{-1})	**1740**	**1646**	**1544**	**1457**	**1381**	**-**	**1223**	**1153**	**1052**	**976**	**-**
		I (a.u.)	0.1758	1.4999	0.9717	0.3727	0.4091	-	0.9762	0.5236	2.0335	0.3416	-
0.125 mM	pH 3	σ (cm^{-1})	**1724**	**1647**	**1547**	**1454**	**1379**	**1323**	**1218**	**-**	**1042**	**-**	**918**
		I (a.u.)	0.1916	1.5000	0.8692	0.2957	0.3105	0.2035	0.9157	-	2.2650	-	0.0380
	pH 4.25	σ (cm^{-1})	**1735**	**1646**	**1542**	**1454**	**1381**	**1318**	**1221**	**1149**	**1051** **1041**	**-**	**918**
		I (a.u.)	0.1239	1.4952	0.9496	0.3338	0.3741	0.2660	0.7835	0.4607	1.9512 1.9630	-	0.0539
	pH 5.5	σ (cm^{-1})	**1734**	**1647**	**1542**	**1457**	**1381**	**-**	**1224**	**1148**	**1052**	**-**	**918**
		I (a.u.)	0.1308	1.5000	0.9733	0.3578	0.3293	-	0.5942	0.3278	1.2169	-	0.0772
0.25 mM	pH 3	σ (cm^{-1})	**1724**	**1646**	**1547**	**1454**	**1379**	**1319**	**1215**	**-**	**1042**	**-**	**919**
		I (a.u.)	0.1735	1.5000	0.8906	0.2878	0.2998	0.1939	0.7384	-	2.0304	-	0.1500
	pH 4.25	σ (cm^{-1})	**1734**	**1646**	**1542**	**1454**	**1380**	**1318**	**1220**	**1149**	**1051** **1041**	**-**	**918**
		I (a.u.)	0.1508	1.5000	0.9515	0.3439	0.3308	0.2206	0.6694	0.3966	1.7243 1.7219	-	0.1586
	pH 5.5	σ (cm^{-1})	**1734**	**1646**	**1542**	**1457**	**1380**	**-**	**1224**	**1147**	**1060**	**-**	**918**
		I (a.u.)	0.1198	1.5000	1.0083	0.3731	0.3505	-	0.4811	0.3252	1.1049	-	0.1796
0.5 mM	pH 3	σ (cm^{-1})	**1724**	**1646**	**1547**	**1454**	**1379**	**1319**	**1207**	**-**	**1042**	**-**	**919**
		I (a.u.)	0.1776	1.4981	0.8785	0.3010	0.3124	0.2088	0.7232	-	2.0473	-	0.3748
	pH 4.25	σ (cm^{-1})	**1734**	**1646**	**1542**	**1454**	**1379**	**1318**	**1215**	**1148**	**1051** **1041**	**-**	**918**
		I (a.u.)	0.1112	1.5000	0.9698	0.3356	0.3393	0.2206	0.5740	0.4123	1.8143 1.7984	-	0.3634
	pH 5.5	σ (cm^{-1})	**1734**	**1646**	**1542**	**1457**	**1380**	**-**	**1224**	**1146**	**1060**	**-**	**918**
		I (a.u.)	0.1155	1.5000	1.0119	0.3713	0.3764	-	0.3996	0.3620	1.0744	-	0.3405
1 mM	pH 3	σ (cm^{-1})	**1724**	**1646**	**1547**	**1454**	**1379**	**1319**	**1199**	**-**	**1047**	**-**	**925**
		I (a.u.)	0.1313	1.5000	0.8951	0.3010	0.3044	0.1765	0.7816	-	2.4817	-	0.8201
	pH 4.25	σ (cm^{-1})	**1734**	**1646**	**1542**	**1457**	**1379**	**1318**	**1206**	**1148**	**1052**	**-**	**920**
		I (a.u.)	0.1122	1.5000	0.9811	0.3380	0.3589	0.2395	0.6436	0.5601	2.2150	-	0.8268
	pH 5.5	σ (cm^{-1})	**1734**	**1646**	**1542**	**1457**	**1380**	**-**	**1224**	**1146**	**1060**	**-**	**918**
		I (a.u.)	0.1118	1.4991	0.9826	0.3568	0.3838	-	0.4152	0.3860	1.3184	-	0.5580
2 mM	pH 3	σ (cm^{-1})	**1724**	**1646**	**1547**	**1454**	**1379**	**1320**	**1199**	**-**	**1052**	**-**	**925**
		I (a.u.)	0.1500	1.4990	0.8744	0.3056	0.3291	0.2144	0.8346	-	2.5839	-	1.0136
	pH 4.25	σ (cm^{-1})	**1734**	**1646**	**1542**	**1458**	**1379**	**1318**	**1199**	**1147**	**1052**	**-**	**925**
		I (a.u.)	0.1606	1.5000	0.9042	0.2894	0.3813	0.2505	0.8281	0.7720	2.9231	-	1.4001
	pH 5.5	σ (cm^{-1})	**1734**	**1646**	**1542**	**1457**	**1380**	**-**	**1207**	**1146**	**1052**	**-**	**918**
		I (a.u.)	0.1061	1.4984	0.8428	0.2565	0.2970	-	0.5441	0.5234	2.2107	-	1.4516
3 mM	pH 5.5	σ (cm^{-1})	**1734**	**1646**	**1542**	**1457**	**1380**	**-**	**1196**	**1146**	**1060**	**-**	**919**
		I (a.u.)	0.1342	1.5000	0.7763	0.2543	0.3778	-	0.6199	0.6384	2.3026	-	2.2581
4 mM	pH 5.5	σ (cm^{-1})	**1734**	**1646**	**1542**	**1457**	**1380**	**-**	**1195**	**1146**	**1060**	**-**	**919**
		I (a.u.)	0.1381	1.4920	0.7408	0.2564	0.3625	-	0.5568	0.6217	2.1468	-	2.3656

Appendix Table 11. Infrared adsorption bands of uranium accumulated *B. subtilis* cell wall isolates and their functional groups

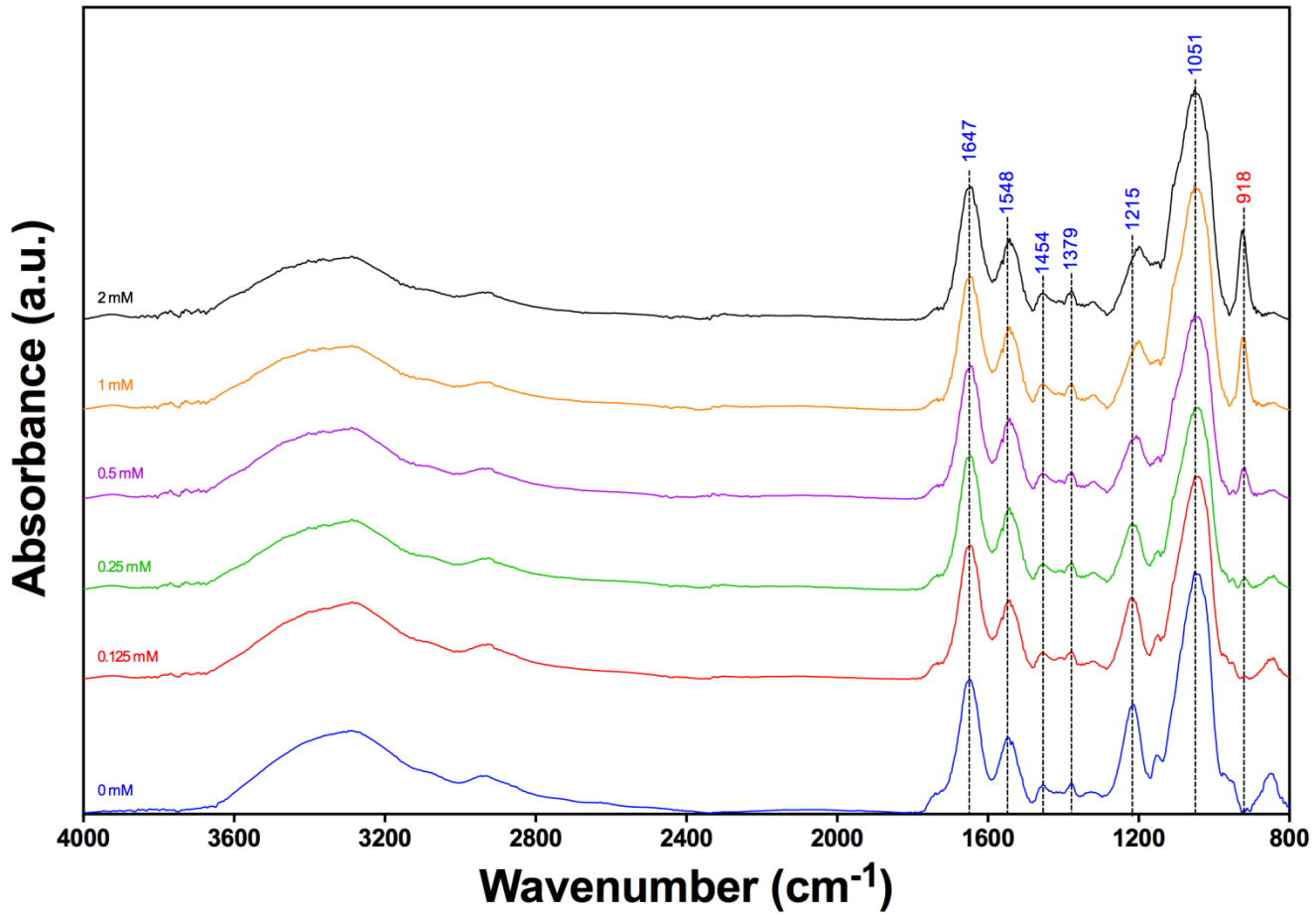

Appendix Figure 20. FTIR spectra of *B. subtilis* cell wall isolates as a function of initial uranium concentration (pH 3, 0.1 M NaCl)

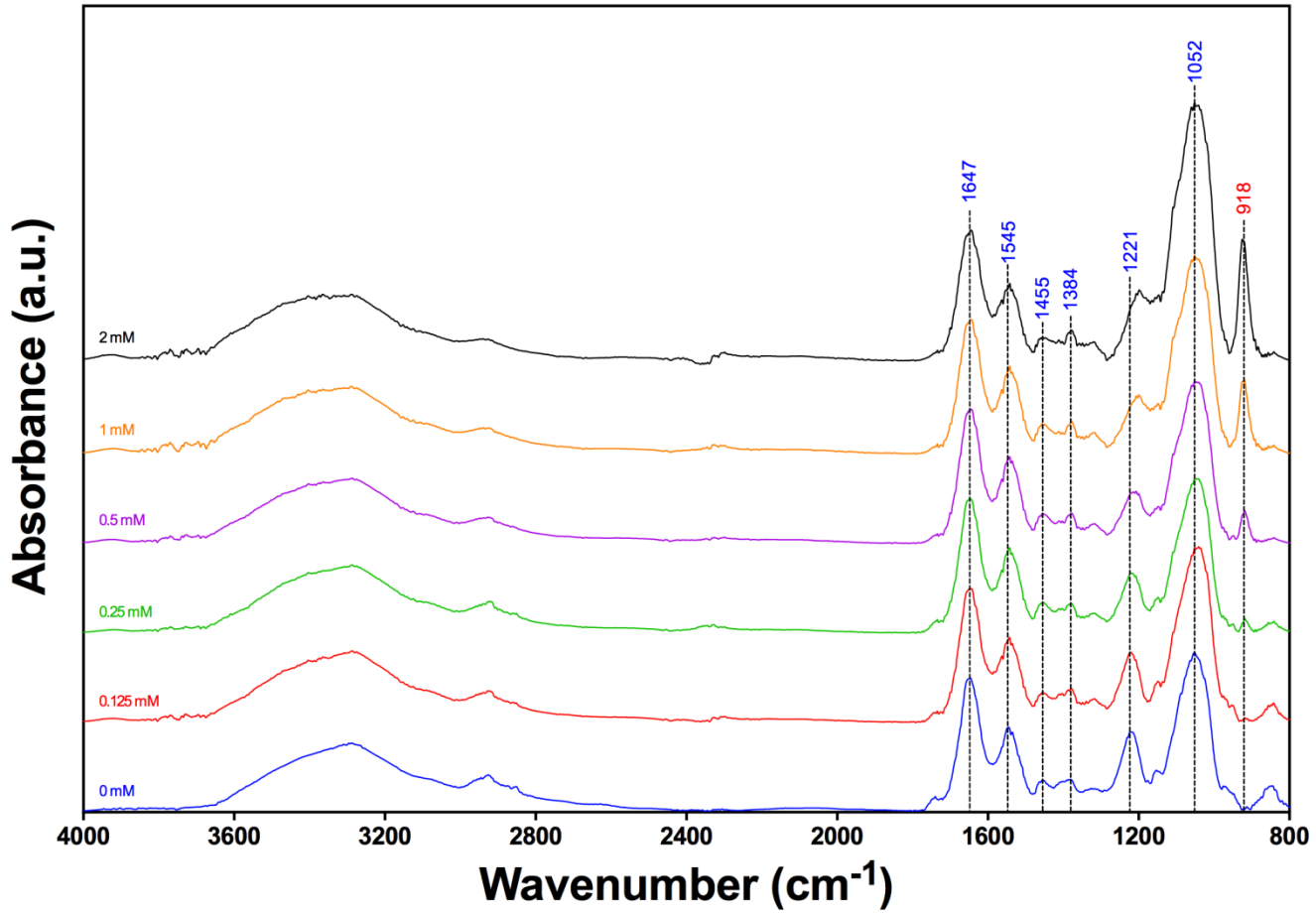

Appendix Figure 21. FTIR spectra of *B. subtilis* cell wall isolates as a function of initial uranium concentration (pH 4.25, 0.1 M NaCl)

Allocation			ν (O-H)	ν_{as} (CH_3)	ν_{as} (CH_2)	ν_s (CH_2)	ν_s (C=O)	ν (C=O)	δ (N-H)	δ_s (CH_2), ν (C-N)	ν_s (COO^-)	ν_{as} (PO_2)	ν_s (PO_2); ν (C-OH, C-0-C, C-C)	ν (U-O)
0 mM	pH 3	σ (cm^{-1})	**3296**	**2952**	**2927**	**2854**	**-**	**1647**	**1543**	**1454**	**1390**	**1232**	**-**	**1078**	**-**
		I (a.u.)	0.5308	0.3197	0.4191	0.2584	-	1.4966	0.8281	0.2914	0.2170	0.5415	-	0.7238	-
	pH 4.25	σ (cm^{-1})	**3295**	**2953**	**2925**	**2853**	**1739**	**1650**	**1543**	**1454**	**1391**	**1232**	**1157**	**1079**	**-**
		I (a.u.)	0.4969	0.2944	0.4418	0.2672	0.1948	1.4986	0.9411	0.3336	0.2900	0.4578	0.2998	0.6160	-
	pH 5.5	σ (cm^{-1})	**3295**	**2953**	**2925**	**2853**	**1739**	**1656**	**1543**	**1456**	**1391**	**1232**	**1160**	**1078**	**-**
		I (a.u.)	0.5130	0.3129	0.4900	0.2905	0.2217	1.4957	0.9735	0.3553	0.3205	0.4447	0.3454	0.6026	-
0.125 mM	pH 3	σ (cm^{-1})	**3296**	**2951**	**2928**	**2854**	**-**	**1646**	**1543**	**1454**	**1390**	**1228**	**-**	**1055**	**917**
		I (a.u.)	0.5082	0.2672	0.3350	0.2041	-	1.4998	0.8232	0.2883	0.2301	0.5587	-	0.9294	0.1674
	pH 4.25	σ (cm^{-1})	**3295**	**2951**	**2926**	**2854**	**1739**	**1647**	**1542**	**1457**	**1391**	**1229**	**1154**	**1055**	**916**
		I (a.u.)	0.5430	0.3142	0.4619	0.2840	0.1900	1.4980	0.9524	0.3608	0.2893	0.4552	0.3995	0.7818	0.1384
	pH 5.5	σ (cm^{-1})	**3295**	**2957**	**2928**	**2854**	**1735**	**1647**	**1542**	**1457**	**1391**	**1230**	**1155**	**1055**	**916**
		I (a.u.)	0.4666	0.3008	0.4277	0.2691	0.1986	1.5000	1.0311	0.3953	0.3117	0.4097	0.3450	0.6477	0.1828
0.25 mM	pH 3	σ (cm^{-1})	**3296**	**2950**	**2929**	**2854**	**-**	**1646**	**1543**	**1454**	**1390**	**1227**	**-**	**1055**	**922**
		I (a.u.)	0.5193	0.2736	0.3425	0.2076	-	1.5000	0.8149	0.3139	0.2400	0.5374	-	1.0519	0.2923
	pH 4.25	σ (cm^{-1})	**3295**	**2950**	**2928**	**2854**	**1734**	**1646**	**1542**	**1457**	**1391**	**1228**	**1152**	**1055**	**917**
		I (a.u.)	0.5009	0.2861	0.3686	0.2289	0.1852	1.5000	0.8679	0.3332	0.2453	0.4875	0.3114	0.8424	0.2390
	pH 5.5	σ (cm^{-1})	**3295**	**2957**	**2928**	**2854**	**1735**	**1647**	**1542**	**1457**	**1391**	**1229**	**1155**	**1055**	**916**
		I (a.u.)	0.4474	0.2838	0.4067	0.2493	0.1808	1.5000	1.0057	0.4023	0.2821	0.3917	0.3338	0.6880	0.2929
0.5 mM	pH 3	σ (cm^{-1})	**3296**	**2950**	**2929**	**2854**	**-**	**1646**	**1543**	**1454**	**1390**	**1227** **1218**	**-**	**1055**	**922**
		I (a.u.)	0.4813	0.2544	0.3275	0.1887	-	1.5000	0.8485	0.3322	0.2338	0.5039 0.5079	-	1.0752	0.4121
	pH 4.25	σ (cm^{-1})	**3295**	**2950**	**2929**	**2854**	**1734**	**1646**	**1542**	**1457**	**1391**	**1227** **1218**	**1152**	**1054**	**920**
		I (a.u.)	0.4626	0.2790	0.3525	0.2222	0.2077	1.4991	0.8907	0.3720	0.2477	0.4771 0.4768	0.3840	1.0227	0.4453
	pH 5.5	σ (cm^{-1})	**3295**	**2950**	**2928**	**2854**	**1734**	**1647**	**1542**	**1457**	**1391**	**1228**	**1155**	**1055**	**916**
		I (a.u.)	0.4645	0.2833	0.3886	0.2393	0.1740	1.4982	0.9551	0.3810	0.2569	0.3805	0.2997	0.7520	0.3701
1 mM	pH 3	σ (cm^{-1})	**3296**	**2950**	**2929**	**2852**	**-**	**1646**	**1543**	**1454**	**1390**	**1227** **1216**	**-**	**1055**	**923**
		I (a.u.)	0.4562	0.3102	0.3851	0.2646	-	1.5000	0.8906	0.3487	0.2514	0.4991 0.4970	-	1.0443	0.5322
	pH 4.25	σ (cm^{-1})	**3295**	**2950**	**2929**	**2854**	**1734**	**1646**	**1542**	**1457**	**1391**	**1225** **1218**	**1152**	**1054**	**922**
		I (a.u.)	0.4816	0.2737	0.3472	0.2118	0.1853	1.4986	0.8913	0.3839	0.2544	0.4508 0.4514	0.3900	1.0307	0.5494
	pH 5.5	σ (cm^{-1})	**3295**	**2957**	**2929**	**2854**	**1734**	**1646**	**1542**	**1457**	**1391**	**1228**	**1155**	**1055**	**916**
		I (a.u.)	0.4485	0.2834	0.3589	0.2261	0.1767	1.4997	0.8980	0.3568	0.2283	0.3848	0.2481	0.7541	0.6224
2 mM	pH 3	σ (cm^{-1})	**3296**	**2950**	**2929**	**2855**	**-**	**1646**	**1543**	**1454**	**1390**	**1225** **1216**	**-**	**1055**	**923**
		I (a.u.)	0.4385	0.2820	0.3503	0.2172	-	1.4996	0.8784	0.3548	0.2690	0.4873 0.4936	-	0.9730	0.5491
	pH 4.25	σ (cm^{-1})	**3295**	**2950**	**2928**	**2854**	**1734**	**1646**	**1542**	**1457**	**1391**	**1225** **1218**	**1152**	**1055**	**923**
		I (a.u.)	0.5340	0.2964	0.3714	0.2342	0.2002	1.4892	0.8854	0.4036	0.2857	0.4110 0.4167	0.3999	1.0048	0.6412
	pH 5.5	σ (cm^{-1})	**3295**	**2956**	**2929**	**2854**	**1734**	**1646**	**1542**	**1457**	**1391**	**1226**	**1155**	**1055**	**916**
		I (a.u.)	0.4650	0.2784	0.3591	0.2235	0.1867	1.4969	0.9428	0.3425	0.2264	0.3036	0.2409	0.7672	0.8993
3 mM	pH 5.5	σ (cm^{-1})	**3295**	**2953**	**2929**	**2852**	**1734**	**1646**	**1542**	**1453**	**1388**	**1218**	**1155**	**1055**	**917**
		I (a.u.)	0.5179	0.2783	0.3297	0.2006	0.1931	1.4885	0.9209	0.3802	0.3679	0.3258	0.2653	0.8100	1.0836
4 mM	pH 5.5	σ (cm^{-1})	**3295**	**2953**	**2929**	**2851**	**1734**	**1646**	**1542**	**1452**	**1388**	**1218**	**1155**	**1055**	**917**
		I (a.u.)	0.5536	0.2456	0.2774	0.1491	0.1724	1.4833	0.8921	0.3733	0.4067	0.3315	0.2489	0.7826	1.1281

Appendix Table 12. Infrared adsorption bands of uranium accumulated *P. putida* cell membrane isolates and their functional groups

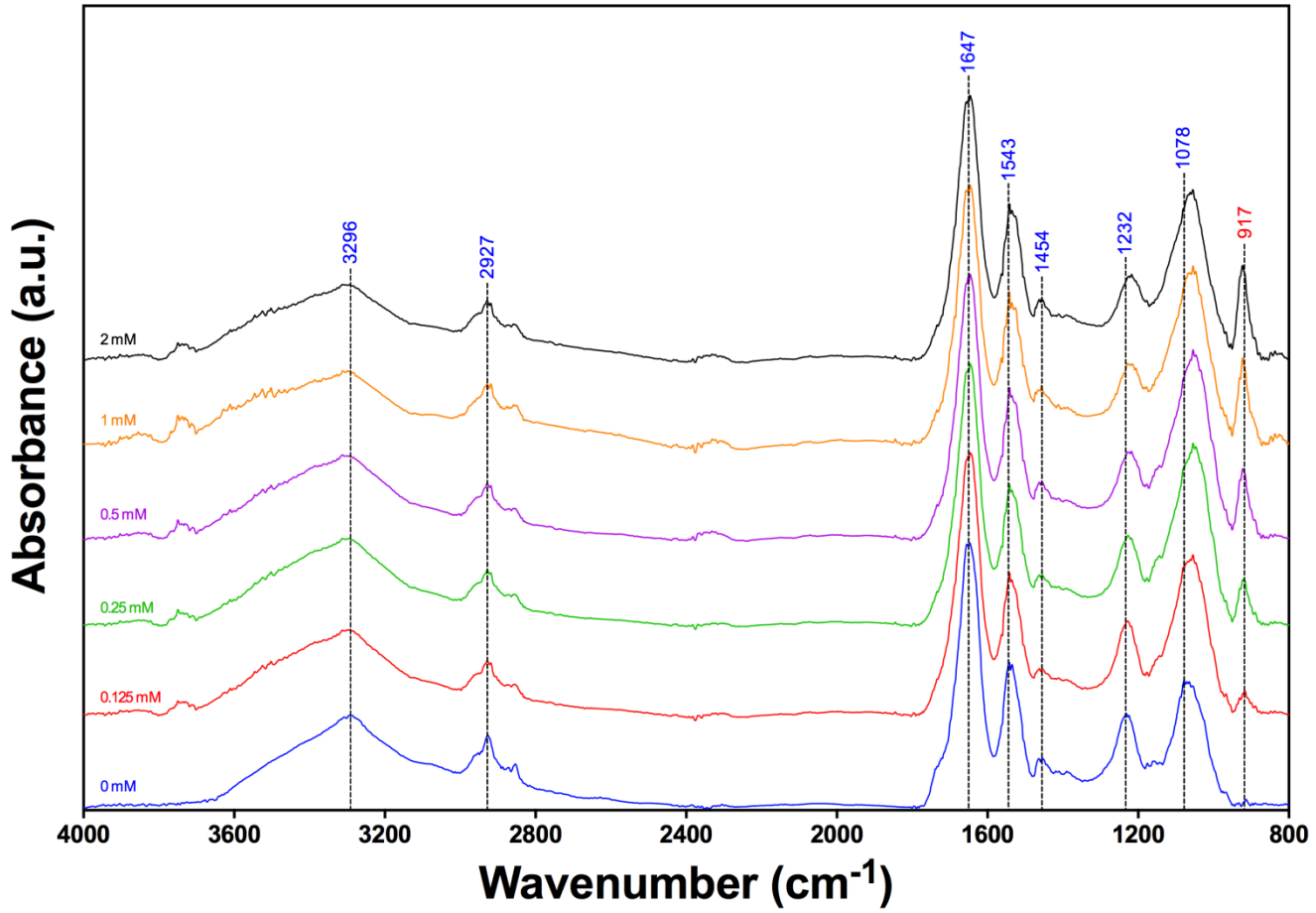

Appendix Figure 22. FTIR spectra of *P. putida* cell membrane isolates as a function of initial uranium concentration (pH 3, 0.1 M NaCl)

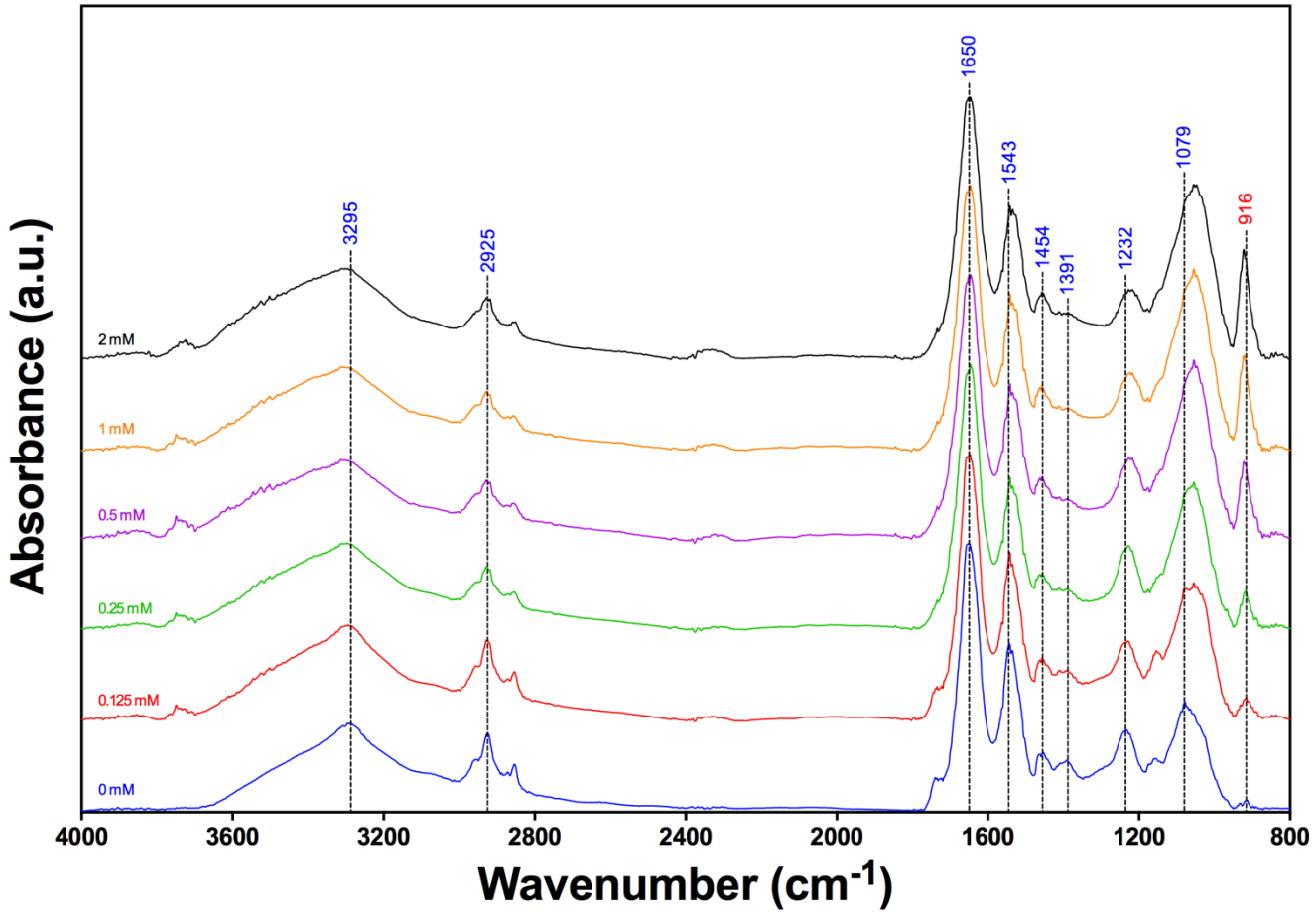

Appendix Figure 23. FTIR spectra of *P. putida* cell membrane isolates as a function of initial uranium concentration (pH 4.25, 0.1 M NaCl)

Allocation			ν (O-H)	ν_{as} (CH_3)	ν_{as} (CH_2)	ν_s (CH_2)	ν_s (C=O)	ν (C=O)	δ (N-H)	δ_s (CH_2), ν (C-N)		ν_s (COO^-)	ν_{as} (PO_2)	ν_s (PO_2); ν (C-OH, C-0-C, C-C)		ν (U-O)
0 mM	pH 3	σ (cm^{-1})	**3289**	**2962**	**2924**	**2853**	**1739**	**1654**	**1542**	**1466**	**1456**	**1387**	**1225**	**1174**	**1065**	**-**
		I (a.u.)	0.4257	0.3313	0.5209	0.3249	0.2763	1.5000	0.9164	0.3580	0.3534	0.2682	0.5392	0.3376	0.5544	-
	pH 4.25	σ (cm^{-1})	**3289**	**2962**	**2923**	**2852**	**1738**	**1653**	**1545**	**1467**		**1388**	**1227**	**1173**	**1071**	**-**
		I (a.u.)	0.4150	0.3257	0.5351	0.3311	0.2543	1.5000	0.9451	0.3548		0.2911	0.4726	0.3151	0.4880	-
	pH 5.5	σ (cm^{-1})	**3289**	**2952**	**2922**	**2852**	**1739**	**1654**	**1545**	**1467**		**1388**	**1226**	**1174**	**1071**	**-**
		I (a.u.)	0.4151	0.3296	0.5563	0.3440	0.2815	1.4999	0.9510	0.3674		0.3050	0.4962	0.3269	0.4973	-
0.125 mM	pH 3	σ (cm^{-1})	**3289**	**2962**	**2925**	**2854**	**1739**	**1653**	**1544**	**1465**	**1451**	**1388**	**1224**	**1176**	**1058**	**922**
		I (a.u.)	0.4484	0.3357	0.5200	0.3226	0.2737	1.5000	0.8983	0.3623	0.3669	0.2544	0.5270	0.3616	0.6231	0.1136
	pH 4.25	σ (cm^{-1})	**3289**	**2962**	**2924**	**2853**	**1739**	**1653**	**1544**	**1457**		**1388**	**1225**	**1175**	**1058**	**916**
		I (a.u.)	0.4145	0.3360	0.5453	0.3368	0.2784	1.4933	0.9408	0.3888		0.2985	0.4995	0.3448	0.5352	0.0649
	pH 5.5	σ (cm^{-1})	**3289**	**2962**	**2924**	**2853**	**1739**	**1654**	**1544**	**1457**		**1388**	**1226**	**1174**	**1058**	**917**
		I (a.u.)	0.3936	0.2989	0.4923	0.2994	0.2452	1.5000	0.9502	0.3653		0.2851	0.4631	0.3140	0.4981	0.0607
0.25 mM	pH 3	σ (cm^{-1})	**3289**	**2962**	**2925**	**2855**	**1738**	**1653**	**1538**	**1451**		**1388**	**1224**	**1176**	**1058**	**922**
		I (a.u.)	0.4252	0.3042	0.4596	0.2756	0.2372	1.5000	0.9189	0.3867		0.2549	0.4747	0.3515	0.5954	0.1816
	pH 4.25	σ (cm^{-1})	**3289**	**2962**	**2925**	**2855**	**1739**	**1653**	**1541**	**1457**		**1388**	**1225**	**1175**	**1057**	**922**
		I (a.u.)	0.4096	0.2926	0.4435	0.2644	0.2117	1.5000	0.9213	0.3895		0.2670	0.4627	0.3241	0.5729	0.1754
	pH 5.5	σ (cm^{-1})	**3289**	**2962**	**2925**	**2854**	**1739**	**1654**	**1543**	**1457**		**1388**	**1226**	**1174**	**1058**	**917**
		I (a.u.)	0.3918	0.2989	0.4855	0.2917	0.2300	1.4991	0.9473	0.3850		0.2779	0.4484	0.3118	0.5210	0.1198
0.5 mM	pH 3	σ (cm^{-1})	**3289**	**2962**	**2925**	**2855**	**1738**	**1653**	**1537**	**1452**		**1388**	**1224**	**1176**	**1058**	**923**
		I (a.u.)	0.4282	0.3029	0.4477	0.2779	0.2152	1.5000	0.9327	0.3999		0.2509	0.4451	0.3655	0.6001	0.2754
	pH 4.25	σ (cm^{-1})	**3289**	**2962**	**2925**	**2856**	**1739**	**1653**	**1541**	**1457**		**1388**	**1225**	**1175**	**1057**	**922**
		I (a.u.)	0.3925	0.2866	0.4334	0.2671	0.2017	1.5000	0.9446	0.4338		0.2753	0.4309	0.3543	0.6153	0.3358
	pH 5.5	σ (cm^{-1})	**3289**	**2962**	**2925**	**2855**	**1739**	**1653**	**1543**	**1457**		**1388**	**1225**	**1175**	**1058**	**917**
		I (a.u.)	0.3871	0.2665	0.4122	0.2487	0.1807	1.5000	0.9656	0.4178		0.2872	0.4024	0.2885	0.4998	0.2309
1 mM	pH 3	σ (cm^{-1})	**3289**	**2962**	**2925**	**2855**	**1738**	**1653**	**1536**	**1452**		**1388**	**1224**	**1176**	**1058**	**923**
		I (a.u.)	0.3979	0.2834	0.4242	0.2559	0.2018	1.4990	0.9407	0.4168		0.2645	0.4331	0.3762	0.6311	0.3554
	pH 4.25	σ (cm^{-1})	**3289**	**2962**	**2925**	**2856**	**1739**	**1653**	**1541**	**1457**		**1388**	**1225**	**1175**	**1057**	**922**
		I (a.u.)	0.3946	0.2732	0.4029	0.2512	0.1880	1.5000	0.9384	0.4347		0.2697	0.4072	0.3589	0.6092	0.4253
	pH 5.5	σ (cm^{-1})	**3289**	**2962**	**2926**	**2856**	**1738**	**1653**	**1541**	**1457**		**1388**	**1224**	**1175**	**1058**	**917**
		I (a.u.)	0.3775	0.2413	0.3536	0.2143	0.1500	1.5000	0.9516	0.4114		0.2705	0.3623	0.2992	0.5458	0.5418
2 mM	pH 3	σ (cm^{-1})	**3289**	**2962**	**2925**	**2855**	**1738**	**1653**	**1535**	**1451**		**1388**	**1224**	**1176**	**1058**	**923**
		I (a.u.)	0.4167	0.2963	0.4407	0.2696	0.2059	1.4994	0.9519	0.4307		0.2972	0.4326	0.3977	0.6153	0.3943
	pH 4.25	σ (cm^{-1})	**3289**	**2962**	**2926**	**2856**	**1739**	**1653**	**1541**	**1457**		**1388**	**1224**	**1175**	**1057**	**923**
		I (a.u.)	0.3902	0.2648	0.3894	0.2378	0.1763	1.5000	0.9399	0.4351		0.2816	0.3958	0.3614	0.6160	0.4852
	pH 5.5	σ (cm^{-1})	**3289**	**2962**	**2926**	**2856**	**1738**	**1653**	**1542**	**1457**		**1388**	**1223**	**1175**	**1058**	**917**
		I (a.u.)	0.4052	0.2498	0.3476	0.2123	0.1515	1.5000	0.9771	0.3923		0.2644	0.3006	0.2912	0.5242	0.8420
3 mM	pH 5.5	σ (cm^{-1})	**3289**	**2962**	**2926**	**2856**	**1738**	**1653**	**1542**	**1457**	**1450**	**1388**	**1223**	**1176**	**1058**	**921**
		I (a.u.)	0.3968	0.2496	0.3439	0.2137	0.1625	1.5000	1.0198	0.4332	0.4379	0.4268	0.3389	0.3439	0.5962	1.0473
4 mM	pH 5.5	σ (cm^{-1})	**3289**	**2962**	**2926**	**2856**	**1738**	**1653**	**1542**	**1457**	**1450**	**1388**	**1223**	**1176**	**1058**	**921**
		I (a.u.)	0.4177	0.2559	0.3417	0.2160	0.1660	1.5000	1.0160	0.4315	0.4409	0.4367	0.3169	0.3209	0.5709	1.1761

Appendix Table 13. Infrared adsorption bands of uranium accumulated *B. subtilis* cell membrane isolates and their functional groups

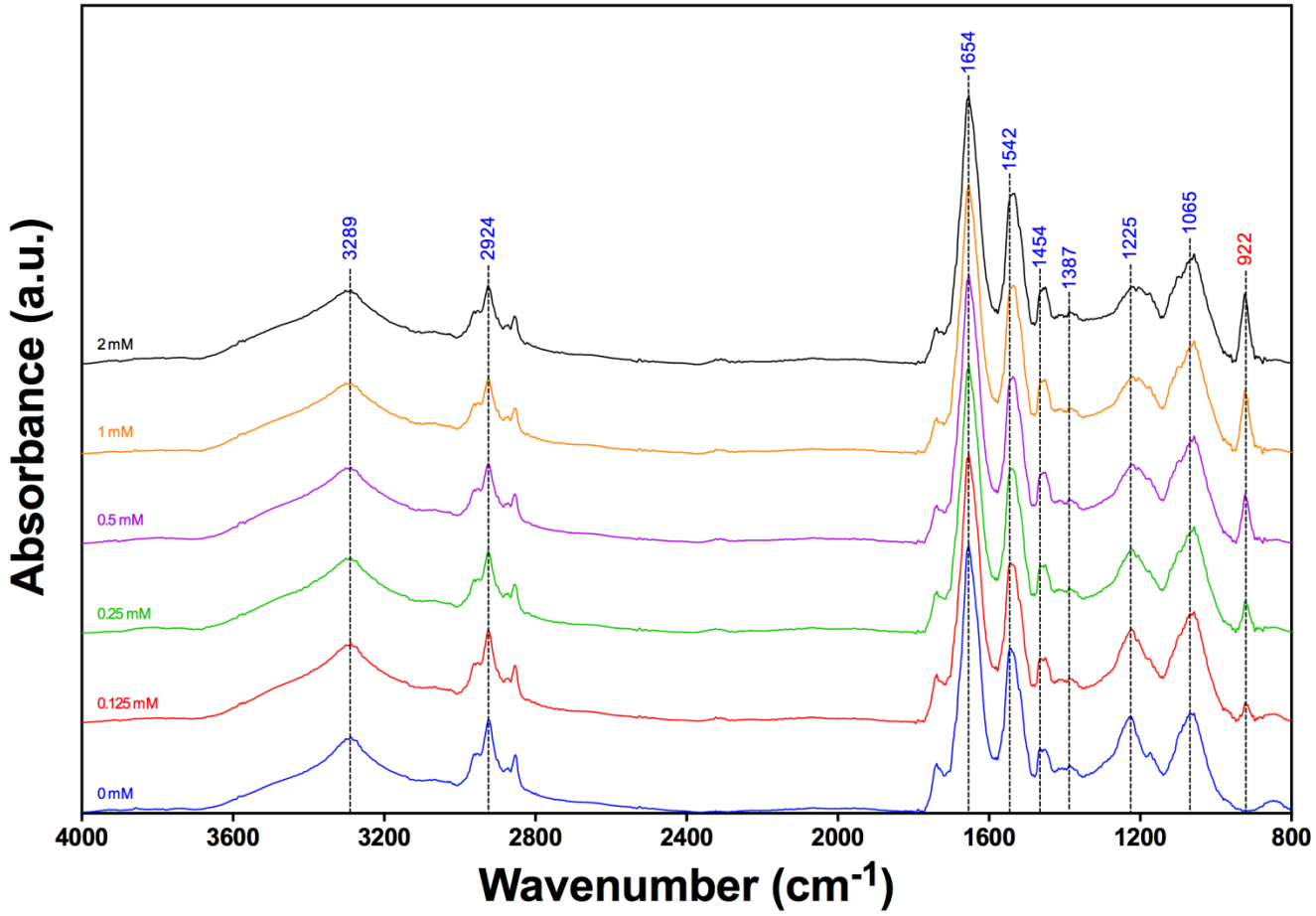

Appendix Figure 24. FTIR spectra of *B. subtilis* cell membrane isolates as a function of initial uranium concentration (pH 3, 0.1 M NaCl)

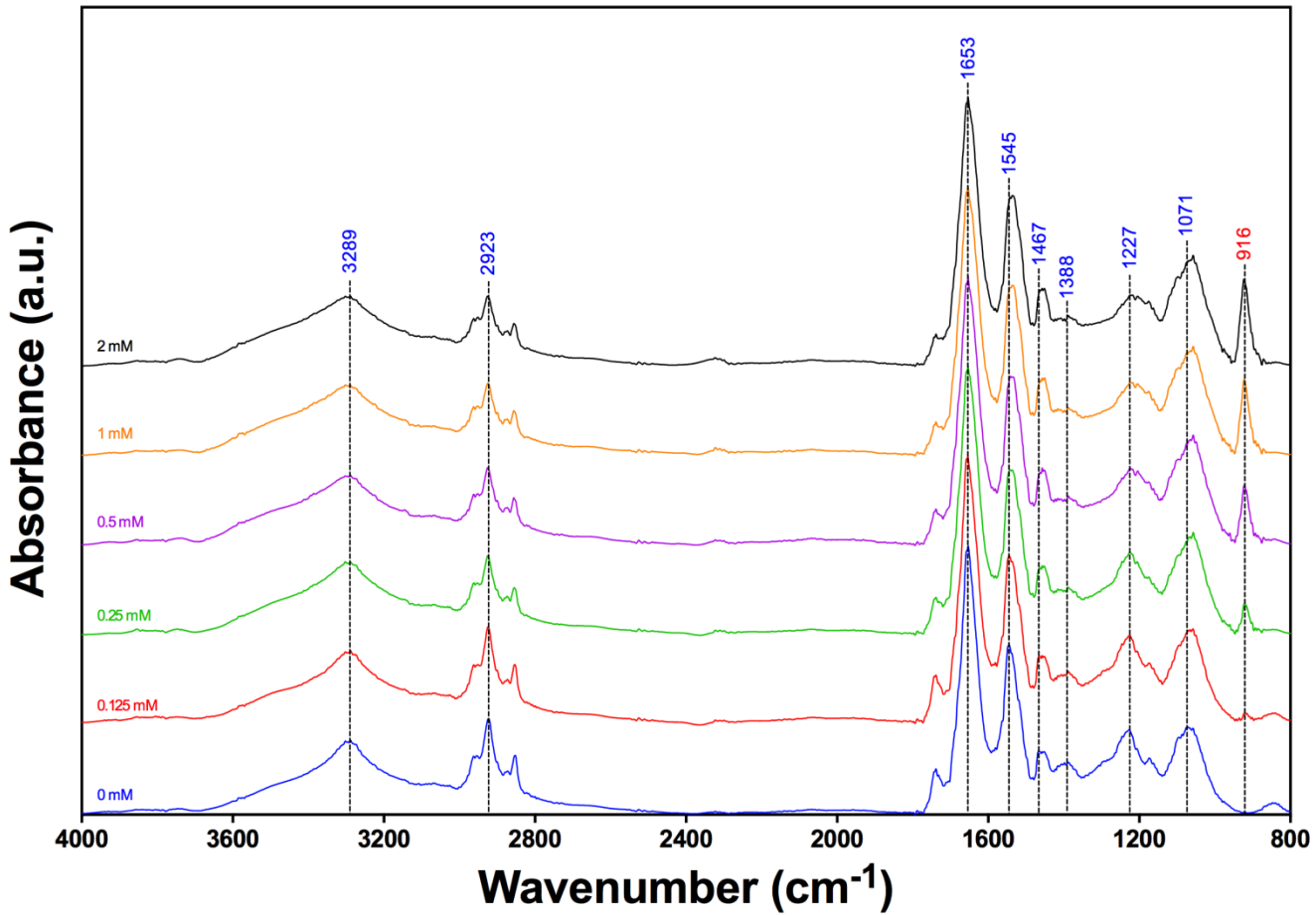

Appendix Figure 25. FTIR spectra of *B. subtilis* cell membrane isolates as a function of initial uranium concentration (pH 4.25, 0.1 M NaCl).

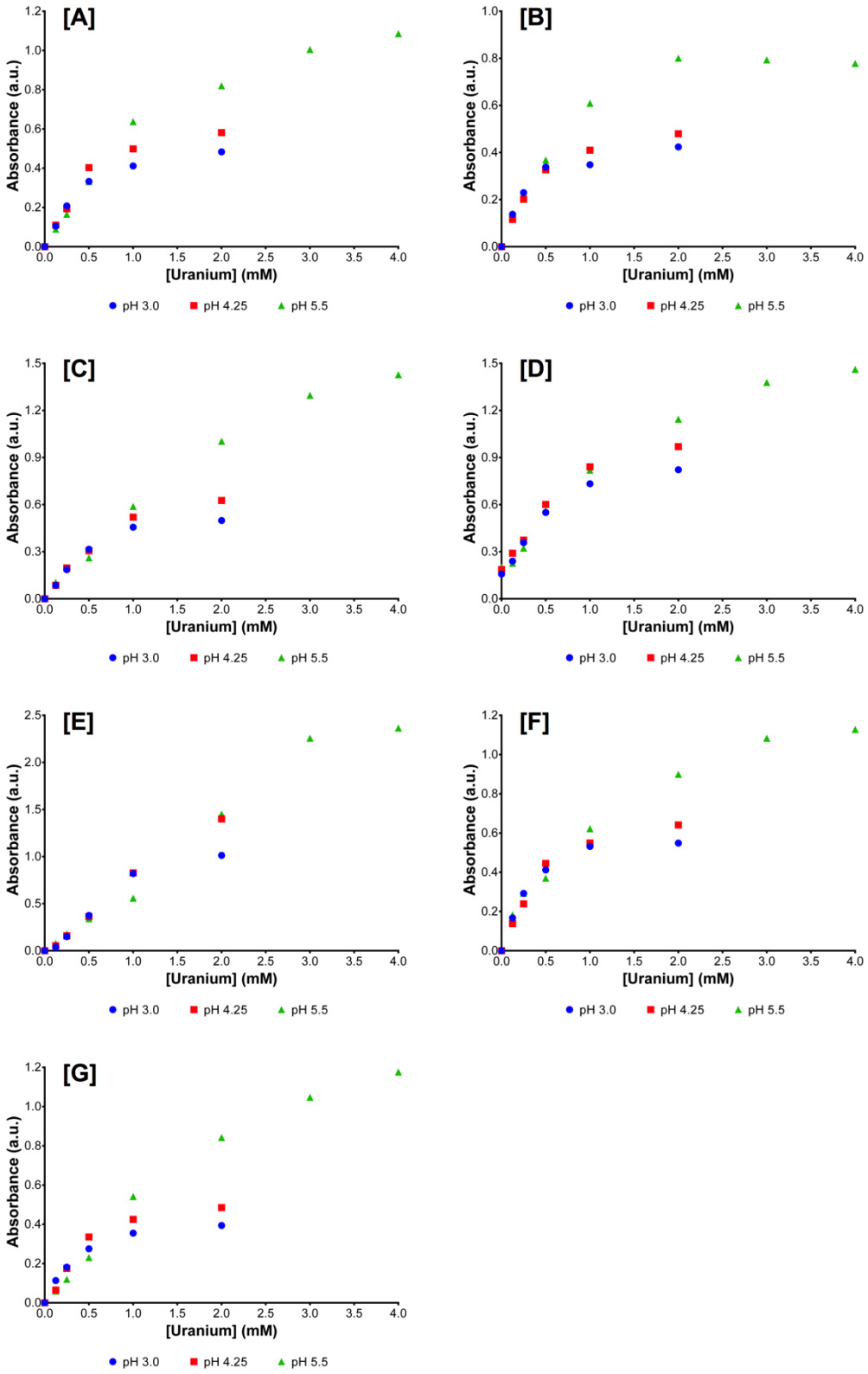

Appendix Figure 26. Changes in absorption intensity of the ν (U-O_{ligand}) present *in P. putida* whole cells [A], *D. radiodurans* whole cells [B], *B. subtilis* whole cells [C], *P. putida* cell wall isolates [D], *B. subtilis* cell wall isolates [E], *P. putida* cell membrane isolates [F] and *B. subtilis* cell membrane isolates [G].

Appendix Table 14. *P. putida* 33015 benzoate media

Component	Empirical Formula	Quantity
Ammonium phosphate dibasic	$(NH_4)_2HPO_4$	3.0 g L^{-1}
Monopotassium phosphate	KH_2PO_4	1.2 g L^{-1}
Sodium chloride	NaCl	5.0 g L^{-1}
Magnesium sulphate heptahydrate	$MgSO_4.H_2O$	0.2 g L^{-1}
Yeast extract	-	0.5 g L^{-1}
Noble agar (added for plate preparation)	-	20 g L^{-1}
60 g L^{-1} Sodium benzoate (0.2 µm filter sterilized)	$NaC_7H_5O_2$	50 mL L^{-1}

Appendix Table 15. *P. putida* 33015 low phosphate media

Component	Empirical Formula	Quantity
10 x salt solution (pH 7.0) (*)	-	100 mL L^{-1}
100 % glycerol	$C_3H_8O_3$	5 mL L^{-1}
50 mg mL^{-1} thiamine hydrochloride (#)	$C_{12}H_{17}ClN_4OS \cdot HCl$	400 µL L^{-1}
10 % peptone	-	100 mL L^{-1}
100 mM calcium chloride dehydrate	$CaCl_2.H_2O$	1 mL L^{-1}
Deionised water	H_2O	793.6 mL L^{-1}

Filter sterilise using 0.2 µm PES syringe filters

* 10 x salt solution (pH 7.0) component	Empirical Formula	Quantity
Sodium chloride	NaCl	46.8 g L^{-1}
Potassium chloride	KCl	14.9 g L^{-1}
Ammonium chloride	NH_4Cl	10.7 g L^{-1}
Ammonium sulphate	$(NH_4)_2SO_4$	4.3 g L^{-1}
1 M magnesium chloride	$MgCl_2$	10 mL L^{-1}
Zinc sulphate	$ZnSO_4$	2.7 mg L^{-1}
Trizma base	$NH_2C(CH_2OH)_3$)	143.3 g L^{-1}

10 x salt solution amended pH adjusted to 7 with concentrated HCl.

Appendix Table 16. *D. radiodurans* R1 TYG media

Component	Empirical Formula	Quantity
Tryptone	-	10 g L^{-1}
Glucose	$C_6H_{12}O_6$	1 g L^{-1}
Yeast extract	-	5 g L^{-1}
Agar (* added for plate preparation)	-	15 g L^{-1}

Appendix Table 17. *D. radiodurans* R1 low phosphate media

Component	Empirical Formula	Quantity
2-(N-Morpholino)ethanesulfonic acid (MES)	$C_6H_{13}NO_4S$	7.8 g L^{-1}
Calcium chloride dihydrate	$CaCl_2.2H_2O$	0.0793 g L^{-1}
Sodium chloride	NaCl	0.008 g L^{-1}
Potassium chloride	KNO_3	0.103 g L^{-1}
Sodium nitrate	$NaNO_3$	0.698 g L^{-1}
Magnesium sulphate heptahydrate	$MgSO_4.H_2O$	0.1 g L^{-1}
Nitrilotriacetic acid (NTA)	$N(CH_2COOH)_3$	0.1 g L^{-1}
Deionised water	H_2O	925 mL L^{-1}
20 % glucose (*)	$C_6H_{12}O_6$	25 mL L^{-1}
2.5 % yeast extract (*)	-	40 mL L^{-1}
5 % ammonium chloride (*)	NH_4Cl	10 mL L^{-1}

* Filter sterilise using 0.2 µm PES syringe filters

Appendix Table 18. U(VI) speciation in *P. putida* 33015 low phosphate media (LPM). Calculations were made with Visual MINTEQ 3.1.

	U(VI) speciation distribution in LPM (%)			
	0.25 mM		0.5 mM	
U(VI) species	pH 5	pH 7	pH 5	pH 7
UO_2^{2+}	22.398		15.766	
UO_2OH^+	6.296	0.21	4.432	0.13
$(UO_2)_2(OH)_2^{2+}$	20.099	0.021	19.918	0.016
$(UO_2)_3(OH)_5^+$	28.686	69.677	40.023	65.733
$(UO_2)_4(OH)_7^+$	1.304	27.057	2.562	31.541
$(UO_2)_3(OH)_7^-$		2.137		2.016
$(UO_2)_3(OH)_4^{2+}$	3.144	0.029	4.387	0.027
$(UO_2)_2OH^{3+}$	0.711		0.704	
$UO_2(OH)^{3-}$		0.238		0.147
$UO_2(OH)_2$ (aq)	0.076	0.626	0.054	0.387
UO_2Cl_2 (aq)	0.257		0.181	
UO_2Cl^+	9.886		6.954	
UO_2SO_4 (aq)	6.916		4.857	
$UO_2(SO_4)_2^{2-}$	0.22		0.154	
$UO_2NO_3^+$	22.398		15.766	

Appendix Table 19. U(VI) speciation in *D. radiodurans* R1 low phosphate media (LPM) at pH 7. Calculations were made with Visual MINTEQ 3.1. Adjustments were made to take into account the chelated U(VI) [(*)] and subsequent bioavailable U(VI).

U(VI) speciation distribution in LPM (%)			
U(VI) species	0.05 mM	0.1 mM	0.25 mM
UO_2^{2+}	0.024	0.016	0.000
UO_2OH^+	0.959	0.633	0.352
$(UO_2)_2(OH)_2^{2+}$	0.077	0.067	0.052
$(UO_2)_3(OH)_5^+$	54.630	62.713	67.037
$(UO_2)_4(OH)_7^+$	8.781	13.298	19.705
$(UO_2)_3(OH)_7^-$	0.295	0.338	0.362
$(UO_2)_3(OH)_4^{2+}$	0.043	0.049	0.053
$UO_2(OH)^{3-}$	0.192	0.126	0.07
$UO_2(OH)_2$ (aq)	1.507	0.994	0.551
(*) UO_2NTA^-	**33.490**	**21.765**	**11.808**

Bioavailable U(VI) speciation distribution in LPM (%)			
U(VI) species	0.033 mM	0.078 mM	0.220 mM
UO_2^{2+}	0.036	0.020	0.000
UO_2OH^+	1.442	0.809	0.399
$(UO_2)_2(OH)_2^{2+}$	0.116	0.086	0.059
$(UO_2)_3(OH)_5^+$	82.138	80.160	76.013
$(UO_2)_4(OH)_7^+$	13.203	17.000	22.343
$(UO_2)_3(OH)_7^-$	0.444	0.432	0.410
$(UO_2)_3(OH)_4^{2+}$	0.065	0.063	0.061
$UO_2(OH)^{3-}$	0.289	0.161	0.079
$UO_2(OH)_2$ (aq)	2.266	1.271	0.625

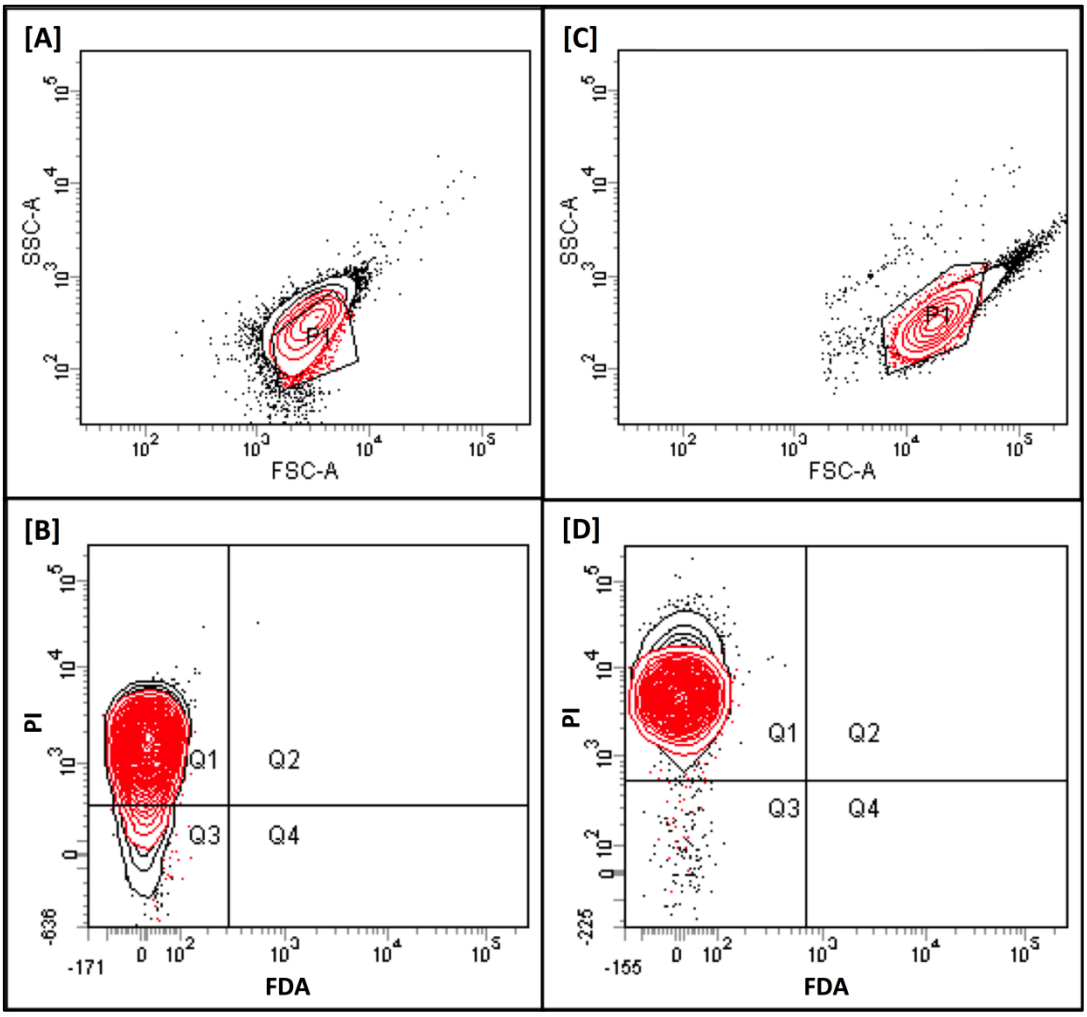

Appendix Figure 27. FDA/PI flow cytometric method adjustment for *P. putida* 33015 [A-B] and *D. radiodurans* R1 [C-D] dead cells. The P1 gate was applied [A, C] to remove cellular debris and other irrelevant material from analysis. Q1-Q4 gates were applied [B, D] and amended accordingly for live cells.

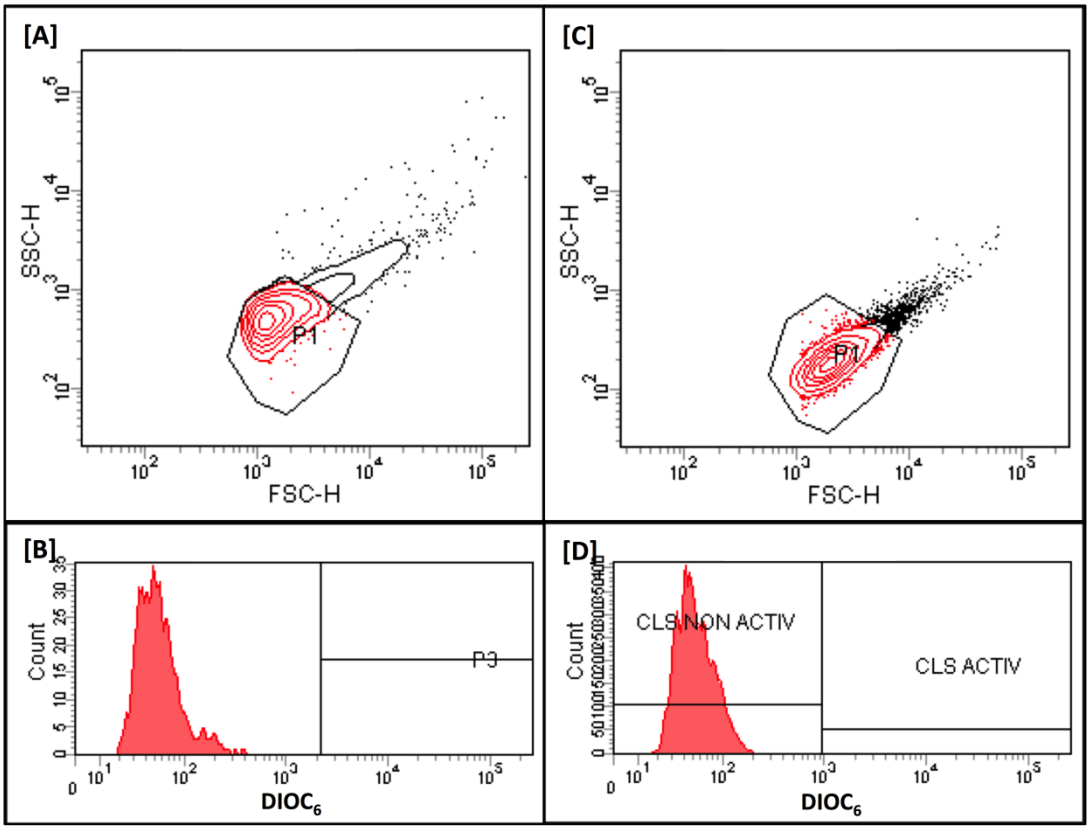

Appendix Figure 28. $DIOC_6$ flow cytometric method adjustment for *P. putida* 33015 [A-B] and *D. radiodurans* R1 [C-D] dead cells. The P1 gate was applied [A, C] to remove cellular debris and other irrelevant material from analysis. The P3/CLS ACTIV gates were applied [B, D] and amended accordingly for live cells.

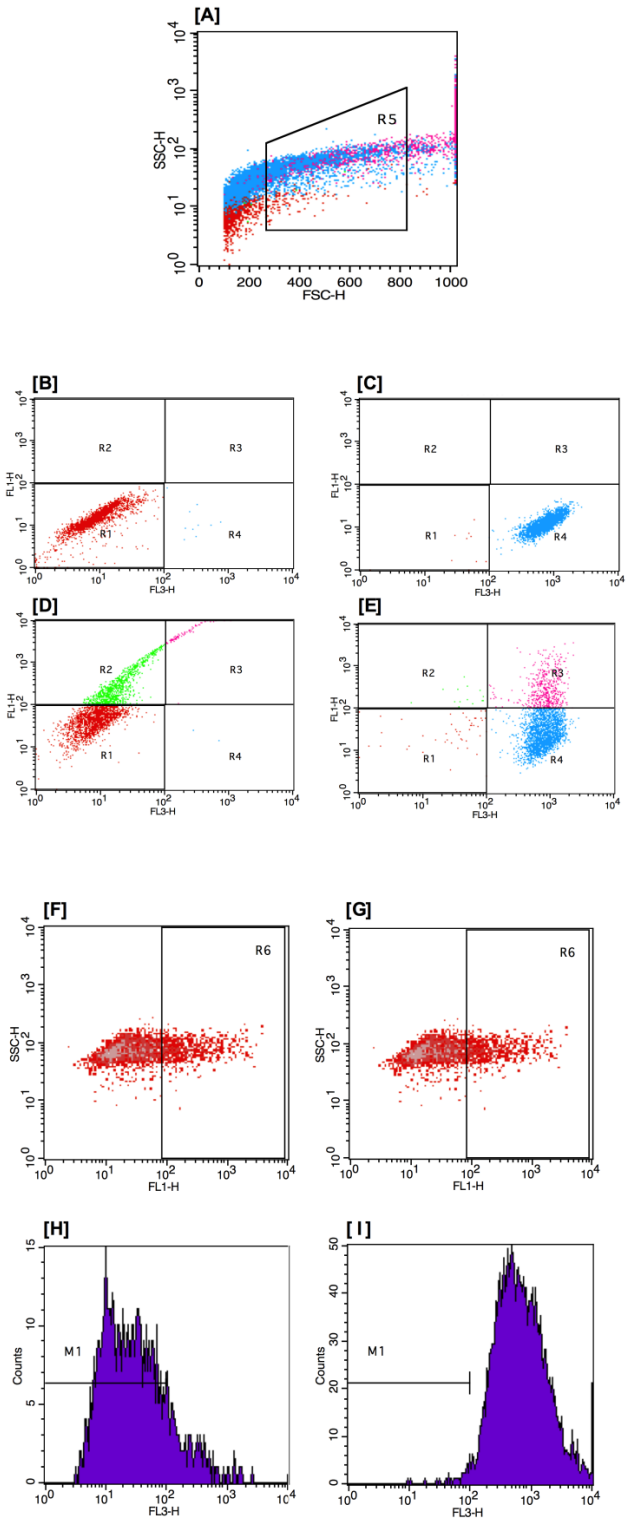

Appendix Figure 29. CTC/SYTO green flow cytometric method adjustment for *P. putida* 3015 control cells. The R5 gate was applied [A] to remove cellular debris and air bubbles from subsequent analysis. SSC-H measures cellular complexity and granularity and FSC-H measures cell size. R1, R2, R3 and R4 gates were applied to measure unstained cells [B], CTC+/SYTO- stained cells [C], CTC-/SYTO+ stained cells [D] and CTC+/SYTO+ stained cells [E]. The R6 gated region is for SYTO green stained cells [F-G]. SYTO green stained cells were only analysed to eliminate any other CTC stained debris as SYTO green is used for total cell counts. Flow cytometric histogram plots of CTC-/SYTO+ [H] and CTC+/SYTO- [I] stained cells. From this method set up, it indicated the concentration of SYTO green needed to be increased to take into account all the cells within suspension. Therefore, the quantity of SYTO green was increased from 2 µL to 6 µL.

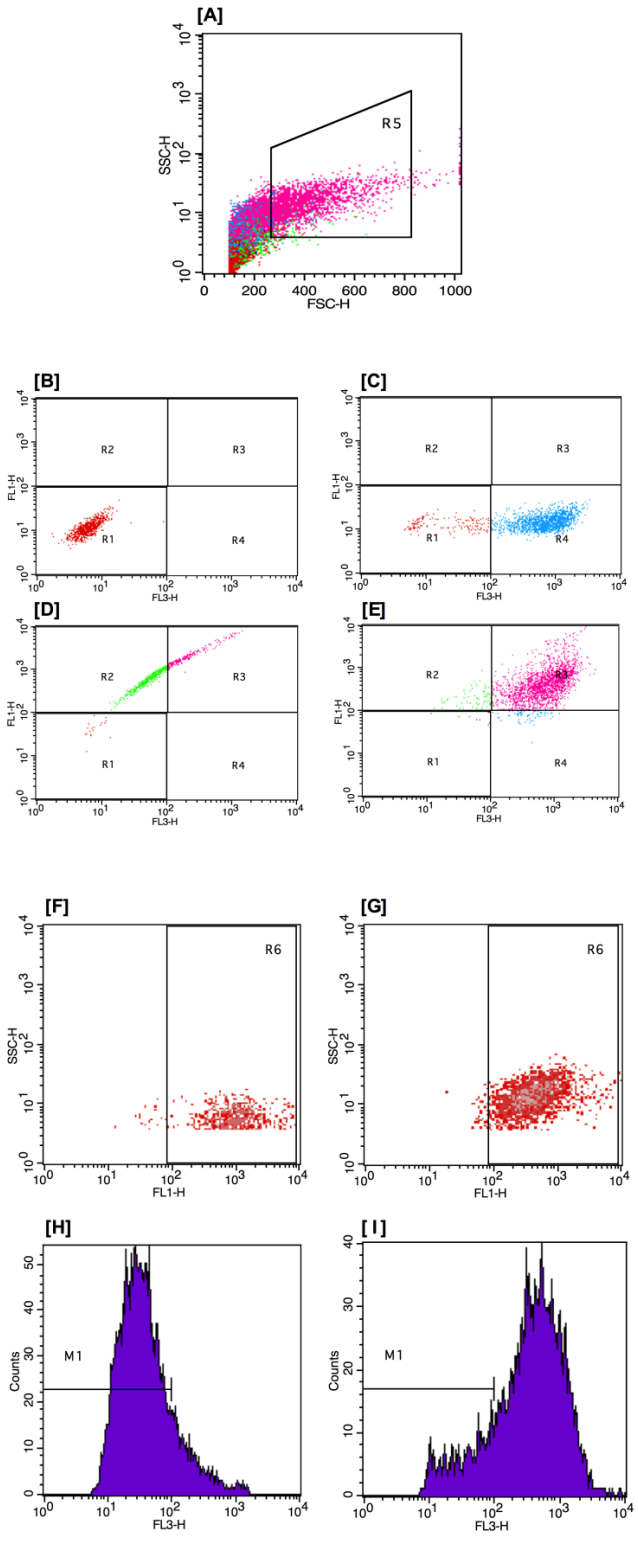

Appendix Figure 30. Flow cytometric method adjustment for *D. radiodurans* R1 control cells. The R5 gate was applied [A] to remove cellular debris and air bubbles from subsequent analysis. SSC-H measures cellular complexity and granularity and FSC-H measures cell size. R1, R2, R3 and R4 gates were applied to measure unstained cells [B], CTC+/SYTO- stained cells [C], CTC-/SYTO+ stained cells [D] and CTC+/SYTO+ stained cells [E]. The R6 gated region is for SYTO green stained cells [F-G]. SYTO green stained cells were only analysed to eliminate any other CTC stained debris as SYTO green is used for total cell counts. Flow cytometric histogram plots of CTC-/SYTO+ [H] and CTC+/SYTO- [I] stained cells. In comparison to the *P. putida* 33015 method set up, *D. radiodurans* cells were already stained with 6 µL of SYTO green.

Appendix Table 20. Cell viability, respiratory activity and metabolic activity of live *P. putida* and *D. radiodurans* cells following 48 hour growth at different uranium concentrations in their retrospective low phosphate media.

[U] (mM)	Cell Viability		Metabolic Activity		Respiratory Activity	
	% Alive	% Dead	% Active	% Inactive	% Active	% Inactive
P. putida 33015 (pH 5)						
0.00	76. 08 ± 4.48	23.92 ± 4.48	44.50 ± 2.26	55.5 ± 2.26	95.96 ± 5.73	4.04 ± 5.73
0.25	42.28 ± 5.26	57.72 ± 5.26	19.30 ± 0.96	80.7 ± 0.96	95.53 ± 3.77	4.47 ± 3.77
0.50	18.25 ± 2.44	81.75 ± 2.43	74.23 ± 10.15	25.77 ± 10.15	90.65 ± 6.08	9.35 ± 6.08
P. putida 33015 (pH 7)						
0.00	79.30 ± 11.74	20.70 ± 11.74	12.18 ± 10.07	87.82 ± 10.07	92.66 ± 7.27	7.34 ± 7.27
0.25	46.47 ± 8.84	53.53 ± 8.84	28.10 ± 3.71	71.90 ± 3.71	85.85 ± 6.16	14.15 ± 6.16
0.50	12.20 ± 4.30	87.80 ± 4.30	22.50 ± 5.78	77.50 ± 5.78	70.26 ± 5.39	29.74 ± 5.39
D. radiodurans R1 (pH 7)						
0.00	88.70 ± 2.80	11.30 ± 2.80	22.67 ± 1.82	77.33 ± 1.82	84.63 ± 16.82	15.37 ± 16.82
0.10	84.56 ± 2.20	15.44 ± 2.20	27.03 ± 1.10	72.97 ± 1.10	85.75 ± 14.89	14.25 ± 14.89
0.25	74.29 ± 20.62	20.61 ± 20.62	45.77 ± 12.09	54.23 ± 12.09	96.63 ± 3.52	3.37 ± 3.52

Standard deviation is included as ± S.D.